INVESTIGATING THE EFFECTS OF PASSIVE COMPLIANT COATINGS ON TRAILING-EDGE NOISE

By

© 2022

Rohith Giridhar

M.S., Aerospace Engineering, The University of Kansas, 2016

B.E., Mechanical Engineering, Bangalore Institute of Technology, 2013

Submitted to the graduate degree program in Aerospace Engineering and the Graduate Faculty of the University of Kansas School of Engineering in partial fulfillment of the requirements for the degree of Doctor of Philosophy

Committee:

_____

Dr. Saeed Farokhi, Co-Chairperson

_____

Dr. Ray Taghavi, Co-Chairperson

_____

Dr. Shawn Keshmiri, Committee Member

_____

Dr. Mark Ewing, Committee Member

_____

Dr. Mario Medina, Committee Member

Date Defended: September 1st, 2022

The dissertation committee for Rohith Giridhar certifies that this
is the approved version of the following dissertation:

INVESTIGATING THE EFFECTS OF PASSIVE COMPLIANT COATINGS ON TRAILING-EDGE NOISE

_____

Dr. Saeed Farokhi, Co-Chairperson

_____

Dr. Ray Taghavi, Co-Chairperson

Date Approved: September 6th, 2022

ABSTRACT

Trailing-edge noise is a significant noise source for various rotorcraft applications such as wind turbine rotors or propellers of unmanned aerial vehicles (UAVs). With growing dependence on wind energy and increasing usage of UAVs in military and commercial applications, it is imperative to address this shortcoming and ensure their wide spread application. In this dissertation, we investigate the noise mitigation potentials of passive compliant coatings through Computational Aeroacoustics Analysis (CAA) and experimentation through wind tunnel testing. It is hypothesized that compliant coatings damp the normal component of turbulent kinetic stresses through elastic surface deformation. Turbulent drag reduction and mitigation of flow-induced noise generated at the surface are direct byproducts. In the present study, CAA was performed on a flat plate for a chord-based Reynolds number of Re_c = 460,000 using the SST k-ω Improved Delayed Detached Eddy Simulation and the Ffowcs Williams and Hawkings acoustic analogy. Trailing-edge noise was accurately predicted from 750 – 7000 Hz. Next, baseline noise results were compared with the case when two coatings with different material properties are applied onto flat plate. It was observed coating-1 may increase trailing-edge noise by 10-15 dB throughout the frequency range of interest. Whereas coating-2 shifted the energy content in trailing-edge noise to a lower frequency range and reduced noise by 2-4 dB from 600-1575 Hz, thus demonstrating that choice of coating material properties plays a crucial role in its ability to mitigate trailing-edge noise. Furthermore, experiments conducted in a closed loop wind tunnel revealed that coating-2 reduced farfield noise by 3 dB from 40 – 1750 Hz with maximum reduction of 5.11 dB at 475 Hz, thus demonstrating the favorable effects of compliant coatings on trailing-edge noise.

Dedicated to Amma, Appa & my sister Amirtha

ACKNOWLEDGEMENTS

Firstly, I wish to convey my sincere gratitude and heartfelt thanks to my advisors Dr. Saeed Farokhi and Dr. Ray Taghavi. It is my privilege to have received both your valuable advice and guidance throughout my graduate education in the Aerospace Engineering Department at the University of Kansas (KUAE). I am extremely grateful for all the opportunities you have given me both in my research and in my teaching roles through my duties as a Graduate Teaching Assistant (GTA) for various courses at KUAE, both of which have been extraordinary learning experiences for me.

I wish to convey my sincere thanks and gratitude to Dr. Shawn Keshmiri for sponsoring our experimental study and procure the raw materials to prepare the compliant coating and for all your valuable inputs to improve this dissertation. My sincere gratitude to Dr. Mark Ewing for your valuable inputs in my experimental studies which helped me gain a greater depth in understanding and interpreting noise measurements. I also wish to sincerely thank you for providing me with acoustic liners that were used in my experimental studies. I am also very grateful to Dr. Mario Medina for all his valuable comments and suggestions that have been incorporated into this dissertation. I wish to convey my sincere thanks Dr. Wang for sponsoring me to use the High-Performance Computing Clusters at KU to perform my computational studies.

Furthermore, I wish to convey my sincere thanks to our Laboratory Co-Ordinator Mr. Brad Schroeder, and graduate students Mr. Robert Bowes, Dr. Mohammad Alhawwary and Ms. Lu Zhao for their help and support in performing my experiments. My thanks and gratitude to under-graduate students Ms. Catherine Craven, Ms. Nupoor Junnare and Mr. Greg Kipp for

TABLE OF CONTENTS

LIST OF FIGURES

LIST OF TABLES

NOMENCLATURE

Latin Letters

c	=	Chord Length, m
C_D	=	Drag Coefficient, ~
D	=	Drag, N
f_{MC}	=	Mesh Frequency Cutoff, Hz
U_∞	=	Freestream Velocity, m/s
k	=	Turbulent Kinetic Energy per Mass, J/kg
PSD	=	Power Spectral Density, Pa^2/Hz
S	=	Span Length of Flat Plate, m
$\overline{u_\iota'}$	=	Root Mean Square of Fluctuating Velocity
L_p	=	Power Spectral Density, dB

Greek Letters

Δ	=	Local Grid Spacing, m
ρ_∞	=	Density of Fluid in Freestream, kg/m^3

Abbreviations and Acronyms

2D	=	Two Dimensional
3D	=	Three Dimensional
BEM	=	Boundary Element Method
BPF	=	Blade Passing Frequency
BVI	=	Blade Vortex Interaction
CAA	=	Computational Aeroacoustics Analysis
CFD	=	Computational Fluid Dynamics
DLR	=	*Deutsches Zentrum für Luft- und Raumfahrt*
FW-H	=	Ffowcs Williams and Hawkings acoustic analogy
FISI	=	Flow Induced Surface Instabilities

IAG = Institute of Aerodynamics and Gas Dynamics, University of Stuttgart

IDDES = Improved Delayed Detached Eddy Simulation

IEC = International Electrotechnical Commission

LES = Large Eddy Simulation

LMFA = *Laboratorie de Mechanique des Fluides et d'Acoustique*

MUSCL = Monotonic Upwind Scheme for Conservation Laws

NACA = National Advisory Committee for Aeronautics

NASA = National Aeronautics and Space Administration

NREL = National Renewable Energy Laboratory

RANS = Reynolds Averaged Navier Stokes

RPM = Revolutions Per Minute

RSNM = RANS Based Statistical Noise Model

SDI = Static Divergence Instabilities

SIMPLE = Semi-Implicit Method for Pressure-Linkage Equations

SST = Shear Stress Transport

TAVU = Tel-Aviv University

TWF = Travelling Wave Flutter

TSI = Tollmien-Schlichting Instabilities

UAV = Unmanned Aerial Vehicles

URANS = Unsteady Reynolds-Averaged Navier Stokes

UWPW = Uncorrelated Wall Plane Wave

1. INTRODUCTION

Wind is now the largest source of renewable energy in the United States contributing 9.7% to its total electricity production [1]. In the year 2020, wind turbine installation in the United States surpassed 150 GW, thus capable of providing power to over 48 million houses. Consequently, it is imperative to address the shortcomings in modern day wind turbines and ensure their widespread application. One such area to be addressed is the noise generated by their rotor blades, with trailing-edge noise being the dominant noise source [2, 3].

1.1. Motivation for Research

When installed closer to residential areas, studies showed that noise generated by wind turbine rotors cause annoyance and sleep disturbance to people living in its vicinity [4]. Further studies revealed the detrimental effects of noise include impaired mental health of residents living within 0.9 miles from the installation [5]. Therefore, wind turbine installations close to residential areas are not well accepted. Mitigating this noise would make their installation closer to residential areas admissible, thus opening more avenues for wider spread of wind power applications.

Various active and passive flow control techniques were investigated to mitigate trailing-edge noise in relevance to wind turbine applications. Passive flow controls include trailing-edge serrations [6-9], trailing-edge brushes [10-11], porous airfoils [12-14] and skin treatment [15-16]. Whereas, active flow controls include flow suction and injection into the boundary layer [17-20] to reduce surface pressure field and turbulent fluctuations.

The present study investigates noise mitigation potentials of homogeneous visco-elastic compliant coating through Computational Aeroacoustics Analysis (CAA) and experimentation through wind tunnel testing using the Closed Loop Subsonic Wind Tunnel in the Aerospace Engineering Department at the University of Kansas, Lawrence.

1.2.   Passive Compliant Coatings

Passive compliant coatings are an inspiration from nature, i.e., dolphin's epidermis, which showed its boundary layer can remain laminar up to a Reynolds number of 20 million [21]. When applied to rigid surfaces, compliant coatings modify boundary layer characteristics upstream of the trailing-edge and provide constructive coupling in wall bounded flows. Laminar to turbulence transition may be delayed resulting in an order of magnitude reduction in skin friction [22]. They also interact favorably in fully turbulent flows to reduce surface skin friction and prevent boundary layer separation. Thus, flow-induced noise may be mitigated as a consequence of constructive coupling with compliant coatings.

Application of passive compliant coating was initially investigated for hydrodynamic flows, since water and coating have comparable densities. This ensured that the compliant wall and would have comparable wall and fluid inertias. Thus, wall compliance offered significant impact on the Tollmien-Schlichting instabilities [23]. In recent years, these investigations were extended to aeronautical applications.

1.3.   Hypothesis

It is hypothesized that when compliant coatings are applied over a surface, it would help damp the normal component of turbulent kinetic stresses through elastic surface

deformation; thus absorb (or soak up) the turbulent kinetic energy (TKE) within the boundary layer. The extent of TKE mitigation depends on coating material properties, surface geometry and Reynolds number. Turbulent drag reduction and mitigation of flow-induced noise generated at the surface are the direct byproducts of turbulence stress modulation caused by an aerodynamic surface covered by compliant coating.

When compared to other noise mitigation techniques, passive compliant coatings represent a practical approach that are both inexpensive and do not require sensors/actuators to control the flow. Structural issues encountered while mitigating noise for instance, from trailing-edge treatment are absent. Using a *stiff* homogeneous compliant coating [24], characterized by a modulus of elasticity greater than 0.5 MPa, not only aids in constructive coupling and enables drag reduction but also ensures material durability. The added benefit of profile drag reduction, favorably impacts torque generated by wind turbine rotors and lessen its bending moment. These benefits, along with their feasibility of use in combination with other noise mitigation techniques, show that compliant coatings are prime candidates for practical applications on large scale wind turbines to achieve noise attenuation.

1.4.   Present Study

In the present study, homogeneous visco-elastic compliant coatings are chosen to investigate their ability to modify the boundary layer characteristics upstream of the trailing-edge and provide constructive coupling with the flowfield., We have chosen a flat plate in fully turbulent flow to demonstrate the technique. Three cases are analyzed in this study:

1.4.1. Validation case

In the present computational study, the far-field noise generated by a flat plate is compared with noise measurements by Moreau et al. [25]. This is used to demonstrate the ability of our present computational analysis to accurately predict trailing-edge noise.

Fig. 1.1: Schematic diagram of flat plate (rigid) model used for Validation

1.4.2. Baseline case

When a compliant coating with certain thickness is uniformly applied to the flat plate shown in Fig. 1, it changes the dimensions and alters its trailing-edge shape, as shown in Fig. 2. This in turn would alter its aerodynamic characteristics. To account for this, the coating's outer profile is used to create a rigid flat plate model with new dimensions and trailing-edge shape. This rigid flat plate model with rounded trailing edge shall be treated as baseline for the present study.

Fig. 1.2: Schematic diagram of Baseline (rigid) model

4

1.4.3. Case of compliant coating applied to a flat plate

Fig. 3 represents a schematic diagram of the case when a compliant coating is applied to the flat plate shown in Fig. 1. Effects of this compliant coating on trailing-edge noise shall be compared to results obtained from the baseline model. Fluid structure Interaction technique shall be used to simulate the compliant coating behavior and its effects on flow boundary layer.

Fig. 1.3: Schematic diagram of compliant coating applied to flat plate

Experimental studies from literature point towards two such compliant coatings, with different stiffness characteristics, that have exhibited constructive coupling with flow boundary layer. These coatings reduce the amplitude of Tollmien-Schlichting (TS) waves, within the transition region of flow boundary layer [26, 27]. They have also shown their ability to reduce skin friction drag in fully turbulent flow [24]. The present study uses materials properties from these coatings, such as stiffness, density and poison's ratio; to simulate coating deformation, predict flow behavior downstream of trailing-edge using unsteady Computational Fluid Dynamics (CFD) analysis and predict farfield noise using the Ffowcs Williams and Hawkings (FW-H) model based on Lighthill's acoustic analogy.

5

1.5. Proposal for Final Defense

Among the two compliant coatings that were studied using CFD and CAA analysis, one of the coatings [27-30] exhibited the desired characteristics in mitigating trailing-edge noise for low frequency ranges. This coating was chosen for experimentation through wind tunnel testing. A prototype of the coating shall be manufactured and applied on a flat plate in fully turbulent flow. Flow measurements shall be recorded downstream of the trailing-edge using pitot static probes and farfield noise measurements shall be recorded using microphones to study the effects of passive compliant coatings on flow boundary layer and trailing-edge noise. A detailed proposal for the same to be completed by the Final defense is presented in this Comprehensive Exam Report.

1.6. Other Applications of Passive Compliant Coatings

It must be noted that the favorable effects of compliant coatings are not limited to wind turbine applications alone. There is an emerging area of research with interest in mitigating propeller noise generated from Unmanned Aerial Vehicles (UAVs), as shown in the works by Brungert et al. [31]. Mitigating propeller noise in UAVs would be useful for stealth applications in the military or for commercial applications, such as drone deliveries. Application of passive compliant coating to mitigate propeller noise would involve the same mechanisms for noise mitigation, though their flow operating conditions would be different from that of wind turbines. This would in turn require suitable modifications to compliant coating materials properties, based on the application.

2. REVIEW OF LITERATURE

In the last few decades, various active and passive flow control techniques were investigated to explore their effect in noise mitigation when applied to flat-plate and airfoil geometries. Based on these results, some noise mitigation techniques were extended to wind turbine rotors to study if their favorable effects translate to a three-dimensional framework.

2.1. Noise Mitigation Studies Explored Previously

2.1.1. Trailing-Edge Serrations

Howe [6] analytically investigated noise mitigation capabilities of a flat plate with serrated trailing-edge at low Mach numbers. These serrations had a saw tooth profile with wavelength λ and a root-to-tip distance of *2h,* as shown in Fig. 2.1.
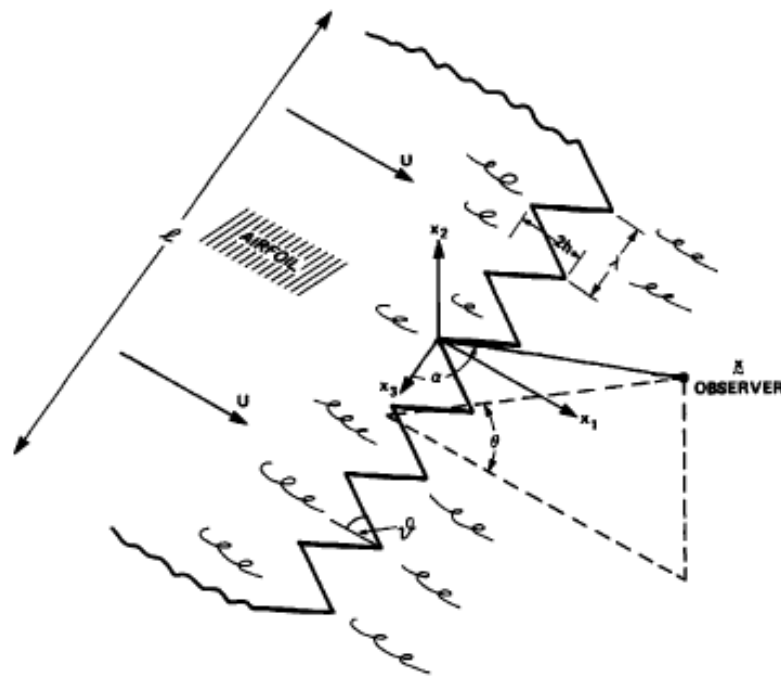
Fig. 2.1: Turbulent flow past a flat plate with serrated trailing-edge [6]

7

The analysis indicated that using serrations helped reduce intensity of noise radiation by $10 \log \left[1 + \left(\frac{4h}{\lambda} \right)^2 \right]$ dB. This was achieved by reducing effective length of the trailing-edge. Numerical studies also indicated that noise attenuation significantly increased if $\frac{\lambda}{h} \lesssim 5$, which ensured that the edges of serrations were inclined at an angle $\nu < 45°$ with respect to the incoming flow.

Experiments were conducted by Moreau et al. [7] to study noise attenuation capabilities of saw tooth trailing-edge serrations on flat plate geometries for chord-based Reynolds number from 160,000 to 420,000 in the anechoic wind-tunnel test chamber located at the University of Adelaide, as shown in Fig. 2.2.
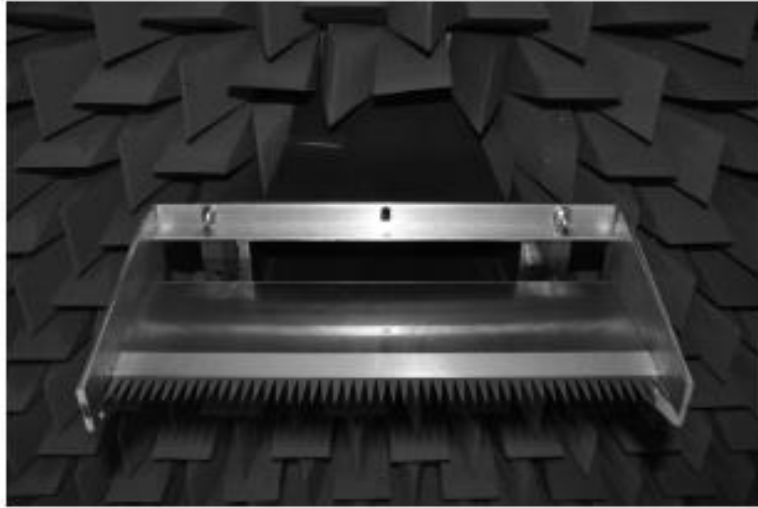
Fig. 2.2: Flat plate model with trailing-edge serrations in anechoic test chamber [7]

The flat plate model was held between two side plates and attached to a contraction outlet at 0° angle of attack. The walls of the test chamber were acoustically treated with foam wedges to provide a reflection free environment above 250 Hz.
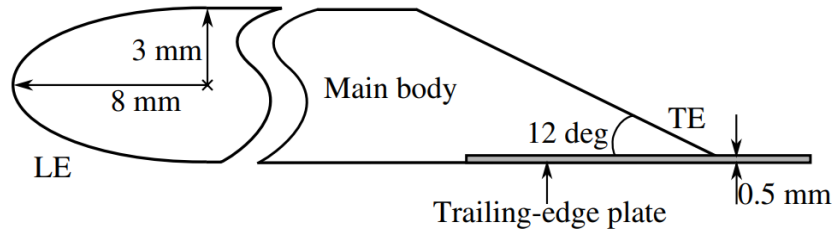
Fig. 2.3: Schematic diagram of flat plate model [7]

The flat plate model used by Moreau et al. consisted of a main body, as shown in Fig. 2.3, with detachable trailing-edge plates, as shown in Fig. 2.4. It was found that trailing-edge serrations minimized broadband noise levels up to 3 dB at low frequencies and up to 13 dB at high frequencies by attenuating blunt vortex-shedding noise.
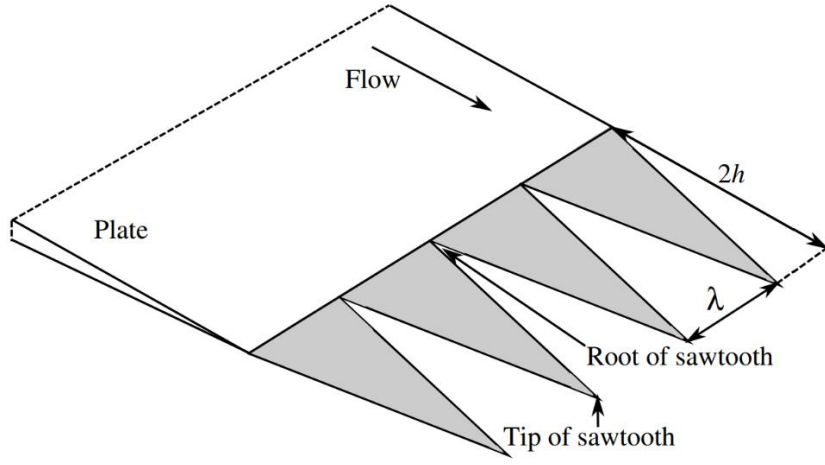
Fig. 2.4: Schematic diagram of sawtooth serrations [7]

Oerlemans et al. [2] conducted acoustic field measurements on a 94 m diameter 2.3 MW three bladed wind turbine rotor; with one standard blade, one blade with trailing-edge serrations as shown in Fig. 2.5 and one blade with acoustically optimized airfoil. The two modified blades showed significant trailing-edge noise attenuation at lower frequencies and an increase in tip noise at higher frequencies. An average overall noise

reduction of 0.5 dB for the optimized blade and 3.2 dB reduction for the serrated blade was observed.

Fig. 2.5: Wind turbine blade with serrated trailing-edge [2]

Oerlemans [3] also conducted optimization studies on a Siemens designed airfoil at 3-4 million chord-based Reynolds number through acoustic wind tunnel tests at Virginia Tech as shown in Fig. 2.6 and full-scale field measurements on a Siemens turbine to study the effects of design parameters such as serration tooth length, aspect ratio, tooth angle and their flexibility.
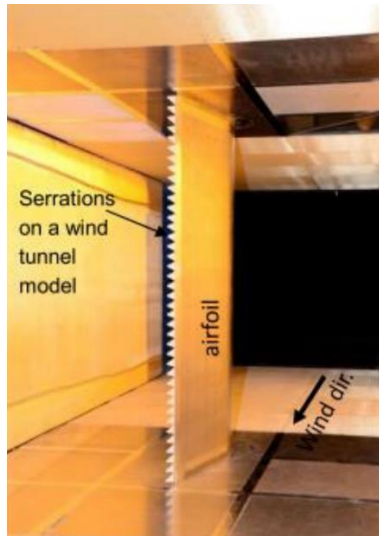
Fig. 2.6: Acoustic wind tunnel at Virginia Tech [3]

Siemens serrations, shown in Fig. 2.7, yielded considerable noise reductions at all wind speeds and the acoustic energy shifted towards higher frequencies. Using serrations with optimum design parameters on the Siemens wind turbine resulted in an overall A-weighted noise reduction of 1.1 dB when noise was measured at the IEC standard position from the turbine. This translates to 2.4 dB at 500 m and 3 dB at 1 km away from the turbine.

Fig. 2.7: Siemens airfoil trailing-edge serrations [3]

Using combed saw tooth serrations, as shown in Fig. 2.8, displayed further noise reduction potential than the optimized serrations.
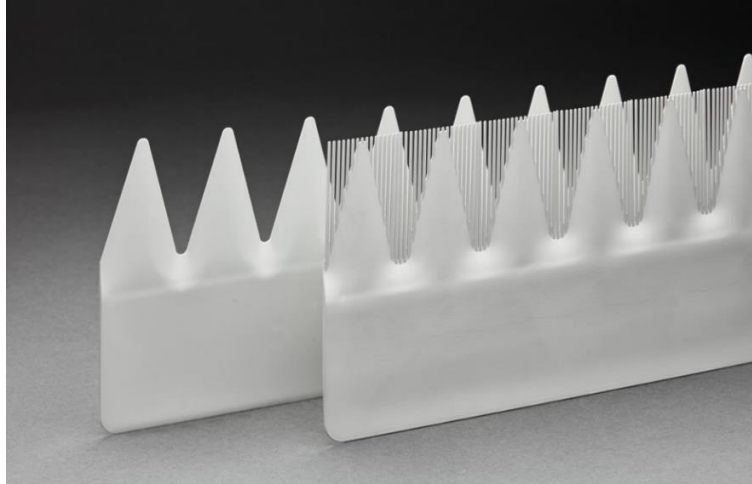
Fig. 2.8: Comparison of optimized serrations and combed teeth [3]

Avallone et al. [8] further explored noise mitigation capabilities of conventional serrations and combed tooth serrations (shown in Fig. 2.9) on turbulent boundary layer trailing-edge noise employing computational analyses using different serration configurations on a NACA 0018 airfoil at 0° angle of attack. CFD simulations were carried out using the compressible Lattice Boltzmann solver for a chord-based Reynolds number of 280,000. The acoustic field was obtained using Ffowcs Williams and Hawkings (FW-H) acoustic analogy.
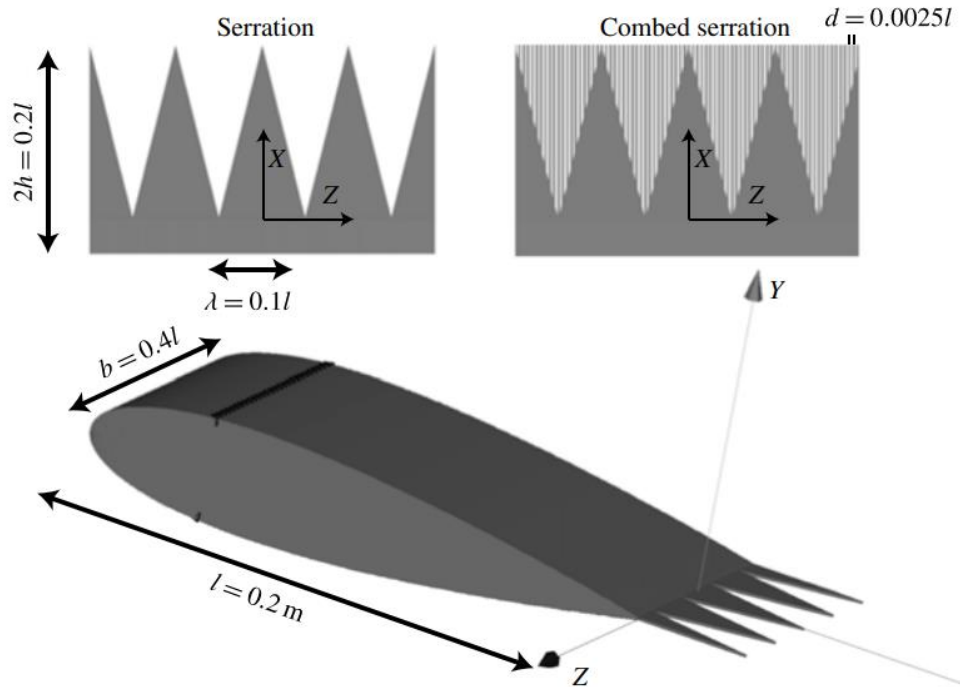
Fig. 2.9: NACA 0018 airfoil retrofitted with serration configurations [8]

Installation of combs minimized flow interaction on either sides of the serrations and helped avoid formation of wake in space between the teeth, thus generating a more uniform distribution of noise sources. Furthermore, using combed saw tooth serrations yielded an additional 3 dB noise reduction when compared to conventional saw tooth serrations.

Avallone et al. [9] also performed further computational analyses to study the effects of curved trailing-edge serrations, as shown in Fig. 2.10, in comparison to conventional saw tooth serrations on trailing-edge noise mitigation and observed a further noise reduction of 2 dB when compared to conventional serrations. This effect was attributed

to the ability of iron shaped serrations to mitigate scattered noise at its root by delaying the flow's tendency to deviate from the serration's centerline to its edge.
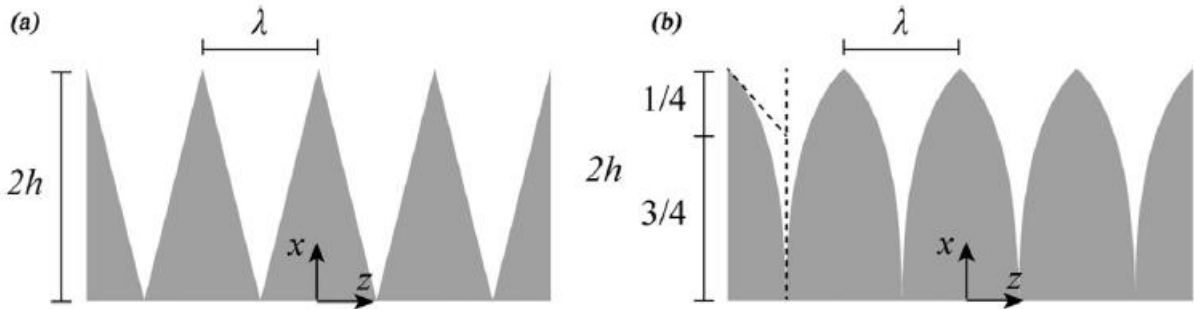
Fig. 2.10: (a) Conventional sawtooth serrations versus (b) Iron shaped saw tooth serrations [9]

2.1.2. Trailing-Edge Brushes

Experiments were conducted by Finez et al. [10] on a cambered NACA 65(12)-10 airfoil by modifying its trailing-edge to include compliant single row of brushes to study its noise mitigation capabilities in a small anechoic room of *Laboratorie de Mechanique des Fluides et d'Acoustique (LMFA)* at Ecole Centrale de Lyon. Trailing-edge brushes consist of polypropylene fibers inserted into a resin extension, as shown in Fig. 2.11.

Fig. 2.11: Trailing-edge brushes with single row of polypropylene fibers [10]

It was found that fine fibers of the trailing-edge brushes could disorganize the turbulent structures, thus achieving a noise reduction up to 3 dB in a frequency range of 600-2000 Hz. The trailing-edge brushes also reduced spanwise coherence length of the boundary layer by 25% which corresponds to 1.3 dB noise reduction.

Experiments were conducted by Herr and Dobrzynski [11] in an open jet anechoic test facility of DLR's aeroacoustic wind tunnel, Braunschweig (AWB), as shown in Fig. 2.12, to perform a parametric study on brush type trailing-edge serrations. Experiments included both acoustic and aerodynamic measurements performed on a flat-plate model at 0° angle of attack at high chord-based Reynolds number from 2,100,000 to 7,900,000.

Fig. 2.12: Flat plate model in test section of DLR's aeroacoustic wind tunnel, Braunschweig [11]

Design parameters such as brush length and fiber diameter were varied and different brush configurations were tested. It was observed that flexible fibers cause minimum disturbance and thus adapt to the flow.

Fig. 2.13: Trailing-edge brush attached to flat plate [11]

The brush edges, as shown in Fig. 2.13, were able to reduce both turbulent boundary layer trailing-edge noise and trailing-edge bluntness noise by 2 dB and up to 14 dB respectively over the frequency range of noise spectrum. This was attributed to the ability of trailing-edge brushes to mitigate the abrupt change in boundary conditions of a solid trailing-edge interacting with turbulent flow. Additionally, the transformation of spanwise vorticity into streamwise vorticity further facilitated this noise mitigation.

2.1.3. *Porous Airfoils*

Experiments were conducted by Geyer et al. [12] to study the effects of porous airfoils and their ability to mitigate noise, an inspiration drawn from soft and elastic downy upper surface of owl's feathers which display characteristics of wing porosity to achieve quiet flight. Sixteen different porous airfoils with different flow resistivity,

as shown in Fig. 2.14, were tested under the same flow conditions and compared to a solid reference SD7003 airfoil.

Fig. 2.14: Different porous airfoils used in the experiment [12]

Tests were conducted in the aerocoustic wind tunnel at the Brandenburg Technical University of Cottbus, as shown in Fig. 2.15, where it was observed that porous airfoils could achieve up to 10 dB noise reduction at low and mid frequencies and the extent of noise reduction correlated to flow resistivity of the porous material. However, at high frequencies, the porous airfoil produced greater noise than the reference airfoil and this was attributed to the increased roughness from the porous surface.
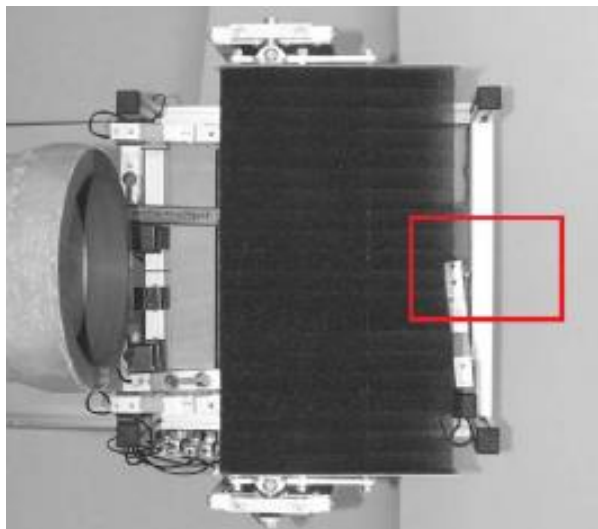
Fig. 2.15: Porous airfoil mounted on a test set-up in an anechoic wind tunnel [12]

[Red box indicates region used to integrate trailing-edge noise sources]

17

Aerodynamic tests revealed that using porous airfoils resulted in reduced lift and increased drag when compared to solid reference airfoil. Hence, it was recommended that partly porous airfoils with non-porous leading-edge and porous trailing-edge be explored for further study.

Numerical studies [13] were conducted on a flat plate geometry using a hybrid Large Eddy Simulation (LES) and Computational Aeroacoustics Analysis (CAA) to investigate the impact of porous materials with variable properties on trailing-edge noise mitigation. Since trailing-edge noise is influenced by the shape of the trailing-edge, two shapes with sharp trailing-edge and rounded trailing-edge were considered for solid and porous surfaces. The porous surface was included near the trailing-edge of the flat plate and extended by a distance of *d=4h*; where *h* is the thickness of the flat plate *(h=0.03c)* as shown in Fig 2.16.
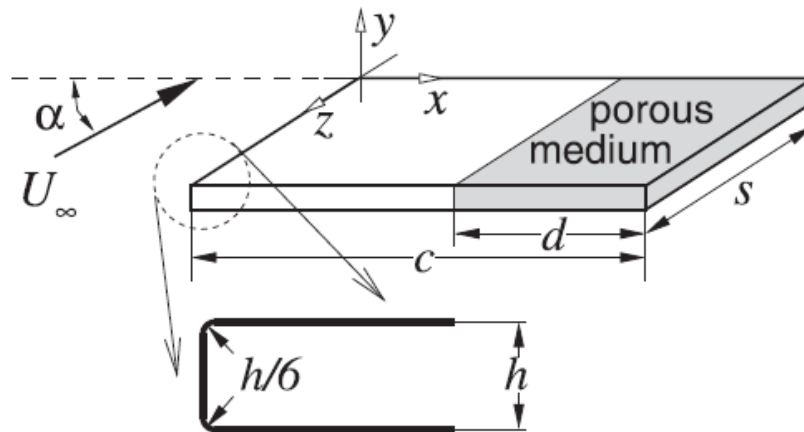
Fig. 2.16: Flat plate with porous medium near trailing-edge [13]

Viscous dissipation in porous structures reduced the correlation length of turbulent eddies and flow acceleration near trailing-edge of the flat plate and thus aided in noise

18

attenuation. A maximum noise attenuation of 4 dB was achieved using porous media near trailing-edge of the flat plate.

Zhou et al. [14] extended this study to develop an algorithm based on discrete adjoint framework to optimize the distribution of porous material near the flat plate to minimize trailing-edge noise. This study was conducted by varying parameters such as material porosity, viscous and thermal permeability which resulted in significant noise mitigation. It was found from this numerical study that optimum design of porous trailing-edge, as shown in Fig. 2.17, resulted in a noise reduction up to 12 dB with respect to a flat plate with no porous trailing-edge and a 3 dB noise reduction with respect to the baseline design with linear porosity variation.
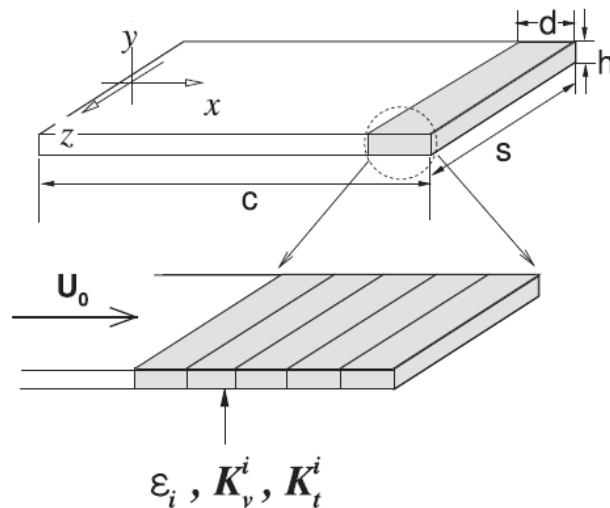
Fig. 2.17: Discrete porous strips used to form porous trailing-edge [14]

2.1.4. Surface Treatments

Clark et al. [15] performed experimental studies at the Virginia Tech stability wind tunnel to mitigate trailing-edge noise by developing surface treatments inspired by the

downy canopy that cover flight feathers of owls that displayed effects of mitigating surface pressure fluctuations.
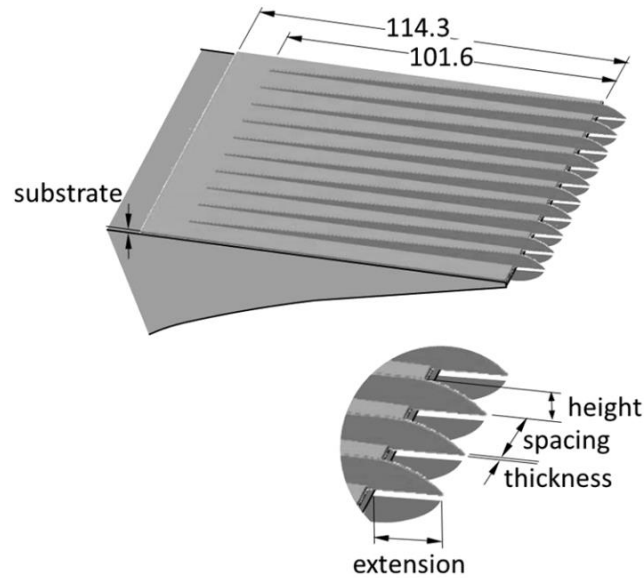
Fig. 2.18: Finlet-fence treatment near airfoil trailing-edge [15]
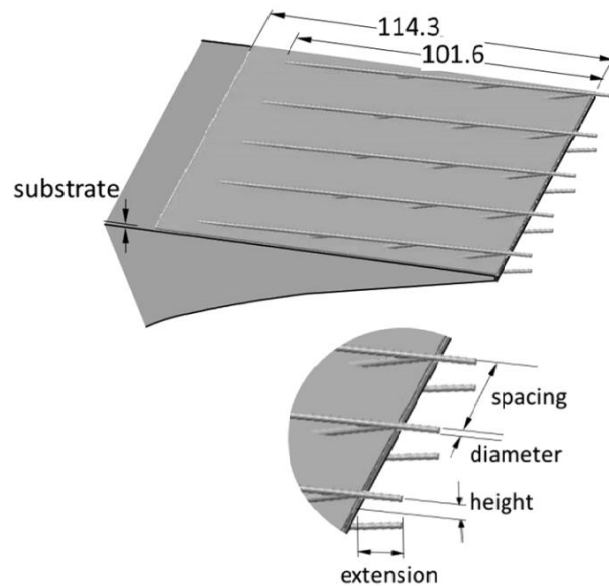
Fig. 2.19: Finlet-rail treatment near airfoil trailing-edge [15]

When compared to an untreated airfoil, the airfoil with skin treatments, as shown in Fig. 2.18 and 2.19, were able to mitigate broadband trailing-edge noise up to 10 dB

and proved to be effective for a range of angles of attack up to 9° from zero lift condition. Airfoil lift was unaffected in the same conditions, though there was as slight increase in drag due to increase in wetted surface area with inclusion of skin treatment. The noise mitigation mechanism is attributed to the ability of finlets to cut, deform and decorrelate turbulent structures present within the boundary layer.

Afshari et al. [16] extended the study on noise mitigation capabilities of fence-type finlets, as shown in Fig. 20, by conducting experiments on a flat plate model with 2D and 3D finlet configurations located upstream of its trailing-edge in the blow-down wind tunnel at Yazd University on a flat-plate model for a chord-based Reynolds number of 773,000 and 0° angle of attack. The boundary layer was tripped at 5% chord downstream of the leading-edge to ensure fully turbulent flow on the flat-plate.
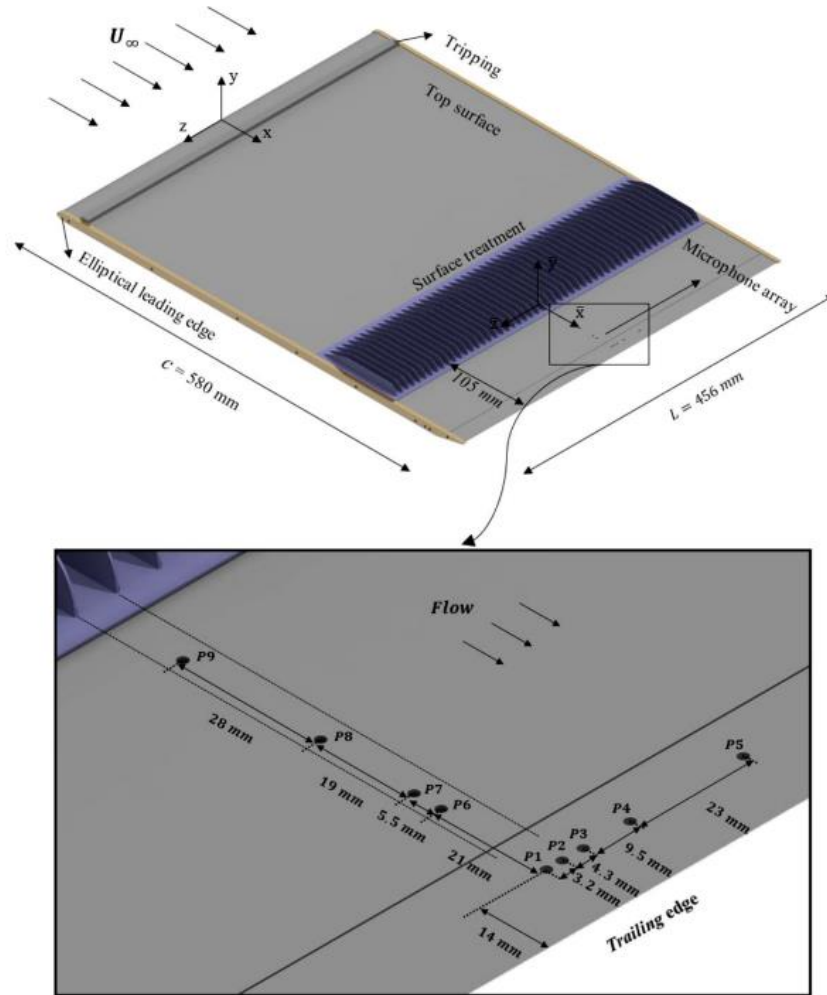
Fig. 2.20: Flat-plate model with finlets located upstream of trailing-edge [16]
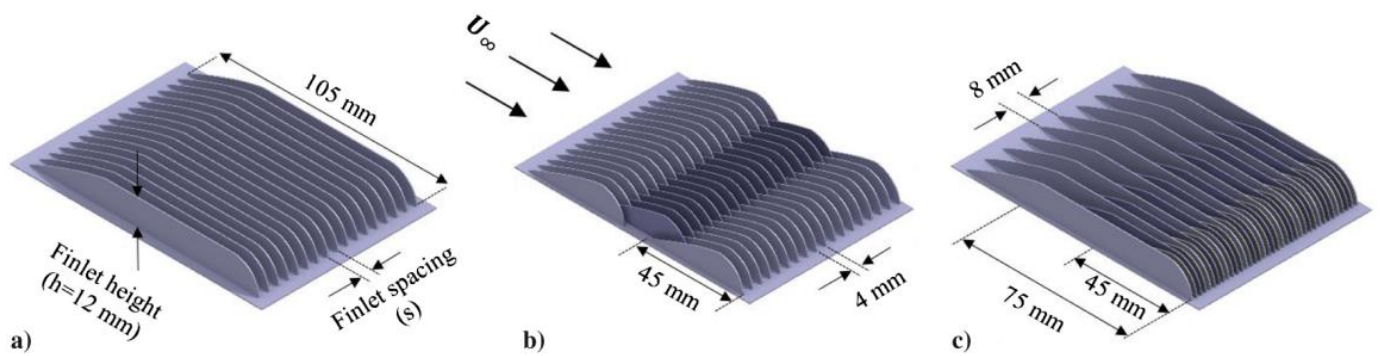
Fig. 2.21: (a) U-type configuration (b) S-type configuration (c) G-type configuration [16]

Though all treatments shown in Fig. 2.21 were effective in reducing noise at mid to high frequencies, the treatments appeared to increase noise at higher frequencies. The U-type finlets produced noise reduction up to 11 dB at higher frequencies of 8kHz but resulted in an increase in noise of 2.5 dB at frequencies lower than 300 Hz and this effect intensified with decrease in finlet spacing. The S-type and G-type configurations showed further reduction in noise measurements when compared to 2D configurations. This was attributed to the ability of 3D skin treatments to lessen flow separation and shear layer formation downstream of the finlets which aided in trailing-edge noise mitigation.

2.1.5. Active Flow Control

Active flow control methods of trailing-edge noise mitigation could be achieved by altering hydrodynamic pressure field present within the boundary layer upstream of the trailing-edge. This can be achieved either by reducing the surface pressure field using flow suction or by injecting flow into the boundary layer. The latter approach requires lower amount of external energy and is more effective than passive noise mitigation techniques and was thus explored Szoke et al. [17] in their experimental studies.

Experiments were conducted on a flat-plate with a sharp trailing-edge at a chord-based Reynolds number of 1,000,000 in an open-jet return type wind tunnel at the University of Bristol. An 80-grit sandpaper located downstream of the semi-elliptical leading edge was used to trip the boundary layer to ensure fully turbulent flow on the flat-plate. A single array of jets nozzles inclined at angle 15° to the streamwise flow

direction was placed along the span upstream of the trailing-edge, as shown in Fig. 2.22.
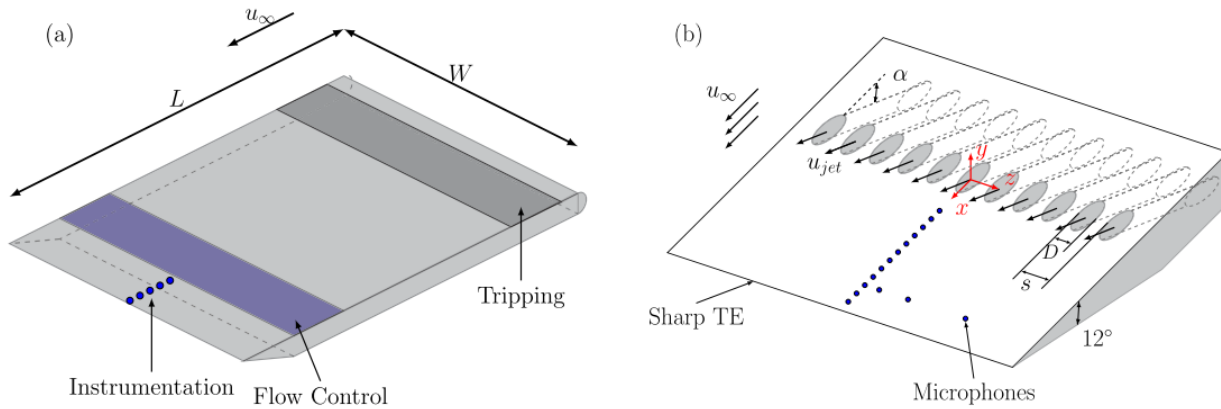
Fig. 2.22: (a) Schematic diagram of flat-plate with active flow control upstream of trailing-edge (b) Array of jet nozzles placed upstream of trailing-edge [17]

Pressure-velocity cross spectral analysis also revealed that velocity fluctuations are decoupled from pressure fluctuations in the low energy content boundary layer, which resulted in attenuation of surface pressure fluctuations and hence lower surface flow noise.

Experiments [18] were performed in the Mixing Layer facility at Tel-Aviv University (TAVU) to study the effects of active flow control technique using distributed wall normal suction on boundary layer parameters of a flat-plate to mitigate trailing-edge noise, as shown in Fig. 2.23.
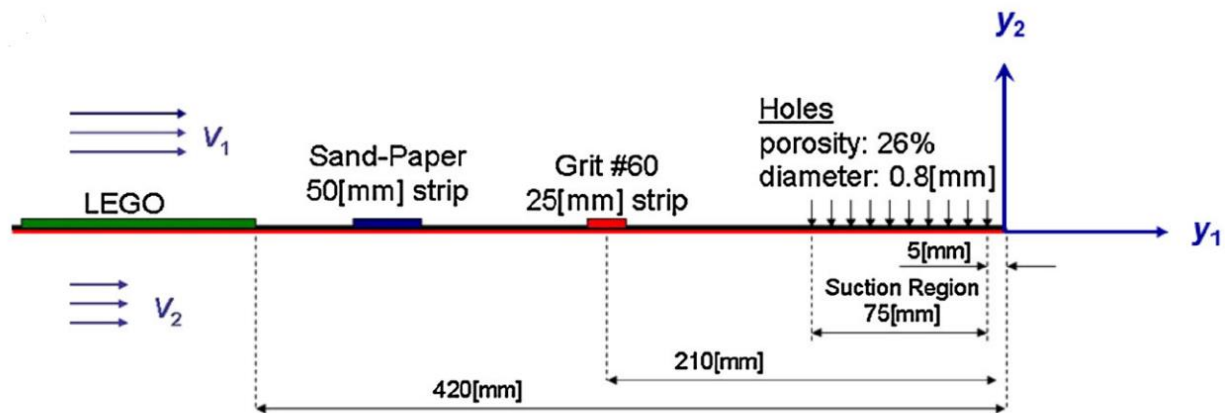
Fig. 2.23: Boundary layer tripping and distributed suction on flat-plate [18]

A splitter plate mounted in the mixing layer facility was used to apply wall-normal suction. The boundary layer was artificially tripped using Legos and sand paper to ensure fully turbulent flow on flat-plate. Unsteady velocity measurements of the boundary layer near trailing-edge using hot wire anemometry showed promising results indicative of trailing-edge noise reduction.

Thus, further experiments were conducted in the laminar wind tunnel at the Institute of Aerodynamics and Gas Dynamics (IAG), as shown in Fig 2.23, where the effects of boundary layer suction were studied using a NACA 64_3-418 airfoil, typically used in the outboard region of wind turbine rotors.
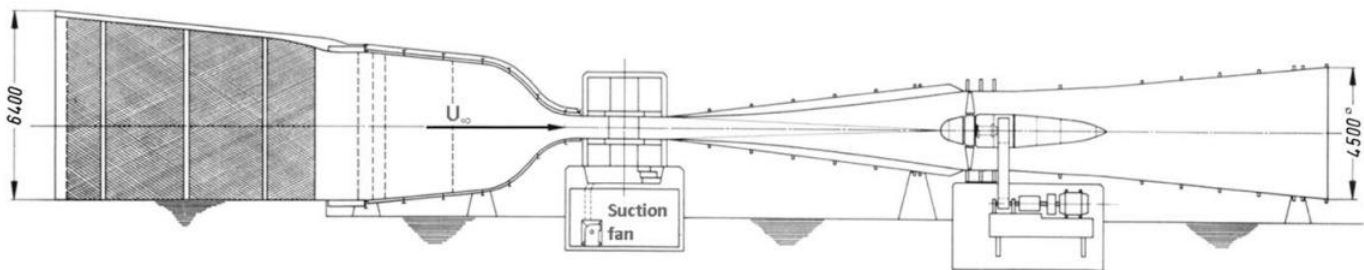
Fig. 2.24: Schematic diagram of the laminar wind tunnel at IAG [18]

It was observed that the active flow control system was able to reduce velocity fluctuations on both suction and pressure sides of the airfoil, with the main noise contribution present on the suction side. A significant reduction in broadband trailing-edge noise measurements were observed in the low frequency range which dominate the overall noise generated. This effect increased with increase in suction flow rate and an overall noise reduction of up to 3.5 dB was achieved.

Arnold et al. [19] investigated the effects of boundary layer suction on the NREL 5 MW wind turbine rotor to study if trailing-edge noise mitigation observed for two dimensional flows was carried over to a wind turbine flow. A fully resolved URANS computation was performed on the NREL 5 MW wind turbine and the effects of boundary layer suction and blowing were studied.

Based on these computational studies, a design method was implemented on the NREL 5 MW wind turbine to understand the effects of pump power requirement to provide the necessary boundary layer suction and its effect on trailing-edge noise mitigation. For a certain design regime corresponding to pump power, both trailing-edge noise reduction and improved aerodynamic performance was observed. A maximum increase in rotor power of 2% was coupled with a trailing-edge noise reduction of 2.5 dB. However, when a maximum trailing-edge noise reduction of 3.2 dB was achieved, there was a cross-over point when the required pump power compensated for the improved aerodynamic power. Beyond this cross-over point, improved aeroacoustics could only be achieved at the cost of poor aerodynamic performance.

To further demonstrate this ability of boundary layer suction in mitigating low frequency noise by thinning of the boundary layer, experiments were conducted on the state-of-the-art industrial N117 turbine with emphasis laid on industrial requirements [20]. It was observed that using this active flow control technique resulted in a noise reduction of 3.6 dB and an aerodynamic benefit of up to 4.75% improvement in rotor power. With increase in pump power, further improvement in noise reduction up to 5 dB was observed beyond which further aeroacoustic benefits were attained at the cost of poor aerodynamic performance.

2.2. Use of Compliant Coatings to Modify Boundary Layer Characteristics

2.2.1. Compliant Coatings for Hydrodynamic Flows

The original idea to stabilize boundary layer by distributed damping was introduced by Kramer [32], who hypothesized that by tuning the damping frequency of a compliant coating, as shown in Fig. 2.25, to the most unstable Tollmein-Schlichting (TS) wave, the instabilities in the boundary layer could partially be dissipated and thus delay the transition from laminar to turbulent flow.
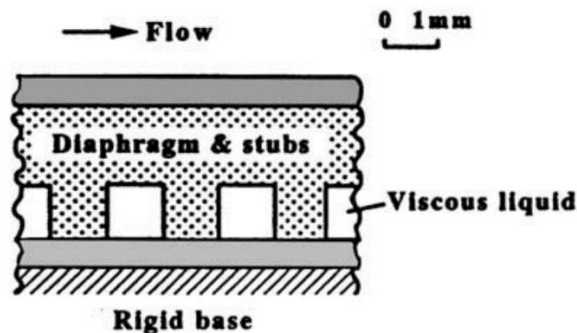
Fig. 2.25: Kramer's Compliant Coating [22, 32]

Initial experiments conducted by Kramer showed more than 50% drag reduction. However, the scientific community were skeptical of these results as experiments were not performed in a sufficiently controlled environment. However, an interest was sparked in this area and subsequent research by Pureyar et al. [33] replicating Kramer's experiment was unsuccessful.

Later, Carpenter and Garrad [34] revisited Kramer's experiment and developed a Kramer type coating to study its ability to stabilize TS waves. Theoretical study from the e^9 method showed significant delay in transition from laminar to turbulent flow using these coatings. Their experiments also revealed that Kramer's coating could favorably modulate the boundary layer, but only for a range of Reynolds number and under favorable pressure gradient and free stream turbulence.

Further numerical investigation by Davies and Carpenter [35] showed the benefits of multiple panel compliant coatings and their ability to stabilize TS waves and maintain laminar flow indefinitely. Benjamin [36] also explored if compliant coatings can favorably influence fully turbulent flow.

2.2.2. Compliant Coatings for Aerodynamic Flows

Experiments were conducted at the University of Oklahoma [37, 38] to study the effects of compliant coatings at low subsonic air speeds, as shown in Fig. 2.26. These studies showed up to 50% drag reduction.
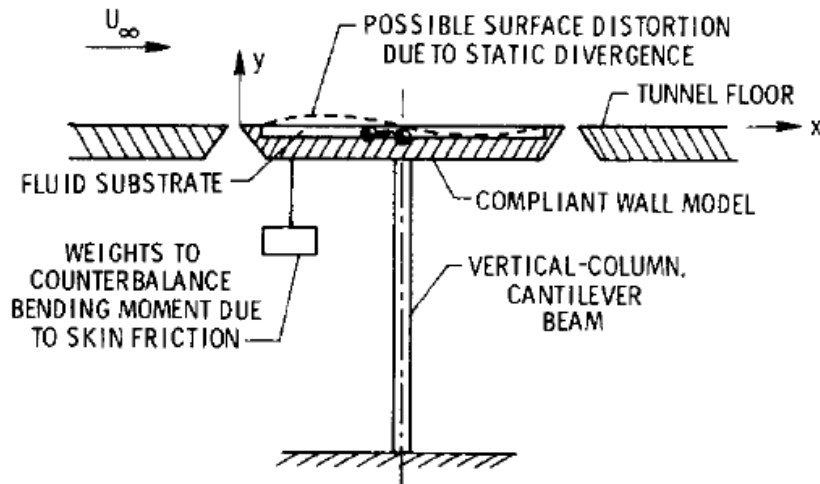
Fig. 2.26: Experimental set up of compliant wall model at the University of Oklahoma [37, 38]

However, when Bushnell et al. [39] from NASA Langley replicated this study using a floating panel compliant wall with liquid substrates in a small subsonic wind tunnel, no drag reductions were observed.

Carpenter, Lucey and Davies [23] explored the feasibility of compliant coatings for aeronautical applications. The significant difference in density and kinematic viscosity of air and water was highlighted. This would yield a mismatch in the compliant wall and fluid inertias, thus having negligible influence on TS waves. Possible challenges in manufacturing compliant coatings for aeronautical applications were also brought to attention.

As Gad-El-Hak [22] noted, the compliant coatings studied until this time were based on plate-spring model, as shown in Fig. 2.27, and they behave differently in comparison to homogeneous visco-elastic compliant coatings, as shown in Figure 2.28.
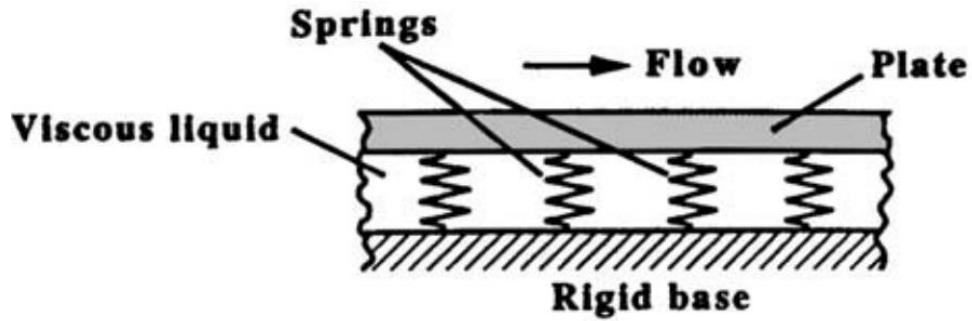
Fig. 2.27: Plate-spring model [22]
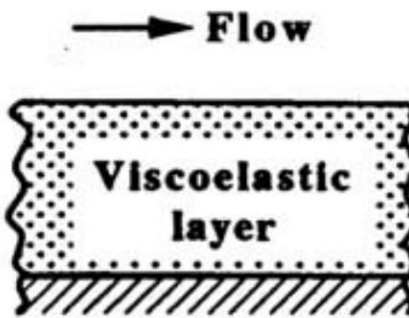
Fig. 2.28: Homogeneous visco-elastic model [22]

2.2.3.   Homogeneous Visco-elastic Compliant Coatings

Lee, Fischer and Schwarz [26] conducted experiments using a single layer homogeneous isotropic visco-elastic compliant coating on a zero-pressure gradient flat plate to understand its ability to modulate boundary layer characteristics. The hydrogen bubble technique was implemented to visualize streak lines at $y^+ \approx 50$ & Re_θ =1348.
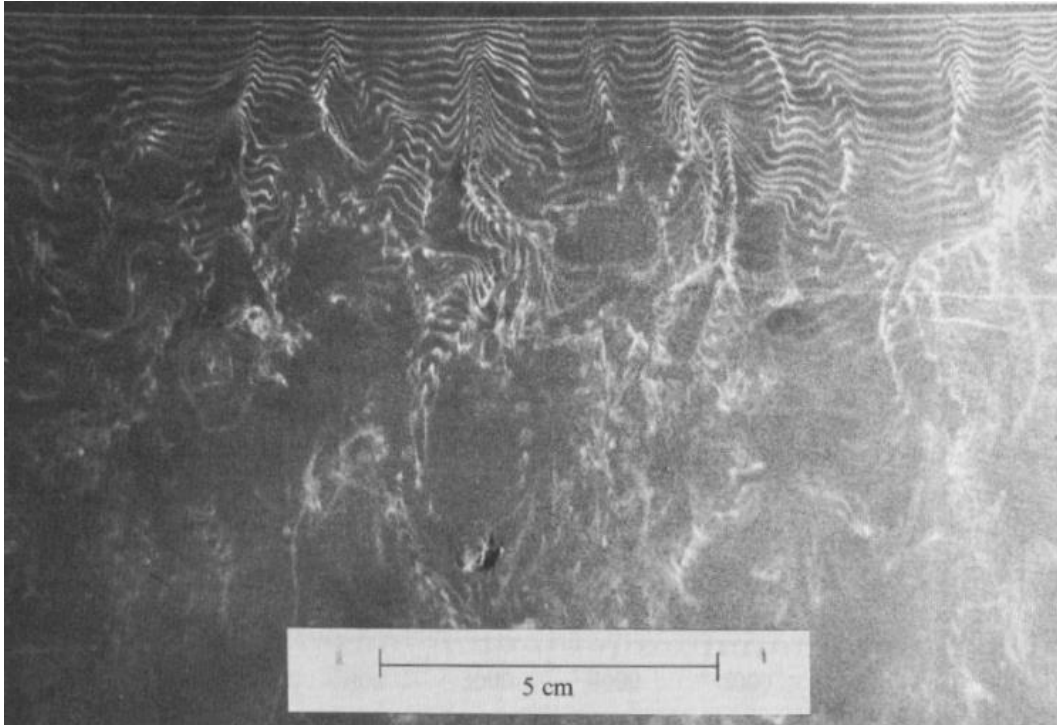
Fig. 2.29: Rigid Surface, Re$_\theta$ = 1348 and y$^+$ = 51 [26]
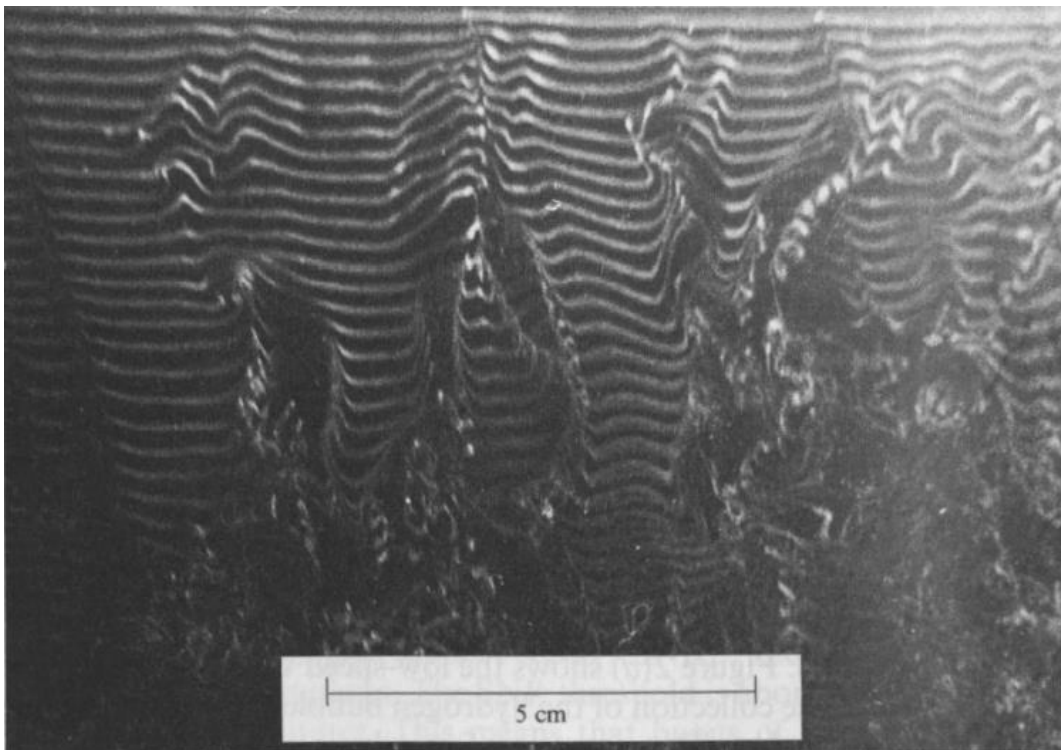
Fig. 2.30: Compliant Surface, Re$_\theta$ = 1348, y$^+$ = 49 at time t$_1$ [26]

31
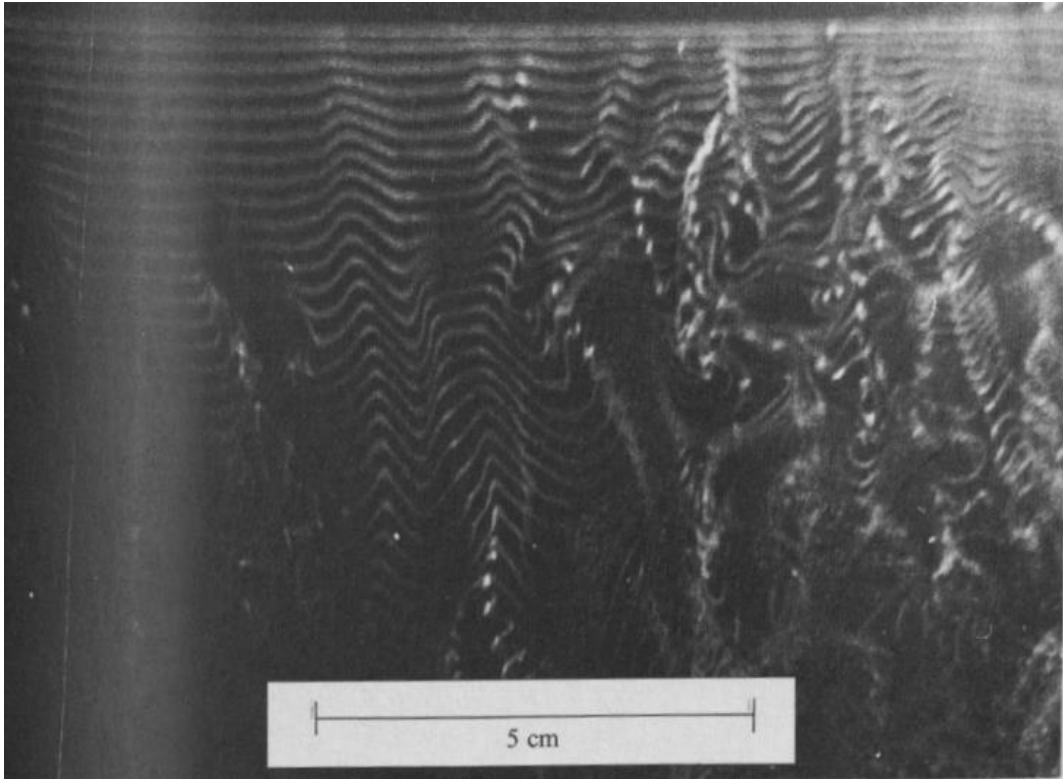
Fig. 2.31: Compliant Surface Re$_\theta$ = 1348 and y$^+$ = 49 at time t$_2$ [26]
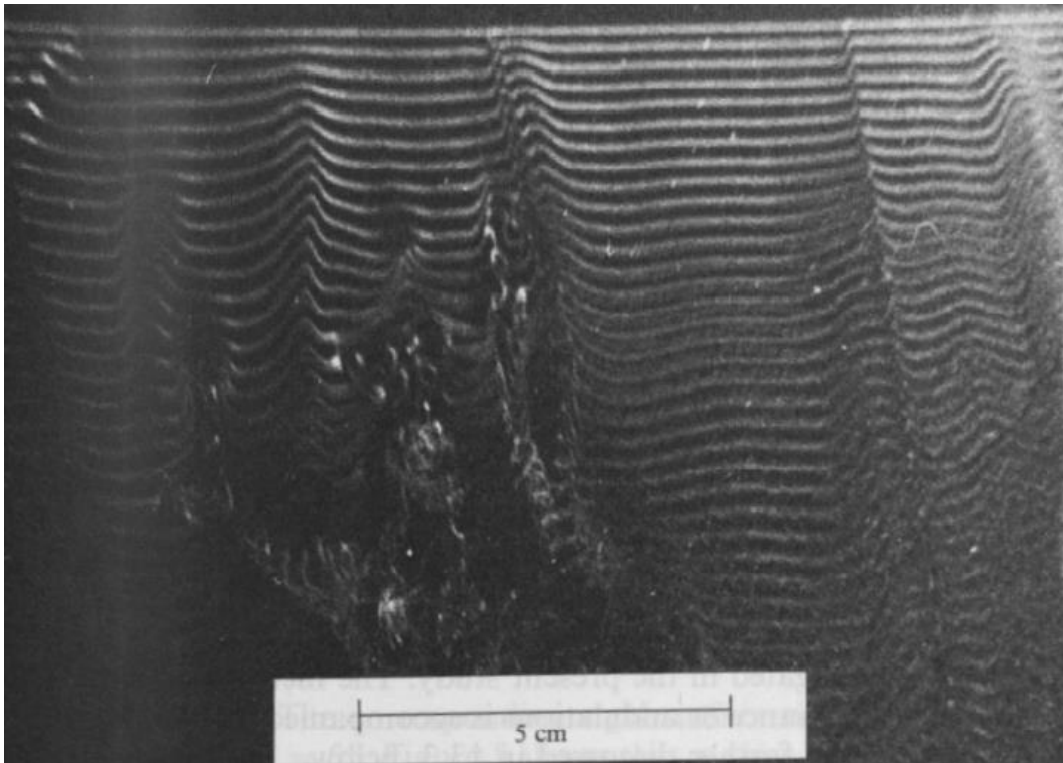
Fig. 2.32: Compliant Surface, Re$_\theta$ = 1348 and y$^+$ = 49 at time t$_3$
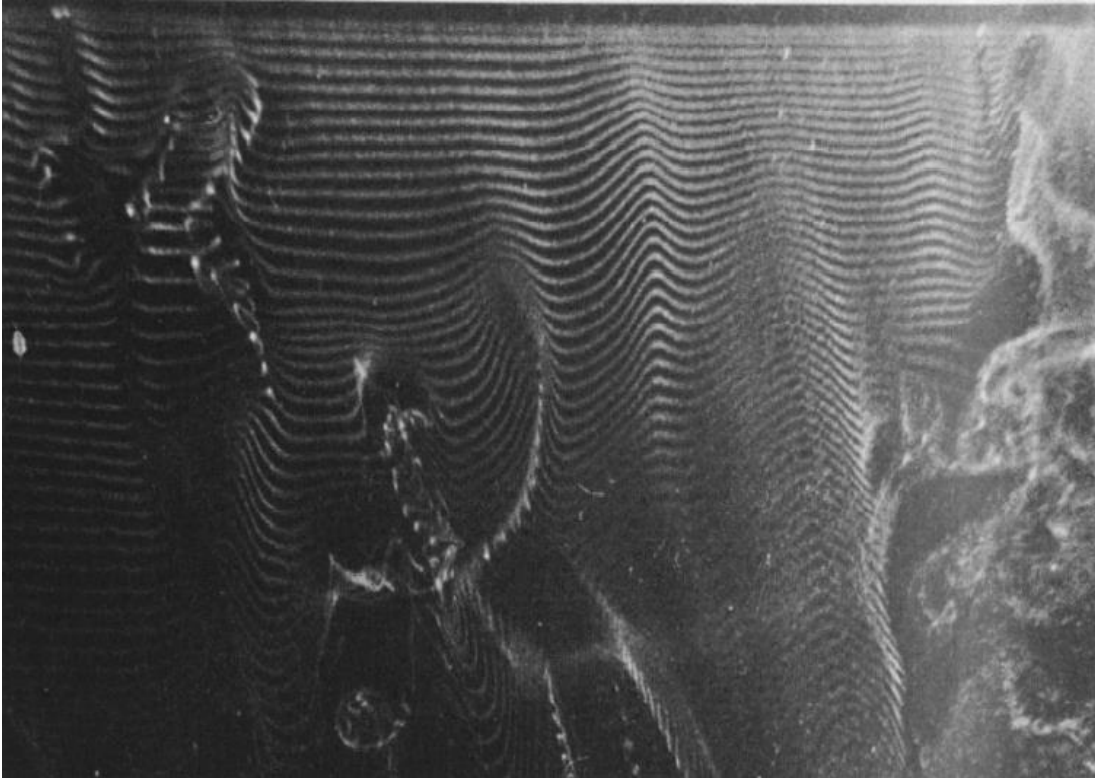
Fig. 2.33: Compliant Surface, $Re_\theta = 1348$ and $y^+ = 51$ at time t_4

Comparison of streak lines between rigid surface and compliant surface at different time intervals, as shown in Fig. 2.29 - 2.33, reveal that compliant coatings favorably modified the boundary layer characteristics and aided in flow relaminarization. Additionally, the viscous laminar sub-layer and buffer layer broadened and an upward shift in the compliant law of the wall was observed. This was also associated with reduction in streamwise turbulence, local skin friction and Reynolds stress across the boundary layer.

Choi et al. [40] further investigated the ability of homogeneous visco-elastic compliant coatings to reduce turbulent drag in boundary layer flow. Experiments were performed on a slender body of revolution in a water tunnel at the University of Newcastle, as shown in Fig. 2.34.

33
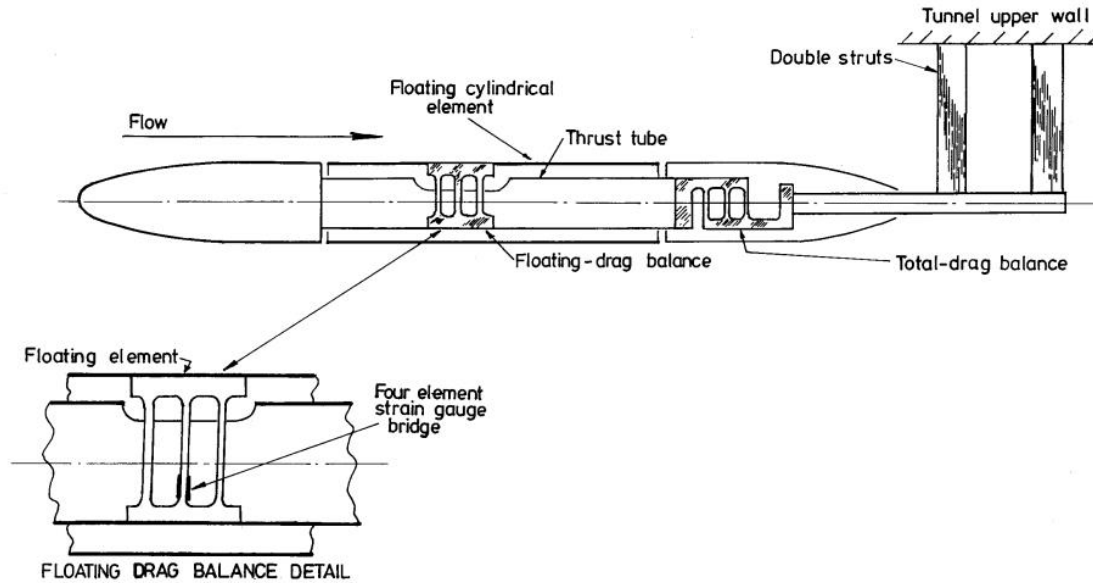
Fig. 2.34: Test model placed in a water tunnel at the University of Newcastle [40]

Studies indicated a turbulent drag reduction of up to 7%, a reduction in turbulence intensity up to 5% and wall pressure fluctuations up to 19% across the entire boundary layer. These studies further indicated that for compliant coatings to exhibit constructive coupling when interacting with the boundary layer, its surface roughness must be small enough so that it is considered hydrodynamically smooth.

In other words, the extent of compliant surface deformation must be within the viscous laminar sub layer. Additionally, according to Sternberg's theory, the natural frequency of the compliant coating must provide the right response to fluctuating pressures at the wall.

Boiko et al. [24] extended this study to aerodynamic flows and suggested the use of *stiff* compliant coatings that are characterized by a hydraulically smooth surface and modulus of elasticity greater than 0.5 MPa. These coatings, unlike the *soft* compliant coatings used previously that aided in transition from laminar to turbulent flow by

34

forming λ shaped wrinkles on their surface, are robust and durable and well suited for large scale wind turbine applications.

For favorable interaction between compliant surface and boundary layer, their study indicated that the convective velocities of the near wall vortical structures must be comparable to the velocity of propagation of disturbances inside the coating. Furthermore, the generation of turbulence above compliant wall was reduced if the coating's non-dimensional resonance frequency is in the range

$$6.67 \times 10^{-3} < \frac{f_0 \nu}{u_\tau^2} < 2.00 \times 10^{-3} \tag{1}$$

where:
f_0 is the resonance frequency
u_τ is the friction velocity
ν is the kinematic viscosity

Experiments were then conducted using stiff compliant coatings mounted on a flat-plate with thickness 80 mm, as shown in Fig. 2.35, in a wind tunnel at Pusan National University for low subsonic wind speeds to identify optimum material properties for these coatings that can modulate boundary layer characteristics and reduce drag in a fully turbulent flow (achieved by artificially tripping boundary layer).
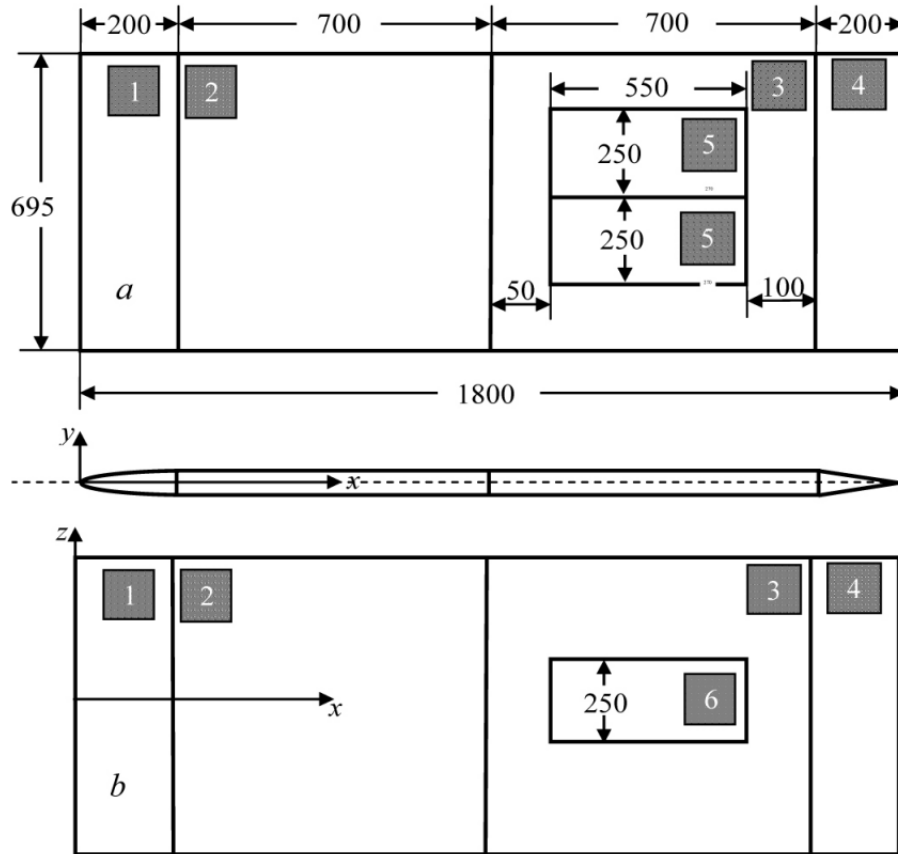
Fig. 2.35: Coupons with compliant coatings on flat plate [24]

Compliant coatings were applied to coupons (number 5 in Fig. 2.35) and mounted on a flat-plate and placed in the wind tunnel. Tests were conducted for wind speeds from 30-40 m/s and experiments showed that coatings with material properties as seen in Table 1 yielded a maximum drag reduction of 4-5%. Significant reduction in turbulent kinetic energy in the near wall region and reduction in turbulent velocity fluctuations further corroborate the ability of stiff compliant coatings to favorably modulate the boundary layer characteristics.

Table 2.1: Optimum Material Properties for Stiff Compliant Coatings [23]

Material properties for optimum compliant coating	Magnitude (Units)
Density	1130 kg/m^3
Poisson's ratio	0.485
Young's Modulus	1.1 MPa
Thickness of compliant coating	7 mm

Experiments were also conducted by Lee, Fisher and Schwarz [27] to study the effects of single layer, viscoelastic, passive compliant coatings in its ability to favorably modulate the flow boundary layer by reducing the growth rates of Tollmien-Schlichting waves and the extent of unstable flow region over the surface. To perform this study, three compliant coatings were chosen with different material properties and applied on a flat plate. As seen in Fig. 2.36, this flat plate with compliant coating was placed inside a low-turbulence wind tunnel at Johns Hopkins University and tests were conducted for wind speeds from 6-15 m/s.
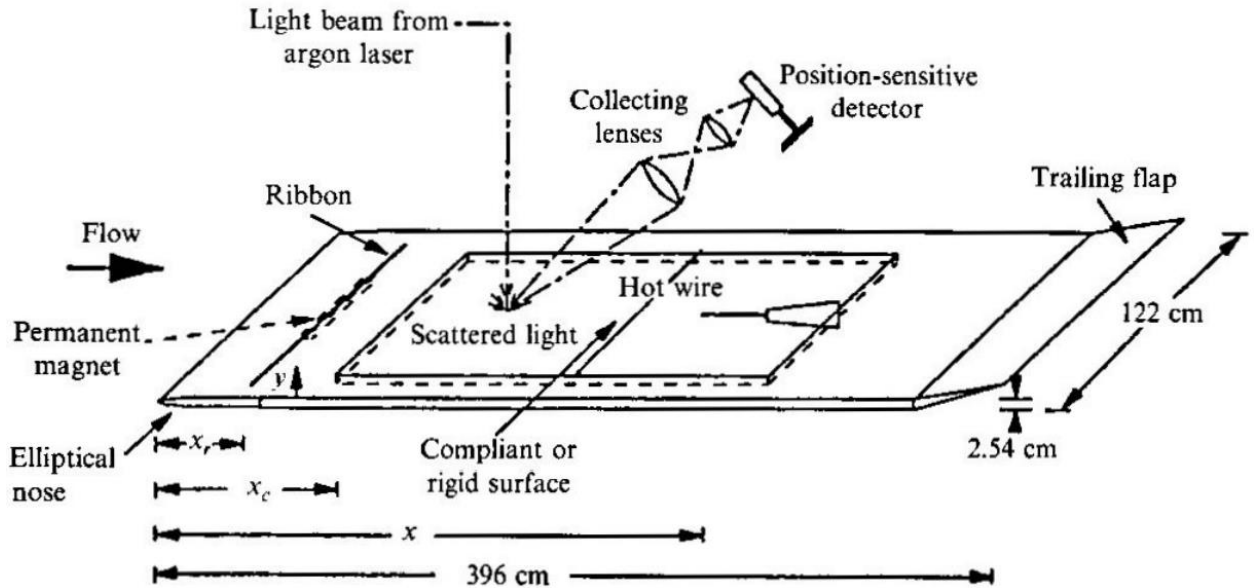
Fig. 2.36: Compliant coating study in a low turbulence wind tunnel at Johns Hopkins University [27]

The first compliant coating {Coating 1: 9/91 (100)} was manufactured by mixing 9% by weight of the binding agent (Dow-Corning Sylgard 184) and 91% by weight of base coating material (Silicone oil: Dow-Corning series 200 with viscosity of 100 mm^2/s). The second coating was obtained by tweaking the ratio of binding agent to base material {Coating 2: 10/90 (100)} and the third coating was obtained by using a base material with lower viscosity {Coating 3: 10/90 (20)}. All these three coatings were cured at a temperature of 175 °F.

A vibrating ribbon was placed 30 cm upstream of the flat plate's leading-edge and was used to create low turbulence in the flow. A hot wire anemometer was positioned 0.8 mm above the surface and 75 cm downstream of the ribbon and traversed up to 50 cm downstream of this location. The hot wire oriented to recorded the x-component of velocity fluctuation as it traversed over the flat plate.

It was observed that Coating 1: 9/91 (100) was capable of suppressing the Tollmien Schlichting instabilities (TSI) and stabilize the Flow Induced Surface Instabilities (FISI). Particularly at a velocity of U_∞ = 10.12 m/s coating, Coating 1helped reduced the RMS amplitude of fluctuating velocity by 40%.

Coating 2: 10/90 (100) demonstrated a reduced suppression of TSI and there was complete absence FISI. On the other hand, Coating 3: 10/90 (20) promoted FISI and less stabilizing influence on TSI.

It was concluded that with appropriate tuning of coating material properties and surface characteristics, suppression of Tollmien Schlichting waves is achievable and is accompanied by coating surface motion driven by flowfield. Additionally, delay in the onset of turbulence is also achievable in aerodynamic flows using coatings with appropriately tuned surface characteristics.

However, if coating properties have not been chosen correctly for a given flowfield, detrimental effects such as Static Divergence Instabilities (SDI) could arise. SDI is associated with increase in turbulent viscous drag and occurs when hydrodynamic forces generated by coating's interaction with flow boundary layer outweighs the restorative structural forces within the coating.

Improper choice of coating material properties may also result in Travelling Wave Flutter (TWF). This involves transfer of irreversible energy from the fluctuating pressure within the flow to the coating wall and is results in a sudden onset of transition within the flow boundary layer.

Based on these studies, coating material properties, as shown in Table 2 displayed favorable effects with flow boundary layer when applied on a flat plate.

Table 2.2: Optimum material properties for compliant coating [27-30]

Material properties for optimum compliant coating	Magnitude (Units)
Density	977 kg/m^3
Poisson's ratio	0.499
Young's Modulus	1.51 MPa
Thickness of compliant coating	5 mm

Lastly, Benjamin [41] and Landahl [42] classified the interaction of fluid-structure waves, which explains the physical mechanism behind the interaction of compliant coatings and fluid boundary layer. Class A disturbances are TS waves in the boundary layer that are modified by a compliant surface. These disturbances are stabilized by irreversible energy transfer from the fluid to the compliant coating and destabilized by wall dissipation. Class B instabilities are associated with the fluid-solid interface. Converse to Class A disturbances, Class B waves are stabilized by wall damping and destabilized non-conservative hydrodynamic forces. Class C instabilities are similar to Kelvin Helmholtz instability and occur when conservative forces from fluid transfer energy to solid.

The present study uses material properties for compliant coating from Table 1 and Table 2 to study their noise mitigation capabilities when used on a flat plate at wind speed of 35 m/s.

2.3. Computational Aeroacoustics

Several numerical studies have been conducted previously on the flat plate geometry used in the present study to accurately predict flowfield behavior and farfield noise characteristics.

Marshallsay et al. [43] performed Computational Aeroacoustics Analysis (CAA) on a sharp-edged symmetric strut at zero angle of attack to predict trailing-edge noise. Flowfield results were obtained using both IDDES and RANS turbulence models and farfield noise was predicted using the RANS based Statistical model (RSNM) and the FW-H solver based on Lighthill's acoustic analogy.

It was observed that there exists a separation bubble immediately downstream of the leading-edge which periodically broke down resulting in large scale turbulent flow structures propagating downstream of the flat plate, thus forming low frequency noise sources. Among the various noise prediction models used, noise spectrum obtained from IDDES and FW-H solution showed good agreement with experiment across entire frequency range.

Karimi et al. [44] developed a novel uncorrelated wall plane waves-boundary element method (UWPW-BEM) technique to predict flow induced noise from a flat plate. This technique was efficient as it employed RANS equations to estimate turbulent boundary layer parameters, which were used to evaluate cross spectrum of wall pressure fluctuations using semi-empirical models namely the Chase, Corcos and generalized Corcos models. The UWPW technique was used to predict wall pressure field which was in turn used by the BEM solver to predict acoustic pressure from the flat plate.

A hybrid LES-BEM technique was also used to validate turbulent boundary layer noise predicted in this study. The incident pressure on the surface due to flow noise sources were obtained using Lighthill's acoustic analogy and the scattered acoustic pressure is predicted using the BEM solver. The periodicity boundary condition was used on the side boundaries of the domain whose spanwise extension was 10% of plate chord. The pressure based segregated algorithm was used during CFD simulation. A comparison of scattered sound predicted with measurements showed good agreement using the UWPW-BEM results based on the generalized Corcos model and LES-BEM results.

Croaker et al. [45] predicted flow induced noise generated by turbulent flow past a flat plate using a hybrid RANS – BEM technique. A 2D steady CFD simulation was performed using the SST k-ω RANS turbulence model and flow field was validated using mean and fluctuating velocities near the wake. Comparison with measurements showed mean flow predicted near the wake agreed well with experiment. However, discrepancy in the fluctuating velocity predicted and was attributed to the assumption of 2D flow during simulation which did not take the spanwise variation of flow-field into account.

It was also observed that a rounded leading-edge caused the incoming flow to separate indicative of high turbulent kinetic energy observed downstream of the leading-edge. The shear layer formed in this region caused significant turbulence and gets transported along the flat plate and convected past the trailing-edge. This interaction between the incoming flow and leading-edge was expected to be a significant low frequency noise source.

The turbulent velocity cross spectra estimated by the RANS based statistical model (RSNM) using flowfield data obtained from this CFD analysis was used with the BEM model

to predict far-field sound at a receiver's location. This farfield sound compared well with experiment at frequencies above 600 Hz.

Numerical studies were performed by Giridhar, Farokhi and Taghavi [46] to obtain flowfield and aerodynamic noise characteristics from the NREL Phase VI wind turbine rotor operating at low subsonic wind speeds. SST k-ω RANS turbulence model was used during steady CFD analysis to predict mean flowfield characteristics, which was used by Curle Broadband Noise Source model to obtain acoustic power distribution around the rotor blade.

Unsteady CFD analysis was performed using SST k-ω IDDES turbulence model, due to its improved accuracy in predicting flowfield when compared to RANS turbulence models. Farassat 1-A formulation of the Ffowcs Williams and Hawkings equation was used to estimate farfield noise generated by this rotor.

Studies revealed that turbulence models used in the present study accurately predicted flow field at low wind speeds of 7 m/s, where flow was mostly attached; and at high wind speeds of 20-25 m/s, where flow separation was complete. However, the accuracy of prediction on suction surface of the rotor reduced at mid-level speeds of 13-15 m/s. This inaccuracy was attributed to partly separated flows along the blade span observed at mid-level speeds and the inability of these turbulence models to accurately predict partly separated flows. Farfield acoustic predictions from this study also revealed that loading noise was the dominant noise source.

Further numerical studies were conducted by Valleru, Taghavi and Farokhi [47] to investigate the impact on aerodynamic performance and noise characteristics of the NREL Phase VI rotor with a modified sinusoidal leading-edge. Studies revealed that modifying the

leading-edge to a sinusoidal profile generated lesser torque at low wind speeds and greater torque at high wind speeds, when compared to experiment.

This response from the modified leading-edge was attributed to the formation of tubercles. At high wind speeds, these tubercles created counter-rotating vortices that energized the boundary layer and thus delayed flow separation. Whereas at low wind speeds, the tubercles disturbed the laminar flow region near the leading-edge which lead to premature flow separation.

2.4.   Trailing-edge Noise Measurements from a Flat Plate

Moreau, Brooks and Doolan [48] conducted experiments on a sharp-edged flat plate to measure far-field acoustic spectra and velocity spectra in the near wake of the trailing-edge. These studies were performed using an anechoic wind tunnel at the University of Adelaide for a chord-based Reynolds number from 200,000 to 500,000. The anechoic chamber has a contraction outlet with a rectangular cross section (75 mm x 275 mm), as shown in Fig. 2.37 and 2.38, where the maximum velocity of the free jet was 40 m/s with free stream turbulence intensity of 0.3%.
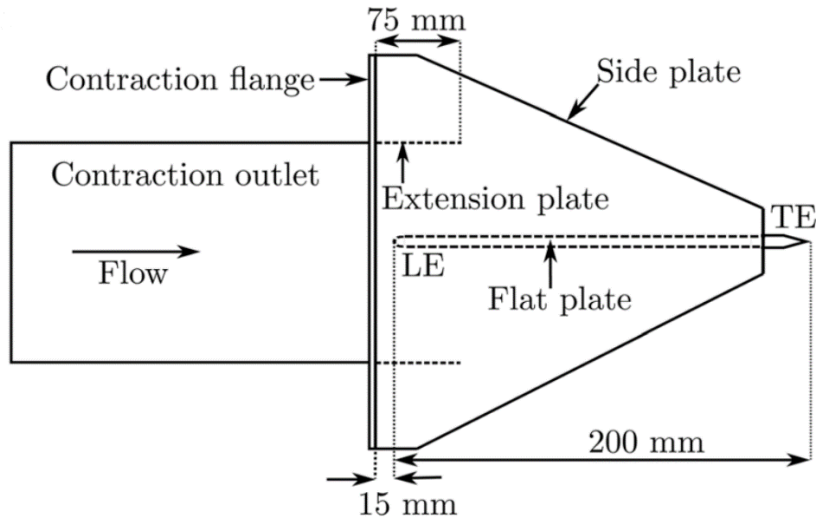
Fig. 2.37: Flat plate model in contraction outlet (side view) [48]
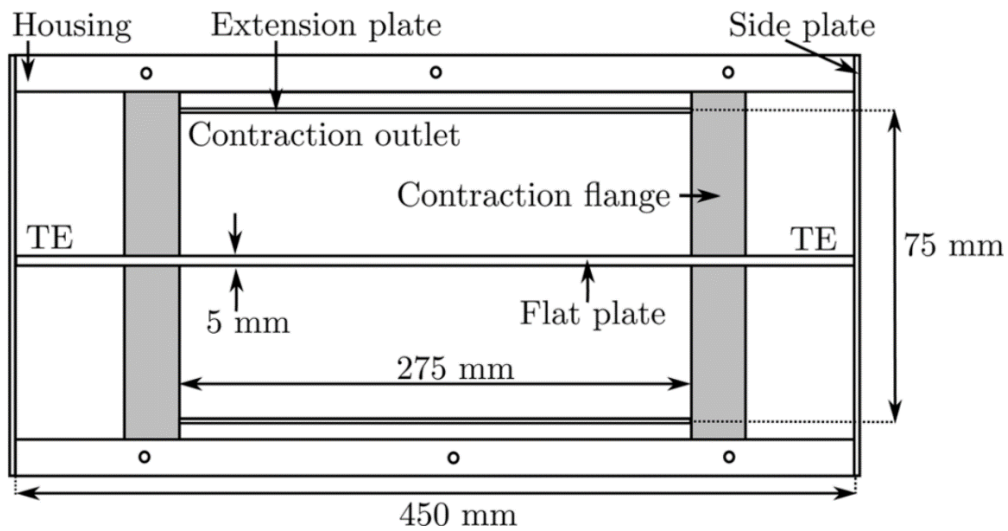
Fig. 2.38: Flat plate model in contraction outlet (front view) [48]

The flat plate model used in this experiment, as shown in Fig. 2.39, has a chord length of 200 mm and a thickness of 5 mm. The circular leading-edge of this flat plate has a radius of 2.5 mm while its trailing-edge has a symmetric wedge shape with an apex angle of 12°.

45
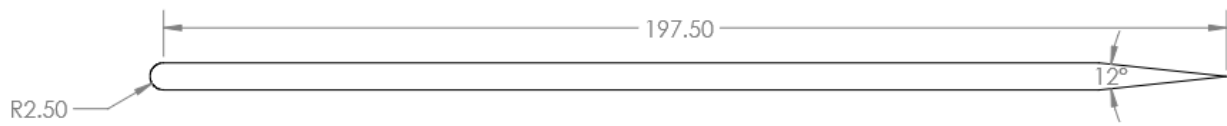
Fig. 2.39: Sharp-Edge Flat Plate *(All dimensions in mm)*

The flat plate model was secured to the housing at 0° angle of attack with the aid of two side plates. Extension plates were included to prevent the interaction of shear layer flow at the outlet with plate trailing-edge, as shown in Fig. 2.40. The test chamber provided a reflection free environment above 250 Hz.
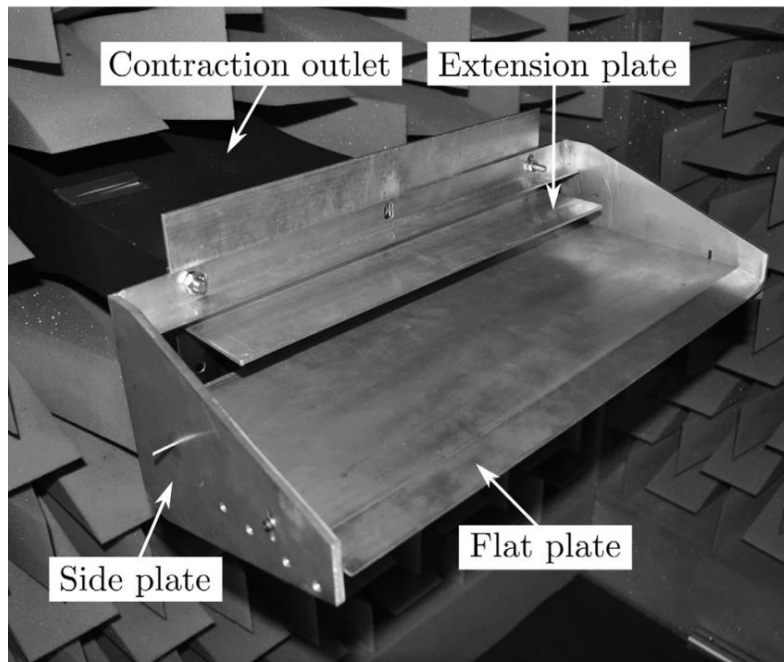
Fig. 2.40: Flat plate in anechoic wind tunnel at the University of Adelaide [48]

Hot wire anemometry was used to measure unsteady velocity data 0.6 mm downstream of the trailing-edge and far-field noise radiated from this flat plate was recorded using a microphone at a distance of 585 mm above the trailing-edge.

46

The measurement data from this experiment, namely farfield acoustic spectra measured 585 mm above the trailing-edge, mean velocity and rms velocity distribution measured 0.6 mm downstream of the trailing-edge are used by the present study to validate flowfield and farfield noise predictions obtained through Computational Aeroacoustics Analysis for the rigid flat-plate shown in Fig 2.38, before the application of visco-elastic compliant coating on its surface.

3. VALIDATION WITH EXPERIMENTS

This chapter is based on a work titled "A Computational Aeroacoustics Analysis To Predict Farfield Noise From A Sharp Trailing-Edge" presented at the ASME International Mechanical Engineering Congress and Exposition, 1-5 Nov 2021.

Abstract

The preliminary step in this analysis involves accurate prediction of farfield noise propagated from the trailing-edge using Computational Aeroacoustics Analysis (CAA), which would serve as the *Baseline* data for comparison with noise mitigation techniques. A flat plate model in fully turbulent flow is chosen to demonstrate the technique. CAA is performed on a flat plate with sharp trailing-edge for a chord-based Reynolds number of Re_c = 460,000 (U_∞ = 35 m/s). Initially, the SST k-ω RANS turbulence model is chosen to perform steady CFD analysis. Next, unsteady CFD analysis is performed using the SST k-ω Improved Delayed Detached Eddy Simulation. To validate our CFD results, comparisons are made with unsteady flow measurements recorded 0.6 mm downstream of the trailing-edge. It is observed that the mean velocity distribution predicted at this location matches well with the experimental data and previous computational studies. The accuracy of prediction is particularly close to measurements near trailing-edge centerline. Further, the RMS of fluctuating velocity distribution, downstream of the trailing-edge, is comparable to predictions from previous computational studies. Noise sources around the flat plate obtained through unsteady CFD analysis are used by Farassat's Formulation 1-A of the Ffowcs Williams and Hawkings equation to predict farfield noise propagated 585 mm above the trailing-edge. The predicted noise accurately follows the magnitude and trend of the

experimental measurements for the frequency range of 750 – 7000 Hz (i.e., Strouhal number, St = 4.28 – 40.00). This trend is well predicted particularly for the frequency range from 900 – 2500 Hz (i.e., St = 5.14 – 14.28), where the trailing-edge noise is dominant. Accurate prediction of flowfield characteristics and farfield noise in the present study demonstrates the validity of this approach. Results from this study will serve as the *Baseline* data to assess the efficacy of the trailing-edge noise mitigation techniques in wind turbines.

3.1.   Introduction

Moreau, Brooks and Doolan [48] conducted experiments on a flat plate to measure farfield noise and velocity spectra in the near wake of its trailing-edge. These studies were performed using an anechoic wind tunnel for a chord-based Reynolds number from 200,000 to 500,000. The anechoic chamber had a contraction outlet where maximum velocity of free jet was 40 m/s with freestream turbulence intensity of 0.3%.

Hot wire anemometry was used to measure unsteady velocity data 0.6 mm downstream of the trailing-edge and farfield noise radiated from this flat plate was recorded using a microphone 585 mm above the trailing-edge.

Measurements from this experiment are used by the present computational study to validate results for the rigid flat plate before application of visco-elastic compliant coating on its surface.

3.2.   Governing Equations

3.2.1.   *SST k-ω RANS Turbulence Model*

In the present numerical study, the semi-circular leading-edge shown in Fig. 1 trips the boundary layer and flow is fully turbulent on the surface of this flat plate. Based on

accurate flowfield predictions from previous studies [49-52], the fully turbulent RANS model, namely the SST k-ω RANS turbulence model was chosen to perform steady CFD analysis.
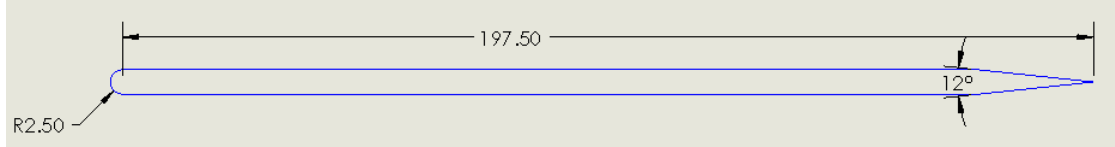
Fig. 3.1: CAD diagram of the flat plate model used in present computational study

The SST k-ω turbulence model combines the robust and accurate k-ω turbulence model in the near wall regions; with the k-ε turbulence model, which has shown accurate predictions in the farfield due to its independence from the free stream. A blending function is used to include the cross-diffusion term in the farfield region but not near the walls.

The transport equations for turbulent kinetic energy k and specific dissipation rate ω are:

$$\frac{\partial}{\partial t}(\rho k) + \nabla.(\rho k \bar{\mathbf{v}}) = \nabla.[(\mu + \sigma_k \mu_t)\nabla k] + G_k + G_{nl} + G_b$$

$$-\rho \beta^* f_{\beta^*}(\omega k - \omega_0 k_0) + S_k \qquad (3.1)$$

$$\frac{\partial}{\partial t}(\rho \omega) + \nabla.(\rho \omega \bar{\mathbf{v}}) = \nabla.[(\mu + \sigma_\omega \mu_t)\nabla \omega] + G_\omega + D_\omega$$

$$-\rho \beta f_\beta (\omega^2 - \omega_0^2) + S_\omega \qquad (3.2)$$

where:

$\bar{v}$ is the mean velocity

μ is the dynamic viscosity

σ_k and σ_ω are model coefficients

G_k, G_b and G_{nl} are turbulent-, buoyancy- and nonlinear production respectively

G_ω and D_ω are specific dissipation production and cross diffusion term respectively

f_{β^*} is the free-shear modification factor

f_β is the vortex-stretching modification factor

S_k and S_ω are the user-specified source terms

k_0 and ω_0 are the ambient turbulent values that counteract turbulence decay [53]

3.2.2. *Improved Delayed Detached Eddy Simulation*

The Improved Delayed Detached Eddy Simulation [46, 50] has shown superior accuracy in its flowfield predictions when compared to SST k-ω RANS turbulence model during unsteady CFD analysis and hence is chosen for the present study. The SST k-ω Detached Eddy turbulence model is a combination of SST k-ω RANS turbulence model used in regions where the flow is irrotational and Large Eddy simulation is used near the flat plate where noise sources are located or in flow separated regions [53].

According to the IDDES formulation [54], specific dissipation rate in the transport equation for kinetic energy k in the SST k-ω turbulence model is replaced by $\widetilde{\omega}$, where $\widetilde{\omega}$ is defined as:

$$\widetilde{\omega} = \frac{\sqrt{k}}{l_{HYBRID}\beta^* f_{\beta^*}} \tag{3.3}$$

where:

β^* is the model coefficient

f_{β^*} is the free shear modification factor; and

$$l_{HYBRID} = \overline{f}_d(1 + f_e)l_t + (1 - \overline{f}_d)C_{DDES}\Delta_{IDDES} \tag{3.4}$$

where:

f_e is the elevating function

l_t is the length scale for RANS model given as $l_t = \frac{\sqrt{k}}{\beta^*\omega}$

The function $\overline{f}_d$ is defined as $\overline{f}_d = \max\left((1 - f_{dt}), f_B\right)$; where f_B is the blending function and Δ_{IDDES} is an altered version of the mesh length scale.

3.2.3. Ffowcs Williams and Hawkings Formulation

The Ffowcs Williams and Hawkings (FW-H) acoustics integral formulation is used to predict far field noise at a point receiver placed 585 mm above trailing-edge of the flat plate. This model predicts acoustic pressure fluctuations at the receiver's location using nearfield flow data obtained from CFD analysis [54]. The Ffowcs Williams and Hawkings formulations used in the present study is based on Farassat's Formulation 1-A [56, 57]. The permeable formulation has been used in the present study. The FW-H equation is obtained by rearranging the continuity and momentum equations into an

inhomogeneous wave equation. The free-space Green's function is used to determine

sound pressure at an observer's location, 'x' which is:

$$p'(\boldsymbol{x}, t) = p'_T(\boldsymbol{x}, t) + p'_L(\boldsymbol{x}, t) + p'_Q(\boldsymbol{x}, t) \tag{3.5}$$

where:

$p'_T(x, t)$ is the monopole term, which occurs due to displacement of the fluid with

passage of the blade, written as:

$$p'_T(\boldsymbol{x}, t) = \frac{1}{4\pi} \left[\left(\frac{\partial}{\partial t} \right) \int_S \left[\frac{Q}{r(1 - M_r)} \right]_{ret} dS \right] \tag{3.6}$$

$p'_L(\boldsymbol{x}, t)$ is the dipole term, which occurs due to the fluctuation of force distribution

on the body surface with time and is written as:

$$p'_L(\boldsymbol{x}, t) = \frac{1}{4\pi} \left[\left(-\frac{\partial}{\partial t} \right) \int_S \left[\frac{L_i}{r(1 - M_r)} \right]_{ret} dS \right] \tag{3.7}$$

$p'_Q(\boldsymbol{x}, t)$ is the quadrupole term, which refers to the volume distribution of noise

sources and can be written as:

$$p'_Q(\boldsymbol{x}, t) = \frac{1}{4\pi} \left[\left(\frac{\partial^2}{\partial x_i \partial x_j} \right) \int_V \left[\frac{T_{ij}}{r(1 - M_r)} \right]_{ret} dV \right] \tag{3.8}$$

with:

$$Q = \rho_0 U_i n_i \tag{3.9}$$

$$U_i = \left(1 - \frac{\rho}{\rho_0}\right) v_i + \frac{\rho u_i}{\rho_0} \tag{3.10}$$

$$L_i = P_{ij} n_i + \rho u_i (u_n - v_n) \tag{3.11}$$

P_{ij} is the compressible stress tensor:

$$P_{ij} = (p - p_0)\delta_{ij} - \sigma_{ij} \tag{3.12}$$

T_{ij} is the Lighthill's stress tensor:

$$T_{ij} = \rho u_i u_j + \delta_{ij}[\,(p - p_0) - c_0^2(\rho - \rho_0)] - \sigma_{ij} \tag{3.13}$$

where:

u_i is the fluid velocity component in the i direction

u_n is the fluid velocity component normal to the surface

v_i is the surface velocity component in the i direction

v_n is the surface velocity component normal to the surface

n_i is the surface unit normal vector

σ_{ij} is the viscous stress tensor

ρ_0 is the farfield density [53]

3.3. Computational Aeroacoustics Analysis

For this numerical study, a segregated flow solver (based on SIMPLE algorithm) of a commercial CFD code STAR-CCM+ v.15.02.009 has been used. The pressure-based segregated algorithm, used in earlier numerical analyses [43-47] to predict accurate farfield noise, is used in the present study. Initially the steady SST k-ω Reynolds Averaged Navier Stokes (RANS) turbulence model with *Near wall y^+ treatment* is used to perform preliminary analysis at wind speed of 35 m/s. The ideal gas law is used to estimate air density, which accounts for the compressible nature of the flow, a necessary requirement while estimating noise sources and predicting farfield noise. The MUSCL 3rd-order scheme is used to discretize convective terms in the energy equation (Segregated Fluid temperature) and a 2nd order upwind scheme is used to discretize convective terms associated with the SST k-ω RANS turbulence model.

Steady CFD analysis is used to check the following:

- Is mesh sufficiently refined in the near wall region of the flat plate to resolve noise sources accurately?

- Wall y^+ on surface of flat-plate – A requirement of $y^+ < 1$ for *Near wall y^+ treatment*

- Does permeable body encompass all major noise sources?

After this step, flowfield results from this steady CFD analysis shall be used to initialize the unsteady CFD simulation. Near wake flow properties downstream of the trailing-edge and farfield noise characteristics shall be extracted for validation with experimental measurements and previous numerical studies.
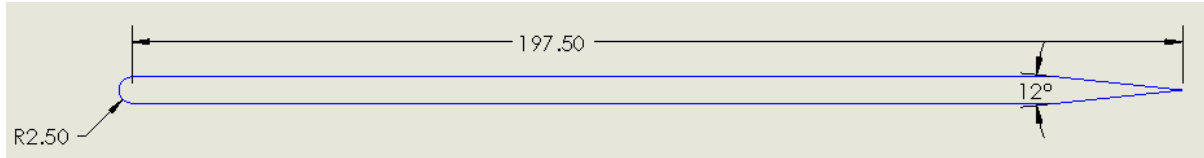
Fig. 3.2: Flat plate geometry used in present study

The flat plate geometry, shown in Fig. 3.2., is used in this present study. It has a chord length of 200 mm and a thickness of 5 mm. The circular leading-edge of this flat plate has a radius of 2.5 mm while its trailing-edge has a symmetric wedge shape with an apex angle of 12°. The circular leading-edge behaves as a boundary layer trip ensuring that the flow is fully turbulent on the flat plate surface [57].

3.3.1. Boundary Conditions

The computational domain consists of two regions as shown in Fig. 3.3, a fluid domain, and a permeable body. The fluid domain is the outer region where boundary conditions are specified, and the permeable body is a region around the flat plate used to encompass noise sources. Noise sources in the permeable body will be used to predict farfield trailing-edge noise using Ffowcs Williams and Hawkings model. The freestream inlet boundary is located 1 m (i.e., 5 chord lengths) upstream of the flat plate's leading edge and extends radially outward. The freestream outlet is located 1.5 m (i.e., 7.5 chord lengths) downstream of the flat plate's trailing-edge.

The domain has a spanwise dimension of 10% chord length to account for three-dimensional nature of vortices present within the boundary layer. Tong et al. [58] indicated that translational periodic boundary conditions are a more accurate choice than symmetry boundaries for either side-planes of the domain. This is because, periodic boundary conditions ensure that flowfield quantities on these side-planes of

56

the domain are fully correlated by enforcing the periodicity condition on them. Whereas, the symmetry boundary condition assumes that the z-component of the flow vanishes on these side-planes of the domain and thus the flowfield remains uncorrelated and less accurate. Therefore, translational periodic boundary conditions are used on either side-planes of the domain.

The Permeable body extends up to 0.16 m (i.e., 0.8 chord lengths) downstream of the trailing-edge and has a height of 0.03 m (i.e., 0.15 chord lengths). The no slip wall boundary condition used in viscous simulations is imposed on flat plate surfaces.
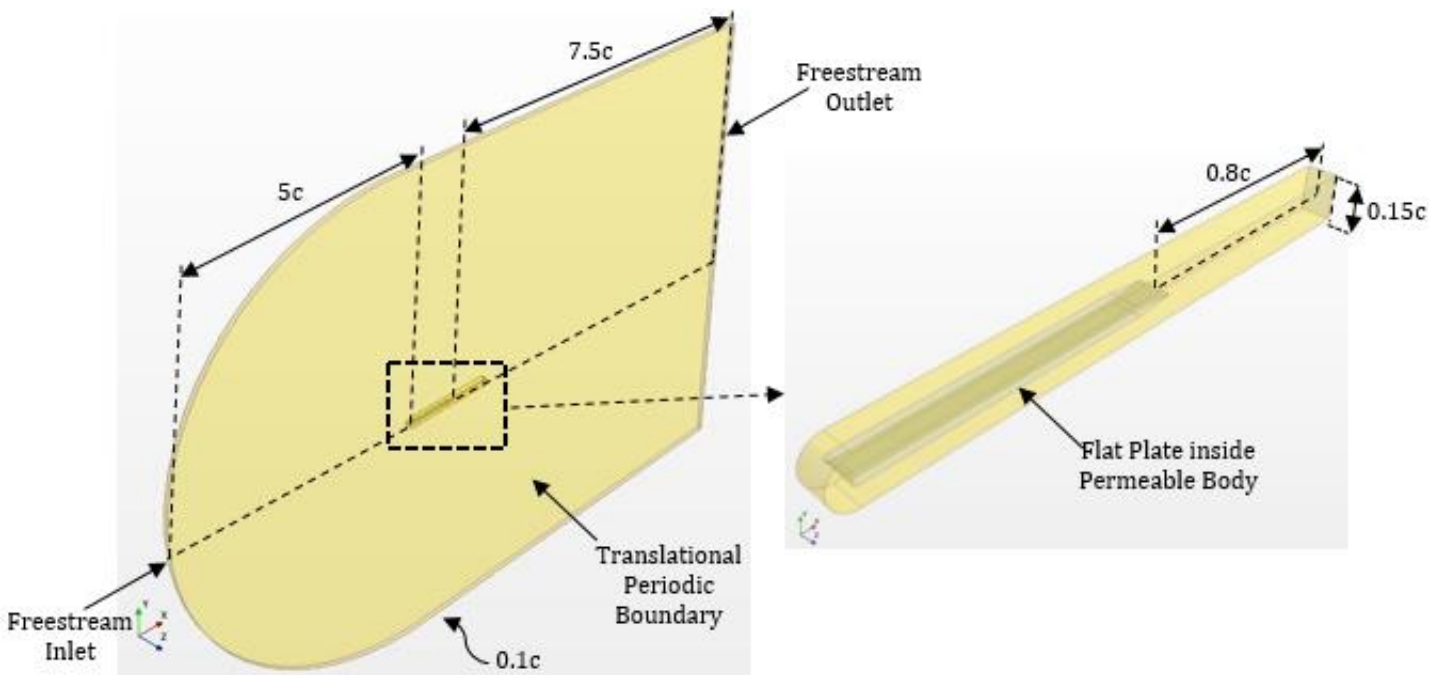
Fig. 3.3: Computational domain with permeable body around flat plate

3.3.2. Mesh Generation

A structured mesh using blocking technique is created for domain discretization with hexahedral cells. The mesh generation using blocking technique is well suited for CAA because it provides a high control on growth of mesh in vicinity of the flat plate,

57

thus ensuring a good quality well refined mesh in the near wall region to resolve noise sources. The domain was divided into 24 blocks, with 16 blocks in the fluid region and 8 blocks in the permeable body region. A near wall thickness of 4 ×10⁻⁶ m was chosen to ensure a wall y⁺ less than 1, a condition necessary for near wall y⁺ treatment used along with the SST k-ω RANS turbulence model.

3.3.2.1. Grid Refinement Study

A grid refinement study has been performed at wind speed of 35 m/s ($Re_c \approx$ 460,000) to ensure that solutions obtained from CFD analysis are independent of mesh resolution. Steady CFD simulations were performed using four different grid resolutions ranging from a coarse grid of 140,000 cells to a fine grid of 1.26 million cells.

Using drag predicted from simulations, drag coefficient was estimated using the relation:

$$C_D = \frac{D}{\left(\frac{1}{2}\rho_\infty U_\infty^2 cS\right)} \qquad (3.14)$$
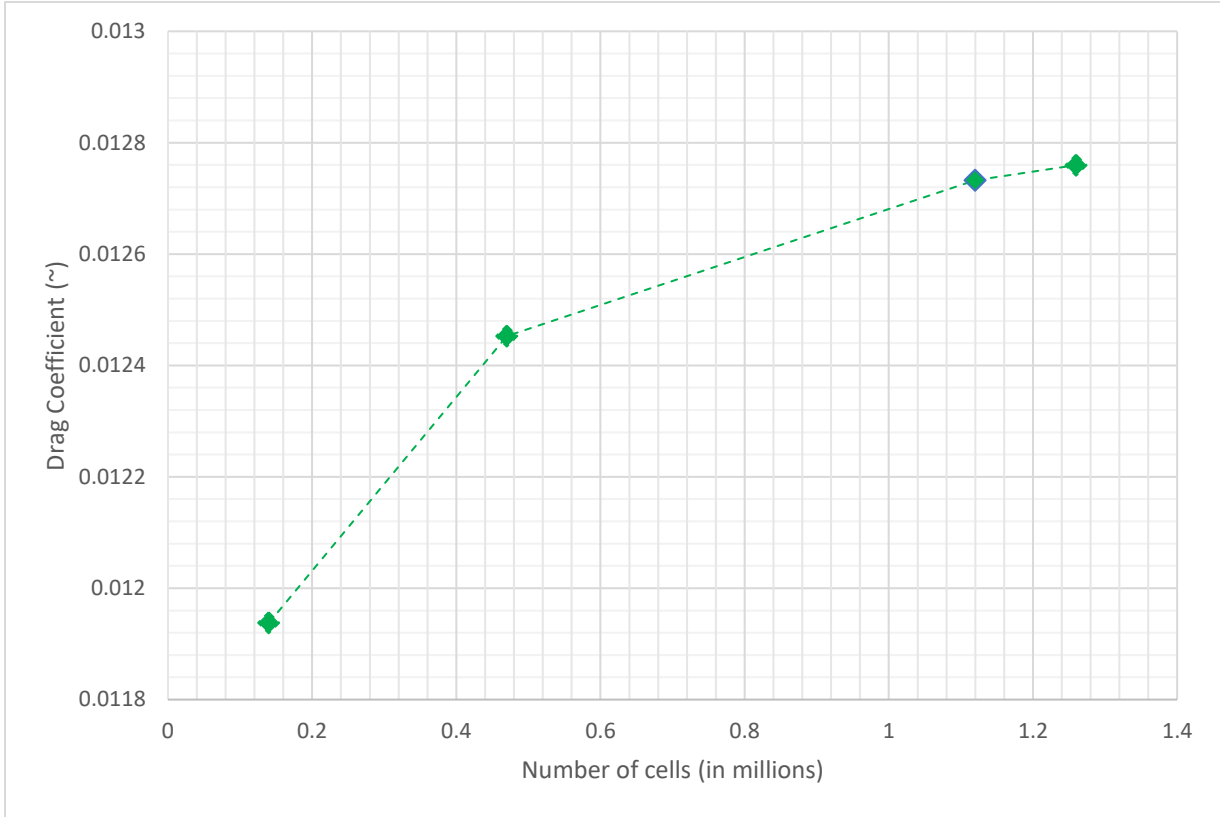
Fig. 3.4: Grid Refinement Study at wind speed of 35 m/s

From Fig. 3.4, it is seen that there is only a 0.21% difference in predicted drag coefficient when grid is refined from 1.12 million cells to 1.26 million cells. Therefore, the grid with 1.26 million cells was chosen for the next step in analysis.

3.3.2.2. Mesh Frequency Cutoff

To understand if the generated grid can resolve noise sources from turbulent flow structures present around the flat plate, the mesh frequency cutoff parameter [59] is used over the frequency range of interest. Mesh frequency cutoff is given by:

$$f_{MC} = \frac{\sqrt{\frac{2}{3}k}}{(2\Delta)}$$

(3.15)

59

In the experiment conducted by Moreau et al. [48], the anechoic test chamber provided a reflection free environment above 250 Hz. Furthermore, noise predictions were made in this study up to a frequency of 8000 Hz. Therefore, ability of grid generated in present study to resolve noise sources in vicinity of the flat plate is evaluated for a frequency range from 250-8000 Hz.
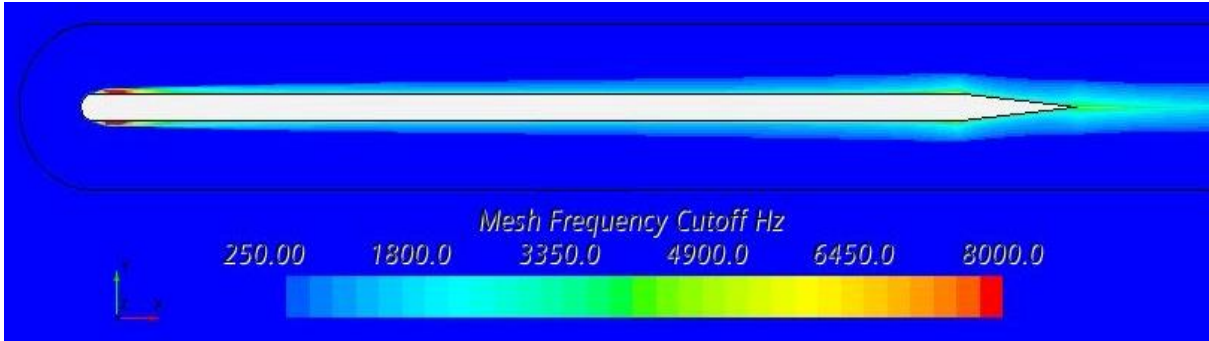
Fig. 3.5: Mesh Frequency Cutoff scalar scene for grid size of 1.26 million cells

As shown in Fig. 3.5, the mesh frequency cutoff scalar scene indicates that a grid size of 1.26 million cells is not sufficient to resolve noise source distribution around the flat plate.
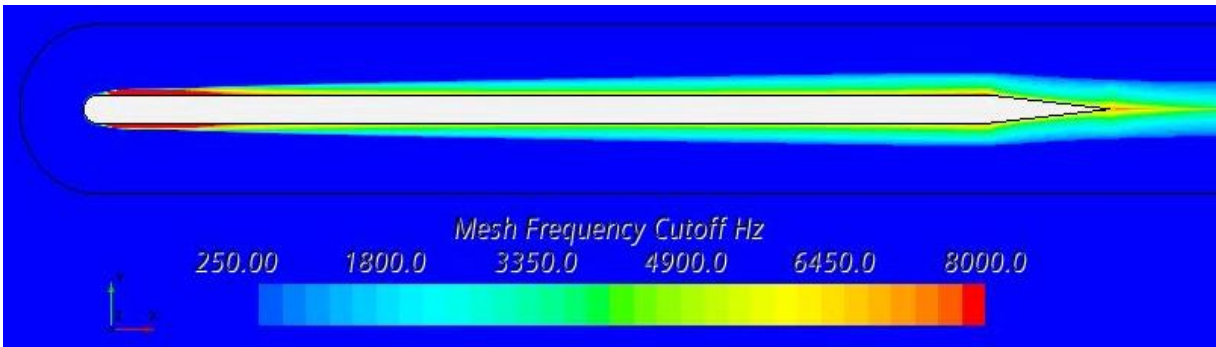
Fig. 3.6: Mesh Frequency Cutoff scalar scene for grid size of 9.55 million cells

Hence further grid refinement was made in vicinity of the flat plate and a grid with size of 9.55 million cells, as shown in Fig. 3.6, was found to resolve noise sources well.
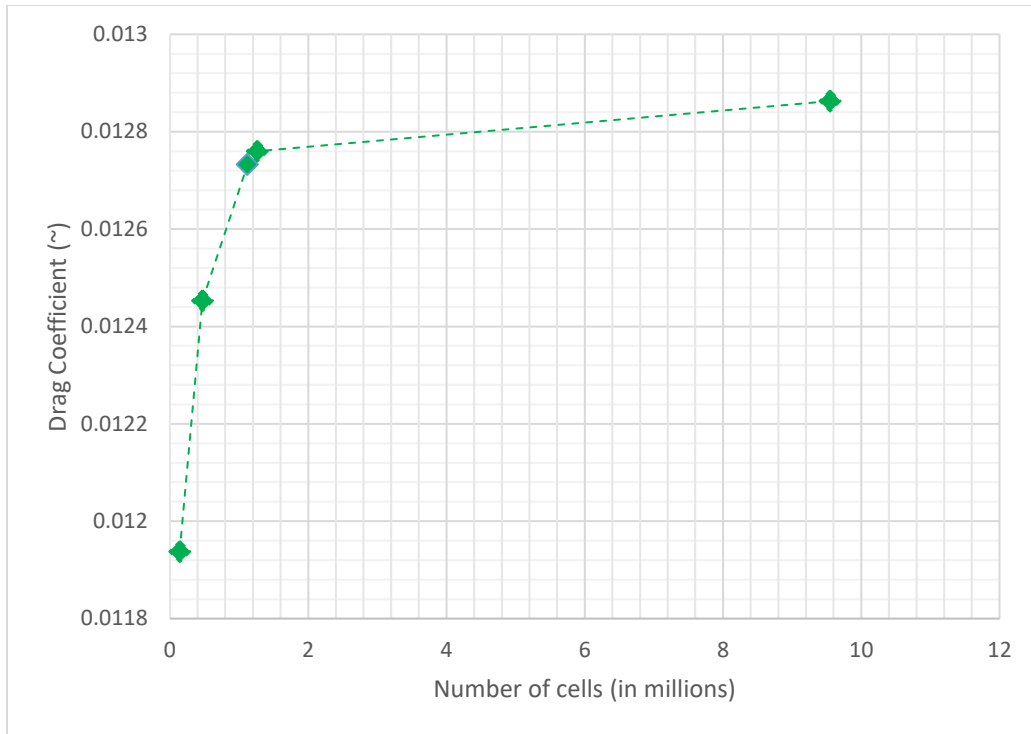
Fig. 3.7: Grid Refinement Study - includes refined mesh used for further CAA analysis

Drag coefficient for the highly refined mesh with grid size 9.55 million cells is included in grid refinement study, as shown in Fig. 3.7. It is seen that there is only a 0.80% difference in predicted drag coefficient when grid is refined from 1.26 million cells to 9.55 million cells. This tells us that the mesh with 9.55 million cells can resolve noise sources accurately and at the same time, predicted flow field continues to be accurate. Therefore, this highly refined mesh shall be used for the next step in our analysis.

3.3.2.3. Dimensions of Permeable Body

The mesh frequency cutoff scalar scene is also used to evaluate if dimensions of the permeable body are accurate. Permeable body containing all the noise sources will

61

be used by Ffowcs Williams and Hawkings model to predict farfield trailing-edge noise.
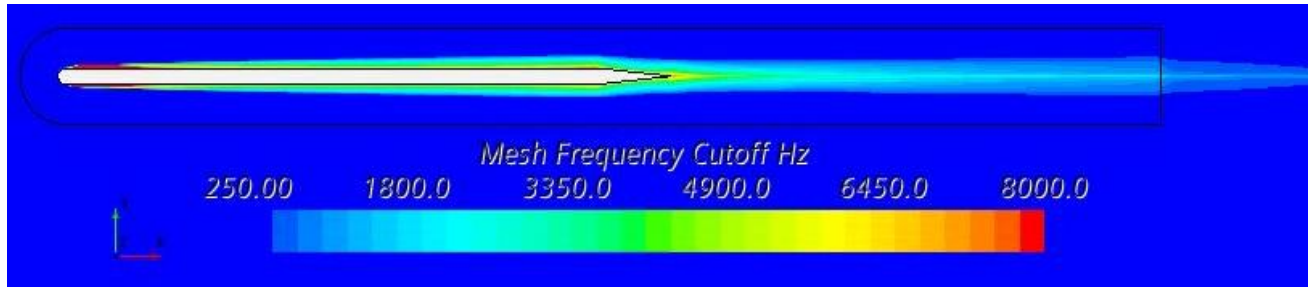
Fig. 3.8: Mesh Frequency Cutoff distribution in the permeable body region

Fig. 3.8 shows that length of the permeable body extending up to 0.8 chord lengths downstream of the trailing-edge is sufficient to encompass majority of noise sources. Similarly, a width of 0.15 chord lengths for the permeable body is sufficient to include noise sources above and below the flat plate.

3.3.2.4. Wall y^+ distribution

As shown in Fig. 3.9, a near wall thickness of 4×10^{-6} m was sufficient to ensure wall y^+ less than 1, a requirement by the near wall y^+ treatment model used along with the SST k-ω RANS turbulence model. This helped ensure the boundary layer characteristics are accurately predicted in this steady CFD analysis.
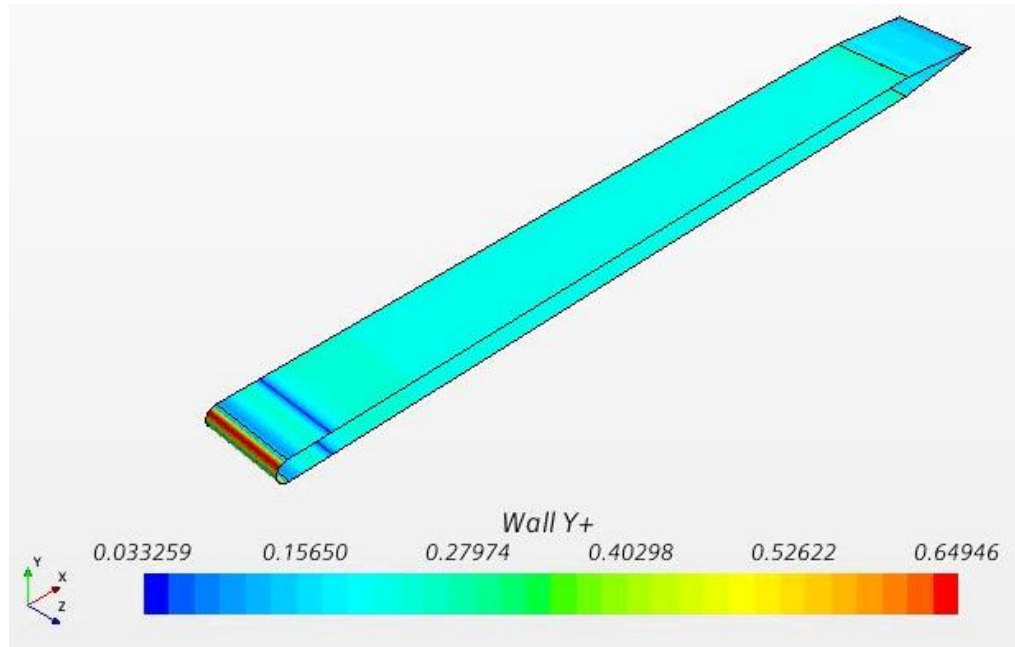
Fig. 3.9: Wall y⁺ on flat plate model

3.3.3. *Unsteady CFD Analysis*

Unsteady CFD analysis is performed using SST k-ω Improved Delayed Detached Eddy simulation. The flowfield from this model is used to estimate farfield acoustic spectra using the Ffowcs Williams and Hawkings equation. The Farassat 1-A formulation of the FW-H equation is well suited for subsonic cases and hence used in the present study. The permeable formulation, which accounts for surface thickness noise, loading noise and quadrupole noise sources, is used. An adaptive time-step control is implemented to estimate the required time-step size at each time-step and 30 sub-iterations were used at each time-step. The automatic time step condition is set such that the following were satisfied in each cell of the grid:

- Mean Convective Courant Number < 0.5
- Maximum Convective Courant Number < 1

63

The smaller time step-size obtained from the above two conditions would be used as the estimated time-step in this unsteady CFD analysis. The minimum time step size chosen in this study was 1×10^{-7} s and the time step size was automatically adjusted based on the above two conditions, with change in physical time. The simulation was run for a duration of 0.084s, which is a flow through time in the fluid domain that corresponds to 14.5 chord lengths. The unsteady CFD solver setting used for this analysis is shown in Table 3.1.

Table 3.1: Unsteady CFD Solver Settings

Parameter	Unsteady CFD Solver Setting
Turbulence model	SST (Menter) k-ω Detached Eddy Simulation
Equation of State	Ideal Gas equation
Energy equation	Segregated Fluid Temperature
k-ω wall treatment	Near wall y$^+$ treatment
Time	Implicit Unsteady
Flow solver	Segregated Flow solver
Convection scheme for Segregated Flow and Segregated Fluid Temperature	Monotonic Upwind scheme for Conservation Laws (MUSCL 3rd order)
Time step size	Automatic time step control
Temporal discretization	2nd order scheme

3.4. Results and Discussions

Flowfield characteristics in the near wake downstream of the trailing-edge and farfield noise predicted using unsteady CFD analysis and FW-H equation respectively are compared with experimental measurements and previous numerical studies.

3.4.1. Flowfield characteristics downstream of trailing-edge

Unsteady velocity measurements in the near wake were collected using hot wire anemometry by Moreau et al. [48]. Data was acquired using a probe located 0.6 mm downstream of the trialing-edge. At this position, the probe collected data by traversing vertically by y = ± 25 mm, with y = 0 mm corresponding to trailing-edge location. The mean velocity and root mean square of fluctuating velocity from unsteady CFD analysis in present study is compared with these measurements and previous numerical methods.

In the present numerical study, mean velocity was extracted using a line probe located 0.6 mm downstream of the trailing-edge. Root mean square of fluctuating velocity was obtained from predicted turbulent kinetic energy distribution downstream of the trailing-edge.

Turbulent kinetic energy is given by:

$$k = \frac{1}{2}((\overline{u'})^2 + (\overline{v'})^2 + (\overline{w'})^2) = \frac{1}{2}\left(\overline{u_\iota'}\right)^2 \tag{3.16}$$

Therefore, root mean square of fluctuating velocity is estimated using:

$$\overline{u_\iota'} = (2k)^{\frac{1}{2}} \tag{3.17}$$

3.4.2. Mean velocity distribution downstream of trailing-edge

From the present study, normalized mean velocity profile in the near wake is symmetric about the trailing-edge. A comparison of the same is made with measurements and results from previous numerical studies (RANS and LES models), as shown in Fig. 3.10 and 3.11.
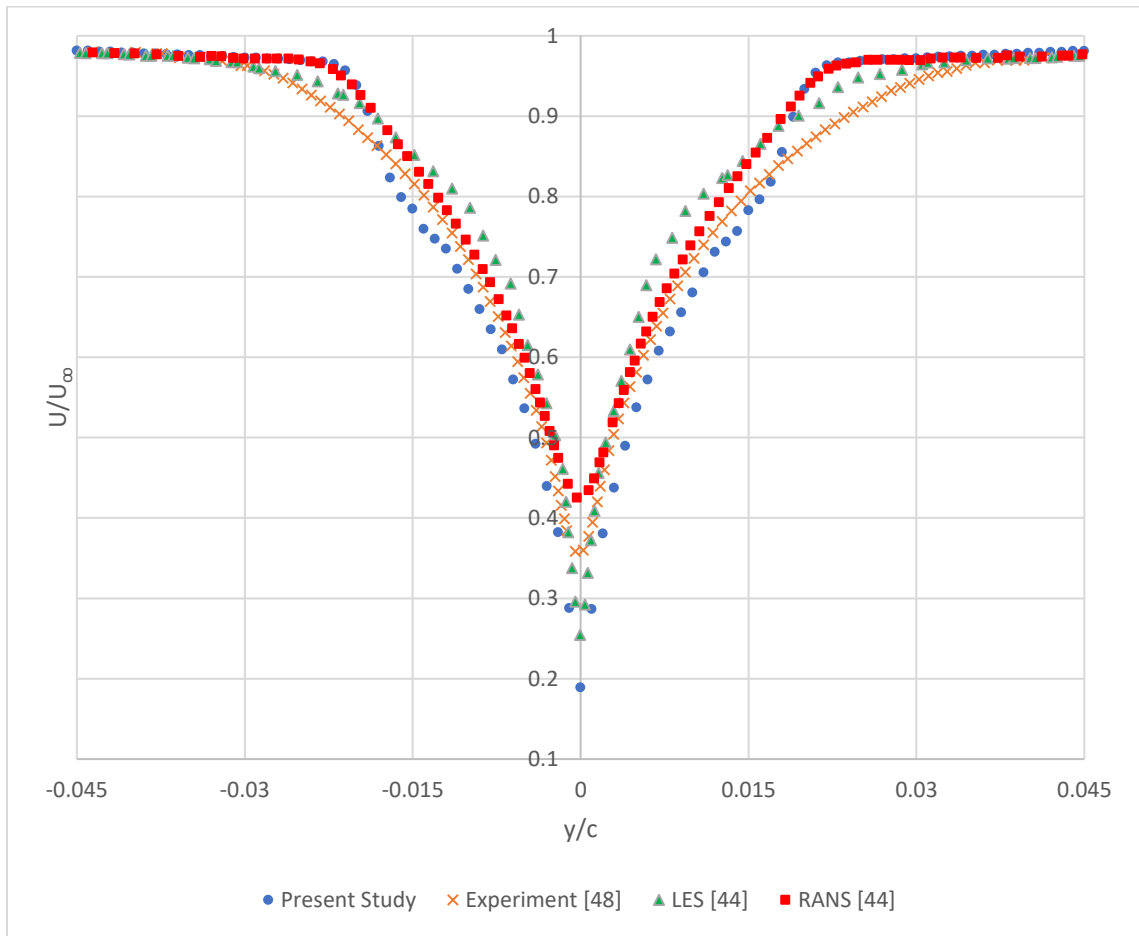
Fig. 3.10: Comparison of computational results and experiment for the mean velocity distribution downstream of trailing-edge

The normalized mean velocity distribution downstream of the trailing-edge matches well with measurements from experiment. The accuracy of prediction in the present

66

study is closer to the measurements than the LES model [44] from previous studies at locations near the trailing-edge centerline. However, this accuracy decreases away from the trailing-edge centerline where prediction from the present study is closer to the RANS model [44] from previous studies.

The mean velocity distribution from present study, using SST k-ω IDDES turbulence model, behaved as expected. The Improved Delayed Detached Eddy simulation is a hybrid modeling approach that combines features of RANS simulation in some parts of the flow and LES simulation in other parts [53]. The IDDES model is set up such that, in regions of the fluid where flow is irrotational, a base RANS closure model is used (in this case the base RANS model used is the SST k-ω RANS turbulence model). The turbulence model is modified such that if the grid is fine enough, it will emulate the basic LES sub-grid scale model in unsteady flow and separated regions.
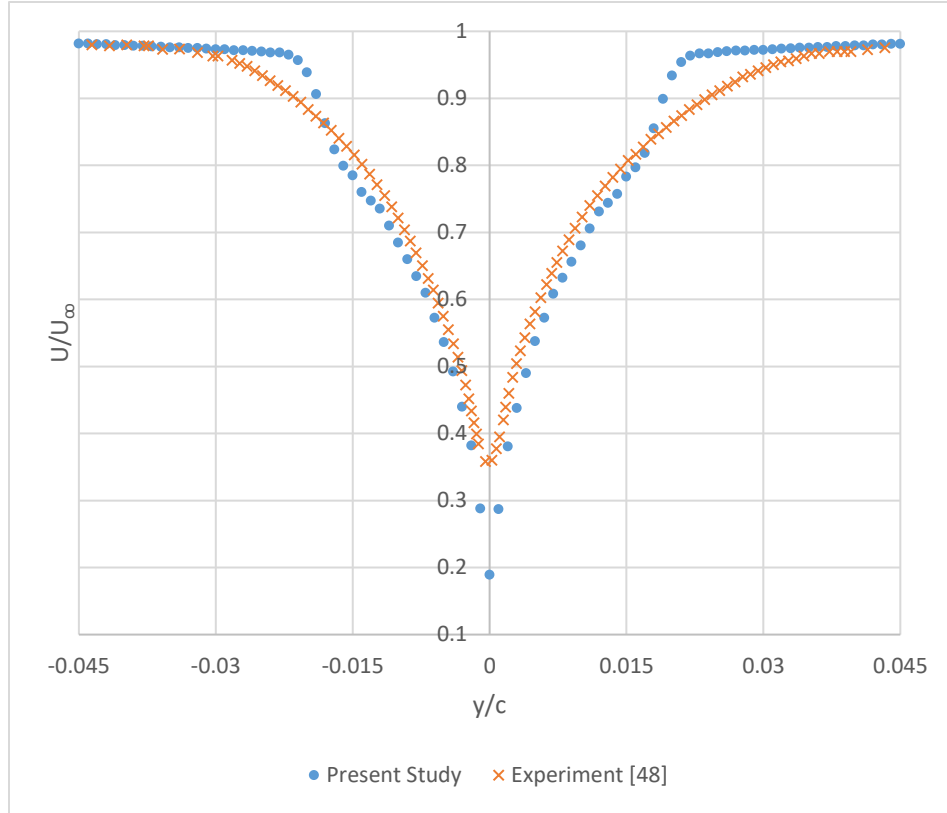
Fig. 3.11: Comparison of mean velocity distribution with experiment

3.4.3. *RMS of fluctuating velocity downstream of trailing-edge*

According to Lighthill [60], fluctuating velocity is the source of aerodynamic noise and the presence of solid boundaries such as flat plate surface or trailing-edge make these noise sources more efficient. Experimental studies [57] performed on flat plates with different trailing-edge profiles showed that broadband trailing-edge noise is governed by small scale random velocity fluctuations in the vicinity of trailing-edge.
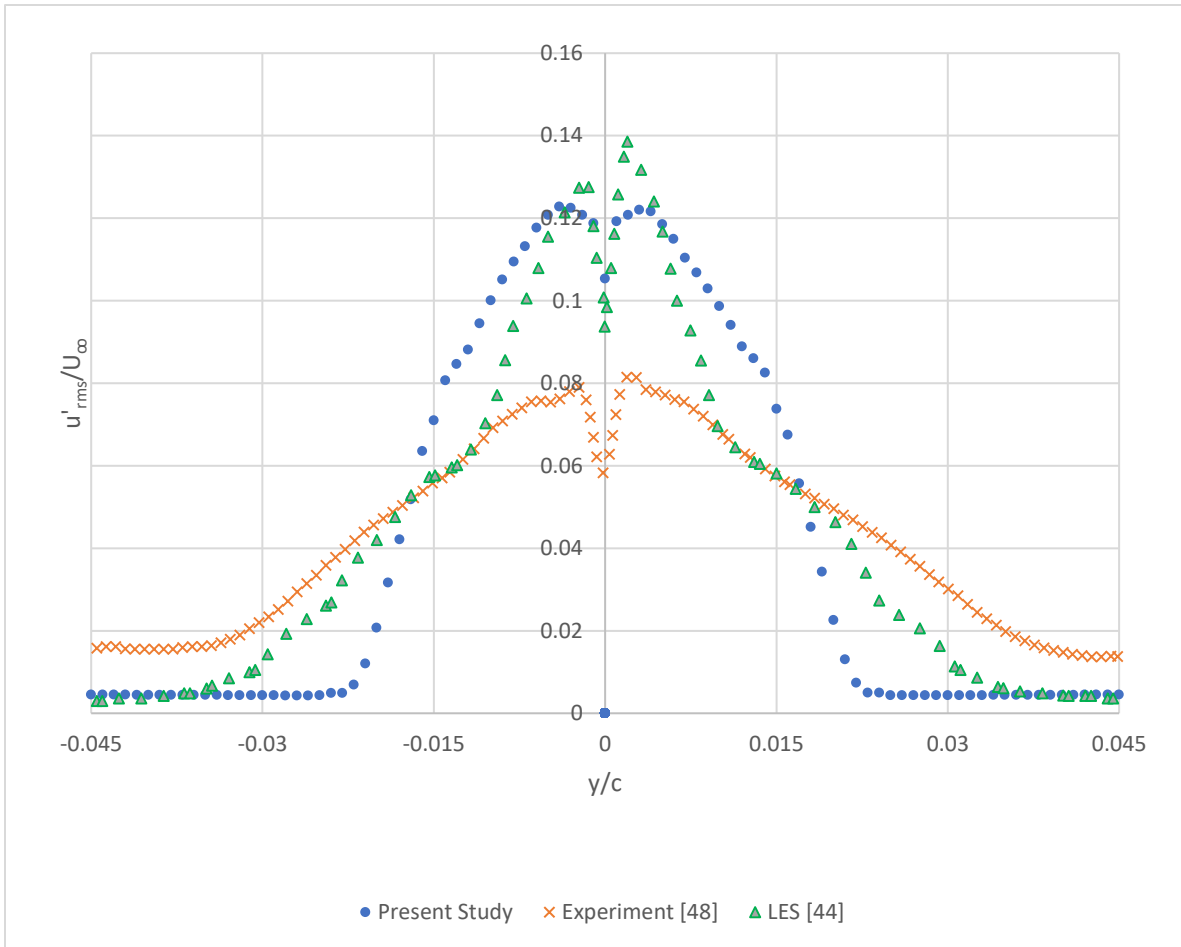
Fig. 3.12: Comparison of RMS of fluctuating velocity distribution downstream of trailing-edge

Fig. 3.12 compares the root-mean square of fluctuating velocity variation predicted at a location 0.6 mm downstream of the trailing-edge from the present study. Results are compared with measurements and LES model from previous studies [44]. Though there is an over prediction in $\overline{u'}$ at or near y/c = 0 with respect to measurement, the extent of over prediction is comparable to that obtained from LES simulation and is deemed acceptable.

3.4.4. Farfield Noise

In the experiment conducted by Moreau et al. [48], a microphone was placed 585 mm above the trailing-edge to measure farfield acoustics spectra that corresponds to trailing-edge noise. The anechoic test chamber provided a reflection free environment above 250 Hz and noise measurements were recorded up to 8000 Hz.

In the present study, pressure fluctuation history data from a point receiver located 585 mm above the trailing-edge was predicted using the Ffowcs Williams and Hawkings equation. This data was converted from time domain to frequency domain using Discrete Fourier Transform. Using this information, Power Spectral Density was estimated at this point receiver.

Power Spectral Density is defined as:

$$L_p(f) = 10 \log_{10} \left(\frac{PSD(f)}{\hat{p}_{ref}^2} \right) \tag{3.18}$$

where,

$\hat{p}_{ref}$ is reference acoustic pressure for air (20 µPa)

It must be noted that pressure fluctuation data was extracted from 0.042s to 0.084s. This sampling time was divided into 3 analysis blocks and a Hanning window function with an overlap factor of 50% was implemented to prevent spectral leakage [53]. Using a characteristic chord length of 0.2 m and free stream velocity of 35 m/s, Strouhal number was estimated for a frequency range from 250-8000 Hz and a plot of Power Spectral Density versus Strouhal number was created, as shown in Fig. 3.13.
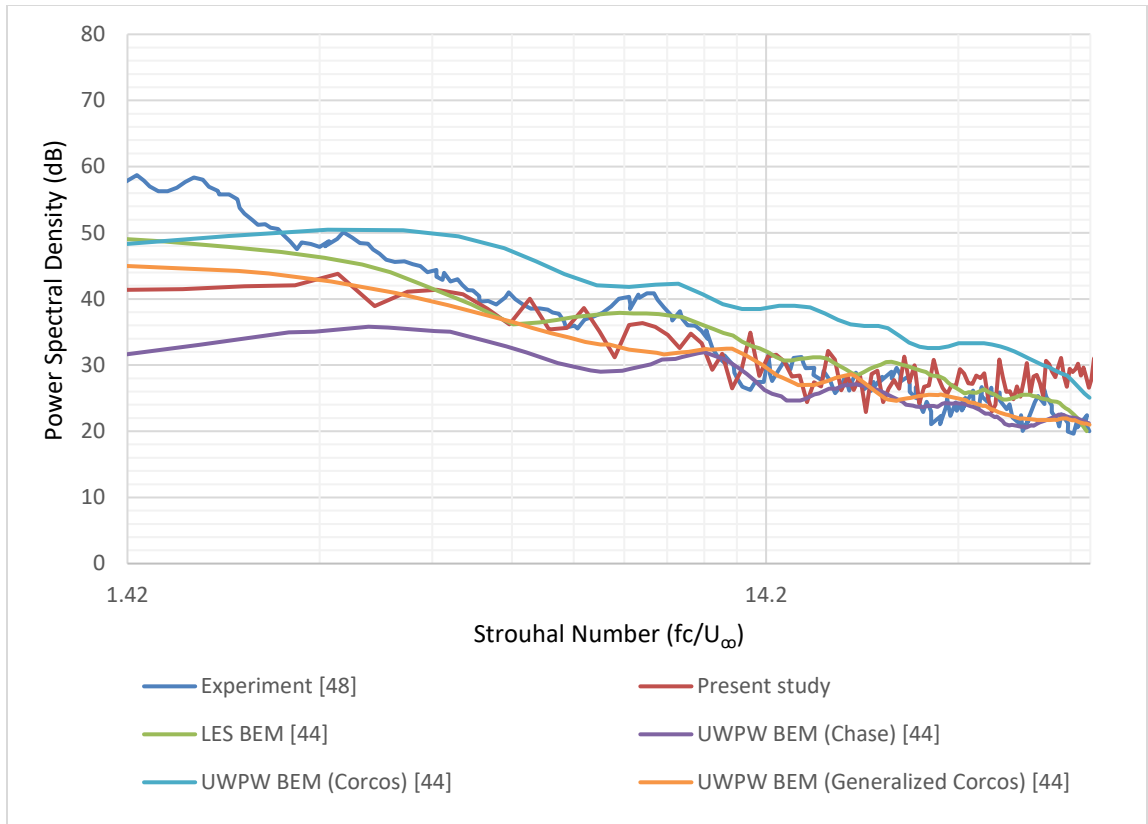
Fig. 3.13: Comparison of Power Spectral Density

Predictions of Power Spectral Density made from present study show good agreement with experimental measurements. The accuracy of results from present study are also comparable with those from previous numerical methods used to predict farfield noise for from this flat plate for the same flow conditions.
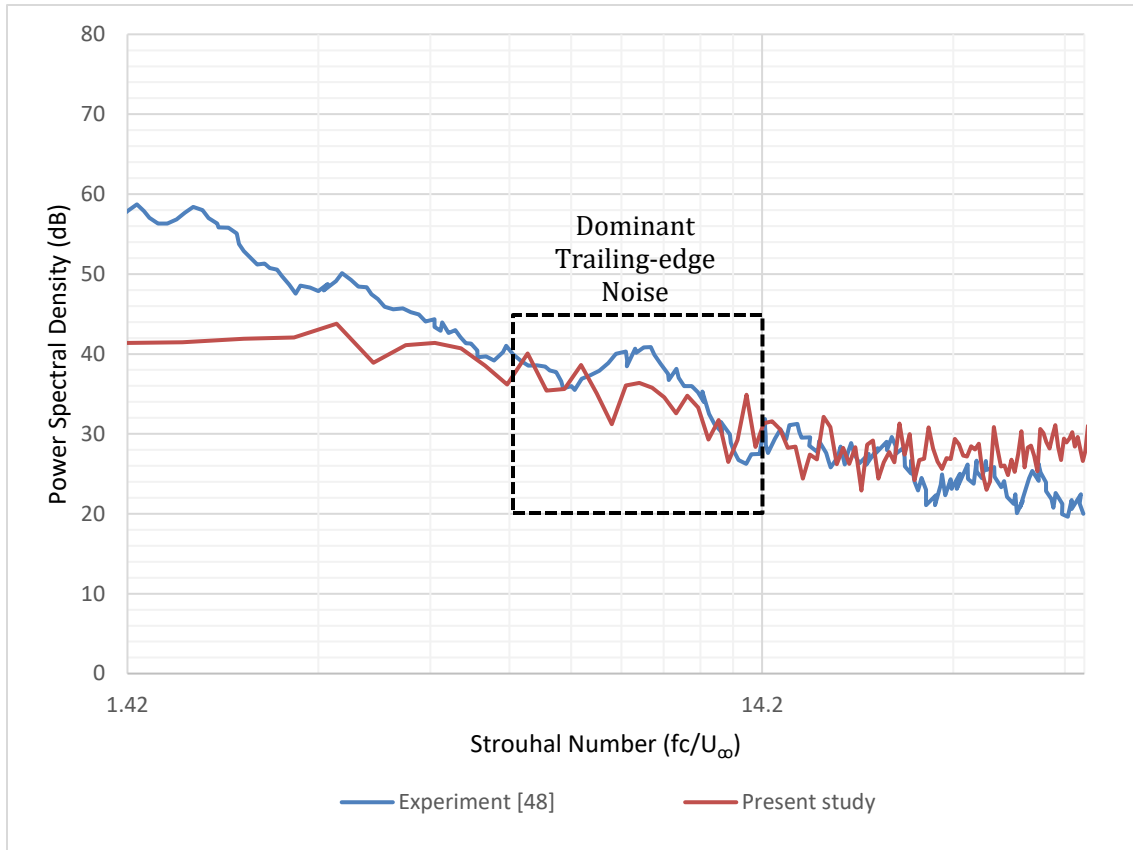
Fig. 3.14: Comparison of Power Spectral Density with Experiment

As shown in Fig. 3.14, the present study accurately predicts farfield noise for a frequency range from 750 – 7000 Hz (i.e., St = 4.28 – 40.00). There is some slight under prediction in noise observed for a frequency below 750 Hz when compared to the experiment. Similarly, for a frequency above 7000 Hz, there is some over prediction in noise from the present study.

Despite the inaccuracies observed at low and high frequencies, the predicted noise accurately follows the general magnitude and trends of experimental measurements particularly from 900 – 2500 Hz (St = 5.14 – 14.28). This frequency range corresponds to trailing-edge noise [61], the dominant noise source [44] in the present study.

72

3.5.   Conclusion

A computational aeroacoustics analysis is performed to predict farfield noise generated by a flat plate with sharp trailing-edge. The results from this study were validated using flow and noise measurements recorded by Moreau et al. [48] at the University of Adelaide. It was observed that the mean velocity distribution matches well with experiments. Accuracy of this prediction is especially high close to trailing-edge centerline. The RMS of fluctuating velocity distribution predicted in the present study is comparable to that from previous computational studies. Farfield noise propagated from trailing-edge of flat plate follows the magnitude and trend of measurements from 750 – 7000 Hz (i.e., St = 4.28 – 40). This noise is particularly well predicted from 900 – 2500 Hz (i.e., St = 5.14 – 14.28), where trailing-edge noise is considered dominant [61]. The results from this study will serve as Baseline data for comparison while investigating suitable noise mitigation techniques.

4. TRAILING-EDGE NOISE WITH PASSIVE COMPLIANT COATING: A COMPUTATIONAL STUDY

This chapter is based on a work titled "Trailing-Edge Noise with Passive Compliant Coating: A Computational Study" presented at the AIAA Science and Technology Forum and Exposition, 3-7 Jan 2022.

Abstract

A computational study to investigate the role of passive compliant coatings and trailing-edge noise is conducted on a flat plate in fully turbulent flow. Farfield noise is predicted for the baseline rigid flat plate model and compared with the case when compliant coating is applied to flat plate. It was observed that application of compliant coating on the flat plate model may result in an increase of trailing-edge noise by 10-15 dB throughout the frequency range of interest, with a reduction in noise of 6 dB at St=4.00. Increase in noise predictions is attributed to the choice of compliant coating material properties. This choice plays a crucial role in determining whether the coating can exhibit the desired response to fluctuating pressure over the compliant wall for a given flowfield. Further computational study is proposed to investigate the relationship between coating's resonance frequency and given flowfield to mitigate trailing-edge noise.

4.1. Introduction

In the present computational study, a homogeneous visco-elastic compliant coating is chosen to study its ability to modify the boundary layer characteristics upstream of the trailing-edge and we investigate its effects on trailing-edge noise. In the present study,

we have chosen a flat plate in fully turbulent flow to demonstrate the technique. Two cases are analyzed in this study:

4.1.1. Baseline Case

When a compliant coating with certain thickness is uniformly applied to the flat plate shown in Fig. 4.1, it changes the dimensions and alters its trailing-edge shape, as shown in Fig. 4.2.

Fig. 4.1: Flat plate model before application of compliant coating

This in turn would alter its aerodynamic characteristics. To account for this, the coating's outer profile is used to create a rigid flat plate model with new dimensions and trailing-edge shape. This rigid flat plate model with rounded trailing edge shall be treated as baseline for the present study.

Fig. 4.2: Baseline rigid flat plate model

4.1.2. Case of compliant coating applied to a flat plate

Fig. 4.3 represents a schematic diagram of the case when a compliant coating is applied to the flat plate shown in Fig. 4.1. Effects of this compliant coating on trailing-

edge noise shall be compared to results obtained from the baseline model. Fluid structure Interaction technique shall be used to simulate the compliant coating behavior and its effects on flow boundary layer.
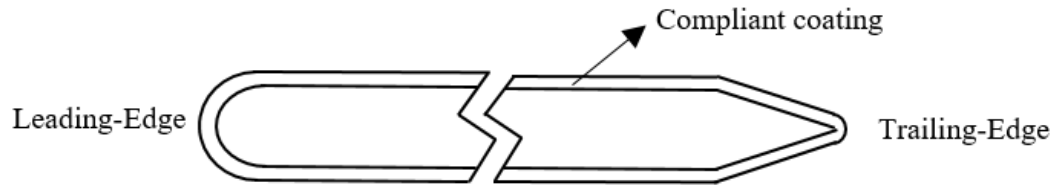
Fig. 4.3: Compliant coating applied to flat plate model

4.2. Baseline Case

In this section, we will present the steps involved in computational analysis of baseline prediction. As outlined in Chapter 4.1, a rigid flat plate model is now created to account for the changes in dimension of flat plate and shape of its trailing-edge when a compliant coating with certain thickness is applied to the flat plate geometry. A scaled geometry of the baseline model is seen in Fig. 4.4.
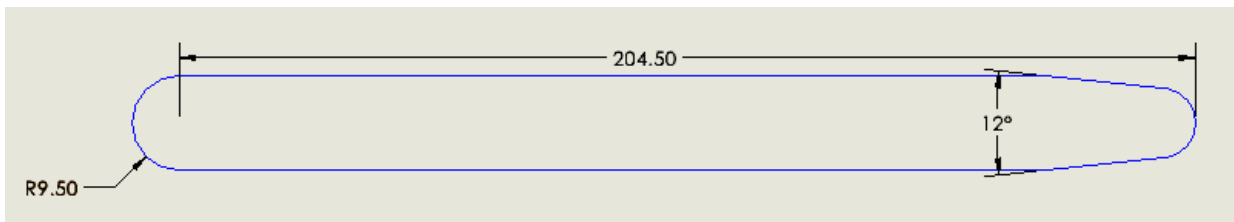
Fig. 4.4: Baseline flat plate geometry (drawn to scale)

4.2.1. Steady CFD analysis

The parameters/settings and boundary conditions used for CFD analysis in the baseline case are identical to what were used for the validation case, described in Chapter 3, Section 3.3. As seen in Figure 4.5, A trimmer mesh with hexahedral cells is

chosen for domain discretization as it offered the least amount of numerical dissipation, thus enabling accurate farfield noise prediction. As seen in Fig. 4.5, a trimmer mesh with hexahedral cells is chosen for domain discretization as it offered the least amount of numerical dissipation, thus enabling accurate farfield noise prediction.
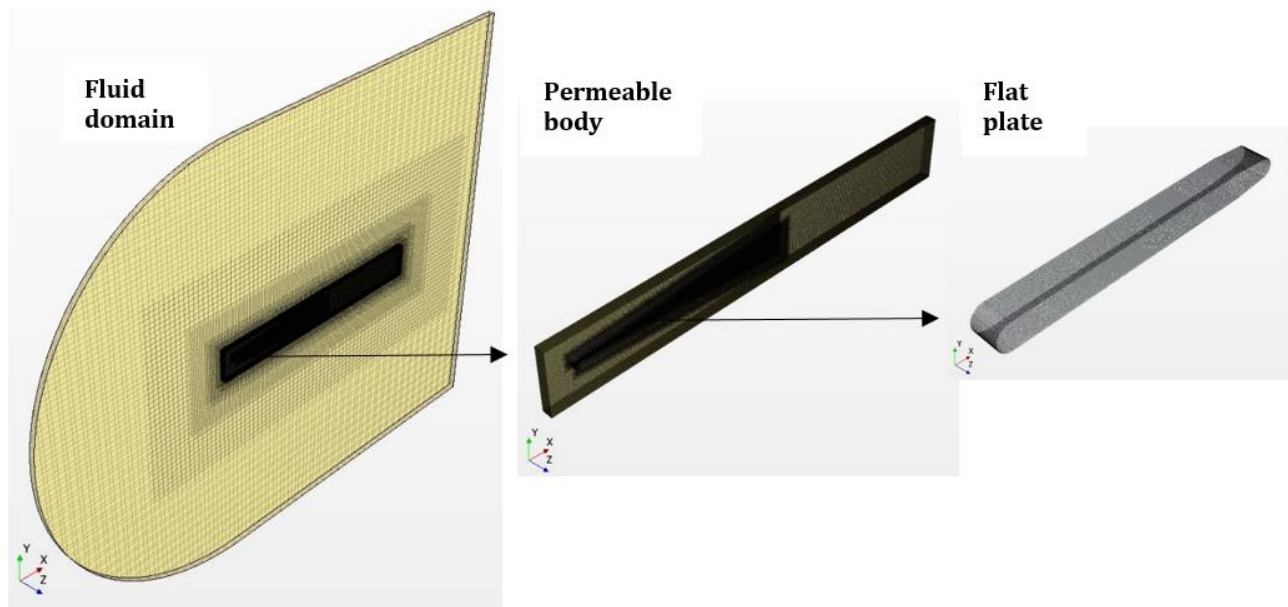
Fig. 4.5: Hexahedral trimmer mesh used for domain discretization

4.2.1.1. Grid refinement study

A grid refinement study is performed for wind speed of 35 m/s ($Re_c \approx 460,000$) to ensure that solutions obtained from CFD analysis are independent of mesh resolution. Steady CFD simulations were performed using four different grid resolutions ranging from a coarse grid of 1.18 million cells to a fine grid of 1.72 million cells.
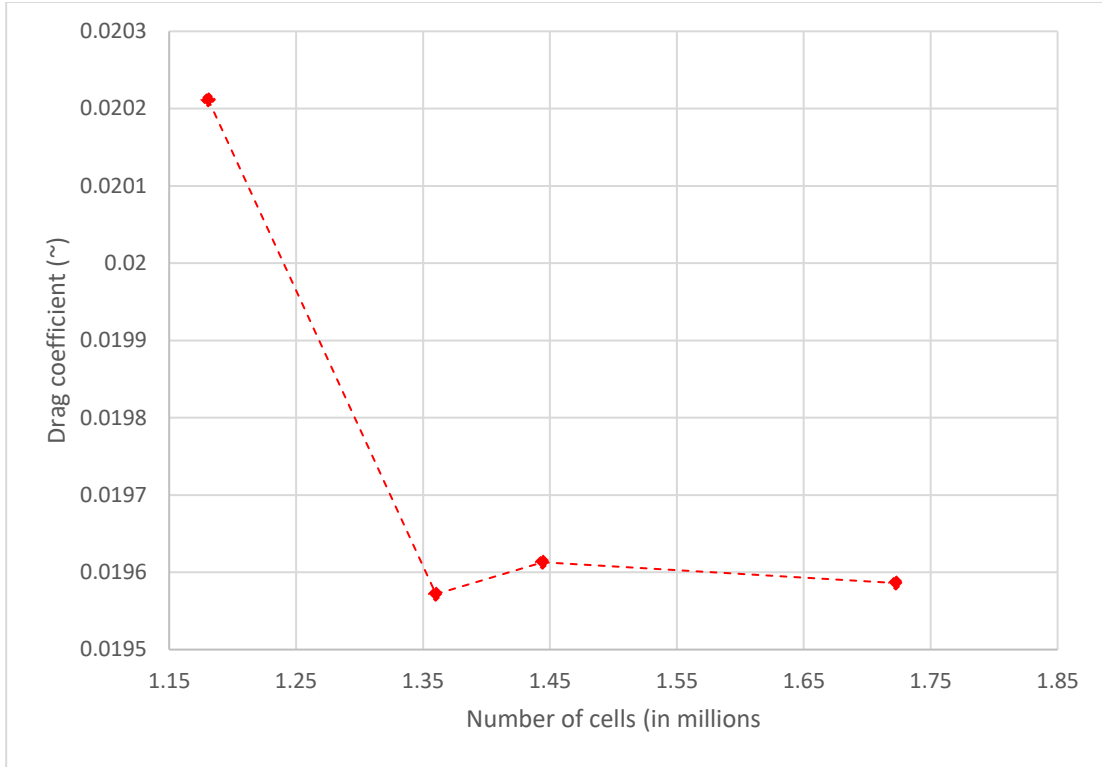
Fig. 4.6: Grid refinement study at wind speed of 35 m/s

From Fig. 4.6, it is seen that there is only a 0.13% difference in predicted drag coefficient when grid is refined from 1.44 million cells to 1.72 million cells. Therefore, the grid with 1.72 million cells was found to resolve flowfield around the flat plate accurately and thus chosen for the next step in our analysis.

4.2.1.2. Mesh Frequency Cutoff

The mesh frequency cutoff parameter, seen in Equation (4.1), is used to identify a grid that can resolve noise sources from turbulent flow structures present around the flat plate in the frequency range of interest (250-8000Hz).

78

$$f_{MC} = \frac{\sqrt{\frac{2}{3}k}}{(2\Delta)}$$

<div align="right">(4.1)</div>
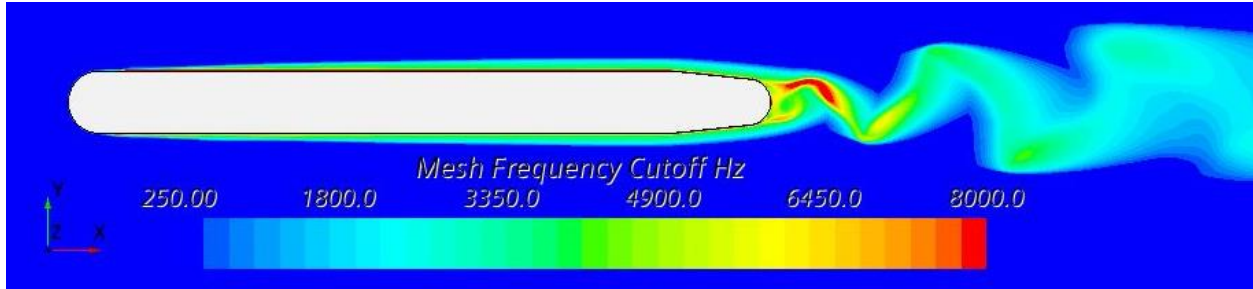
Fig. 4.7: Mesh frequency cutoff scalar scene for grid size of 17.84 million cells

It was found that the grid size of 1.72 million cells was not sufficient to resolve noise source distribution around the flat plate. Hence a volumetric refinement region was included around the flat plate and inside the permeable body, as seen in Fig. 4.5. This was used to refine the cells to a size of 3×10^{-4}m in vicinity of the flat plate model (including downstream wake) to resolve the noise sources well, as seen in Fig. 4.7. Inclusion of volumetric refinement increased the mesh size from 1.72 million cells to 17.84 million cells.

4.2.2. Unsteady CFD analysis

Unsteady CFD analysis is performed using SST k-ω Improved Delayed Detached Eddy simulation and farfield noise is estimated using the Ffowcs Williams and Hawkings equation. The solver settings used in this analysis were identical to that used in Table 3.1 of Chapter 3, Section 3.3.3, except that a constant time-step of 5×10^{-6}s was chosen to ensure that the mean convective courant number is less than 1 in the computational domain. It was observed that after a physical time of 0.08s, the residuals for continuity equation was in the order of 10^{-10}, the momentum equations were in the

order of 10^{-9} and energy equation was in the order of 10^{-7}. Thus, flow-solver had attained convergence. However, having modified the flat plate geometry to account for coating thickness, there is no experimental data available to validate the baseline results. Therefore, a more rigorous analysis, as outlined in the following section, has been performed to ensure that the results from unsteady CFD simulation can be considered reliable and accurate.

4.2.3. Results and Discussions

To ensure that predicted farfield noise uses reliable flowfield data obtained from unsteady CFD analysis, the variance and co-variance of velocity was monitored at 4 locations 0.6 mm, 1 mm, 5 mm and 10 mm downstream of the trailing-edge. If there is no numerical dissipation, it is expected that variance and co-variance of velocity would roughly be constant over time with some dissipation due to viscosity of air. This helped us identify a physical time in our unsteady CFD analysis when the numerical dissipation significantly reduces and simulation is considered to have attained statistical convergence, after which farfield noise data shall be collected.

4.2.3.1. Variance of velocity downstream of the trailing-edge

Variance of velocity was estimated along the three directions in the cartesian plane using the equations:

$$S(u) = \frac{\sum(u_i - \bar{u})^2}{n - 1} \tag{4.2}$$

$$S(v) = \frac{\sum(v_i - \bar{v})^2}{n - 1} \tag{4.3}$$

$$S(w) = \frac{\sum (w_i - \bar{w})^2}{n - 1} \tag{4.4}$$

where,

u_i, v_i, and w_i are the instantaneous velocities in the x, y and z directions

$\bar{u}$, $\bar{v}$ and $\bar{w}$ are the mean velocities in the x, y and z directions

n is the number of time-steps.
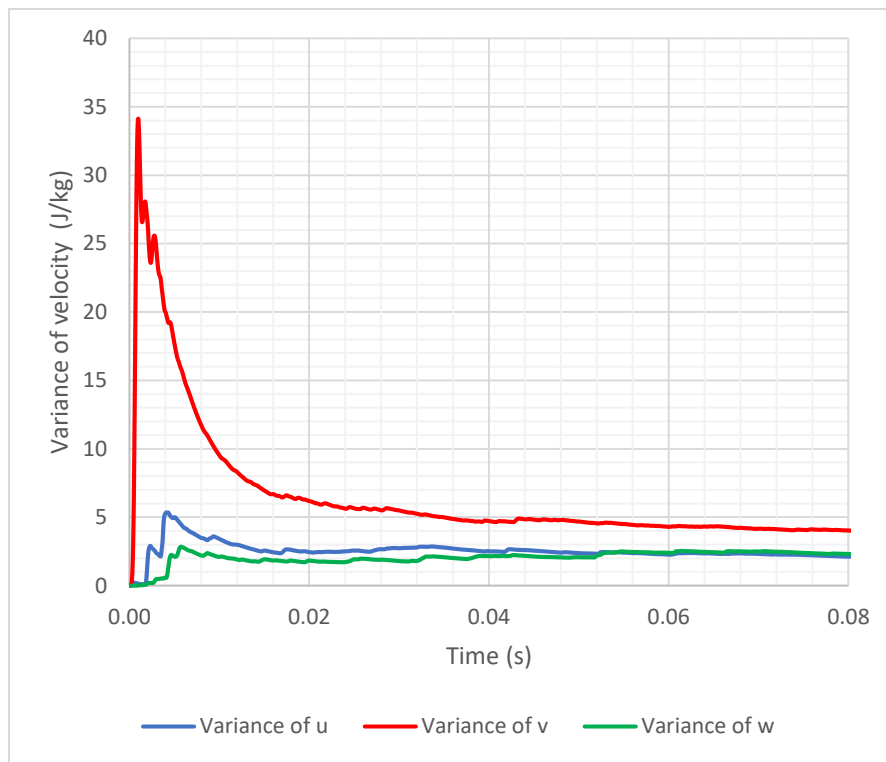
Fig. 4.8: Variance of velocity 0.6 mm downstream of trailing-edge
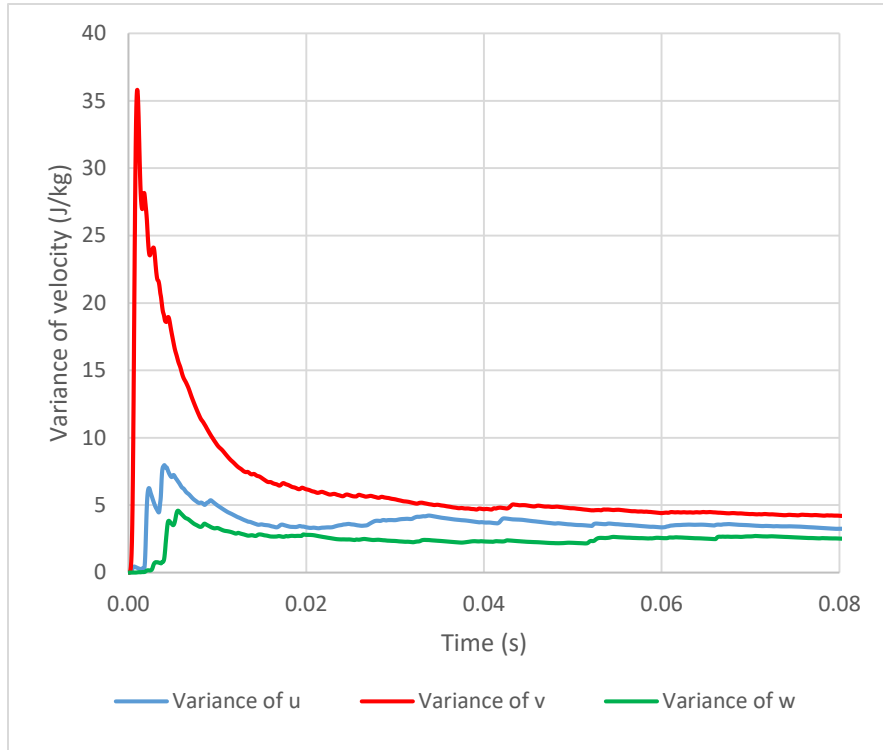
Fig. 4.9: Variance of velocity 1 mm downstream of trailing-edge
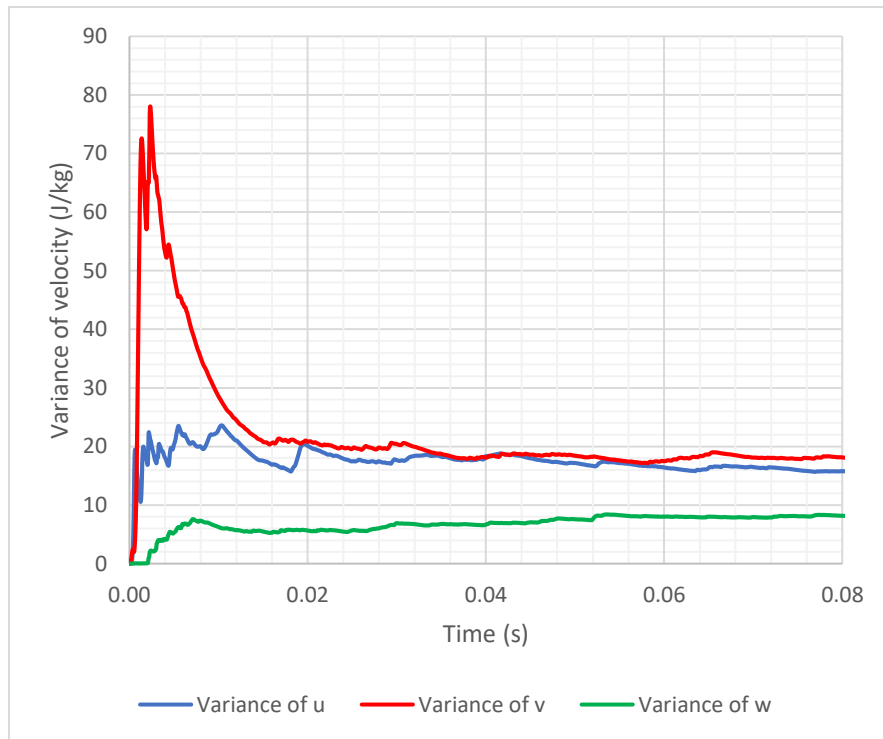
Fig. 4.10: Variance of velocity 5 mm downstream of trailing-edge
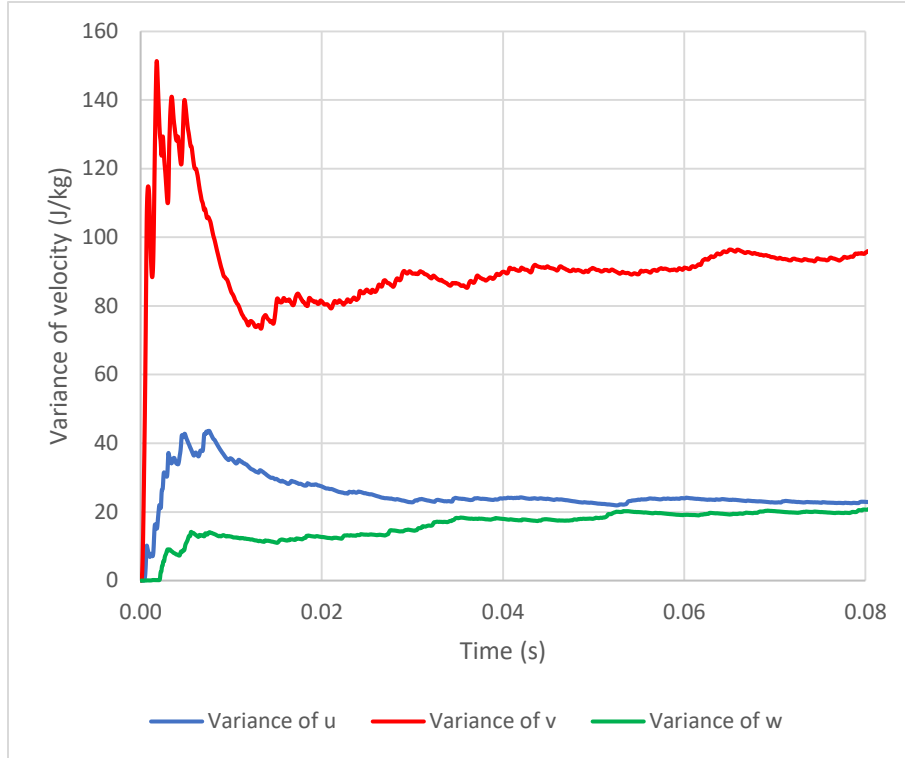
Fig. 4.11: Variance of velocity 10 mm downstream of trailing-edge

As seen from Figures 4.8 - 4.11, the variance of velocity along the x, y and z direction has approximately attained constant values by 0.08s and hence considered to have attained statistical convergence. To verify this, the process was repeated for covariance of velocity as well.

4.2.3.2. Covariance of velocity downstream of the trailing-edge

Covariance of velocity was estimated along the three directions in the cartesian plane using the equations:

$$C(u,u) = \frac{\sum(u_i - \bar{u})(u_i - \bar{u})}{n-1} \tag{4.5}$$

$$C(u,v) = \frac{\sum(u_i - \bar{u})(v_i - \bar{v})}{n-1} \tag{4.6}$$

$$C(u, w) = \frac{\sum (u_i - \bar{u})(w_i - \bar{w})}{n - 1} \qquad (4.7)$$

where,

u_i, v_i, and w_i are the instantaneous velocities in the x, y and z directions

$\bar{u}$, $\bar{v}$ and $\bar{w}$ are the mean velocities in the x, y and z directions

n is the number of time-steps.
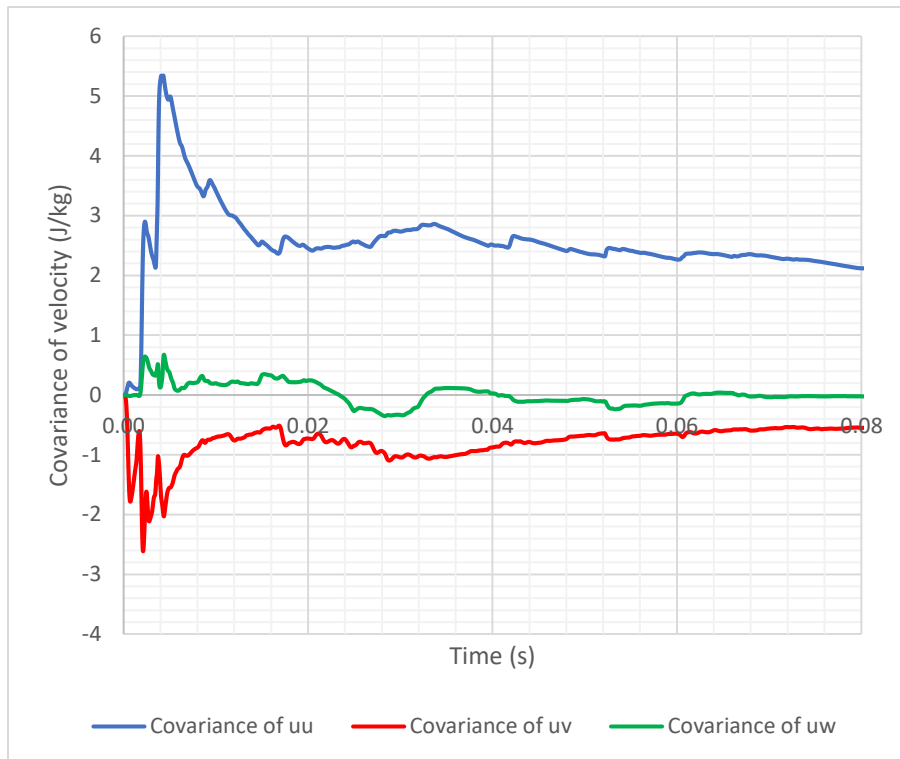
Fig. 4.12: Co-variance of velocity 0.6 mm downstream of trailing-edge
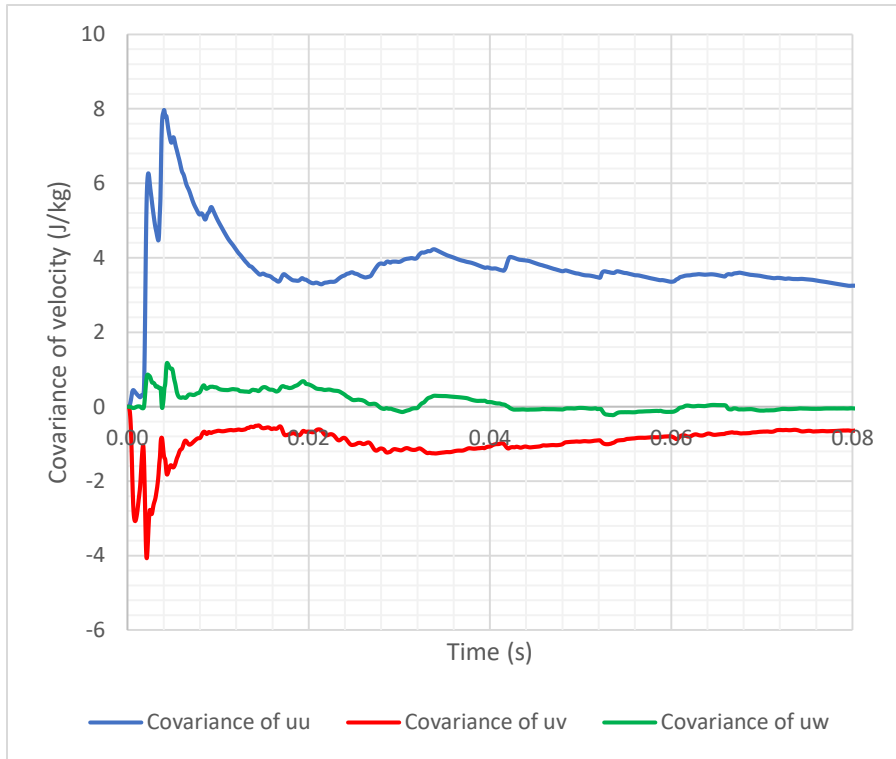
Fig. 4.13: Co-variance of velocity 1 mm downstream of trailing-edge

Fig. 4.14: Co-variance of velocity 5 mm downstream of trailing-edge

85

Fig. 4.15: Co-variance of velocity 10 mm downstream of trailing-edge

As seen from Figures 4.12-4.15, the co-variance of velocity along the x, y and z direction has approximately attained constant values by 0.08s and hence considered to have attained statistical convergence. Thus, noise data estimated after 0.08s can be considered reliable, as the FW-H model would use accurate flowfield predicted in the vicinity of the flat plate.

4.2.3.3. Mean velocity distribution

Mean velocity distribution is predicted 0.6 mm downstream of the trailing-edge for the baseline model, as seen in Fig. 4.16. This result, indicative of wake characteristics downstream of trailing-edge, shall be used to compare with the case when compliant coating is applied to flat plate and investigate its ability to favorably modulate flow boundary layer and thus aid in drag reduction.
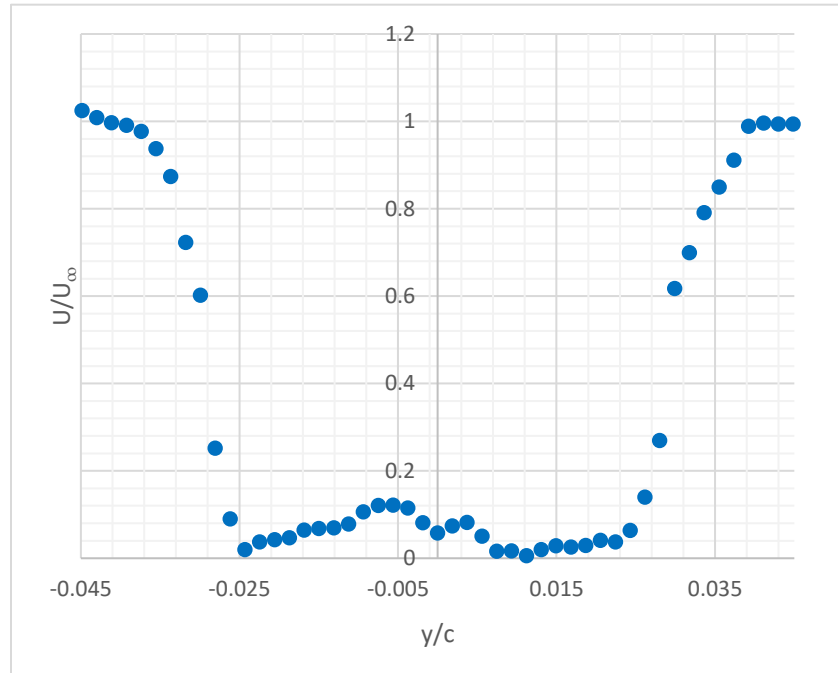
Fig. 4.16: Mean velocity distribution 0.6 mm downstream of trailing-edge
(Baseline Case)

4.2.3.4. Farfield Noise

Pressure fluctuation history data was recorded by a point receiver placed 585 mm above the trailing-edge from 0.08-0.12s. The duration of 0.04s used for noise data collection was estimated based on the minimum frequency of interest to be resolved (250 Hz) and 10 time-cycles corresponding to is minimum frequency, which enabled accurate farfield noise prediction. The data was converted from time domain to frequency domain using Discrete Fourier Transform and Power Spectral Density was estimated using Equation (4.8). This sampling time was divided into 3 analysis blocks and a Hanning window function with an overlap factor of 50% was implemented to prevent spectral leakage. Using a characteristic chord length of 0.214 m and free stream velocity of 35 m/s, Strouhal number was estimated for a frequency range from

87

250-8000 Hz and a plot of Power Spectral Density versus Strouhal number was created, as shown in Fig. 4.17. This plot would be used as our baseline noise prediction to compare with the case when compliant coating is applied to the flat plate.

$$L_p(f) = 10 \log_{10}\left(\frac{PSD(f)}{\hat{p}_{ref}^2}\right) \qquad (4.8)$$

where,

$\hat{p}_{ref}$ is reference acoustic pressure for air (20 µPa)
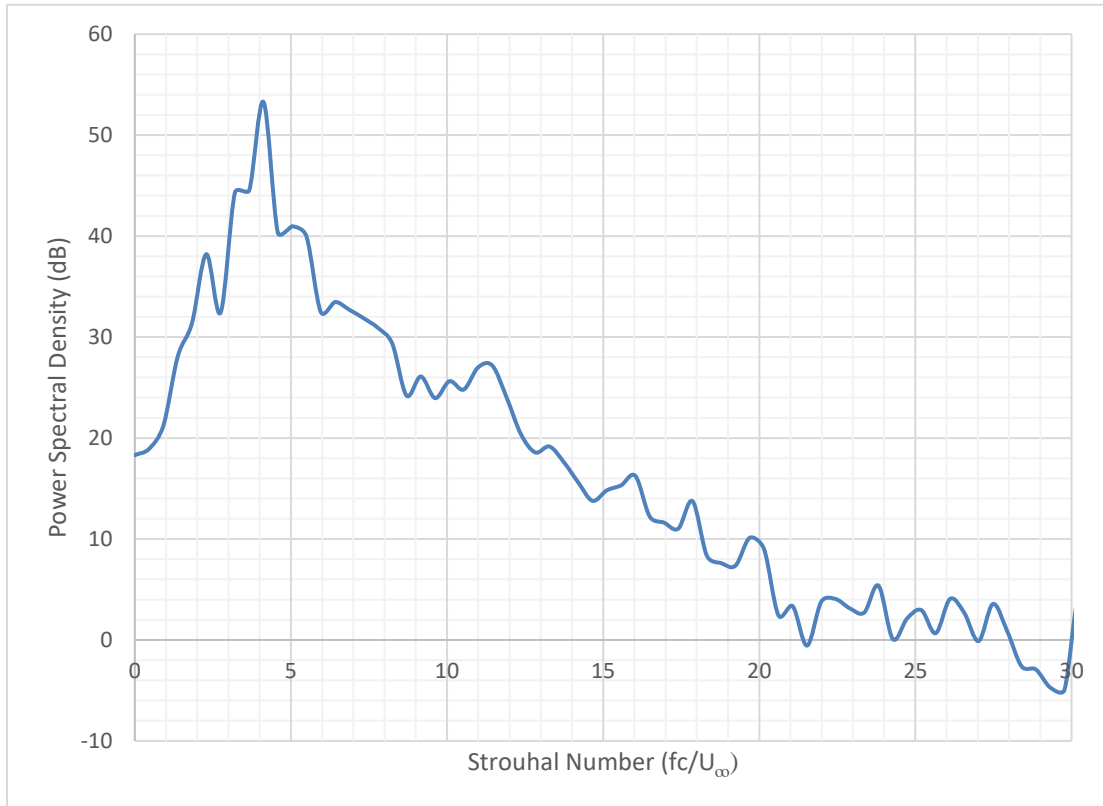
Fig. 4.17: Power Spectral Density predicted 585 mm above trailing-edge
(Baseline Case)

4.3. Case of compliant coating applied to flat plate

This part of the computational study involves simulating the effects of a compliant coating with thickness of 7 mm and material properties as outlined in Table 4.1, to study its effects on trailing-edge noise.

Table 4.1: Optimum Material Properties for Stiff Compliant Coating [24]

Material properties for optimum compliant coating	Magnitude (Units)
Density	1130 kg/m^3
Poisson's ratio	0.485
Young's Modulus	1.1 MPa
Thickness of compliant coating	7 mm

When compliant coating is applied to the flat plate geometry, as shown in Fig. 4.18, the chord length increases to 214 mm and shape of the sharp trailing-edge is altered.
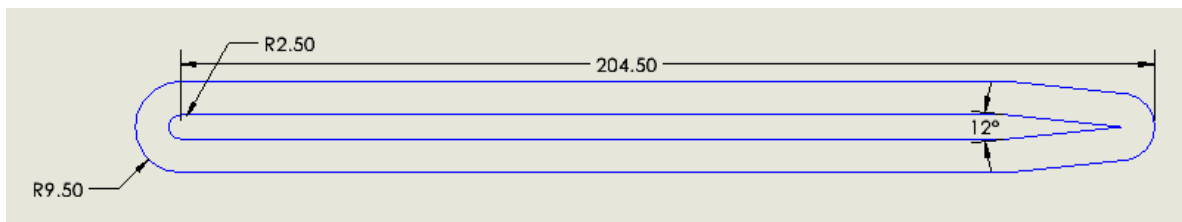
Fig. 4.18: Compliant coating applied to flat plate geometry *(All dimensions in mm)*

For this computational study, the *Fluid Structure Interaction* technique of a commercial CFD code STAR-CCM+ v.15.02.009 has been used. Modelling of the elastomer's behavior when it interacts with the impinging wind involves complex interactions between the two. Therefore, the *Two-way coupling* technique is used to simulate the momentum and energy transfer between the fluid and a homogeneous

isotropic viscoelastic compliant coating. Deformation of the passive compliant coating can be achieved using a *morphing mesh*. Initially, a solid stress model with *isotropic linear elasticity* has been used to perform static analysis, in which a steady CFD and FSI simulation is run so that both the flowfield and the compliant coating reach an equilibrium condition.

4.3.1. Mesh and boundary conditions

The computational domain and boundary conditions used for the fluid region were identical to what were used for the used for the validation case, described in Chapter 3, Section 3.3. However, the rigid flat plate from baseline case was replaced by the flat plate model with compliant coating applied to it as seen in Fig. 4.18.

The boundary conditions and meshing technique applied for the solid compliant coating region are different from that of the fluid region to accommodate its solver requirements. A non-conformal *Mapped Contact Interface* is created between the outer surface of the coating and fluid region in contact. This interface helps exchange information between the fluid and structure solvers. Symmetry boundary conditions are used on either side-planes of the coating. A fixed constraint is applied to the inner surface of coating that is in contact with the flat plate while rest of the *morphing mesh* can change its position. A structured mesh with a mesh size of 1.26 million was created using hexahedral cells for the solid compliant coating region. Whereas, a trimmer mesh with a mesh size of 17.84 million was created using hexahedral cells. The fluid region's mesh parameters were identical to the baseline case.

90
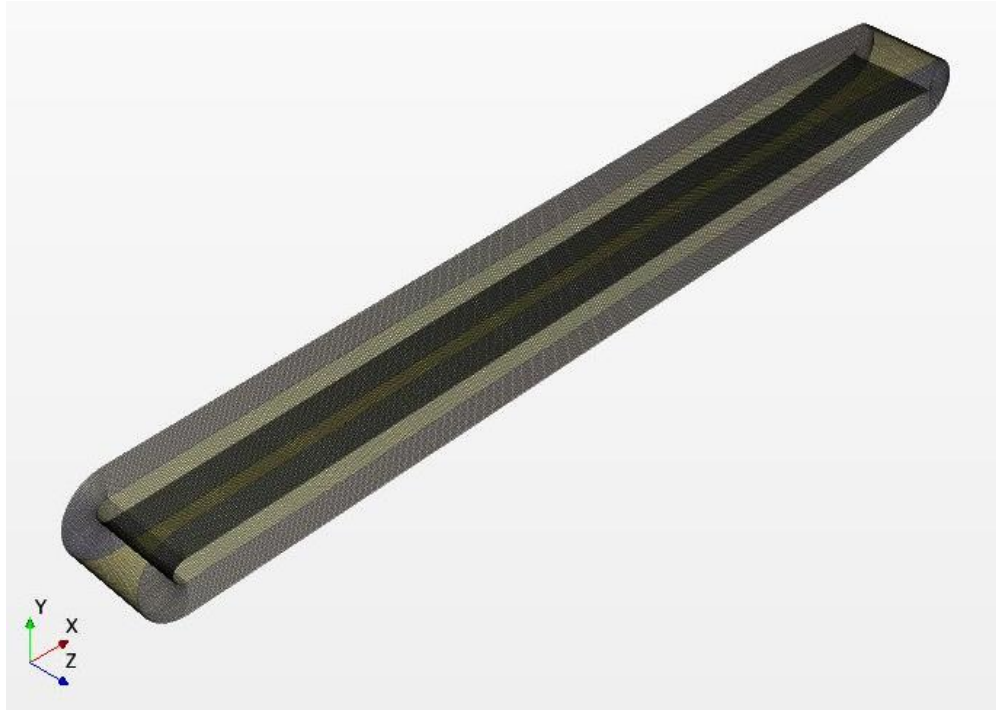
Fig. 4.19: Structured mesh with hexahedral cells to discretize coating region

4.3.2. Steady CFD-FSI analysis

The CFD solver settings used in this analysis were identical to what were used in the baseline case. The solid stress solver settings are listed in Table 4.2. Initially, a steady CFD simulation was run up to 2100 iterations which was sufficient for the flow solver to attain residual convergence. Next, the aerodynamic forces exerted by air impinging on the compliant coating was converted into body loads and applied on the compliant coating surface by linearly ramping the loads through gradual increments from 2100 – 2300 iterations. The loads were linearly incremented over 200 iterations to ensure stability of simulation. Finally, both the CFD solver and the Solid Stress solver was run from 2300 – 3700 iterations to ensure that the steady FSI simulation attains convergence.

91

Table 4.2: Solid Stress Solver Settings

Parameter	Solid Stress Solver Setting
Space	Three Dimensional
Time	Steady
Material Stiffness model	Linear Elasticity
Linear Elastic Material model	Isotropic Linear Elasticity
Coupling	Two way
Motion Specification	Solid Displacement

4.3.3. *Compliant coating deformation: Steady CFD-FSI results*

After steady CFD-FSI analysis is performed, the compliant coating deformation is studied to identify if the extent of deformation is comparable to literature. The deformation of compliant coating is observed to be in the order of microns, with maximum deformation of 5.92μm at center of leading-edge. Since it is difficult to visualize deformation in this order of magnitude, the coating displacement is scaled to 100 times and 200 times respectively and presented in Fig. 4.20 and 4.21 for illustrative purposes.
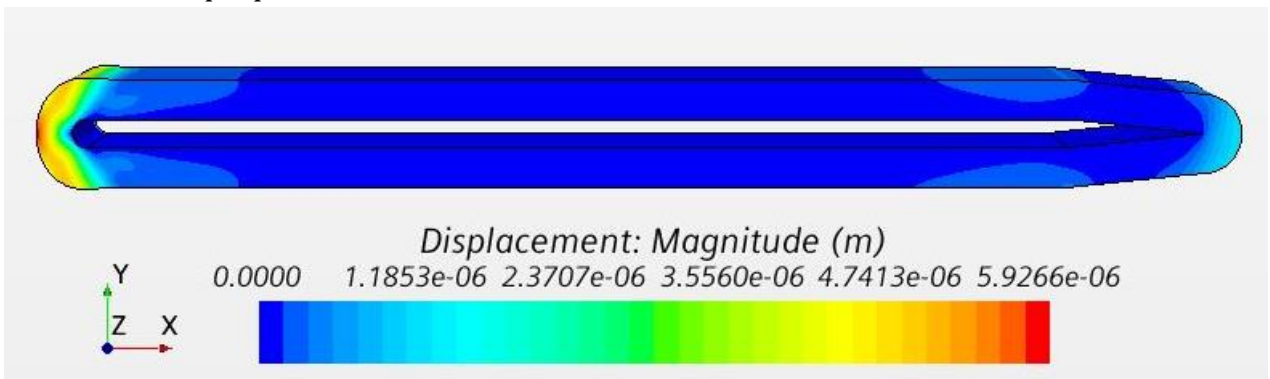
Fig. 4.20: Visualization of compliant coating deformation (scaled 100 times)

It must be noted that the magnitude of deformation experienced by the compliant coating is comparable to experimental studies performed by Lee, Fisher and Schwarz [26] who studied the effects of homogeneous isotropic viscoelastic coatings in its ability to favorably modulate flow boundary layer.
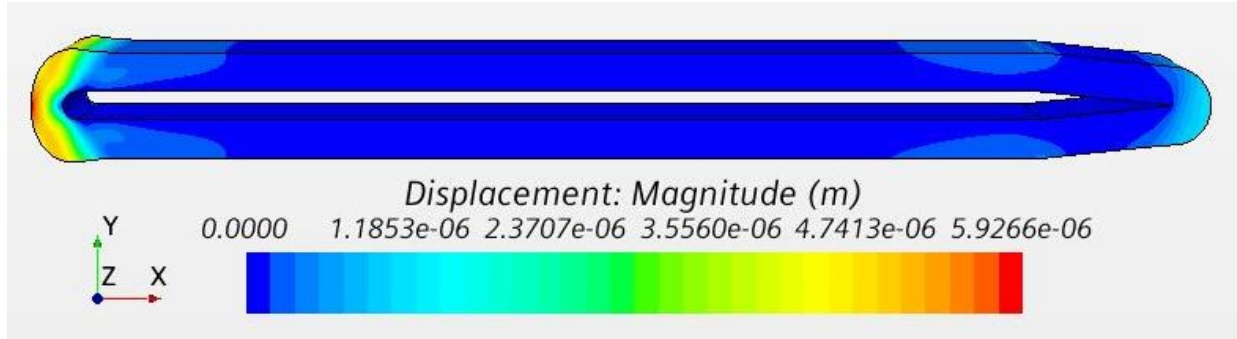
Fig. 4.21: Visualization of compliant coating deformation (scaled 200 times)

Their study estimated that coating experienced surface displacement in the order of microns with peak-to-valley displacement of d_{pv} = 1.67-3.82μm and rms displacement of d_{rms}= 0.32-0.72μm.

4.3.4. *Unsteady CFD-FSI results*

Since unsteady Fluid Structure Interaction involves complex morphing of compliant coating mesh and fluid mesh around it, the simulation tends to be unstable if care is not taken. To ensure stability in simulation, the fluid solver is initially run up to a physical time of 0.05s, by which time the residuals for continuity equation was in the order of 10^{-10}, the momentum equations were in the order of 10^{-9} and energy equation was in the order of 10^{-7}. Additionally, the variance and co-variance of velocity downstream of the trailing-edge almost attains statistical convergence. After this physical time, the solid stress solver converts the aerodynamic forces from the fluid solver into body loads and applies the same on the compliant coating from 0.05 – 0.056s. Once statistical convergence of variance and co-variance of velocity is attained after 0.056s for both

93

the fluid and solid stress solver, pressure fluctuation data, predicted using the Ffowcs

Williams and Hawkings model, is recorded at the receiver's location from 0.056 – 0.06s.

The duration of noise data collection is estimated based on the minimum frequency

interest that is to be resolved (i.e., 250 Hz). Results from the study outlined above is

presented in this Section, as follows:

4.3.4.1. Variance of velocity downstream of the trailing-edge

Variance of velocity was estimated along the three directions in the cartesian plane

using the equations (4.2), (4.3) and (4.4). As seen from Fig. 4.21 – 4.24, after running

the fluid solver up to 0.05s, the variance of velocity monitored at different locations

downstream of the trailing-edge has almost attained statistical convergence and

hence can be considered stable for solid stress solver to start applying body loads on

the compliant coating.
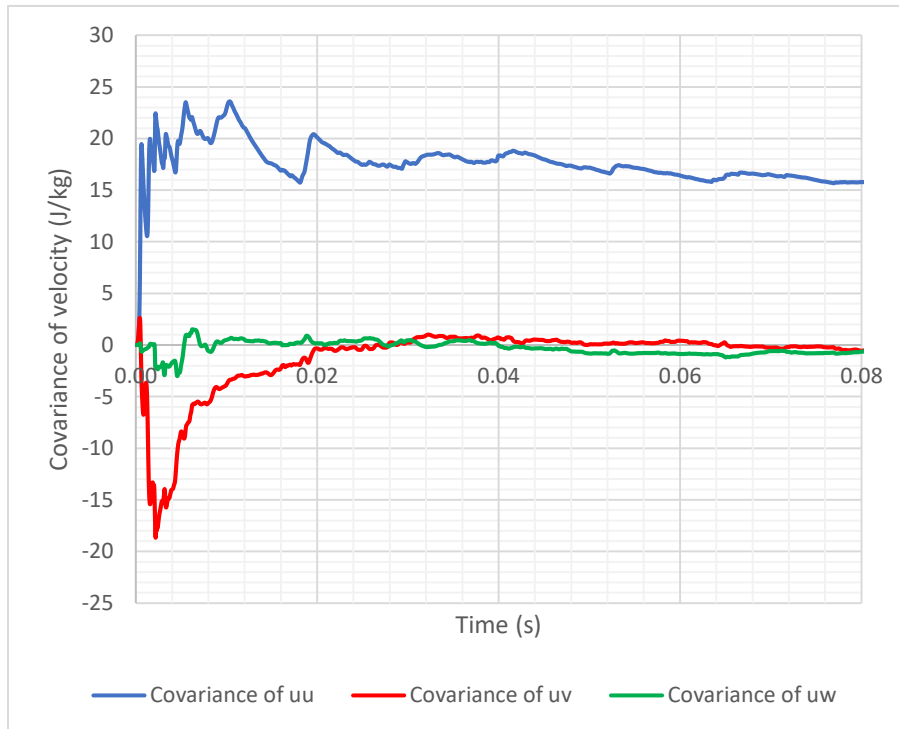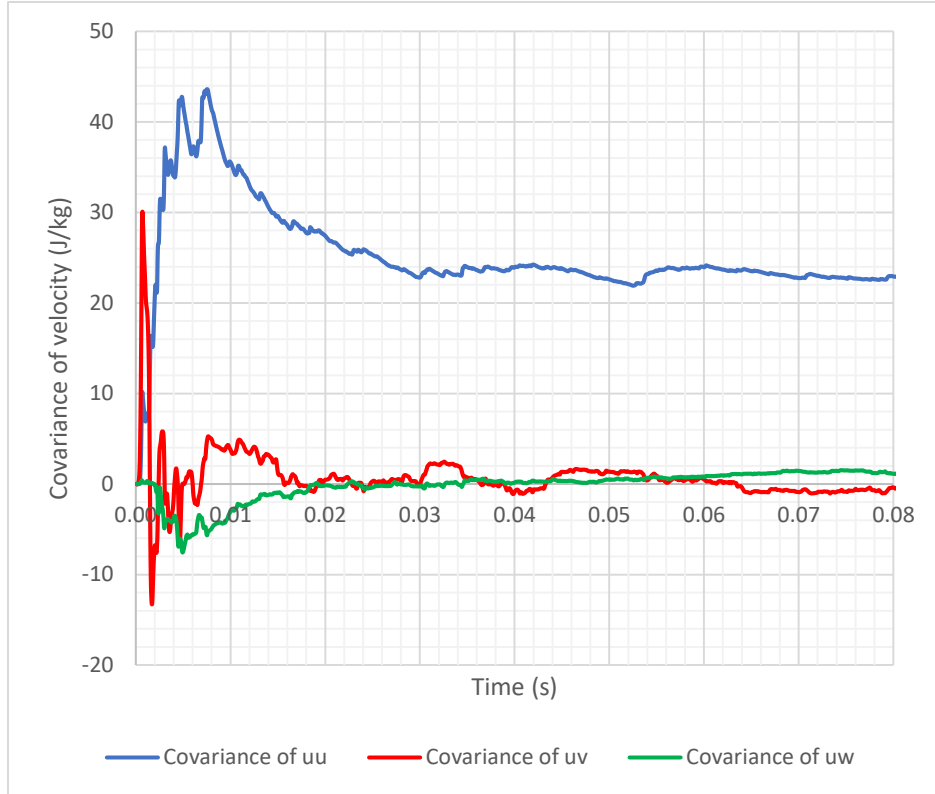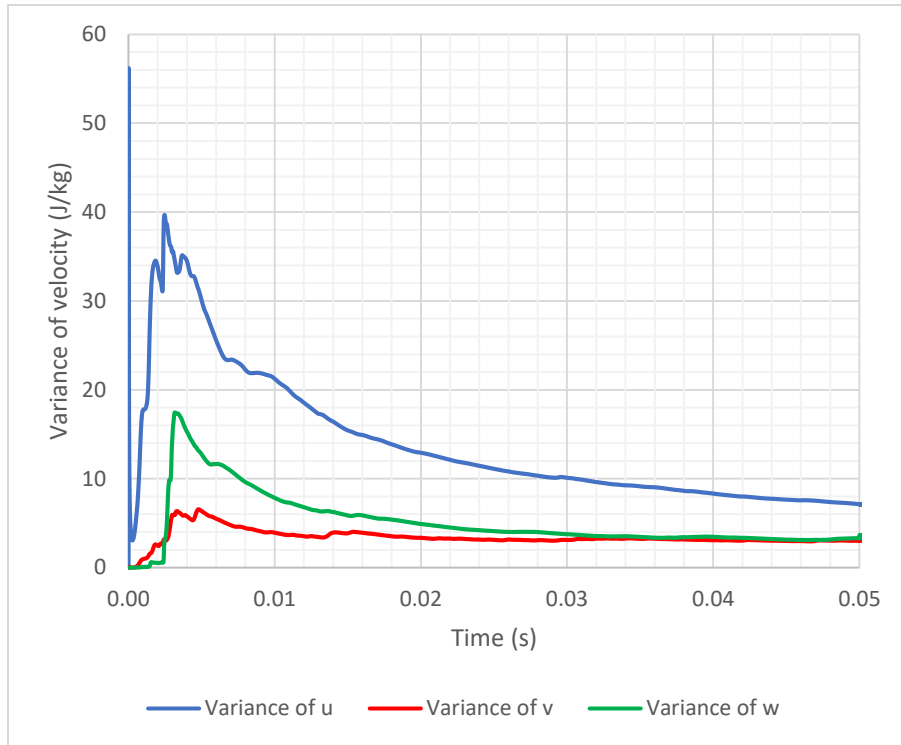
Fig. 4.22: Variance of velocity 0.6 mm downstream of trailing-edge
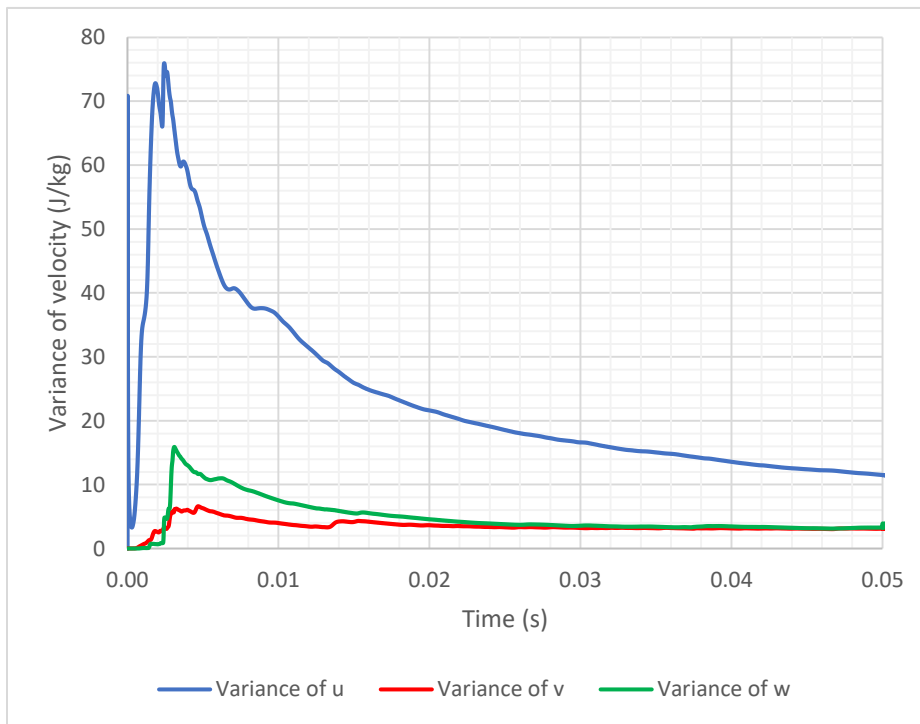
Fig. 4.23: Variance of velocity 1 mm downstream of trailing-edge
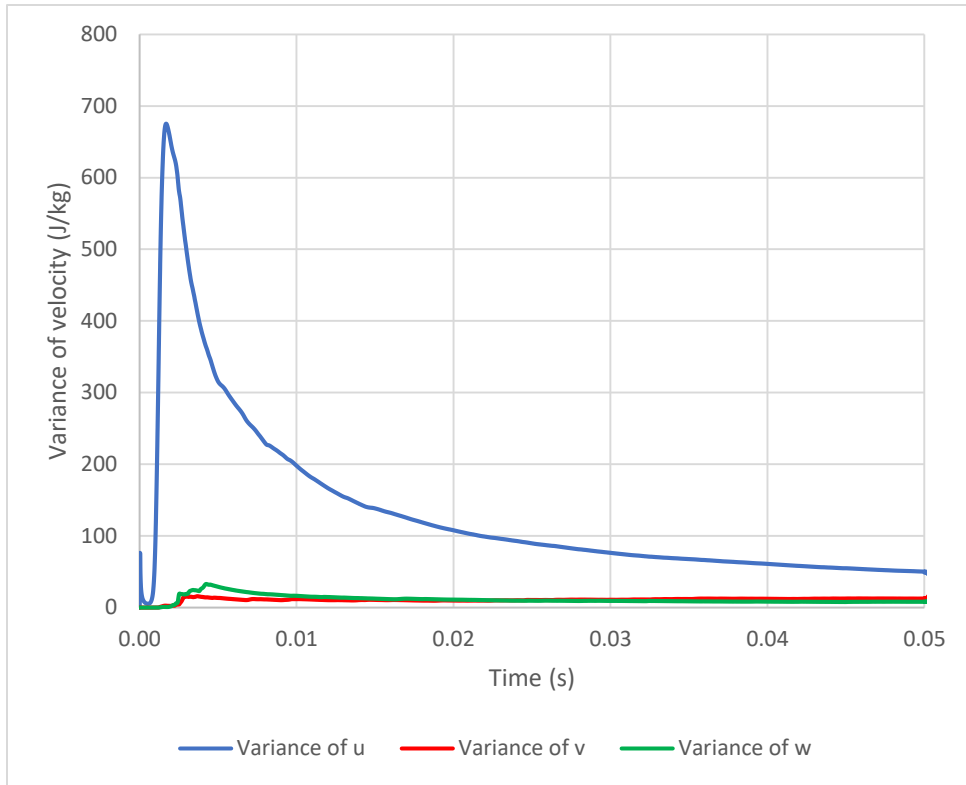
Fig. 4.24: Variance of velocity 5 mm downstream of trailing-edge
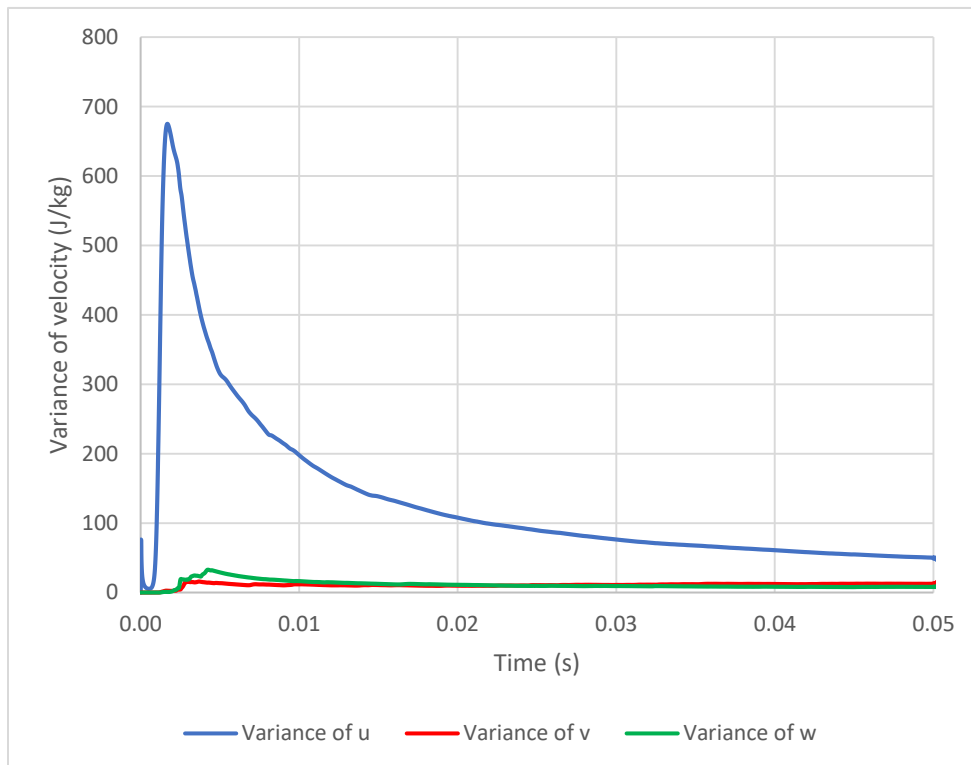
Fig. 4.25: Variance of velocity 10 mm downstream of trailing-edge

96

4.3.4.2. Co-variance of velocity downstream of the trailing-edge

As seen from Fig. 4.26 – 4.29, the co-variance of velocity at different locations downstream of the trailing-edge has almost attained statistical convergence by 0.05s and hence can be considered stable enough for body loads to be applied by the solid stress solver on compliant coating. The benefits of decoupling the fluid solver and solid stress solver up to 0.05s is twofold; this not only ensures stability in solution but also advances physical time of flow solver by a great extent and enabling its convergence. It must be noted that including the solid stress solver after 0.05s initiates the mesh morpher that simulates deforming compliant coating, which incurs very high computing costs.
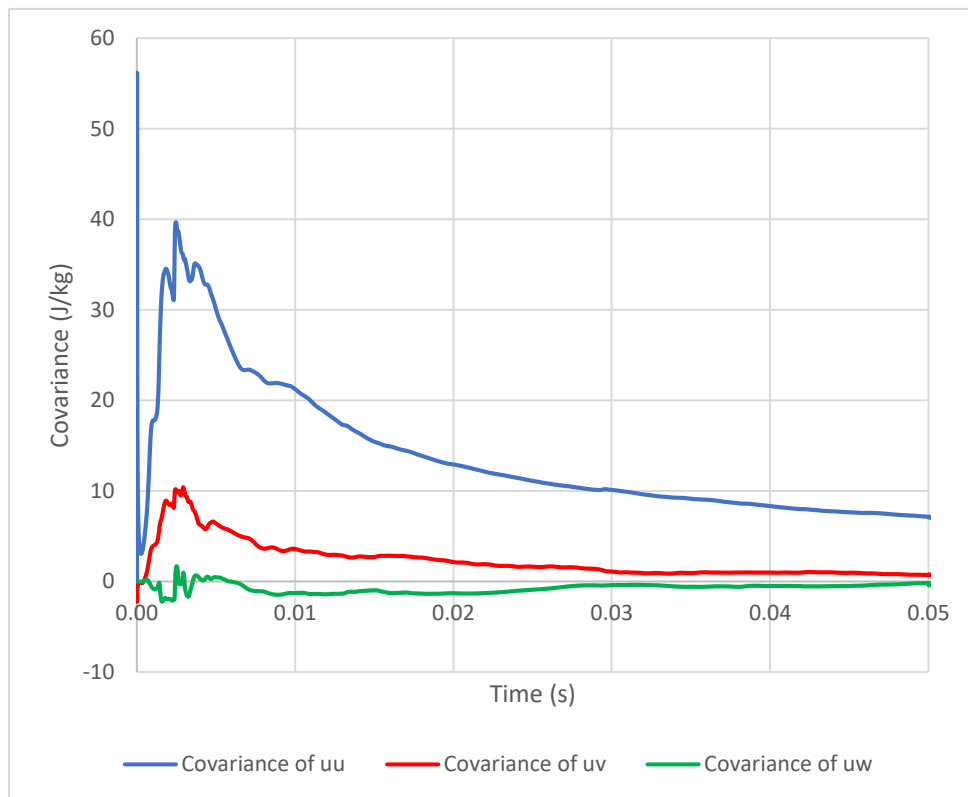
Fig. 4.26: Co-variance of velocity 0.6 mm downstream of trailing-edge
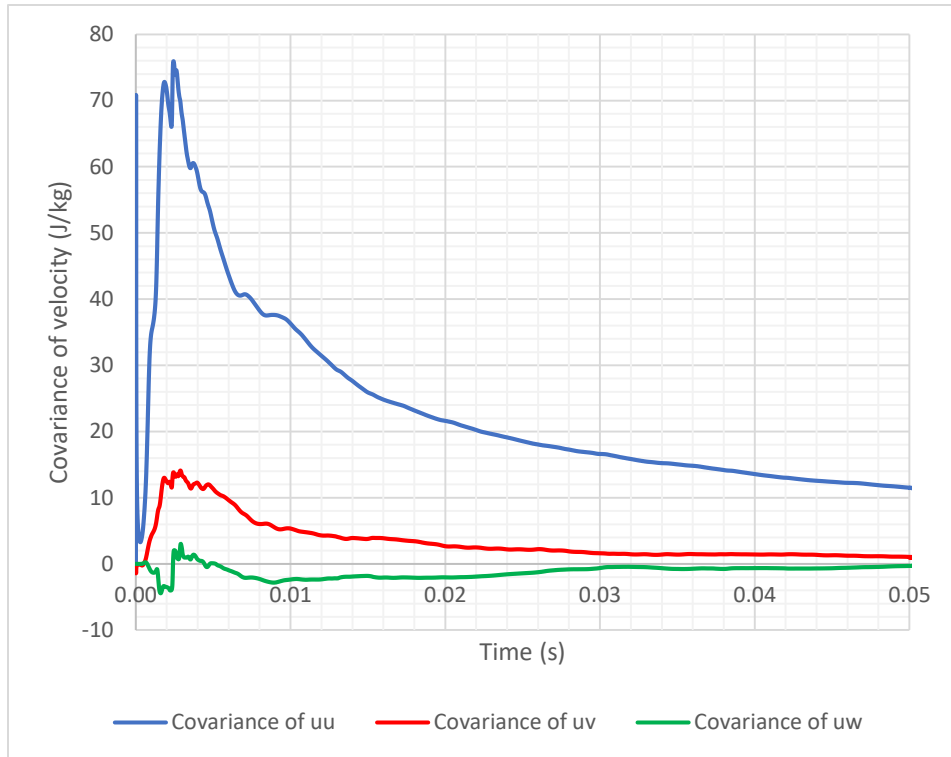
Fig. 4.27: Co-variance of velocity 1 mm downstream of trailing-edge
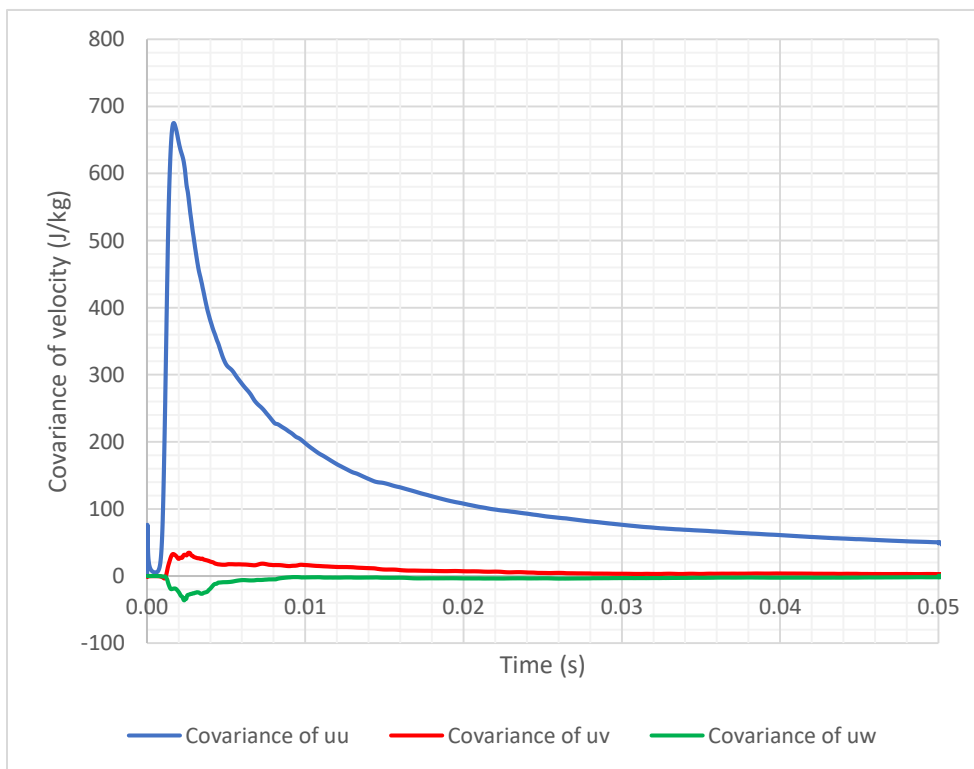
**Fig. 4.28: Co-variance of velocity 5 mm downstream of trailing-edge**

98

Fig. 4.29: Co-variance of velocity 10 mm downstream of trailing-edge

4.3.4.3. Compliant coating deformation

After 0.05s, both the flow solver and solid stress solver are run up to 0.056 seconds until statistical convergence is attained. The solid stress solver converted the aerodynamic forces into body loads and applied the same on the coating. As seen from Fig. 4.30 – 4.31, the variance and covariance of velocity downstream of the trailing-edge attained statistical convergence.

99
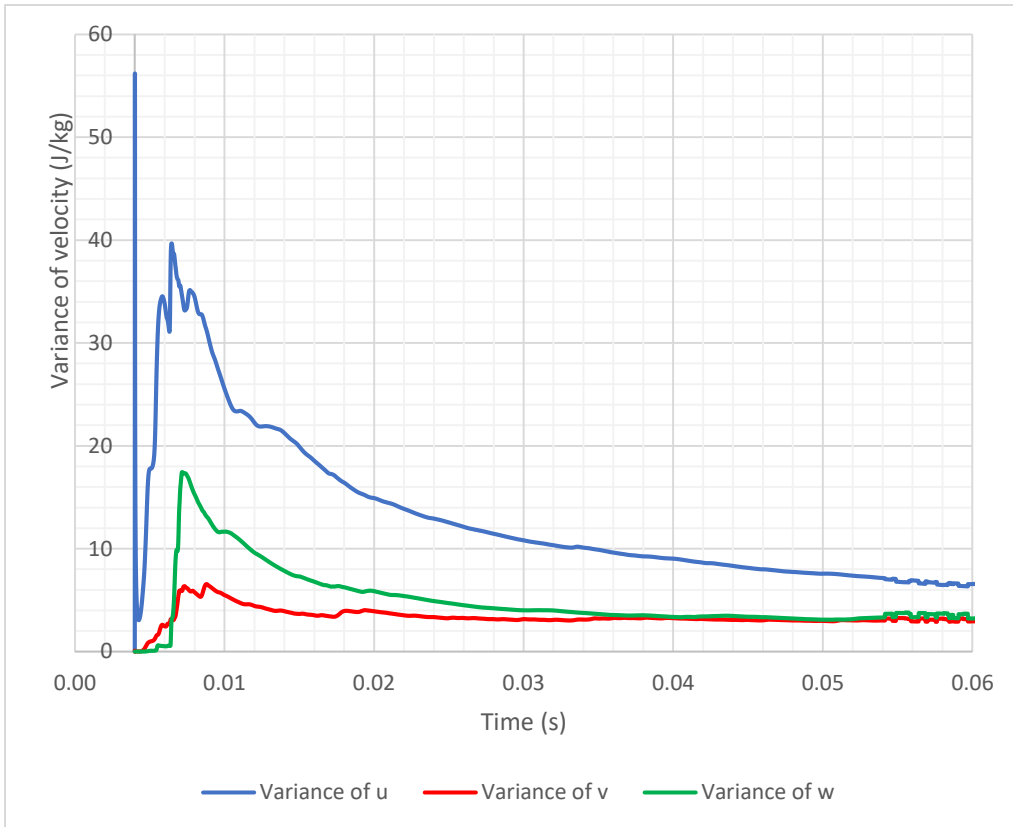
Fig. 4.30: Variance of velocity 0.6 mm downstream of trailing-edge
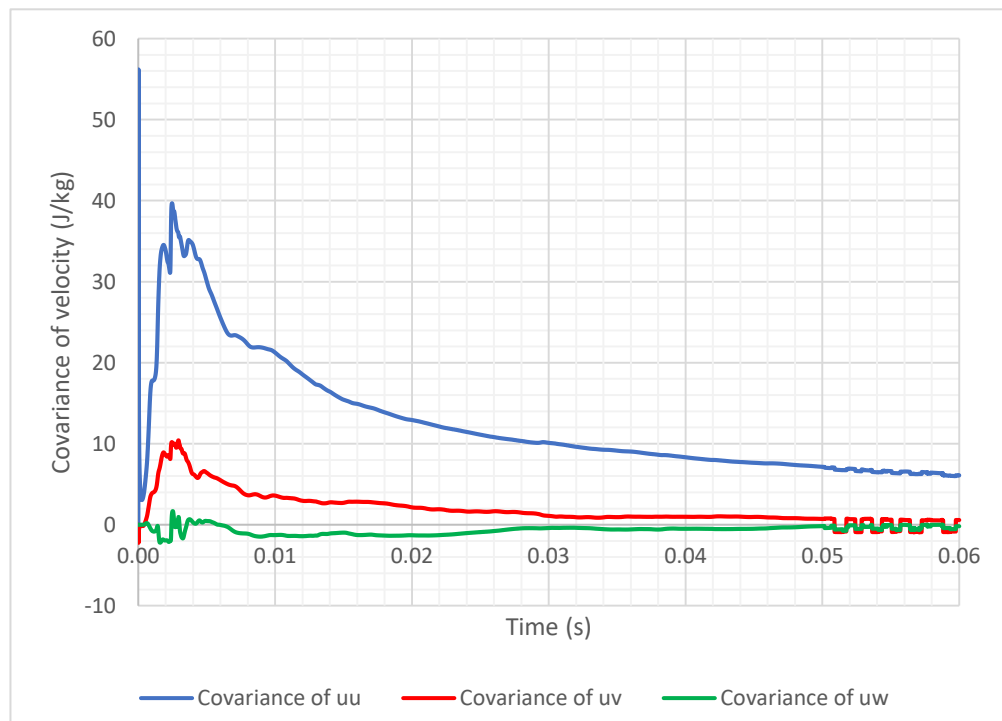
Fig. 4.31: Co-variance of velocity 0.6 mm downstream of trailing-edge

100
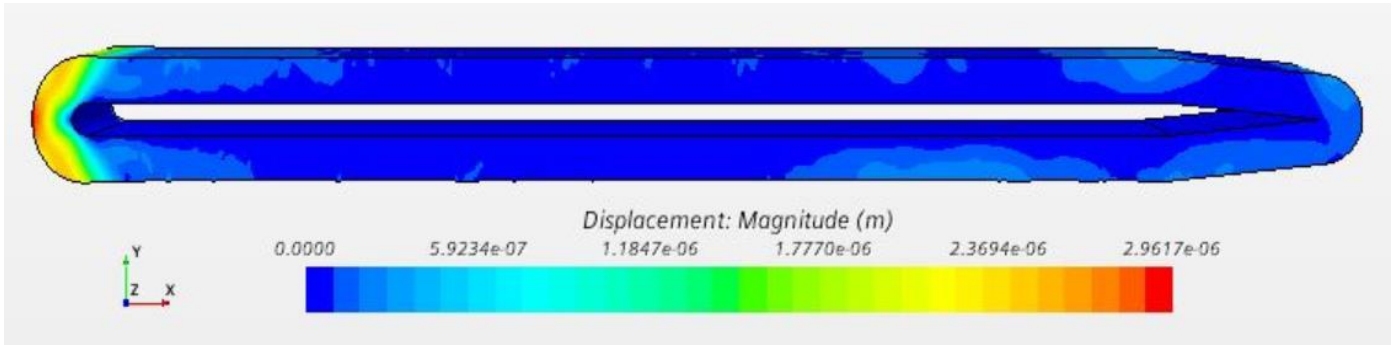
Fig. 4.32: Visualization of instantaneous compliant coating deformation at 0.06s

(scaled - 200 times)

Fig. 4.32 illustrates the instantaneous deformation of compliant coating at 0.06s, which is in the order of microns with maximum deformation of 2.96μm observed at leading-edge centerline. As noted earlier, the extent of deformation is comparable to measurements from Lee, Fisher and Schwarz [26], whose peak-to-valley coating displacement was d_{pv} = 1.67-3.82μm and rms displacement of coating was d_{rms}= 0.32-0.72μm.

4.3.4.4. Comparison of mean velocity distribution

Fig. 4.33 shows the comparison of mean velocity distribution estimated 0.6 mm downstream of the trailing-edge for the baseline case and the case when compliant coating is applied to flat plate. We see that the compliant coating has negligible effect on the mean velocity profile in the near wake region, which is indicative that the drag experienced by the two cases are about the same ($C_d \approx$ 0.02520).

101
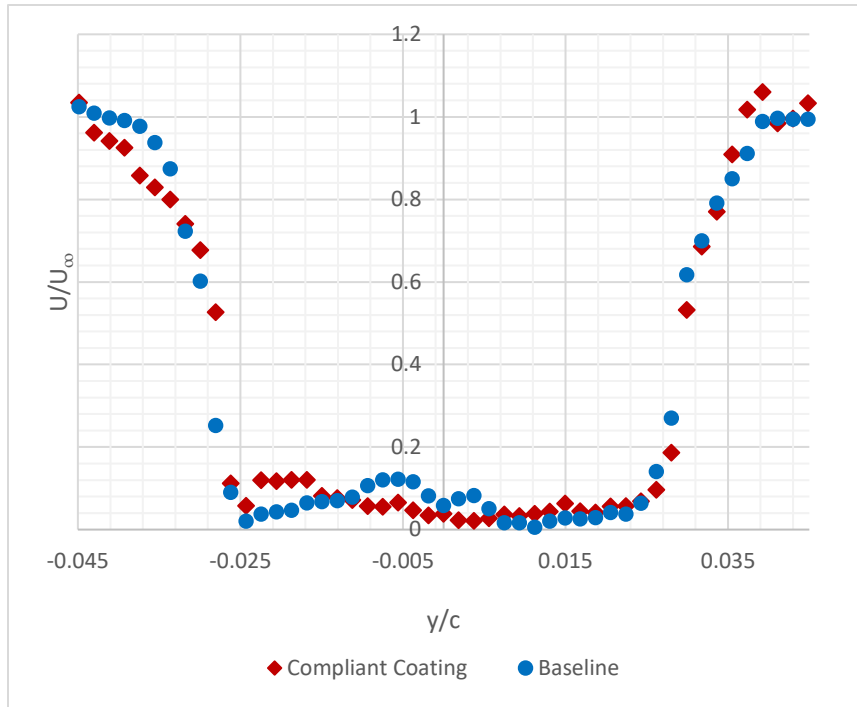
Fig. 4.33: Comparison of mean velocity distribution 0.6 mm

downstream of trailing-edge
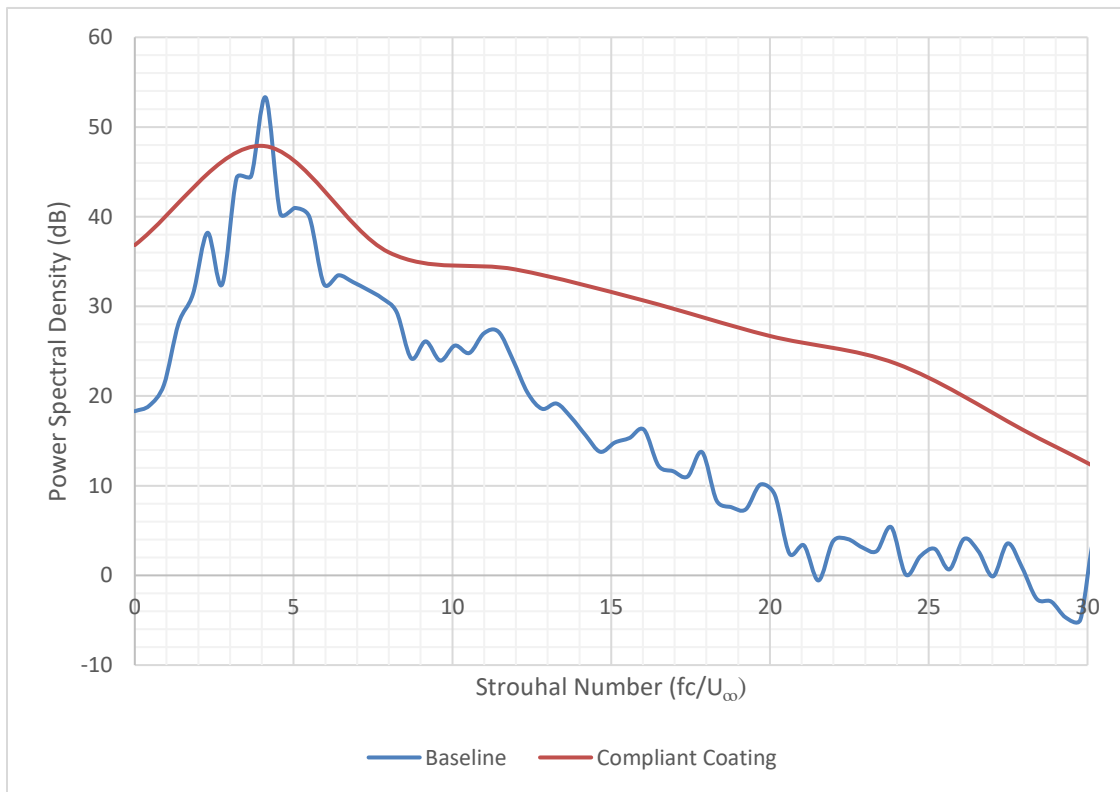
Fig. 4.34: Comparison of farfield noise predicted 585 mm above trailing-edge

Once variance and covariance of velocity attained statistical convergence after 0.056s, pressure fluctuation history data was recorded at a point receiver located 585 mm above the trailing-edge from 0.056-0.06s. This data was converted from time domain to frequency domain using Discrete Fourier Transform and represented as Power Spectral Density using equation (4.8). Finally, a graph of Power Spectral Density versus Strouhal number was created and compared with results from the baseline case.

On comparing results from the two cases, we note that using compliant coating on the flat-plate resulted in increase in farfield noise by almost 10-15 dB throughout the frequency range of interest, with a reduction in noise of 6 dB at St=4.00.

To understand why compliant coating could have detrimental effects on farfield noise, experimental studies conducted by Choi et al. [40] reveal that the compliant coating material properties must be chosen carefully based on the flow conditions such that that the coating's resonance frequency must satisfy the condition as shown in equation (4.9), estimated using Sternberg's theory, for it to provide the desired response to fluctuating pressure at the wall.

$$50 < \frac{1}{f_0} < 150 \tag{4.9}$$

And,

$$f_0^{-1} = \frac{t_0(u^*)^2}{\nu} \tag{4.10}$$

where,

f_0 is the resonance frequency or resonant frequency in Hz

ν is the kinematic viscosity

u^* is the friction velocity

Thus, we understand that careful choice of compliant coating material properties is crucial for its constructive coupling with flow boundary layer for a given flowfield. Further study is necessary to explore the relationship between choice of coating material properties, coating resonance frequency and its ability to favorably modulate flow boundary layer and mitigate trailing-edge noise.

4.4. Conclusions

In this computational study, farfield noise was predicted for the baseline rigid flat plate, which accounts for the change in outer-profile of the model when coating is applied to flat plate. These results were compared with the case when compliant coating is applied to flat plate. It is observed that application of compliant coating on the flat plate model resulted in increase of trailing-edge noise by 10-15 dB throughout the frequency range of interest, with a reduction in noise of 6 dB at St=4.00. Increase in noise predictions is attributed to the choice of compliant coating material properties and the need for coating's resonance frequency to satisfy the relation $50 < \frac{1}{f_0} < 150$, for it to reduce turbulence generation over the coating and provide the desired response to fluctuating pressure at the wall for a given flowfield. Thus, further computational study is necessary to investigate the relationship between coating resonance frequency and given flowfield to mitigate trailing-edge noise.

It must be noted that the analysis performed in the present study was computationally expensive. Computational Aeroacoustics requires long run times due to constraints such as small time-step size and small mesh size to resolve the time-scales and length-scales of turbulent eddies within the flow boundary layer. Using 600 cores, the simulation was run for a month to extract farfield noise data for the baseline case. Implicit Fluid Structure Interaction, on the other hand, has its own set of constraints such as updating the morphing mesh at every sub-iteration of each time-step. When the solid stress solver was combined with the flow solver, the constraints of the two problems were also coupled, thus slowing down the simulation to $1/10^{th}$ its original processing-speed. It is for this reason, that there was lesser pressure fluctuation history data recorded for the point receiver used in the case when compliant coating was applied to flat plate. The results gave us the general magnitude and trend of farfield noise predictions when compliant coating was applied on flat plate. However, the tonal noise at different frequencies could not be accurately resolved in this case. To overcome this issue, it is recommended that this analysis be performed by decoupling the two solvers. A structural analysis solver can be used to independently simulate deformation of the compliant coating at different instants of time, when body loads obtained from aerodynamic forces exerted by air impinging on the flat plate, are applied on the compliant coating. The deformation of compliant coating obtained at different instants of time from the structural analysis solver, can be used by the flow solver to independently simulate flow over a deforming boundary and study its effects on trailing-edge noise.

Literature points towards a second compliant coating with homogeneous viscoelastic material properties that was investigated by Lee, Fisher and Schwarz [27]. This coating

was applied onto a flat plate and mounted inside a low turbulence wind tunnel at Johns Hopkins University to perform experiments. This coating displayed desirable characteristics by suppressing the Tollmien Schlichting instabilities (TSI) and stabilizing flow induced surface instabilities (FISI). As a preliminary step towards understanding the effects of coating materials properties on trailing-edge noise, computational studies shall be performed using this coating henceforth referred to as Coating-2. Results from this study shall be compared with the trailing-edge noise characteristics of Coating-1 investigated in Chapter 4.

5. A COMPARATIVE STUDY OF PASSIVE COMPLIANT COATINGS ON TRAILING-EDGE NOISE

This chapter is based on a work titled "A Comparative Study of Passive Compliant Coatings on Trailing-Edge Noise" presented at the 181st Meeting of Acoustical Society of America in session 2pCA, Computational Aeroacoustics.

Abstract

Studies that involve mitigating aerodynamic noise in rotating components such as rotors of wind turbines or propellers of Unmanned Aerial Vehicles have gained immense interest in the research community over the last few years. The present computational study explores the effects of passive compliant on trailing-edge noise which is considered to be the dominant noise source in these rotating components. Two coatings with different material properties are applied on a flat-plate geometry to compare the effects of coating material properties on trailing-edge noise. Unsteady CFD analysis was performed using the SST k-ω Improved Delayed Detached Eddy Simulation and flowfield data obtained from this study was utilized by the Ffowcs Williams and Hawkings model to predict farfield trailing-edge noise. Fluid Structure Interaction is employed to simulate coating deformation. Application of Coating-1 on the flat plate results in an increase of trailing-edge noise by 10-15 dB over the frequency range of interest with a noise reduction of 6 dB at St = 4.00. Whereas, application of Coating-2 reveals that the energy content present in trailing-edge noise is slightly shifted towards the lower frequency range and there is reduction in noise at low frequency ranges from St = 3.50 – 9.00 with a maximum noise reduction of 5 dB at St = 4.00. However, Coating-2 also results in an increase in noise of 8-10 dB for high frequency ranges

beyond St = 18.00. This preliminary study that compares the effects of coating material properties on trailing-edge noise reveals that choice of coating material properties plays a significant role on trailing-edge noise characteristics and further study is necessary to explore the relationship between coating material properties, coating resonance frequency and their effects trailing-edge noise.

5.1. Introduction

With growing dependence on wind energy as a clean source of electricity and the need for silent drones used by the military for stealth applications or recent interest commercial drone deliveries provides the necessary impetus for this research to reduce aerodynamic noise. Trailing-edge noise is considered to be the dominant noise source [2,3] in these rotating components and various techniques have been explored to mitigate this noise. Both active and passive flow control techniques have been investigated to mitigate trailing-edge noise. Passive flow controls include trailing-edge serrations [6-9], trailing-edge brushes [10-11], porous airfoils [12-14] and skin treatment [15-16]. Whereas, active flow controls include flow suction and injection into the boundary layer [17-20] to reduce surface pressure field and turbulent fluctuations.

In the present study, we will explore the effects of passive compliant coatings on trailing-edge noise. Passive compliant coatings have shown their ability to reduce turbulence intensity by 5% across the entire flow boundary layer along with a 7% drag reduction for hydrodynamic flows [40]. Further studies by Lee, Fisher and Schwarz [26] in a low turbulence wind tunnel at Johns Hopkins University reveal the ability of homogeneous viscoelastic coatings to relaminarize flow boundary layer when applied on

a flat plate. Zhang et al. [62, 63] explored the effects of a compliant coating made from polydimethylsiloxane (PDMS) immersed in a sodium iodide solution with flow over the coating surface. Surface deformation was analyzed using tomographic particle image velocimetry (TPIV) and Mach-Zehnder interferometry.

Experiments also show that homogeneous compliant coatings can favorably modulate the flow boundary layer in aerodynamic flows. Wind tunnel tests conducted by Boiko et al. [24] show that compliant coatings made from polydimethylsiloxane with material properties as shown in Table 5.1 are capable of reducing drag by 4-5% when applied on a flat plate.

Table 5.1: Optimum material properties for Coating-1 [24]

Coating material properties	Magnitude (Units)
Density	1130 kg/m^3
Poisson's ratio	0.485
Young's modulus	1.1 MPa
Coating thickness	7 mm

Similarly, experiments conducted by Lee, Fisher and Schwarz [27] revealed that compliant coatings made from polydimethylsiloxane with material properties as shown in Table 5.2 were capable of reducing the amplitude of fluctuating velocity by 40%. This resulted in suppressing the Tollmien Schlichting instabilities (TSI) and stabilize the flow induced surface instabilities (FISI).

Table 5.2: Optimum material properties for Coating-2 [27-30]

Coating material properties	Magnitude (Units)
Density	977 kg/m^3
Poisson's ratio	0.499
Young's Modulus	1.51 MPa
Thickness of compliant coating	5 mm

The two coatings with material properties listed in Table 5.1 and 5.2 are used by the present computational study to compare their effects on trailing-edge noise.

Simulating the effects of coating deformation when aerodynamic forces act on its surface involves complex interaction between the solid compliant coating and surrounding flow boundary layer. Thus, *Fluid Structure Interaction* is necessary to simulate this behavior. Endo and Himeno [64] performed Fluid Structure Interaction studies using Direct Numerical Simulations and simulated the effects of turbulent flow over a homogeneous isotropic compliant material. Their results indicated that use of coating reduced drag by 2.7%. Fukagata et al. [65] studied the effects of anisotropic compliant coating on turbulent flow. They optimized the material properties of the coating and found that optimum coating was capable of reducing drag up to 8% . Xia et al. [66] simulated the turbulent boundary layer over a rectangular with focus on flow dynamics and wall deformation and not on optimizing the coating material properties. Their study assumed that coating surface displacement had negligible effects on surrounding fluid compared to the normal component of coating velocity on the fluid. It

was found that compliant wall motion increased Reynolds shear stress and mean convection term as a consequence of which the skin friction drag always increased for the flow regimes considered in this study. Nakanishi et al. [67] simulated the effects of traveling wave-like deformation of a compliant wall in a fully developed turbulent channel and demonstrated that skin friction drag reduced through suppression of turbulence and relaminarization of flow boundary layer. Kim and Choi [68] investigated the space-time characteristics of a compliant wall in a turbulent channel flow by modeling the compliant wall as a homogeneous plane supported by spring-and-damper arrays. To achieve mesh independence of compliant wall, mean pressure gradient and wall motion was monitored in their study. More recently, Xia et al. [69] explored the effects of a spatially developing turbulent boundary layer over an anisotropic compliant wall through Direct Numerical Simulation.

For this computational study, the *Fluid Structure Interaction* technique of a commercial CFD code STAR-CCM+ v.15.02.009 has been used. The *Two-way coupling* technique is used to simulate the momentum and energy transfer between the fluid and a homogeneous isotropic viscoelastic compliant coating. Deformation of the passive compliant coating is achieved using a *morphing mesh*.

The present computational study is divided into two parts:

5.1.1. Baseline case
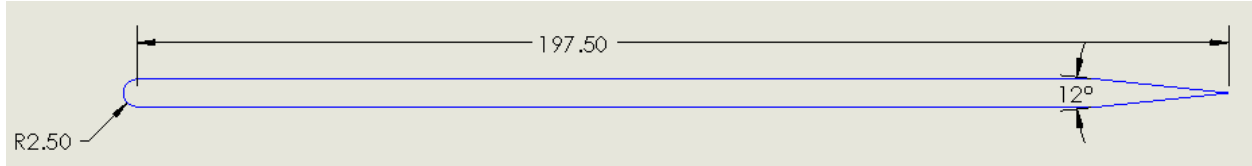
Fig. 5.1: Flat plate model before application of compliant coating

When the two compliant coatings outlined in Tables 5.1 and 5.2 are applied uniformly around a flat plate shown in Fig. 5.1, it alters the trailing-edge shape and thickness of flat plate. This would in turn alter the flow behavior around the flat plate.

To account for this change in shape and size, a new geometry called the Baseline model is created as shown in Fig. 5.2 and 5.3.
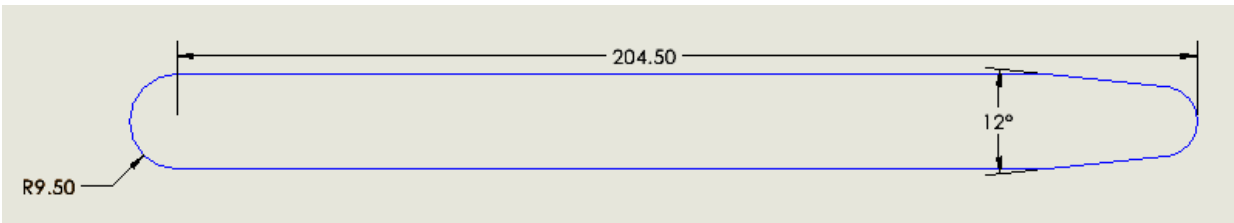
Fig. 5.2: Baseline rigid flat plate corresponding to Coating-1

Unsteady flow behavior around flat plate models shown in Fig. 5.2 and 5.3 shall be simulated using Improved Delayed Detached Eddy Simulation and this flowfield data shall be used by the Ffowcs Williams and Hawkings model to predict farfield trailing-edge noise. Results from these simulations would be used as baseline for comparison when compliant coating is applied to flat plate geometry.
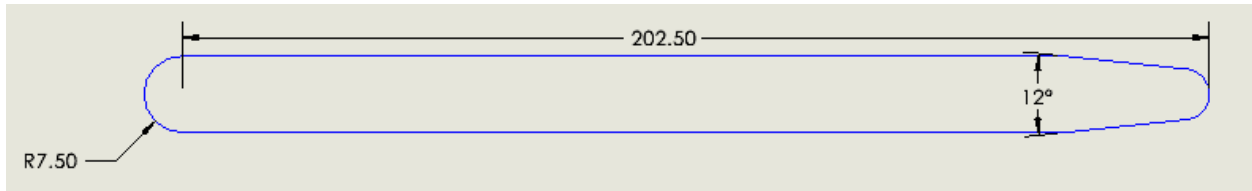
Fig. 5.3: Baseline rigid flat plate corresponding to Coating-2

5.1.2.   Compliant coating applied to flat plate

Fig. 5.4 and 5.5 show cases when the two compliant coatings are respectively applied on to the flat plate model seen in Fig. 5.1.
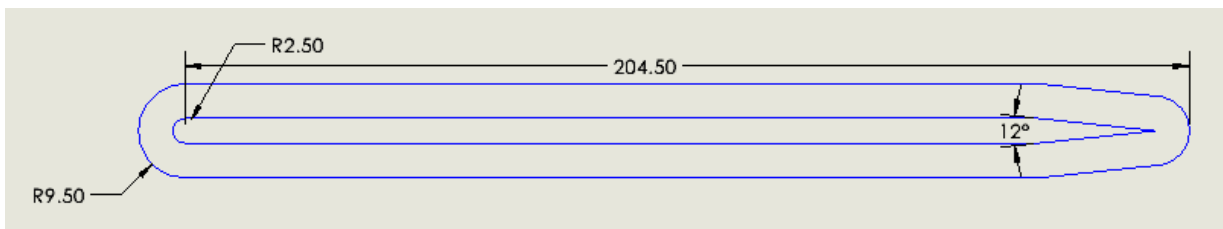
Fig. 5.4: Coating-1 of 7 mm thickness applied to flat plate

Effects of these compliant coatings shall be compared with their corresponding baseline cases to understand how coating material properties influence trailing-edge noise characteristics.
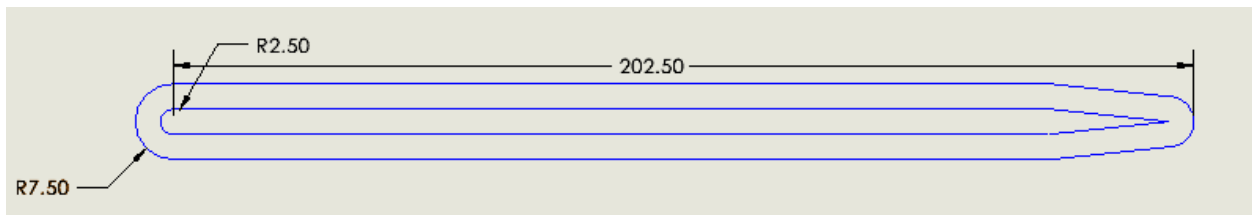
Fig. 5.5: Coating-2 of 5 mm thickness applied to flat plate

5.2.   Baseline Case

In this section, the steps involved in computational aeroacoustics analysis for the two baseline geometries shown in Fig. 5.3 and 5.4 shall be presented.

113

5.2.1.   Steady CFD analysis

The computational domain consists of two regions as shown in Fig. 5.6, a fluid region and a permeable body region. The permeable body is the region around the flat plate where noise sources are located. The mesh in this region will be very finely refined to resolve the noise sources present around the flat plate geometry. The fluid region consists of a Freestream Inlet located 0.8 m (i.e., 4 chord lengths) upstream of the flat plate's leading-edge. The free stream outlet is located 1.0 m (i.e., 5 chord lengths) downstream of the flat-plate's leading-edge. 5 chord lengths) downstream of the flat-plate's trailing-edge. The domain's span is 10% chord to account for three-dimensional nature of vortices present within the flow boundary layer [44].
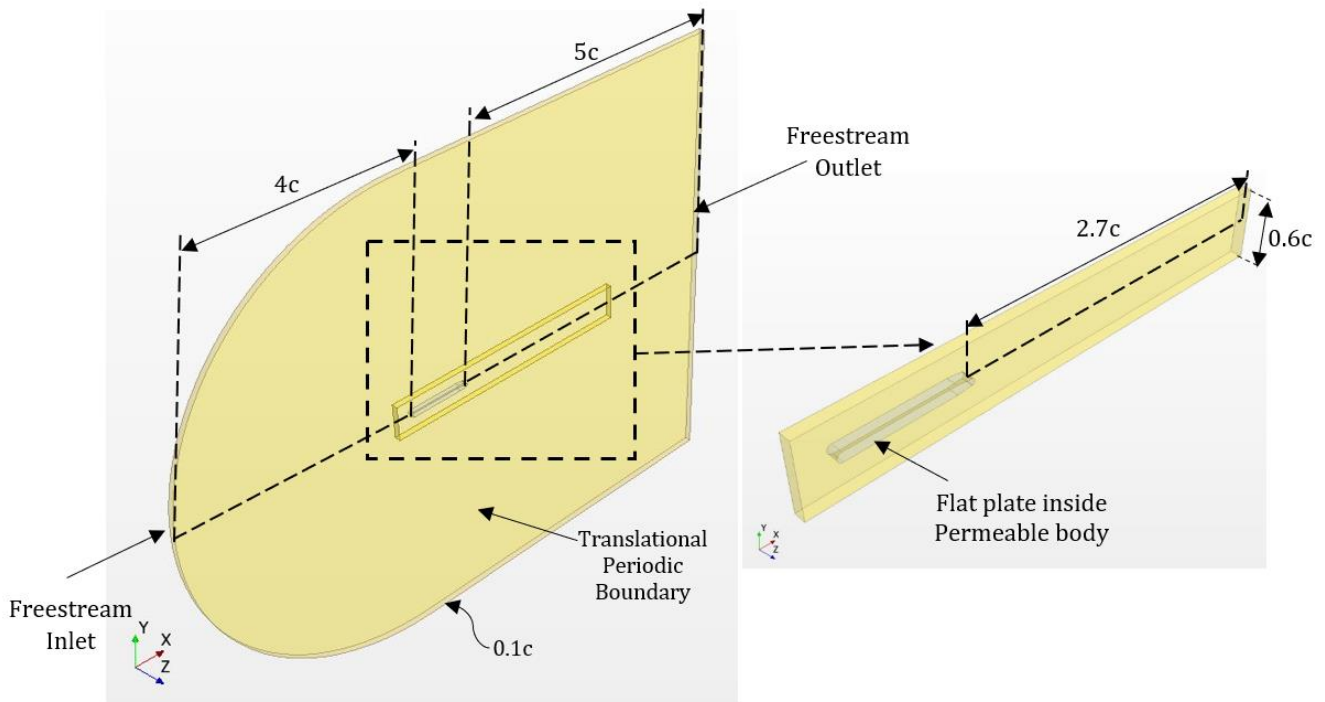
Fig. 5.6: Permeable body inside fluid domain

5.2.2. Mesh Generation

A hexahedral trimmer mesh is generated for the two computational domains consisting of baseline-1 and baseline-2 flat plate geometries respectively. A near wall thickness of 4×10^{-6}m is chosen which ensured that the wall y^+ was less than 1 on the flat plate surfaces. This condition is necessary for the near wall y^+ treatment used along with the SST k-ω RANS turbulence model.

5.2.2.1. Grid refinement study

Initially, a grid refinement study is carried out for the two computational domains at a wind speed of 35 m/s. This is done to identify meshes that are capable of resolving the flowfield around the two flat plate geometries accurately seen in Fig. 5.2 and 5.3. In both cases, steady CFD analysis was carried out using four different grid resolutions. For baseline-1 case, mesh was refined from a coarse grid of 1.18 million cells to a fine grid of 1.72 million cells. For baseline-2 case, mesh was refined from a coarse grid of 1.31 million cells to a fine grid of 1.73 million cells. From these simulations, drag coefficient was estimated using the relation:

$$C_D = \frac{D}{\left(\frac{1}{2}\rho_\infty U_\infty^2 cS\right)} \qquad (5.1)$$
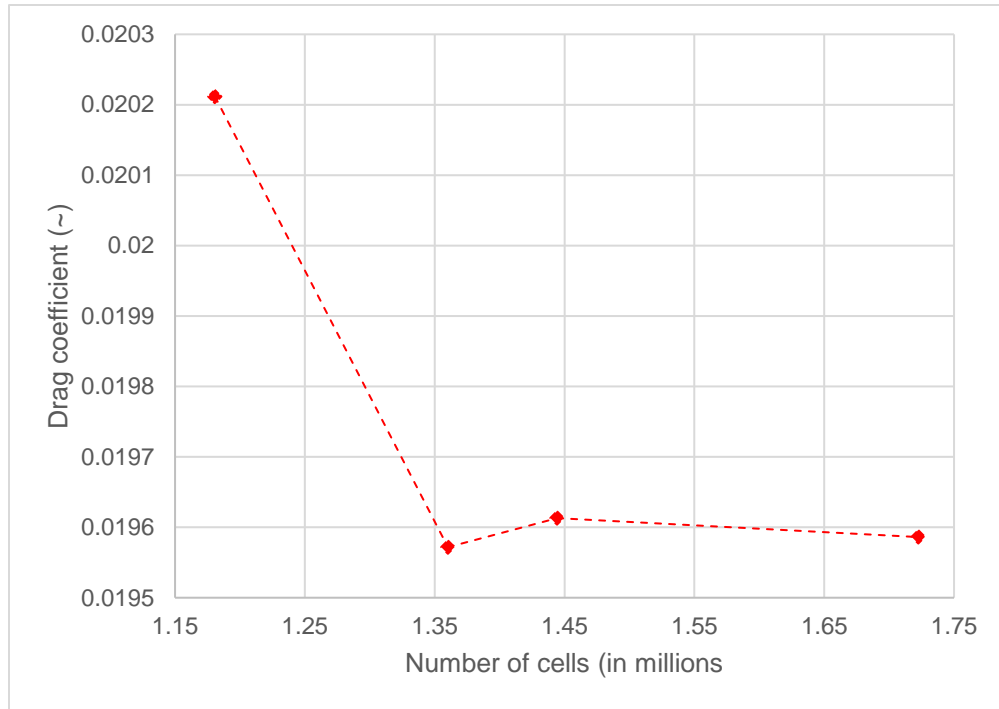
Fig. 5.7: Mesh independence study for baseline-1 case at wind speed of 35 m/s

From Fig. 5.7 we see that for the baseline-1 case, there is only a 0.13% difference in predicted drag coefficient when grid size is increased from 1.44 million cells to 1.72 million cells. Therefore, the flowfield predicted using the grid with 1.72 million cells can be considered as mesh independent and thus chosen for the next step in our analysis.
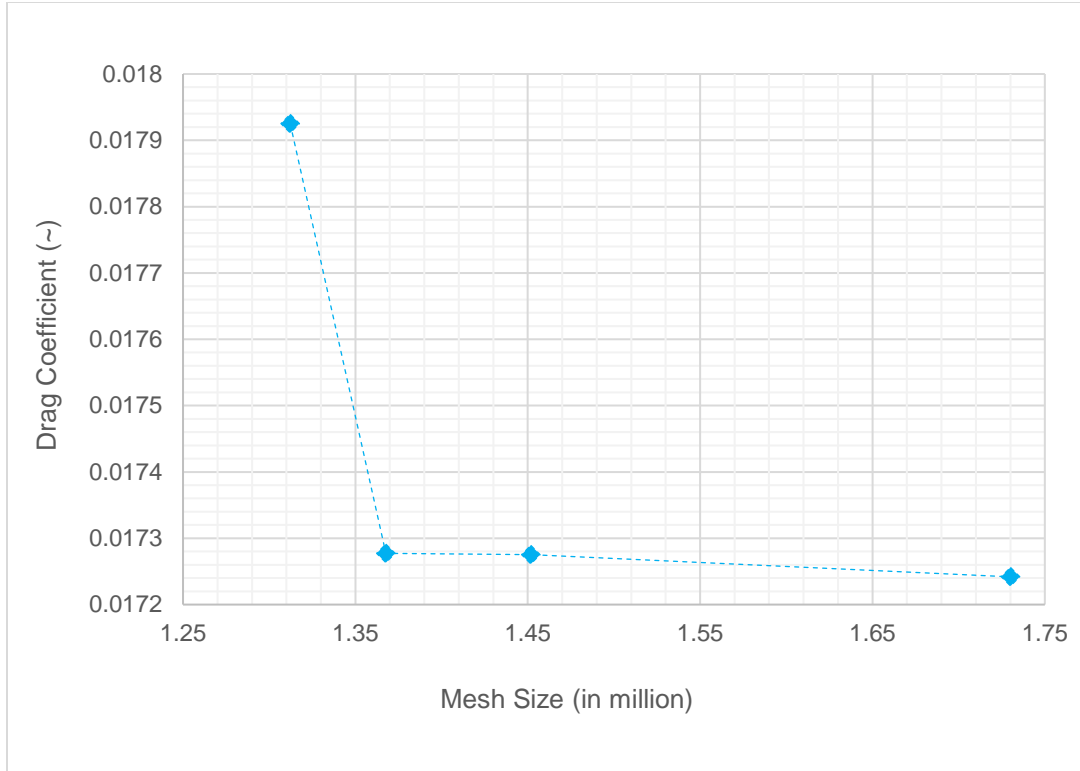
Fig. 5.8: Mesh independence study for baseline-2 case at wind speed of 35 m/s

Similarly, from Fig. 5.8 we see that for the baseline-2 case, there is only a 0.19% difference in predicted drag coefficient when grid size is increased from 1.31 million cells to 1.73 million cells. Therefore, the flowfield predicted using the grid with 1.73 million cells can be considered as mesh independent and thus chosen for the next step in our analysis.

5.2.2.2. Mesh Frequency Cutoff

The two grids chosen in the previous section are further refined to resolve the noise sources present around the flat plate geometry for the frequency range of interest. To identify if the grid has been sufficiently resolved, the mesh frequency cutoff parameter is used [59], which is given by the equation:

$$f_{MC} = \frac{\sqrt{\frac{2}{3}}k}{(2\Delta)}$$

The mesh frequency cutoff parameter is a function of turbulent kinetic energy k, and local grid spacing Δ. Turbulent kinetic energy is a characteristic of noise sources present around the flat plate. As equation 5.2 indicates, reducing the grid size for a given frequency range of interest ensures that the noise sources can be accurately resolved.

In the experiment conducted by Moreau et al. [48], the anechoic test chamber provided a reflection free environment above 250 Hz and their microphone was capable of measuring farfield noise up to a maximum frequency of 8000 Hz. Based on this, we choose 250-8000 Hz as our frequency range of interest to resolve noise sources around the flat plate.
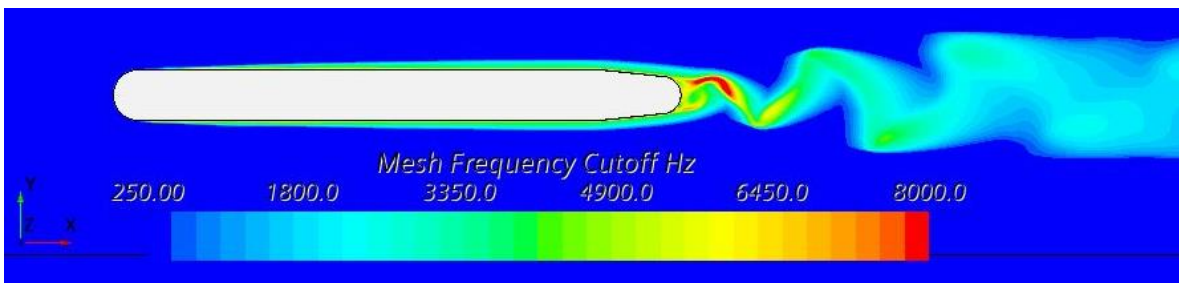
Fig. 5.9: Mesh frequency cutoff scalar scene for baseline-1 case
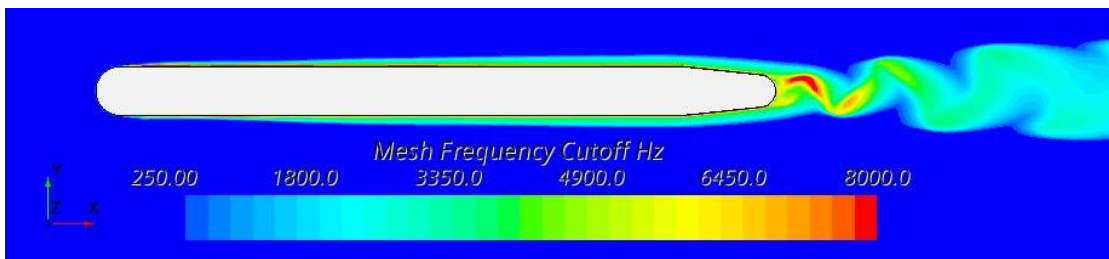
Fig. 5.10: Mesh frequency cutoff scalar scene for baseline 2 case

As shown in Fig. 5.9 and 5.10, the two grids corresponding to baseline-1 and baseline-2 case was further refined to 17.83 million cells and 18.50 million cells after

118

which noise sources were well resolved around the flat plate geometry. Now that the mesh is well resolved to refined noise source accurately, unsteady CFD analysis can be performed using a high fidelity CFD solver to accurately predict instantaneous flowfield around the flat plate geometry.

5.2.3. *Unsteady CFD analysis*

To perform unsteady CFD analysis, the SST k-ω Improved Delayed Detached Eddy Simulation is chosen for both the cases. This model was chosen because of its superior accuracy in flow predictions compared to the SST k-ω RANS turbulence model during unsteady CFD analysis [46, 50]. The flowfield data predicted by this model would be used by the Ffowcs Williams and Hawkings acoustic analogy to predict farfield trailing-edge noise. A constant time step size of 5×10^{-6}s was chosen for both baseline cases which ensured that the convective courant number was less than 1. It was observed that after a physical time of 0.08s for baseline-1 case and after a physical time of 0.1s for baseline-2 case, the residuals for continuity equation was in the order of 10^{-10}, residuals for momentum equation were in the order of 10^{-9} and residuals for energy equation was in the order of 10^{-7} and below. Thus, we can conclude that baseline-1 simulation attained statistical convergence after 0.08s and baseline-2 simulation attained statistical convergence after 0.1s. The unsteady CFD solver settings used in this analysis is outlined in Table 5.3.

Table 5.3: Unsteady CFD Solver Settings

Parameter	Unsteady CFD Solver Settings
Turbulence model	SST (Menter) k-ω Improved Delayed Detached Eddy Simulation
Equation of State	Ideal Gas Equation
Energy Equation	Segregated Fluid Temperature
k-ω wall treatment	Near wall y^+ treatment
Time	Implicit Unsteady
Flow solver	Segregated Flow solver
Convection scheme for Segregated Flow and Segregated Fluid Temperature	Monotonic Upwind Scheme for Conservation Laws (MUSCL 3rd order)
Time step size	5×10^{-6} s
Temporal discretization	2nd order scheme

5.2.4. *Results and Discussions*

During unsteady CFD analysis, as physical time gradually increases for a given time-step, the numerical dissipation gradually decreases until statistical convergence is attained. Considering this, the variance and co-variance of velocity was monitored at 4 locations 0.6 mm, 1 mm and 5 mm downstream of the trailing-edge. This was done to ensure that the unsteady CFD simulation had indeed attained statistical convergence and that there was no numerical dissipation in the flowfield data. In this section, we present the variance and co-variance of velocity monitored for baseline-2 case.

5.2.4.1. Variance of velocity downstream of trailing-edge

Variance of velocity was estimated along the three directions in the cartesian plane using the equations:

$$S(u) = \frac{\sum(u_i - \bar{u})^2}{n - 1} \tag{5.3}$$

$$S(v) = \frac{\sum(v_i - \bar{v})^2}{n - 1} \tag{5.4}$$

$$S(w) = \frac{\sum(w_i - \bar{w})^2}{n - 1} \tag{5.5}$$

where,

u_i, v_i, and w_i are the instantaneous velocities in the x, y and z directions

$\bar{u}$, $\bar{v}$ and $\bar{w}$ are the mean velocities in the x, y and z directions

n is the number of time-steps.

As seen in Fig. 5.11 – 5.13, the variance of velocity at different locations downstream of the trialing-edge in baseline-2 simulation attains statistical convergence after 0.1s. Similar results were obtained for baseline-1 case (as shown in Chapter 4) which attained statistical convergence after 0.08s.
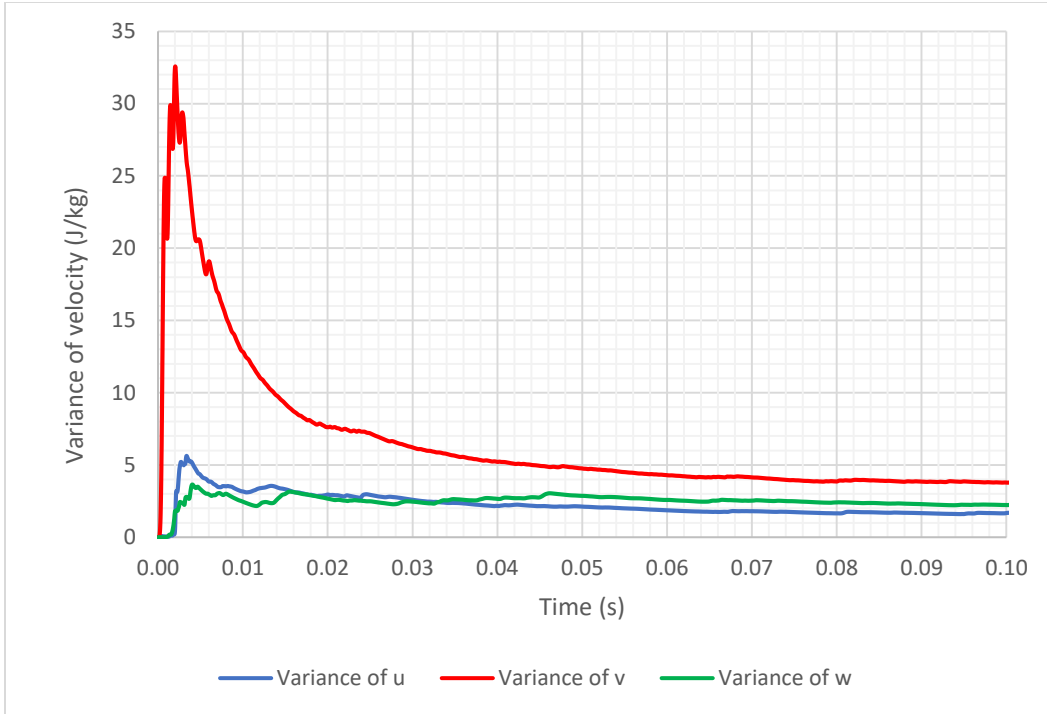
Fig. 5.11: Variance of velocity 0.6 mm downstream of trailing-edge (baseline-2)
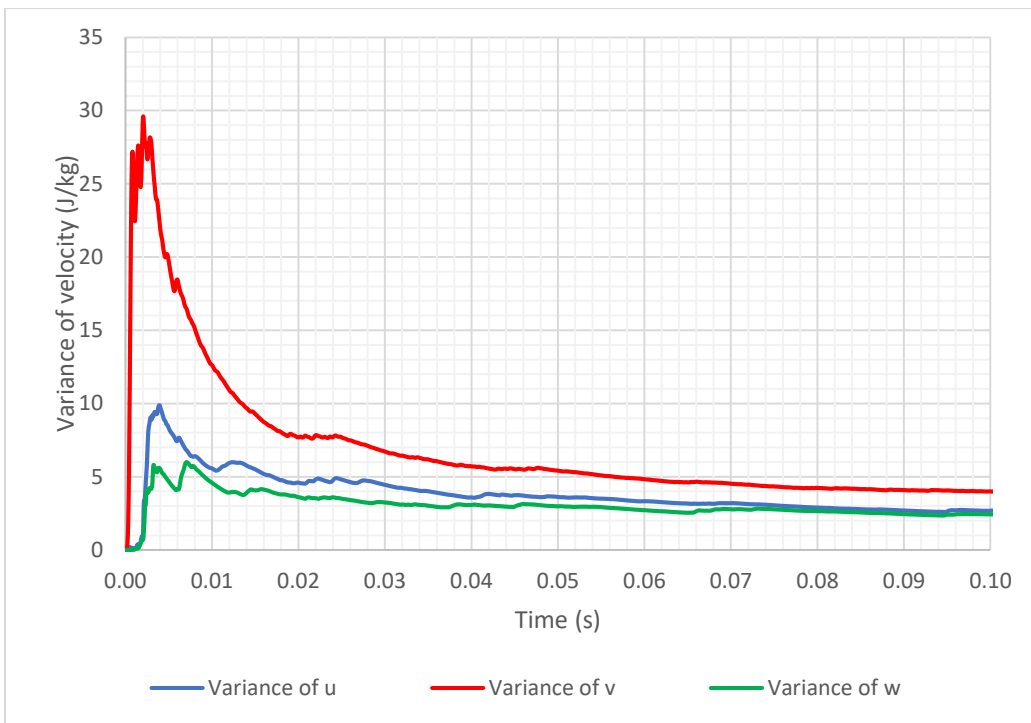
Fig. 5.12: Variance of velocity 1 mm downstream of trailing-edge (baseline-2)
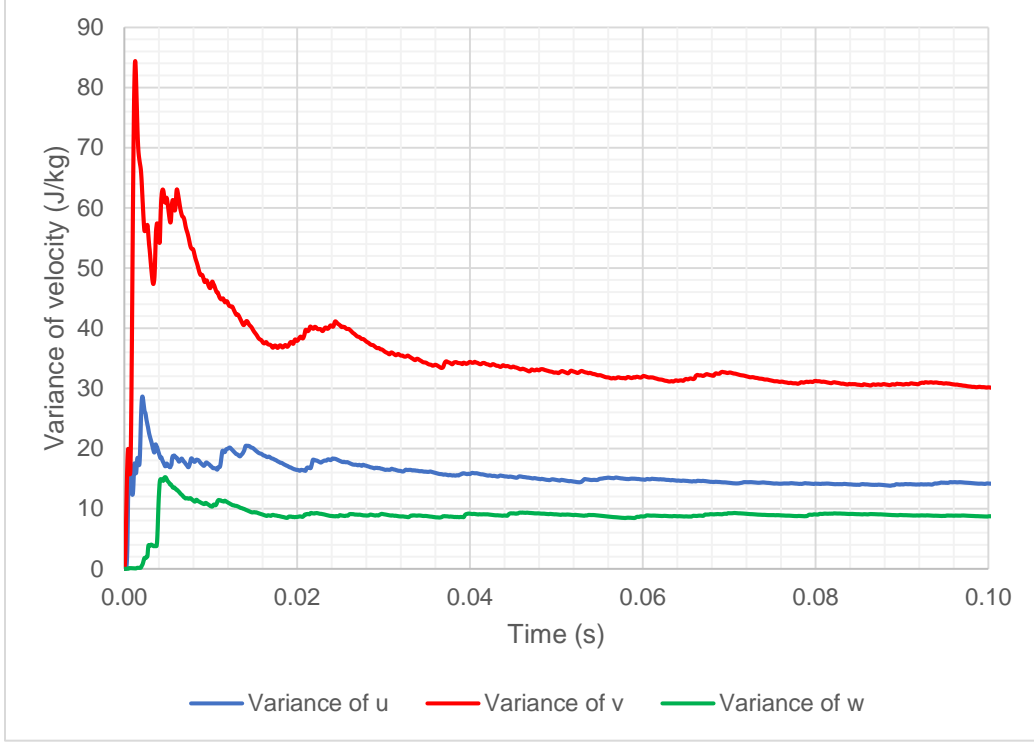
Fig. 5.13: Variance of velocity 5 mm downstream of trailing-edge (baseline-2)

5.2.4.2. Covariance of velocity downstream of trailing-edge

Covariance of velocity was estimated along the three directions in the cartesian

plane using the equations:

$$C(u,u) = \frac{\sum(u_i - \bar{u})(u_i - \bar{u})}{n-1} \tag{5.6}$$

$$C(u,v) = \frac{\sum(u_i - \bar{u})(v_i - \bar{v})}{n-1} \tag{5.7}$$

$$C(u,w) = \frac{\sum(u_i - \bar{u})(w_i - \bar{w})}{n-1} \tag{5.8}$$

where,

u_i, v_i, and w_i are the instantaneous velocities in the x, y and z directions

123

$\bar{u}, \bar{v}$ and $\bar{w}$ are the mean velocities in the x, y and z directions

n is the number of time-steps.

As seen from Fig. 5.14-5.16, the covariance of velocity monitored at 0.6 mm, 1 mm and 5 mm downstream of trailing-edge has attained statistical convergence after 0.1s. Since variance and covariance of velocity downstream of trailing-edge have attained statistical convergence in addition to convergence of residuals in continuity (order of 10^{-10}), momentum (order of 10^{-9}) and energy equations (order of 10^{-7}), we can conclude that the unsteady flow data recorded around the flat plate after 0.1s are reliable and can be used by the Ffowcs Williams and Hawkings model to predict farifeld trailing-edge noise.
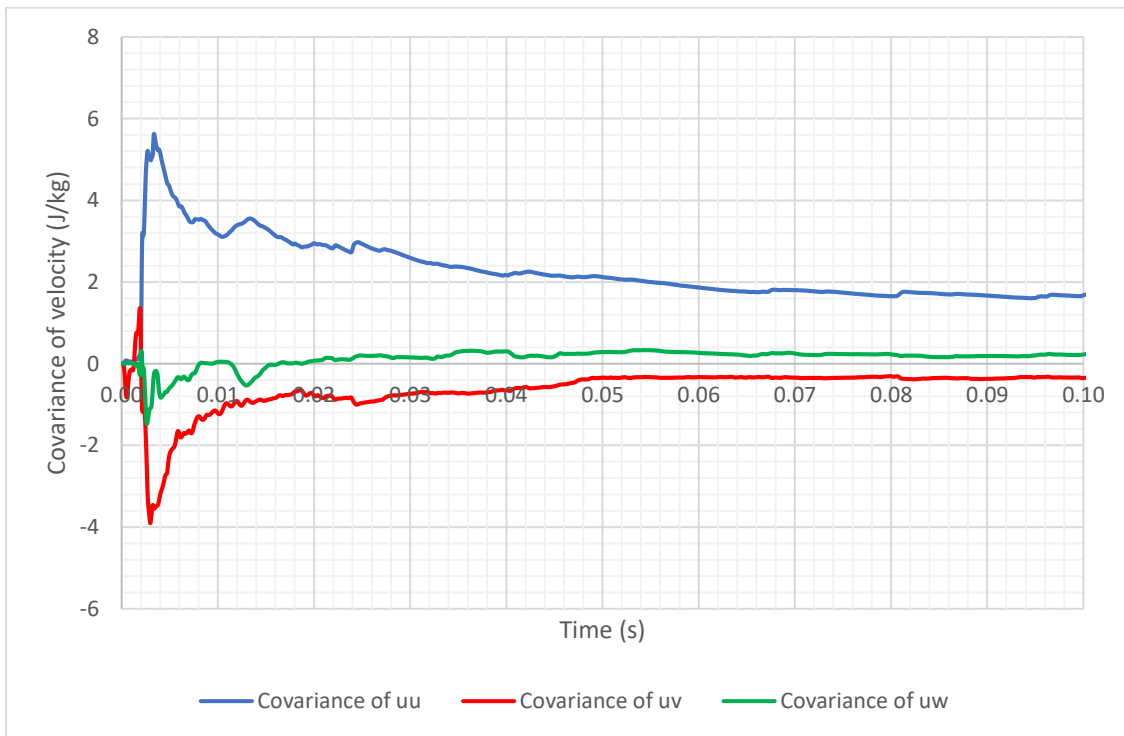
Fig. 5.14: Covariance of velocity 0.6 mm downstream of trailing-edge (baseline-2)
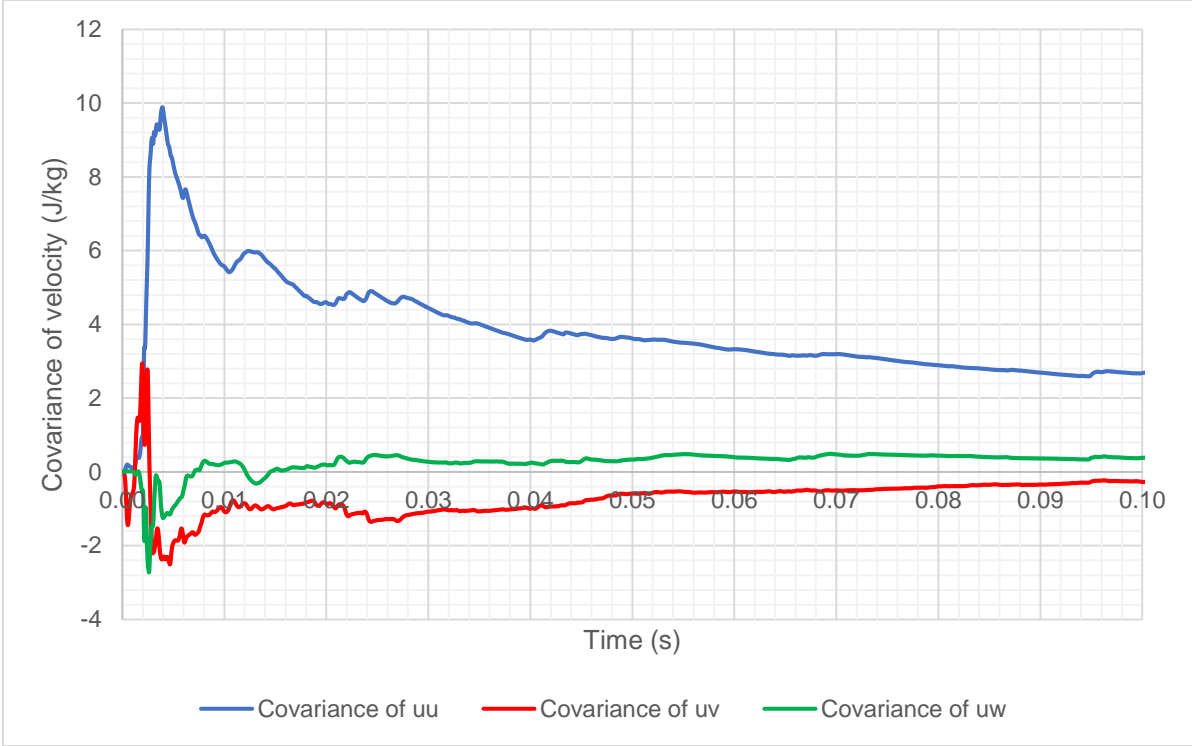
Fig. 5.15: Covariance of velocity 1 mm downstream of trailing-edge (baseline-2)
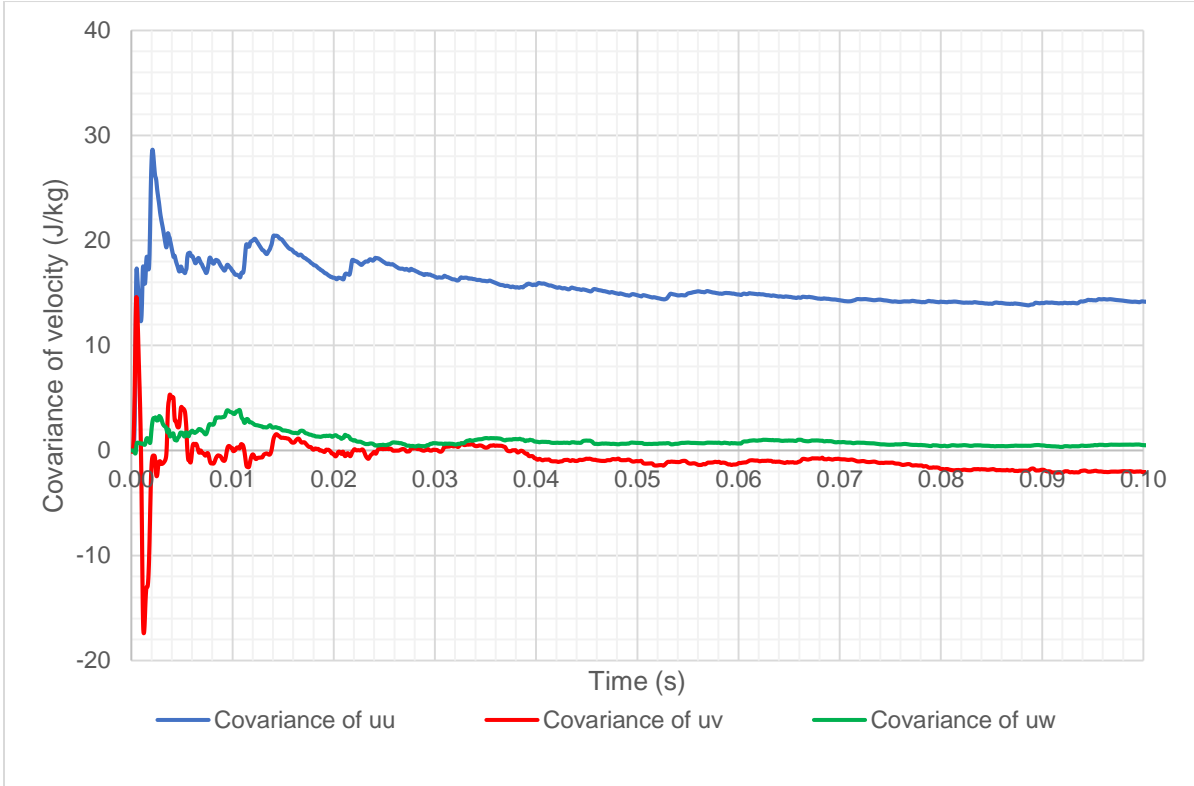
Fig. 5.16: Covariance of velocity 5 mm downstream of trailing-edge (baseline-2)

125

5.2.4.3. Farfield Noise

For baseline-1 simulation, pressure fluctuation history data was recorded by a point receiver placed 585 mm above the trailing-edge from 0.08-0.12s. For baseline-2 simulation, pressure fluctuation history data was recorded by a point received placed at the same location of 585 mm above the trailing-edge from 0.1-0.14s. Noise data was collected in both simulations for 0.04s. The duration of 0.04s used for noise data collection was estimated based on the minimum frequency of interest to be resolved (250 Hz) and 10 time-cycles corresponding to is minimum frequency, which enabled accurate farfield noise prediction. The data was converted from time domain to frequency domain using Discrete Fourier Transform and Power Spectral Density was estimated using Equation (5.9). This sampling time was divided into 3 analysis blocks and a Hanning window function with an overlap factor of 50% was implemented to prevent spectral leakage. Using a characteristic chord length of 0.214 m and 0.21m for baseline-1 and baseline-2 simulations respectivly and free stream velocity of 35 m/s in both cases, Strouhal number was estimated for a frequency range from 250-8000 Hz and a plot of Power Spectral Density versus Strouhal number was created, as shown in Fig. 5.17 and 5.18. These plot would serve as our baseline noise prediction to compare with the case when the two compliant coatings are applied to the flat plate geomemtry seen in Fig. 5.1.

$$L_p(f) = 10 \log_{10}\left(\frac{PSD(f)}{\hat{p}_{ref}^2}\right) \tag{5.9}$$

where,

$\hat{p}_{ref}$ is reference acoustic pressure for air (20 µPa)
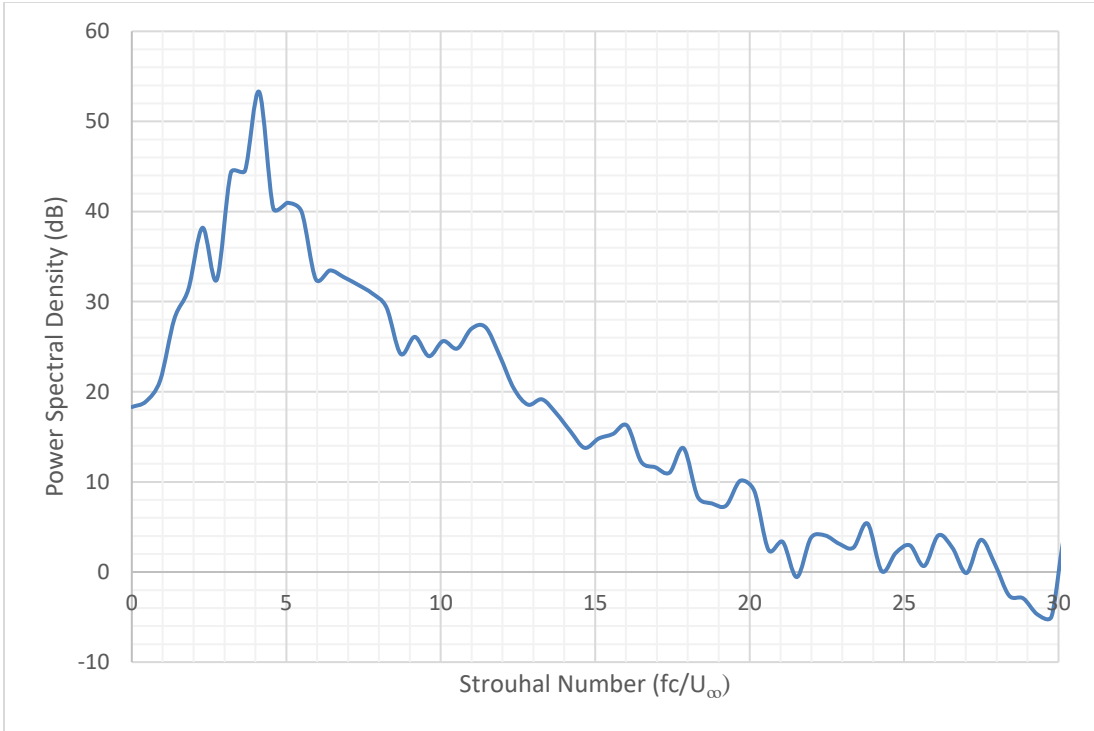
Fig. 5.17: Power Spectral Density 585 mm above trailing-edge (baseline-1)
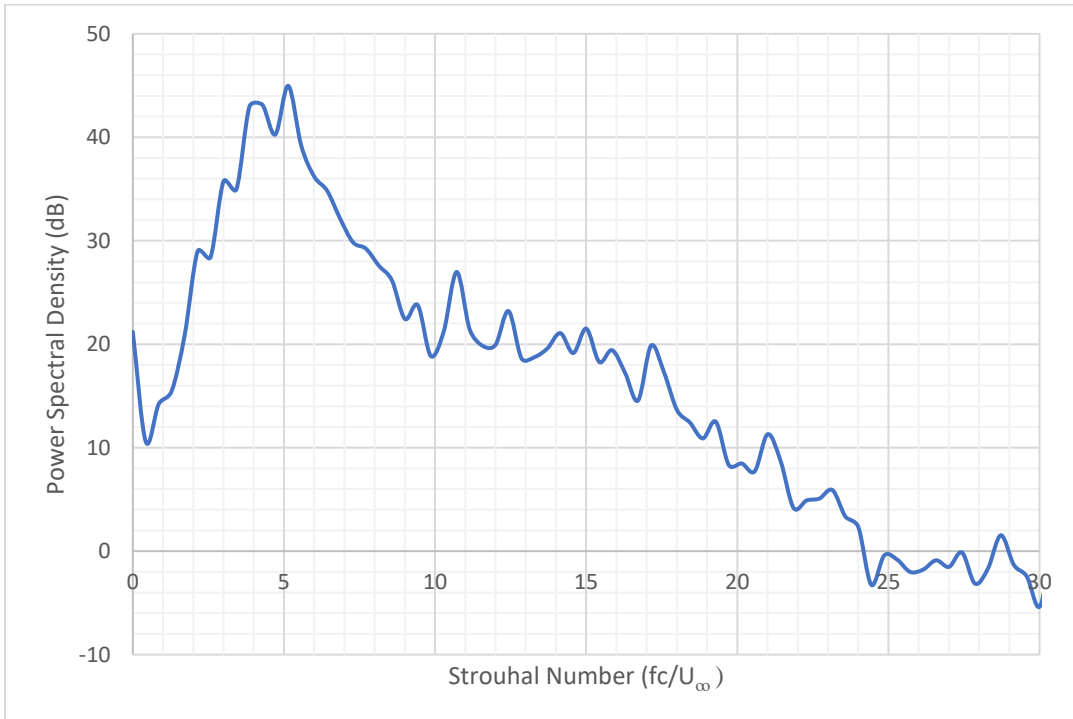
Fig. 5.18: Power Spectral Density 585 mm above trailing-edge (baseline2)

127

5.3.   Compliant coating applied to flat plate

In this section, we will present the methodology involved in our computational study that compares the effects of coating-1 of 7 mm thickness and material properties shown in Table 5.1 with coating-2 of 5 mm thickness and material properties shown in Table 5.2 on trailing-edge noise. The two coatings will be applied to the flat plate geometry shown in Fig. 5.1.
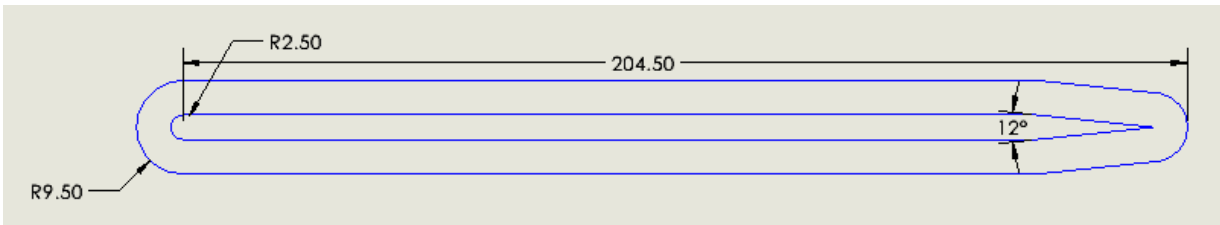
Fig. 5.19: Coating-1 of 7 mm thickness applied to rigid flat plate

When coating-1 of 7 mm thickness is applied on the rigid flat plate seen in Fig. 5.1, it changes the plate thickness and trailing-edge shape as seen in Fig. 5.19. Similarly, when coating-2 of 5 mm thickness is applied on the rigid flat plate seen in Fig. 5.1, it changes the plate thickness and trailing-edge shape as seen in Fig. 5.20.
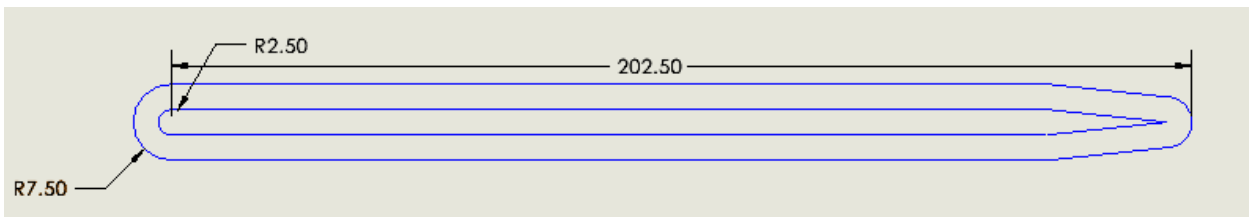
Fig. 5.20: Coating-2 of 5 mm thickness applied to rigid flat plate

To perform this computational study, the *Fluid Structure Interaction* technique of a commercial CFD code STAR-CCM+ v.15.02.009 has been used. The *Two-way coupling* FSI technique is used to simulate the momentum and energy transfer between the fluid and compliant coating. Furthermore, a *morphing mesh* is used to simulate coating deformation. Initially, a solid stress model with *isotropic linear elasticity* has been used

to perform static analysis, in which a steady CFD and FSI simulation is run so that both the flowfield and the compliant coating reach an equilibrium condition.

5.3.1. Mesh generation and boundary conditions

The computational domain and boundary conditions used for the fluid region were identical to what were used for the used for the baseline cases, described in Section 5.2.1. However, the rigid flat plate from the two baseline cases are replaced by corresponding flat plate models with compliant coating applied to them as shown in Fig. 5.19 and 5.20.

A non-conformal *Mapped Contact Interface* is created between the outer surface of the coating and fluid region in contact. This interface helps exchange information between the fluid and structure solvers. Symmetry boundary conditions are used on either side-planes of the coating. A fixed constraint is applied to the inner surface of coating in contact with the flat plate while rest of the compliant coating can deform due to the *morphing mesh*.
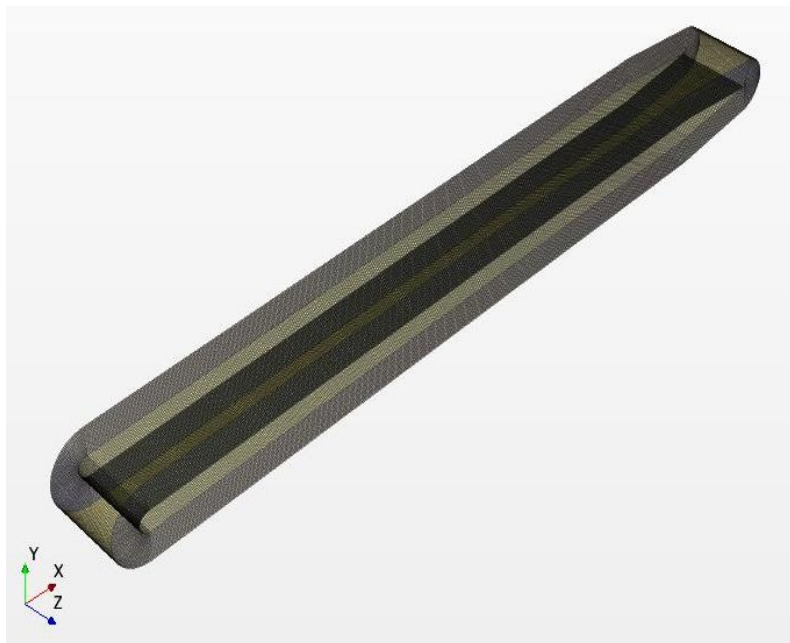
Fig. 5.21: Compliant coating mesh

5.3.2. Steady CFD-FSI analysis

The SST k-ω RANS turbulence model along with the two-way coupling FSI technique was used to perform steady CFD-FSI analysis using the steps outlined in Table 5.4.

Table 5.4: Steady CFD-FSI analysis

Parameter	Coating-1	Coating-2
Run steady CFD simulation	0-2100 iterations	0-3700 iterations
Run steady FSI simulation (i.e., include solid stress solver)	2100-3500 iterations	3700-5000 iterations

As outlined in Table 5.4, steady analysis was carried out to ensure that CFD solver first attains residual convergence. After this, the aerodynamic forces exerted by flow boundary layer was converted into body loads and applied on the compliant coating surface. Finally, both the CFD solver and the Solid Stress solver with settings shown in Table 5.5 was run until residual convergence and coating attains static equilibrium. This procedure ensured that steady CFD-FSI simulation remains stable during analysis.

Table 5.5: Solid Stress Solver Settings

Parameter	Solid Stress Solver Setting
Space	Three Dimensional
Material Stiffness model	Linear Elasticity
Linear Elastic Material model	Isotropic Linear Elasticity
Coupling	Two-way
Motion Specification	Solid Displacement

5.3.3. Compliant coating deformation

Once coating attains static equilibrium through steady CFD analysis, its deformation is compared with that from literature.
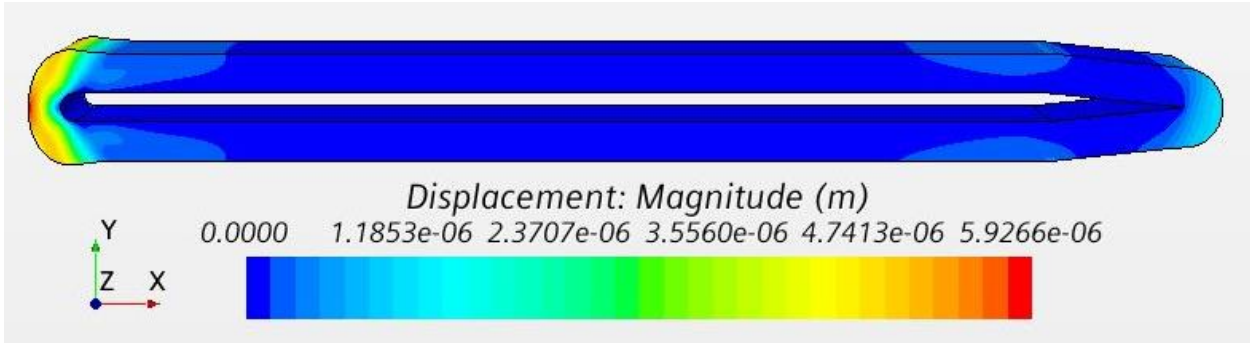
Fig. 5.22: Coating-1 deformation (scaled 200 times)

As seen in Fig. 5.22, coating-1's deformation is in the order of microns everywhere along the chord with maximum deformation of 5.92µm at leading-edge center.
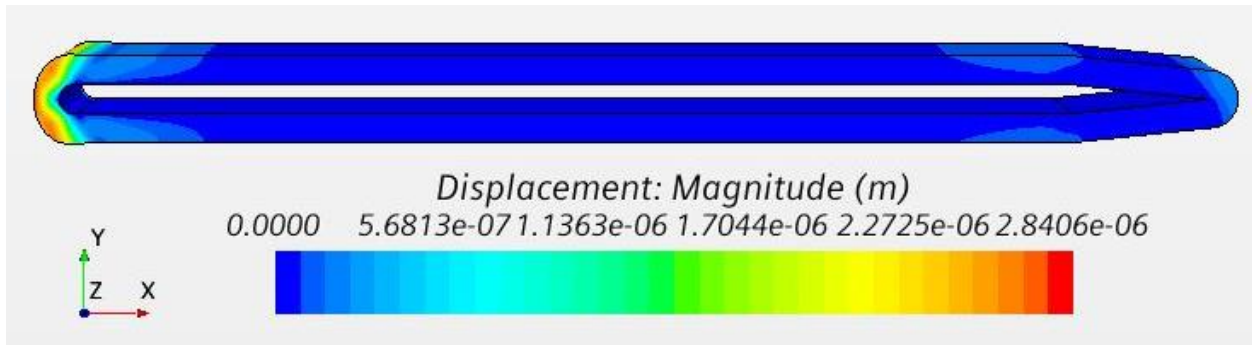
Fig. 5.23: Coating-2 deformation (scaled 200 times)

Similarly, maximum coating deformation of 2.84µm was observed at leading center for coating-2. Literature points to experimental studies by Lee, Fisher and Schwarz [26] who studied the effects of homogeneous isotropic compliant coatings on flow boundary layer and measured coating deformation in the order of microns with peak-to-valley displacement of d_{pv} = 1.67-3.82µm and rms displacement of d_{rms} = 0.32-0.72µm. These measurements are comparable to predictions made in our study and hence simulated coating deformation can be considered as reliable.

5.3.4. Unsteady CFD-FSI analysis

Unsteady CFD-FSI analysis was performed using the SST k-ω Improved Delayed Detached Eddy Simulation along with the two-way coupling FSI technique. To ensure stability of unsteady CFD-FSI analysis, the following procedure as outlined in Table 5.6 was used.

Table 5.6: Unsteady CFD-FSI analysis

Parameter	Coating-1	Coating-2
Run unsteady CFD simulation	0.00-0.05s	0.00-0.045s
Run unsteady FSI simulation (i.e., include solid stress solver)	0.05-0.056	0.045-0.0495s
Collect farfield noise data	0.056-0.06s	0.0495-0.0535s

Initially, unsteady CFD simulation was run until residuals of continuity was in the order of 10^{-10}, residuals for momentum equations were in the order of 10^{-9} and residual for energy equation was in the order of 10^{-7}. In addition to this, the variance and co-variance of velocity was also monitored downstream of the trailing-edge until they almost attain statistical convergence. After this physical time, the solid stress solver was included and unsteady FSI analysis was performed until variance and covariance of velocity attained statistical convergence. Finally, pressure fluctuation data was collected for 0.004s in both simulations which would be used by the Ffowcs Williams and Hawkings model to predict farfield trailing-edge noise. The duration of noise data collection is estimated based on the minimum frequency of interest to be resolved (i.e., 250 Hz).

5.3.4.1. Variance of velocity downstream of trailing-edge

Similar to the baseline case, variance of velocity was estimated along the three directions in the cartesian plane using the equations (5.3), (5.4) and (5.5) at 0.6 mm, 1 mm, 5 mm and 10 mm downstream of the trailing-edge. After running the fluid solver up to 0.05s for coating-1 and 0.045s for coating-2, the variance of velocity monitored at different locations downstream of the trailing-edge has almost attained statistical convergence and hence can be considered stable for solid stress solver to start applying body loads on the compliant coating. Results for coating-2 are presented in Fig. 5.24-5.26.
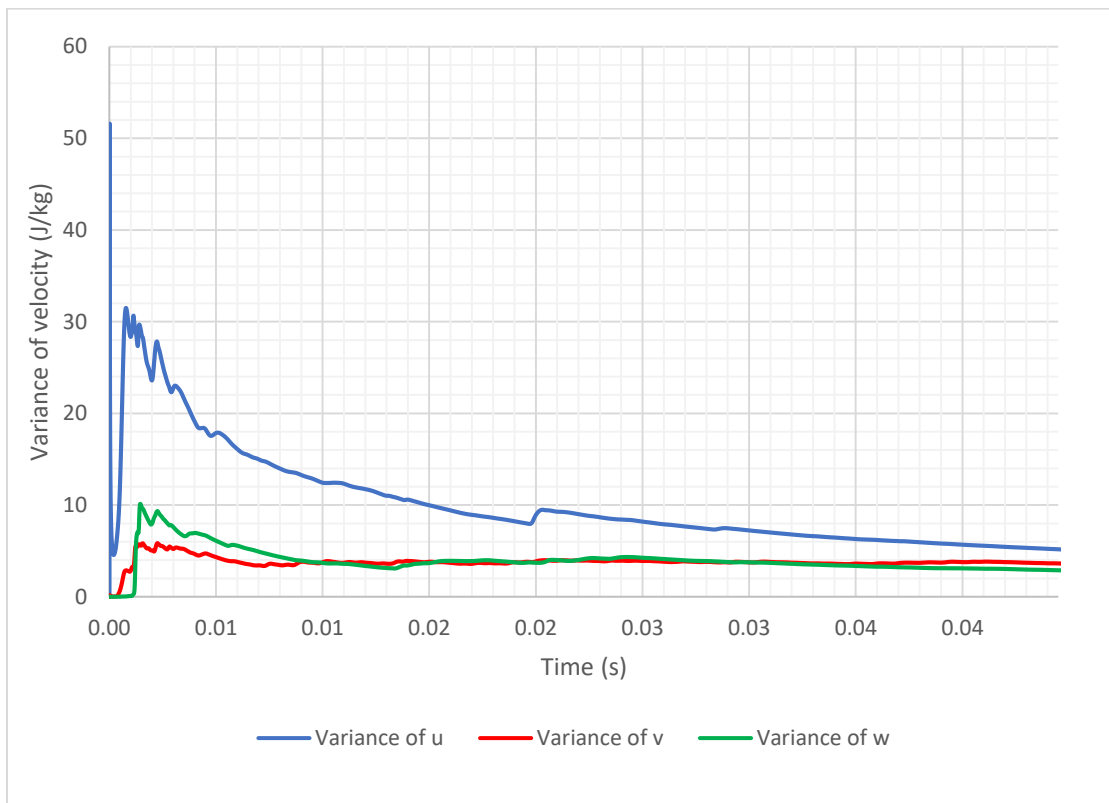
Fig. 5.24: Variance of velocity 0.6 mm downstream of trailing-edge (coating-2)
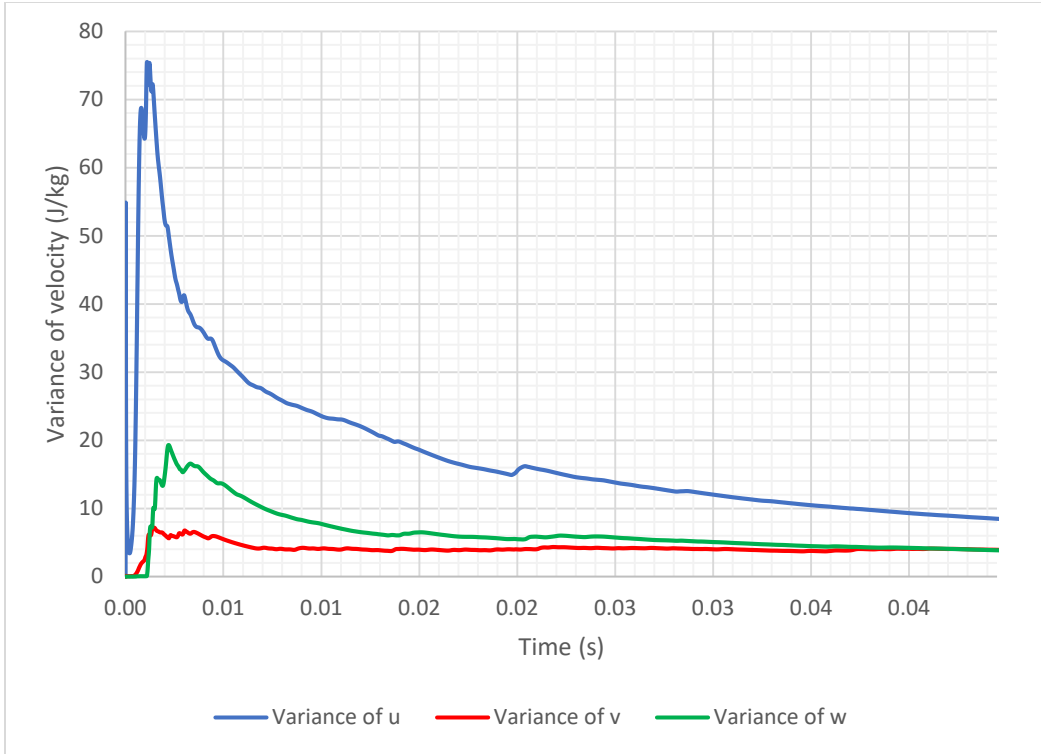
Fig. 5.25: Variance of velocity 1 mm downstream of trailing-edge (coating-2)
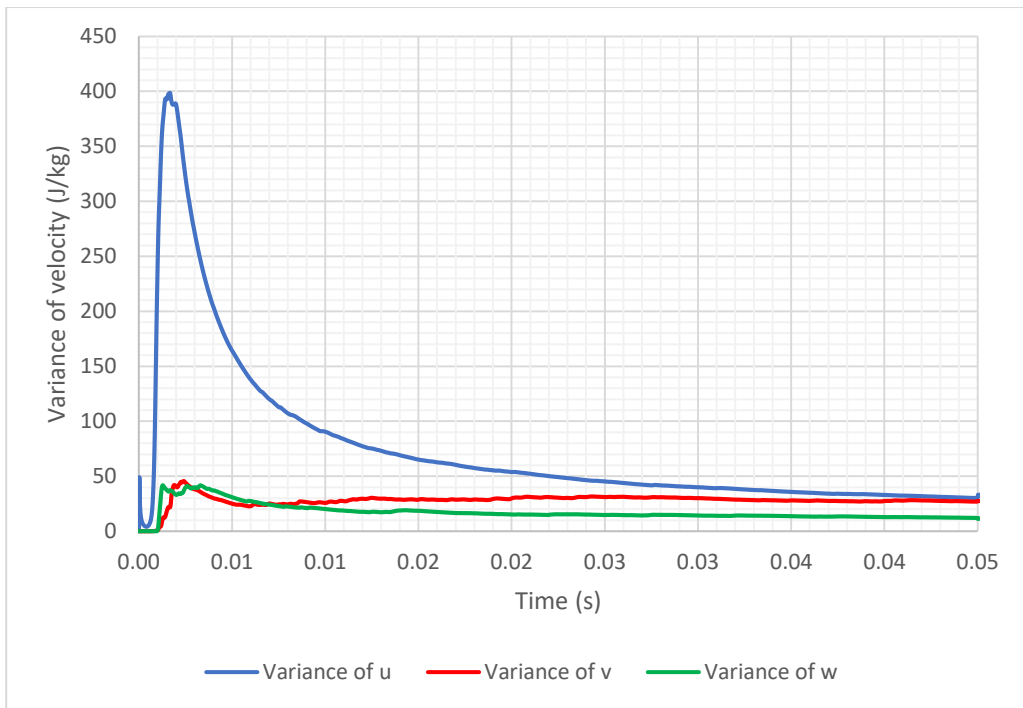
**Fig. 5.26: Variance of velocity 5 mm downstream of trailing-edge (coating-2)**

134

5.3.4.2. Covariance of velocity downstream of trailing-edge

Similar to the baseline case, variance of velocity was estimated along the three directions in the cartesian plane using the equations (5.3), (5.4) and (5.5) at 0.6 mm, 1 mm, 5 mm and 10 mm downstream of the trailing-edge and results for coating-2 are presented in Fig. 5.27-5.29.
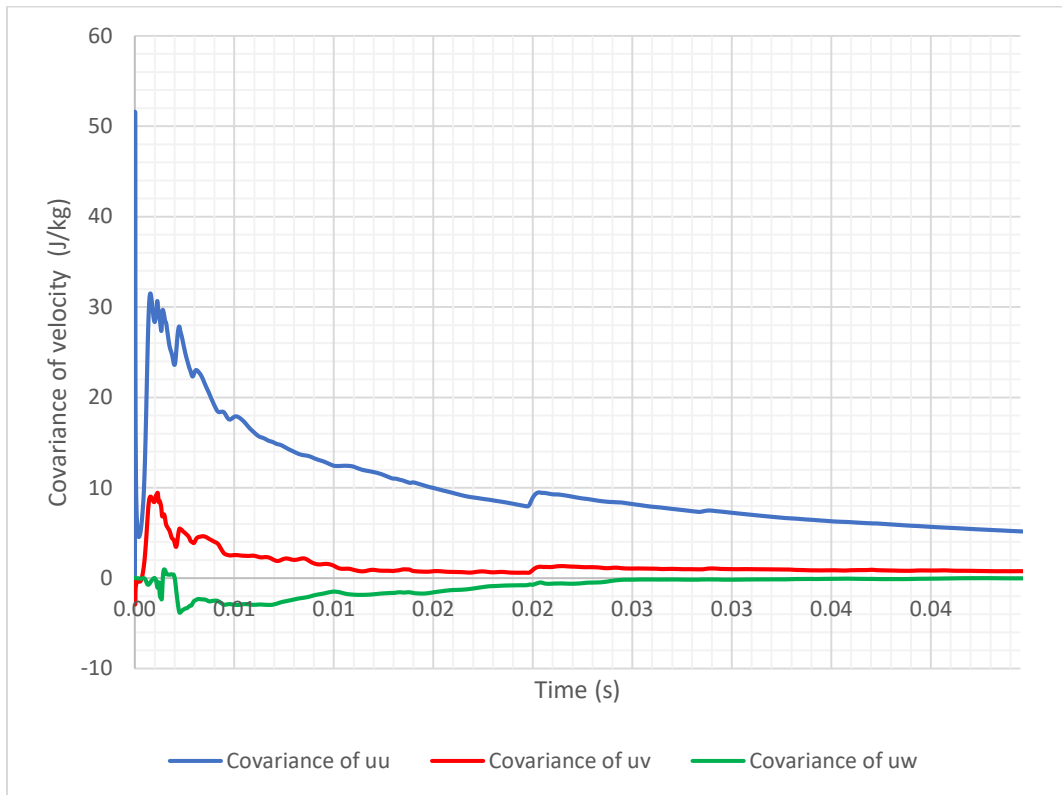
Fig. 5.27: Covariance of velocity 0.6 mm downstream of trailing-edge (coating-2)
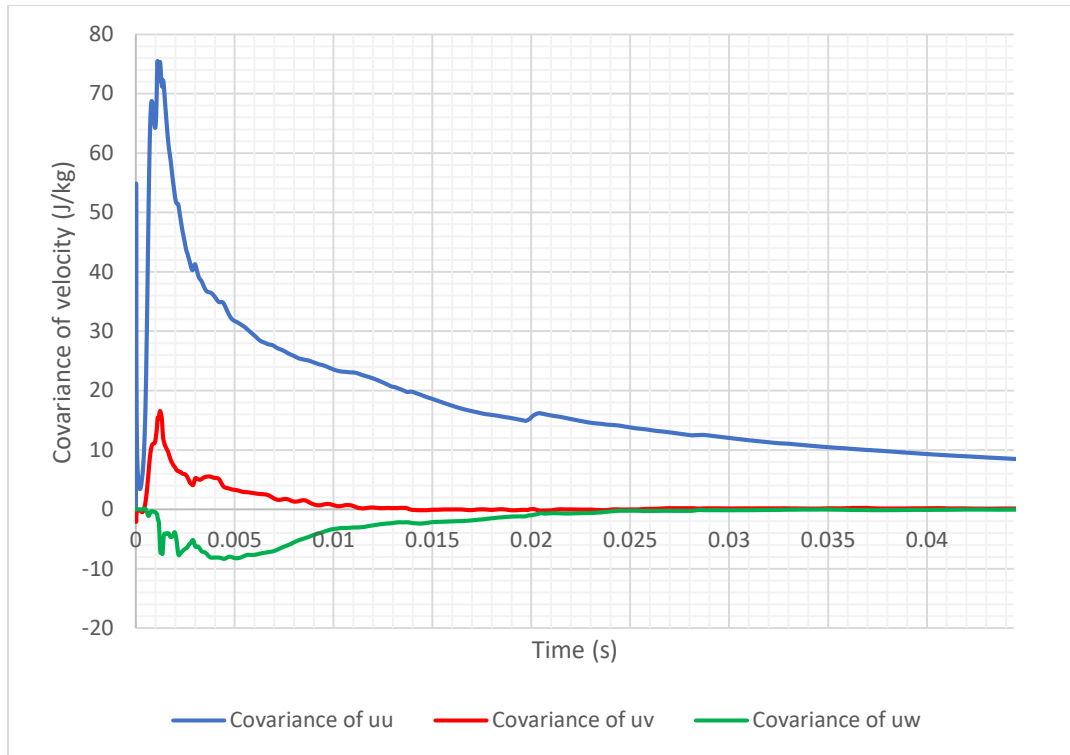
Fig. 5.28: Covariance of velocity 1 mm downstream of trailing-edge (coating-2)
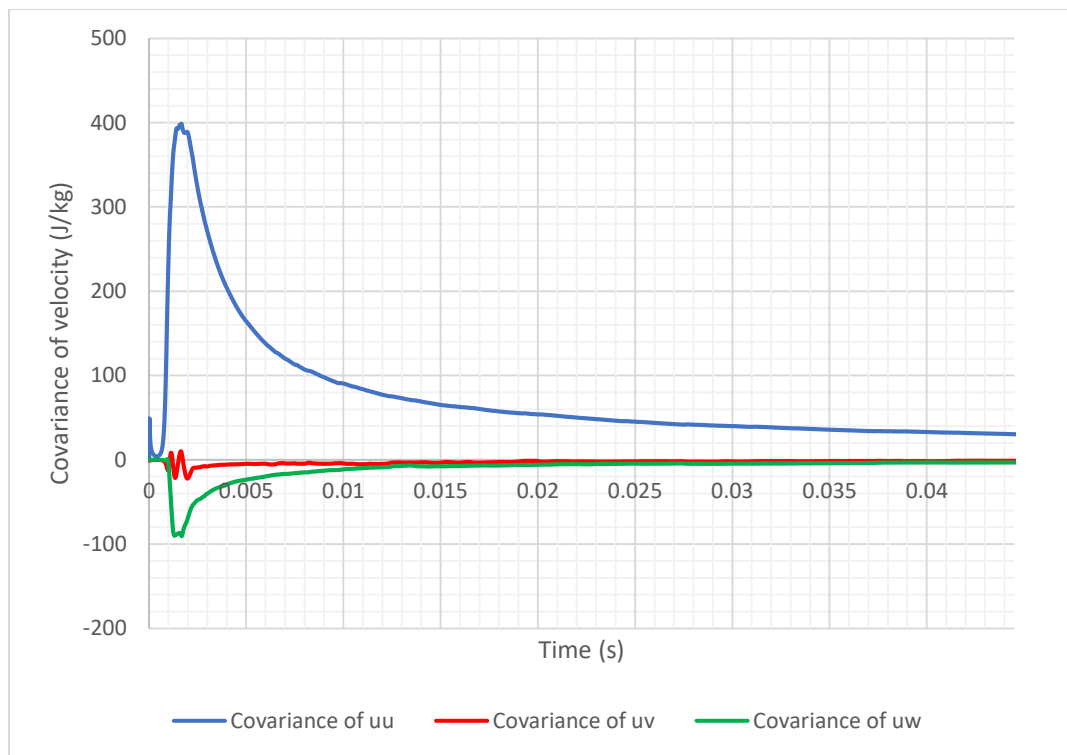
Fig. 5.29: Covariance of velocity 5 mm downstream of trailing-edge (coating-2)

136

5.3.4.3. Statistical convergence

After 0.05s for coating-1 and 0.045s for coating-2, both the flow solver and solid stress solver are run up to 0.056s and 0.0495s respectively until statistical convergence is attained. During this time, the solid stress solver converted the aerodynamic forces into body loads and applied the same on the coating. To illustrate this, Fig. 5.30 – 5.31 presents results from the coating-2 case where we see that the variance and covariance of velocity 0.6 mm downstream of the trailing-edge has attained statistical convergence after 0.0495s.
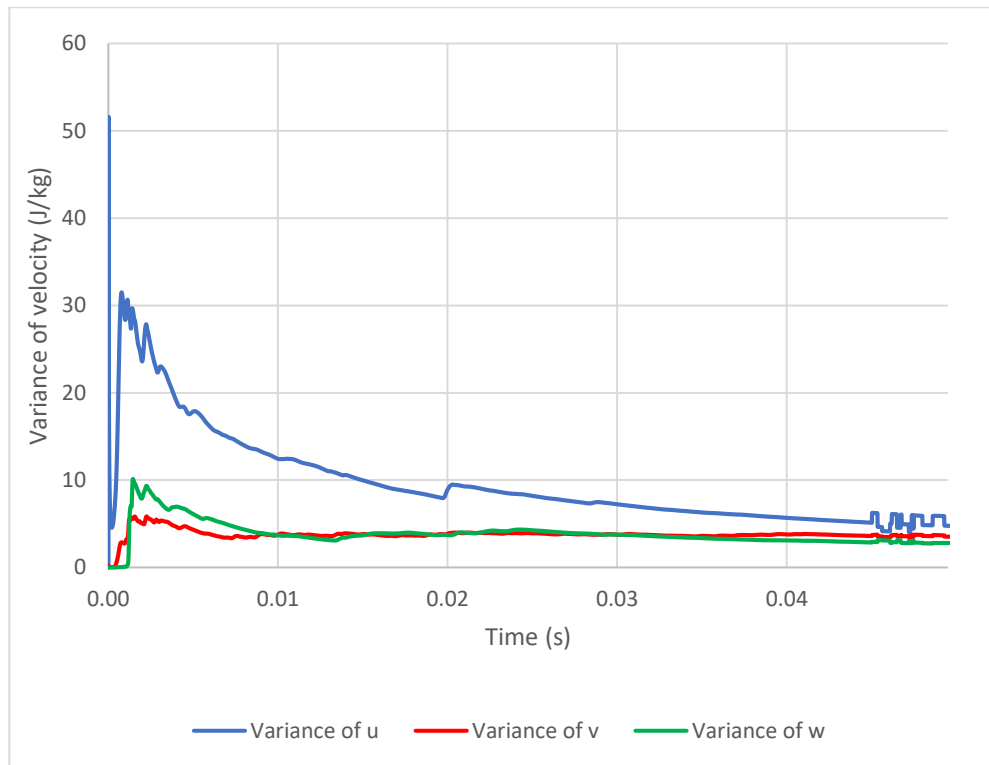
Fig. 5.30: Variance of velocity 0.6 mm downstream of trailing-edge (coating-2)
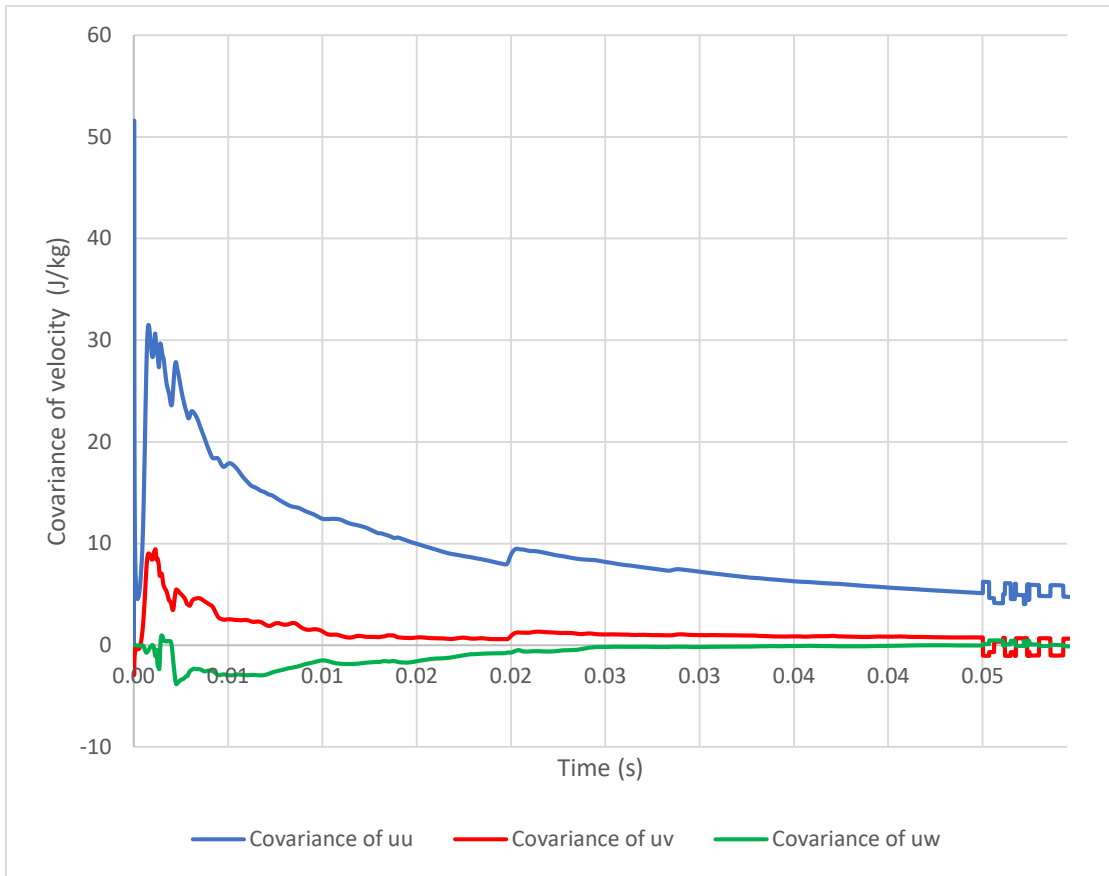
Fig. 5.31: Covariance of velocity 0.6 mm downstream of trailing-edge (coating-2)

5.3.4.4. Farfield noise

Once simulations attained statistical convergence, pressure fluctuation history data was collected at a point receiver placed 585 mm above the trailing-edge from 0.056-0.06s for coating-1 case and from 0.0495-0.0535s for coating-2 case. Thi data was converted from time domain to frequency domain using Discrete Fourier Transform and Power Spectral Density was estimated using Equation (5.9). Finally, a graph of Power Spectral Density versus Strouhal number was created and compared with their corresponding baseline results, as seen in Fig. 5.32 and 5.33.

138
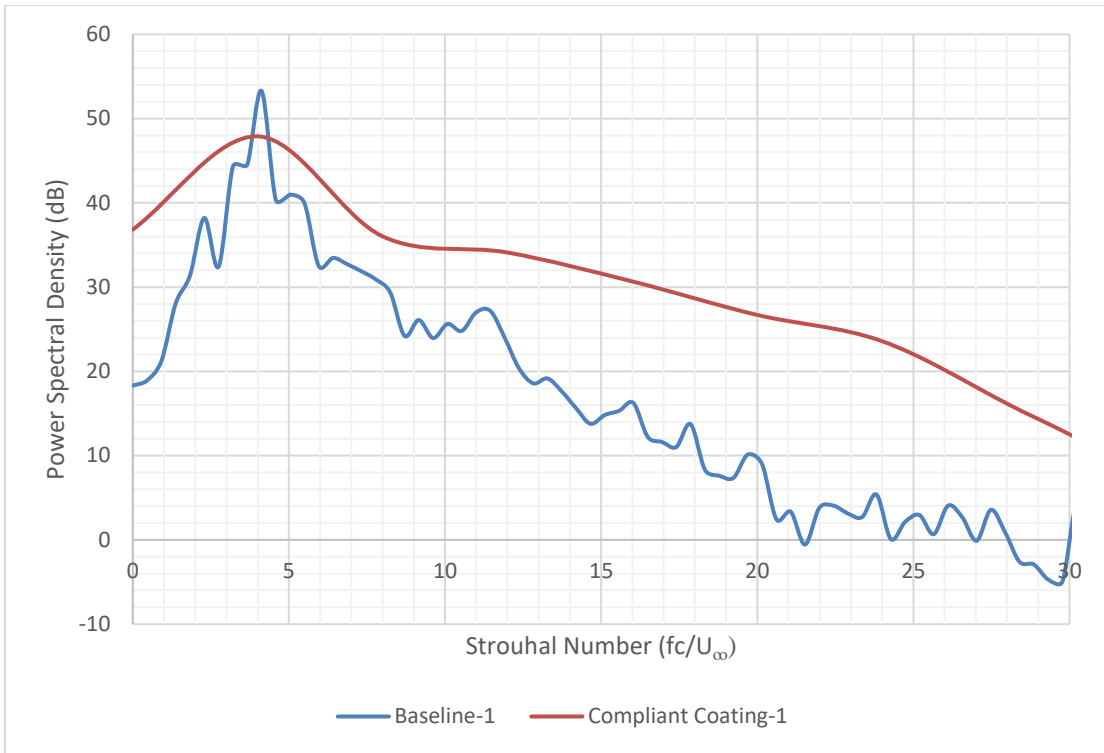
Fig. 5.32: Farfield noise comparison at 585 mm above trailing-edge (coating-1)
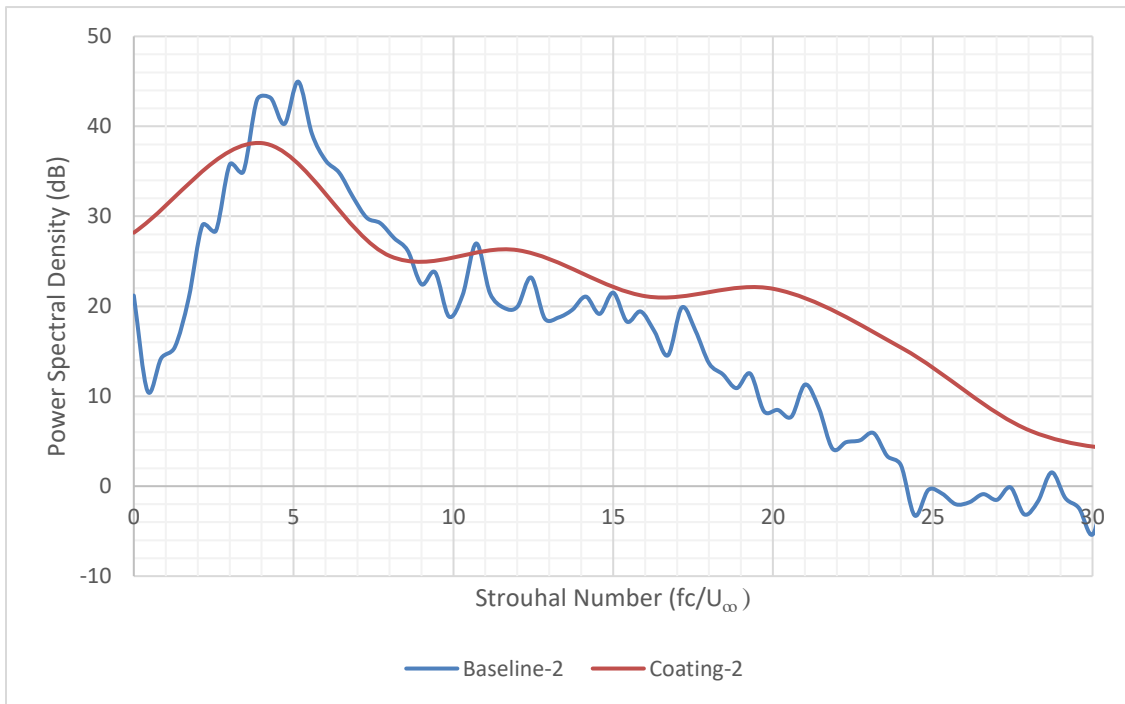
Fig. 5.33: Farfield noise comparison at 585 mm above trailing-edge (coating-2)

As seen from Fig. 5.32, use of coating-1 on the flat plate geometry resulted in an increase in noise by 10-15 dB throughout the entire frequency range of interest except at St=4.00 (i.e. 700 Hz) where we observe a fall in noise by 6dB. Whereas Fig. 5.33 indicates that coating-2 could reduce noise by 2-4 dB at low frequency ranges corresponding to St = 3.50 – 9.00 (i.e. 600 – 1575 Hz) with a maximum noise reduction of 5dB at St=4.00 (i.e. 700 Hz). We also observe that the energy content in noise is shifted slightly to the lower frequency range when coating-2 is applied on the flat plate geometry. However, we must note that coating-2 also results in an increase of 8-10 dB for St > 18.00 (i.e. 3150 Hz). Thus, the present computational study reveals that coating material properties play a significant role on how it affects trailing-edge noise.

Further literature review points to experimental studies conducted by Choi et al. [40] which reveal that coating material properties must be carefully chosen so that their resonance frequency satisfies the condition shown in equation (5.10), according to Sternberg's theory, for it to favorably modulate the flow boundary layer.

$$50 < \frac{1}{f_0} < 150 \qquad (5.10)$$

And,

$$f_0^{-1} = \frac{t_0 (u^*)^2}{\nu} \qquad (5.11)$$

where,

f_0 is the resonance frequency or resonant frequency in Hz

ν is the kinematic viscosity

u^* is the friction velocity

Thus, further computational studies are necessary that to understand the relationship between coating material properties, its resonance frequency and how it affects trailing-edge noise.

5.4. Conclusions

A computational aeroacoustics analysis is performed to compare the effects of two compliant coatings on trailing-edge noise. It was observed that use of coating-1 may result in an increase in noise by 10-15 dB throughout the entire frequency range of interest, with a reduction of 6 dB at St=4.00 (i.e. 700 Hz). Whereas coating-2 may reduce noise by 2-4 dB at low frequency ranges corresponding to St = 3.50 – 9.00 (i.e. 600 – 1575 Hz) with a maximum noise reduction of 5dB at St=4.00 (700 Hz). Coating-2 also shifted the energy content in noise to the lower frequency range. These studies reveal that material properties significantly affect trailing-edge noise characteristics and further computational study is necessary to understand the relationship between coating material properties, its resonance frequency and how these parameters affect trailing-edge noise.

In addition to this, it is also recommended that experimental studies be performed through wind tunnel testing by recording flow and noise measurements to understand the effects of passive compliant coatings on trailing-edge noise.

6. EXPERIMENTS TO INVESTIGATE THE EFFECTS OF COMPLIANT COATINGS ON TRAILING-EDGE NOISE

Over the years, passive compliant coatings, with homogeneous viscoelastic isotropic material properties, have been investigated through experiments to study their ability to favorably modulate flow boundary layer. Their application was initially investigated for hydrodynamic flows since water and compliant coating have comparable densities. This ensured that the compliant wall and water would have comparable wall and fluid inertias. Thus, wall compliance offered significant impact on the Tollmien-Schlichting instabilities [23]. In recent years, these investigations were extended to aeronautical applications. Experiments conducted to study the effects of wall compliance in aerodynamic flows showed that compliant coatings offer constructive coupling and favorably modulate flow boundary layer through the following mechanisms:

1. Passive compliant coatings have shown their ability to delay transition from laminar to turbulent flow

2. Passive compliant coatings have also shown their ability to reduce skin friction drag in fully turbulent flow

6.1. Hypothesis

Application of compliant coating over a surface would help damp the normal component of turbulent stresses through elastic surface deformation; thus absorb (or soak up) the turbulent kinetic energy (TKE) within the boundary layer. The extent of TKE mitigation depends on coating material properties, surface geometry and Reynolds

number. Turbulent drag reduction and mitigation of flow-induced noise generated at the surface are the direct byproducts of turbulence stress modulation caused by an aerodynamic surface covered by compliant coating.

6.2.   Present Study

As outlined in Chapter 5, Computational Aeroacoustics Analysis conducted at the University of Kansas showed that coating-2 displayed favorable noise mitigation characteristics with a 2-4 dB reduction from 600 – 1575 Hz compared to coating-1. Therefore, coating-2 was chosen to further investigate its effects on noise characteristics through experimentation and wind tunnel testing on a flat plate geometry with a sharp trailing-edge, with same dimensions as used by Moreau et al [48] at the University of Adelaide. The methodology and results from experiments conducted for this flat plate model in the closed loop subsonic wind tunnel of the Aerospace Engineering Department at the University of Kansas is presented in this chapter.

6.3.   Review of Literature

Though this experimental study is a fundamental research that investigates the effects of passive compliant coatings on trailing-edge noise demonstrated using a flat plate in a fully turbulent flow, a feasibility study of compliant coating usage to broader applications such as rotor-dominated noise where trailing-edge noise may be a significant noise source, as in the case of propellers of unmanned aerial vehicles or helicopter rotors, are explored through a review of literature in this section before discussing results from the present study.

6.3.1. *Noise mitigation studies – UAV Propellers*

Researchers at the University of Southern California [70] conducted experiments to investigate the effects of trailing-edge noise serrations on noise generated by UAV propellers. A base APC 9x6E propeller was chosen and thrust and noise measurements were recorded for the baseline geometry at a Reynolds number of 97,000. This propeller was suitably modified to include trailing-edge serrations with teeth depth varying from 1/8" to 3/8" and measurements were repeated to compare with baseline case. It was observed that inclusion of trailing-edge serrations enabled noise reduction and is attributed to the reduction of tip vortices and trailing-edge wake. Furthermore, increase in tooth depth enabled greater noise reduction with a maximum reduction observed corresponding to a serration depth of 35% with respect to the mean aerodynamic chord. This noise reduction was attained while maintaining the thrust within $\pm 5\%$ of the baseline propeller.

Fig. 6.1: Serrated trailing-edge propellers with varying teeth depths [70]

Treuren et al. from Baylor University [71] in collaboration with the Department of Aeronautics, US Airforce Academy performed experimental studies on the propellers of

a DJI Phantom 2 quadcopter with a rotor diameter of 9.5", as shown in Fig. 6.2, in the low speed wind tunnel at the USAF Academy.

Fig. 6.2: DJI Phantom 2 quadcopter [71]

Near field sound pressure level are recorded when the quadcopter is maintained in a static hover condition. To achieve this, the propellers are required to generate a thrust of 0.7 lbf. Various noise mitigation techniques such as leading-edge notch, trailing-edge notch, vortex generators and sawtooth trailing-edge amongst others were investigated to address noise generated by tip vortices. It was found that many of these techniques could achieve a noise reduction upto 8-10 dBA. However, they had a significant impact on the amount of power drawn to generate the 0.7 lbf of thrust and maintain the quadcopter in hover condition. The most promising noise mitigation technique was found to be the trailing-edge notch with depth of 0.25", as shown in Fig. 6.3, which achieved a noise reduction of 7.2 dBA with an acceptable increase of only 3.96% of power requirement to maintain the quadcopter in hover condition.

Fig. 6.3: Trailing-edge notches used for propellers of Phantom 2 quadcopter [71]

Brungart et al. from Penn State University [72] developed scaling relationships for propeller noise and showed that noise reductions in UAV propellers can be achieved by increasing the propeller diameter while reducing its rotational speed to produce the same thrust. To corroborate their scaling relationship, experiments were conducted using propellers of various diameters varying from 15.2 - 60.9 cm, as shown in Fig. 6.4.

Fig. 6.4: Propellers of different diameters tested for noise measurements [72]

Their experiments revealed that increasing propeller diameter from 30.5 cm to 60.9 cm to produce the same thrust helped achieved a 9dBA noise reduction. This was

attributed to the lower tip speed at which the larger diameter propellers were operating at. Furthermore, the energy content in noise shifted towards lower frequencies and reduction in blade rate tones were observed, which are the cause of annoyance in propeller noise. It was also observed that the power required by the propeller to generate the same thrust was inversely proportional to the propeller diameter. Therefore, a larger diameter propeller required lower power to produce the same thrust and also resulted in significant noise reduction.

Experiments were conducted by Leslie et al. [73] at the University of Sydney to investigate the effects of leading-edge boundary layer trips on UAV propeller noise. Flow visualization techniques indicated that for propellers with short chord lengths (1.5 – 3 cm) and at low Reynolds number flow conditions, a laminar separation bubble was developed near the leading-edge of the suction surface. By introducing a boundary layer trip at 10% chord, as shown in Fig. 6.5, the laminar boundary layer (indicated by light blue arrow marks) trips to a turbulent boundary layer (indicated by dark blue arrow marks) and the separation bubble is eliminated resulting in a 4dB noise reduction.

Fig. 6.5: Boundary layer trip at 10% chord of UAV propeller. [73]

This technique is effective only at low angles of attack experienced by cruise flight conditions. However, during take-off or increased loading conditions, the effectiveness of the boundary layer trip is reduced as the separation bubble is no-longer present in such

conditions. The mechanism attributed to boundary layer trip's effectiveness is that the forced transition to turbulent boundary layer prior to laminar separation and bubble formation results in a reduction in turbulent boundary layer thickness. This in-turn aids in reducing turbulent boundary layer trailing-edge noise.

Guo et al. [74] developed an optimal sound absorber using multiple inhomogeneous Helmholtz resonators with extended necks, as shown in Fig 6.6 and performed experimental studies using duct that was lined with these Helmholtz resonators through-out its circumference to absorb noise generated by small scale propellers. These noise measurements were then compared to a baseline case consisting of a rigid duct without any lining. Their experimental studies revealed that the duct lined with Helmholtz resonators was capable of reducing propeller noise by 3dB compared to the duct without any lining.
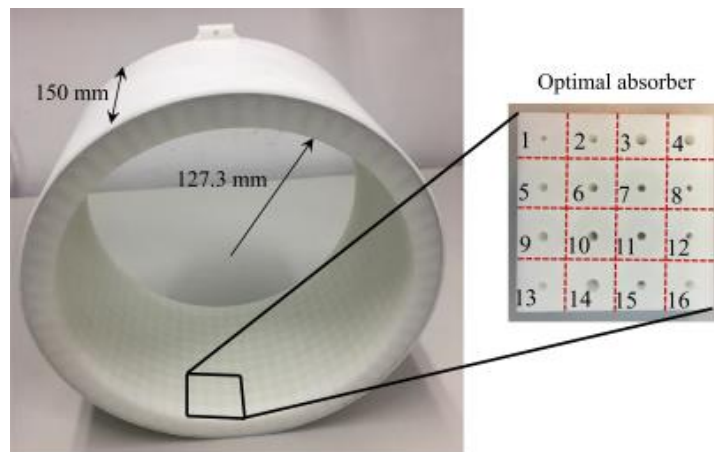
Fig. 6.6: Duct lined with multiple inhomogeneous Helmholtz resonators. [74]

Experiments were performed by Ning et al. at Iowa State University [75] to investigate the effects of trailing-edge serration width on noise reduction in UAV propellers. Studies were conducted on small UAV propellers in hover condition and

forward flight conditions at a Reynolds number of 53,000. The height of each serration was chosen to be 6 mm, which corresponds to a thickness greater than $1/4^{th}$ the boundary layer thickness at propeller's trailing-edge. This thickness is sufficient to enable trailing-edge noise reduction. Three propellers with different width to height ratios (λ/h) of 0.6, 0.9 and 1.2 was chosen for this study. Farfield noise measurements indicated that propellers with λ/h ratios of 0.6, 0.9 and 1.2 reduced noise by 0.9 dB, 1.4 dB and 1.6 dB compared to the baseline geometry. Therefore, propellers with larger serration width displayed better noise attenuation characteristics compared to propellers with smaller sized serrations.

At the same time, their studies revealed that the modified propellers continued to generate equal thrust to the baseline propeller under a constant power input.
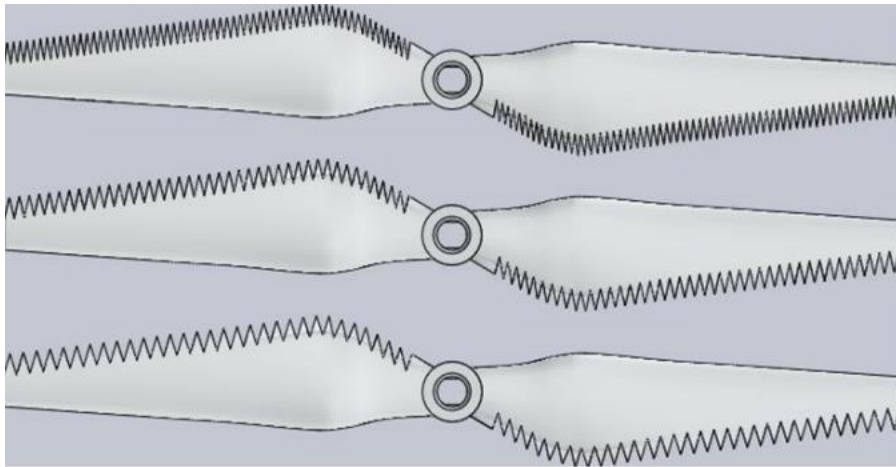
Fig. 6.7: Sawtooth trailing-edge serration with variations in width. [75]

Further experiments were conducted by Ning et al. at Iowa State University [76] to explore the performances of a bio-inspired UAV propeller based on the wings of a cicada and a maple seed, as shown in Fig. 6.8. A unique planform shape for the UAV propeller was designed, as shown in Fig. 6.9, and studied in their experiments. The bio-inspired

propeller and the baseline propeller were operated at hover flight conditions that required a thrust of 3N. Their studies revealed that the bio-inspired propeller could reduce noise up to 4 dB compared to the baseline geometry in this condition. Furthermore, Particle Image Velocimetry studies revealed that the bio-inspired propeller generated a smaller wake region and a faster decay rate of tip vortex strength was observed. Lastly, the baseline propeller and the bio-inspired propeller required the same power to generate the design thrust.

Fig. 6.8: Bio-inspiration – Cicada's wing and a maple seed [76]
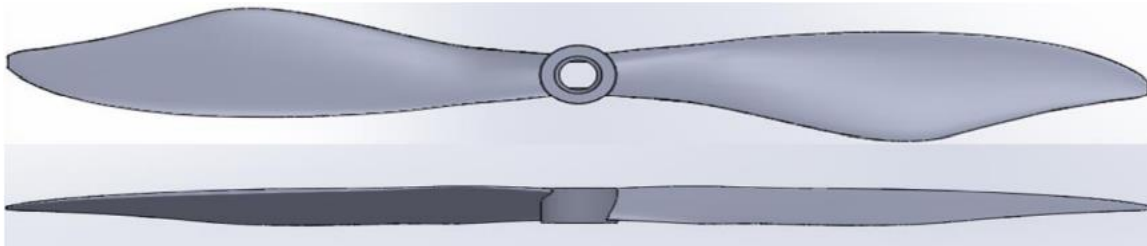
Fig. 6.9: Bio inspired UAV propeller designed at Iowa State University [76]

Experimental studies were conducted by Malgoezar et al. [77] at Delft University of Technology, Netherlands to investigate the effects of ducts around a UAV propeller, as shown in Fig. 6.10, and its effects on broadband noise. The UAV propeller was set at 95% of maximum power and noise measurements were recorded for both the case with and without the duct for two conditions. In the first condition where there was no incoming flow on the propeller, it was found that including the duct resulted in an increase in

broadband noise by almost 12 dB across the frequency range of interest. However, the harmonics were no longer visible beyond 2kHz. Whereas, for the second condition where and incoming flow impinges on the UAV propeller, the noise characteristics for the two cases were very close to each other. It was hypothesized that when airflow impinges on the UAV propeller, the turbulent structures created by the propeller could be convected with the air flow which may change the location of the noise sources.

Fig. 6.10: Effects of duct around a UAV propeller investigated at TU Delft [77]

Ben-Gida et al. from the Institute of Technology at Haifa [78] in collaboration with the Israeli Air Force performed experiments to study the effects of grit-type boundary layer trips in their ability to mitigate propeller noise at a Reynolds number of 20,000. The boundary layer trip was applied at 10% chord on both the suction surface and pressure surface of the propeller and studies were conducted to investigate the effects of grit particle size ranging from a diameter of 0.25 mm – 0.56 mm (i.e., #30-#60 grit papers) on propeller noise. Their results revealed that placement of grit-type particles increased broadband noise at high frequencies compared to the baseline measurements, with smaller grit size generating greater noise. However, a noise reduction of 2-6 dB was

151

observed for a wide range of propeller RPMs at lower frequencies, which is key to acoustic stealth applications.

Fig. 6.11: Grit-type boundary layer trip applied near leading-edge of propeller [78]

Researchers at the Institute of Turbomachinery in Lodz University, Poland [79] investigated the effects of propeller pitch on noise radiation. Experiments were performed in their anechoic test chamber, as shown in Fig. 6.12 using a KDE propeller with variable pitch.

Fig. 6.12: Noise measurements from a variable pitch propeller in the anechoic test chamber at the Institute of Turbomachinery, Poland [79]

Their studies revealed that propeller pitch has significant influence on sound pressure levels. An increase in pitch angle from 0° to 3° resulted in 4-8 dB increase in SPL. Further increase in pitch angle from 3° - 11° resulted in an additional SPL increase of 0-1.5 dB.

Like earlier studies, researchers at the University of Bristol [80] performed experiments to investigate the effects of propeller pitch angle and effects of trailing-edge serrations on radiated noise. Their study found that increase in pitch angle leads to a greater broadband and tonal noise. Inclusion of serrated trailing-edges showed that high frequency farfield noise can be effectively reduced. For a propeller rotating at 3000 rpm, a noise reduction of 3dB was observed at 3000 Hz which increased to 5 dB reduction at 10,000Hz. Similarly, for propellers rotating at 5000 rpm, a 3 dB reduction was observed at 10,000 Hz which increased to a 6 dB reduction at 20,000 Hz.

153

6.3.2. Noise mitigation studies – Helicopter rotors

Researchers from the Aeroflightdynamics Directorate, Ames Research Center [81] in collaboration with DLR Braunschweig, *Office of National E'tudes et da Researcheres Aerospatiales* (ONERA) France and NASA Langley Research Center created a comprehensive review the most severe noise source from helicopter rotor blades namely blade-vortex interaction noise and compiled various techniques explored to minimize the same. Some of the techniques include blade feathering, controllable twist, leading-edge and trailing-edge blowing, advanced center propellers and trailing-edge flaps.

Numerical studies were conducted by the Institute of Fluid-Flow Machinery, Polish Academy of Sciences [82] to explore the effects of active suction and blowing through blade tip perforations on helicopter rotor thickness noise.
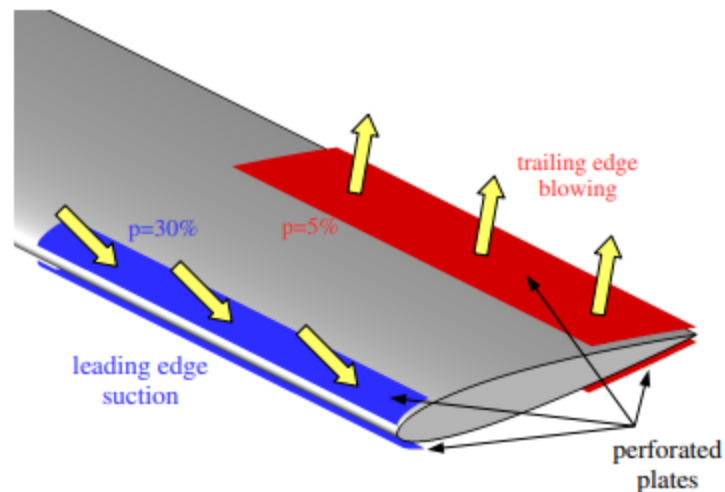
Fig. 6.13: Perforated plates near LE and TE of helicopter rotor at 80% span [82]

Four cavities were made near the leading-edge and trailing-edge of the helicopter rotor at 80% of its blade span and covered with perforated plates. Leading-edge cavities were designed for flow suction, whereas trailing-edge cavities were designed for

blowing. When this rotor was modeled at hover conditions, it was observed that the overall sound pressure level reduced by 3.4 dB with at 45% attenuation of its peak amplitude. However, this mechanism resulted negatively impacted the aerodynamic performance of the rotor with a 38% torque penalty.

Further numerical studies were conducted by Sun et al. [83] from the National Key Laboratory of Rotorcraft Aeromechanics, Nanjing University of Aeronautics and Astronautics, China to investigate the effects of jets blowing through slots provided near the leading-edge and trailing-edge of a helicopter blade, as shown in Fig. 6.14, to mitigate noise generated due to rotor blade vortex interaction. The AH-1 helicopter main rotor blade was chosen as the baseline geometry for this study and the blade vortex interaction noise was predicted through Computational Aeroacoustics analysis using a compressible RANS turbulence model and the Ffowcs Williams and Hawkings equations. Noise predictions from the baseline model were compared with that from the modified rotor blade containing slots for jet flow. It was observed that the modified blade geometry reduced sound pressure levels by 2.6 dB and the peak amplitude was attenuated by more than 30%. However, these benefits came at a cost of 9.8% loss in rotor thrust.

To root

Slot location of blowing
near leading edge

Slot location
near trailing edge of blowing

Tip

15×5 (spanwise, streamwise) cell faces

Trailing edge

Normal to the blade surface

V_{jet}

Leading edge

Slot locations on the blade surface   Slice of slot locations on the airfoil
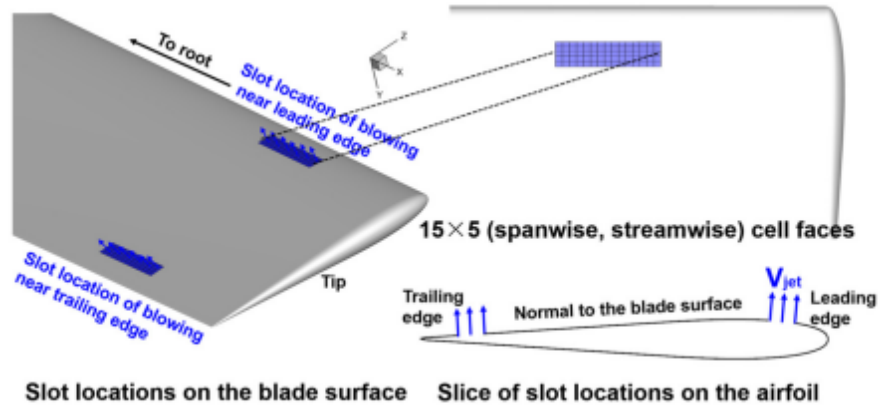
Fig. 6.14: Jet blowing through slots near LE and TE of rotor blade tip [83]

Analytical and computational studies were conducted by Chen et al. [84] at the University of Maryland, College Park to investigate the effects of active twist control of rotor on blade-vortex interaction noise.

Fairing   Spar laminate

Foam
core

Active
plies
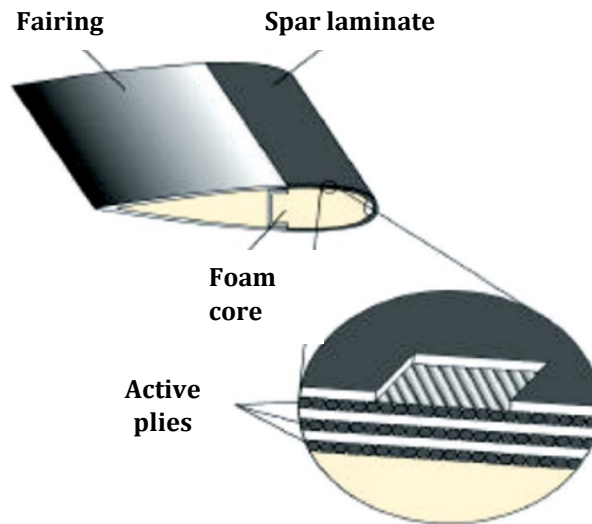
Fig. 6.15: Cross section of blade displaying actuators to control blade twist [84]

Three control points were positioned at 65%, 80% and 95% of blade span where piezoelectric fiber composites and piezoceramic fibers could be integrated into the host structure in the laminate lay-up process, as shown in Fig. 6.15. These actuators could change the twist response by 1°-2°, which would result in a linear twist distribution from

root of the blade to 65% span, a second linear twist distribution from 65%-80% span and a third twist distribution from 80%-100% span. Through active twist control, 2-4 dB BVI noise reduction was predicted for strong vortex interactions and 7-10 dB noise reduction was predicted for weaker vortex interactions.

Edwards and Cox from Bell Helicopter [85] Textron Inc. in collaboration with NASA Langley Research Center compiled various techniques to mitigate helicopter rotor noise. Two of these techniques are presented below:

6.3.2.1. *Modulated Blade Spacing*

Helicopter main rotors are typically designed with blades that are equally spaced. The noise generated by such rotors are characterized by a single blade passage frequency and its corresponding harmonics. By adjusting the angles between the blades, as shown in Fig. 6.16, it is possible to make these blades unevenly spaced. The rotor noise with such a *modulated blade spacing* is characterized by several blade-passage frequencies, one for each unique angle, and their corresponding harmonics. This helps spread the energy content in the noise across the frequency range of interest, rather than being concentrate at a single blade passage frequency.
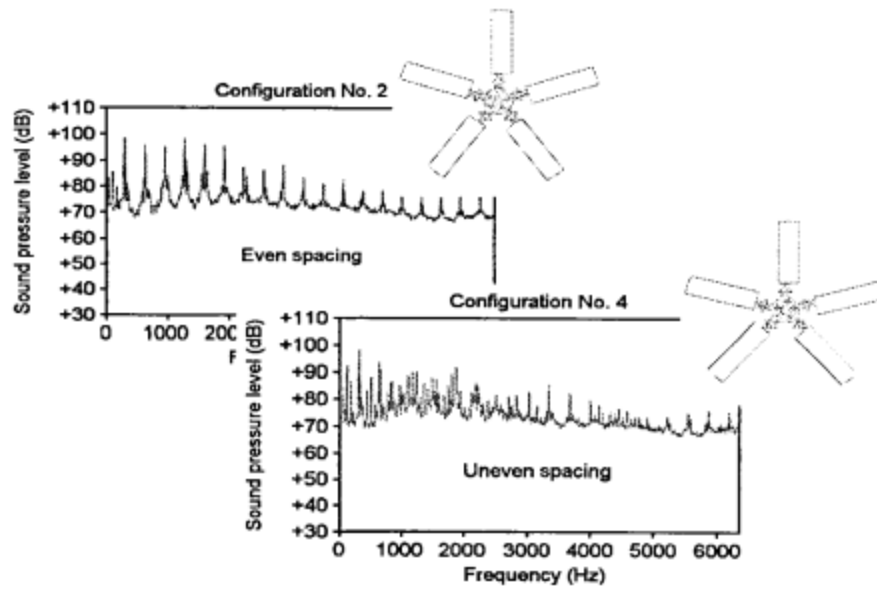
Fig. 6.16: Cross section of blade displaying actuators to control blade twist [85]

6.3.2.2.   Blade tip modifications

Various blade tip modifications, as shown in Fig. 6.17, have been developed, tested and incorporated on helicopter for their improved aerodynamics and reduced noise characteristics. Aerodynamic improvements are primarily associated with reduced drag, delay of transonic flow, reduced tip loading and tip loss.
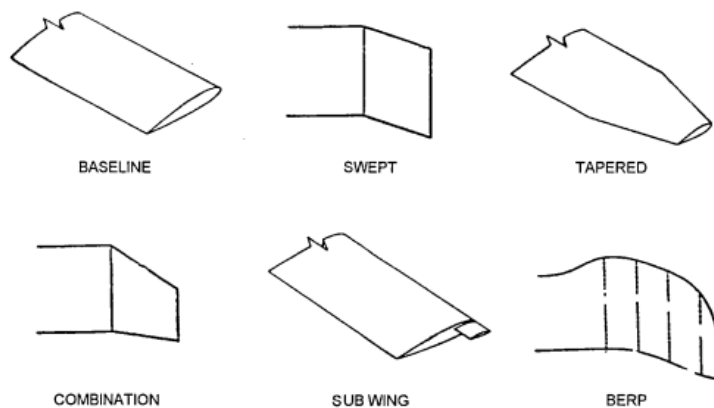
Fig. 6.17: Blade tip modifications for helicopter rotors [85]

158

Furthermore, diffusing the tip vortices through these blade modifications reduces the interaction between these vortices and the rotating blades, thus reducing blade vortex interaction noise.

Pegg et al. conducted experimental studies on a full-scale helicopter rotor at the NASA Langley Research Center to investigate the effectiveness of a turbulent blade tip air mass injection system in reducing impulsive noise (i.e., blade slap) caused by blade vortex interaction. As shown in Fig. 6.18, a convergent divergent nozzle was included inside the blade tip. The jet flow injected from this nozzle interacts with the swirl flow of the vortices generated by the blade. This flow injection system required 7% of the total power supplied to the helicopter rotor. Experimental data obtained from these studies showed that at inflight conditions, sound pressure levels of the harmonics between 100 – 500 Hz reduced by as much as 25 dB.
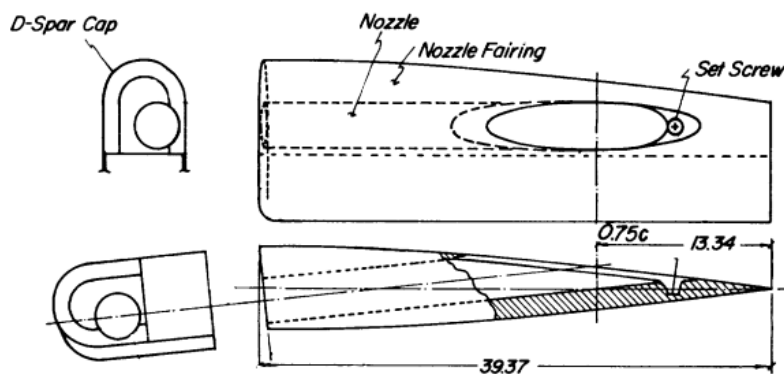
Fig. 6.18: Nozzle inside blade tip of helicopter rotor [86]

From this literature review survey, we see that the noise sources from a UAV propeller are primarily related to trailing-edge noise, noise from tip vortices, interaction between trailing-edge noise sources near the blade-tip and blade-tip vortices, noise due to laminar to turbulence transition and finally noise due to blade passing frequency and

blade tip speed. Most of the noise mitigation techniques used to address UAV propeller noise mitigation are passive flow control techniques such as trailing-edge serrations, boundary layer-trips, trailing-edge notches, propeller sizing, bio-inspired propellers and duct usage.

On the other hand, we see that noise sources from a helicopter rotor are primarily due to blade vortex interaction and blade thickness noise. Most of the noise mitigation techniques used to address helicopter rotors noise are active flow control techniques such as blade feathering, controllable twist, flow suction or blowing near leading-edges and trailing-edges, active twist control, air mass injection and trailing-edge flaps.

The use of compliant coating is a passive flow control technique that may favorably modulate the flow boundary layer and aid in mitigating turbulent boundary layer trailing-edge noise or address noise associated with laminar to turbulence transition. Based on this feasibility study, we see that compliant coating would be well suited to investigate its effects on UAV propeller noise.

6.4. Compliant coating

A compliant coating with thickness of 5 mm is prepared using silicone oil and Dow Corning Sylgard 184 by mixing the two in the ratio of 9:1 by mass [27]. Its molecular formula is polydimethylsiloxane and a structural formula $[-O-Si(CH_3)_2-]_n$ [24]. The mixture takes 48 hours to cure through room temperature vulcanization and is ready for use after 7 days [87]. A detailed step-by-step procedure on coating preparation is outlined in Appendix, Section 9.1.

Fig. 6.19: Compliant coating sheet prepared at the University of Kansas

Next, the compliant coating is applied onto the flat plate model using 30-minute epoxy resin and sand bags are used to apply pressure on the coating as it binds to the flat plate surface. A detailed step-by-step procedure on the flat plate preparation and application of coating on its surface is outlined in Appendix, Section 9.2.

Fig. 6.20: Compliant coating applied on flat plate surface

The flat plate model shown in Fig. 6.20 is mounted inside the closed loop wind tunnel at the University of Kansas and experiments were conducted at wind speed of 15 m/s. Noise measurements recorded from this plate were compared with that from a baseline flat plate model, shown in Fig. 6.21.

Fig. 6.21: Baseline flat plate

6.5. Results and Discussions

To investigate the effects of passive compliant coatings on trailing-edge noise, experiments were conducted using the closed loop wind tunnel in the Aerospace Engineering Department at the University of Kansas. Two flat plates were tested in this study. Fig. 6.22 shows a schematic diagram of the baseline flat plate model with a plate-thickness of 15 mm. Baseline farfield noise measurements are recorded from this plate.
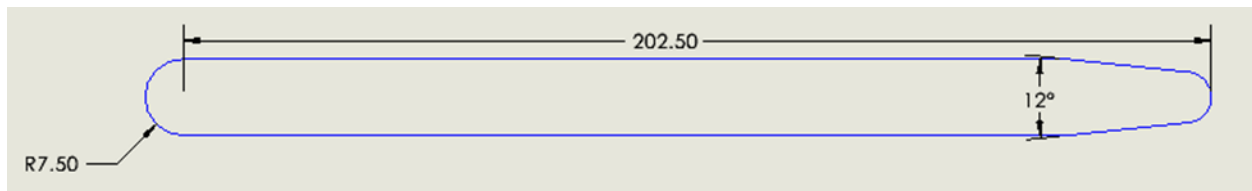
Fig. 6.22: Schematic diagram of baseline flat plate model

Similarly, Fig. 6.23 shows a schematic diagram of the flat plate model with compliant coating applied on its surface. This flat plate model has a plate thickness of 5 mm and a coating of thickness 5 mm is wrapped around this plate. Therefore, the total plate thickness is 15 mm and has the same outer profile as the baseline flat plate model.
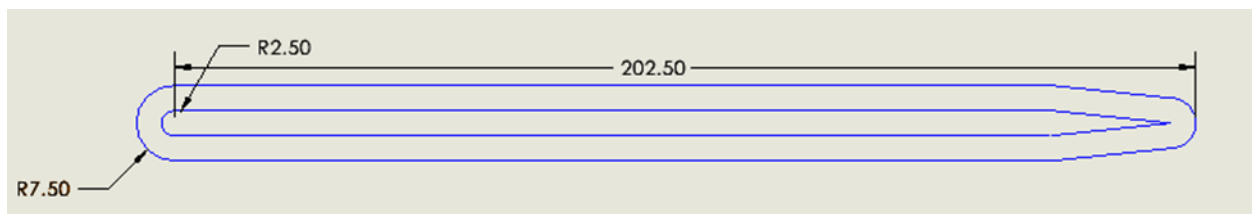
Fig. 6.23: Schematic diagram of compliant coating applied on flat plate

The farfield noise measurements from this plate is compared with the baseline flat plate model to understand the effects of passive compliant coating on trailing-edge noise. Experimental results obtained from this study are presented in this section, as follows:

6.5.1. *Noise data collection and microphone calibration*

To perform noise measurements in this study, noise data was collected at the rate of 5×10^{-5}s for a time period of 20s using a microphone from PCB Piezotronics (microphone model: 378A06) and data is recorded using LabVIEW. A total of 400,000 data points was recorded for each trial. Out of these data samples, 2^{18} data samples (i.e., 262,144 data samples) were used to perform Fast Fourier Transform. Choosing this sample size helps minimize the time required by an in-house code developed at KUAE to post-process noise data faster by taking lesser time to compute the coefficients in the Fourier series.

Firstly, the microphone was calibrated using the pistonphone calibrator using the procedure outlined in Appendix, Section 9.3. The multiplication factor in LabVIEW was adjusted accordingly until the Sound Pressure Level at a frequency of 1000 Hz was close to 94 dB. After calibration, the microphone measured an SPL of 93.988 dB at 1000 Hz, as shown in Fig. 6.23.
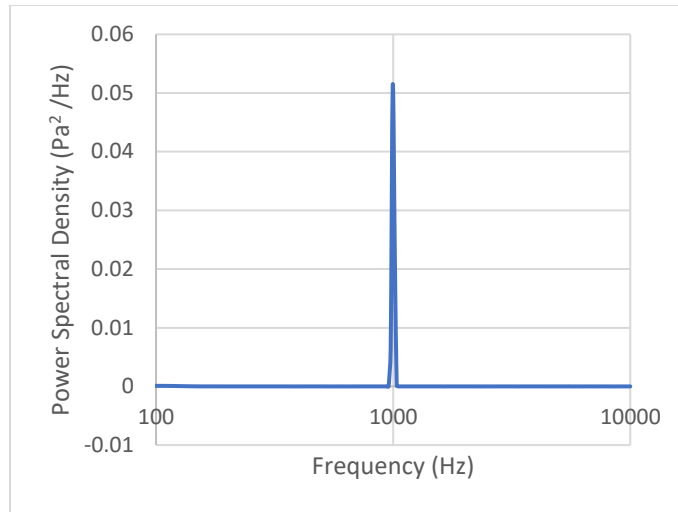
Fig. 6.24: Microphone calibration – Power Spectral Density

Fig. 6.22 illustrates a single tone of Power Spectral Density (Pa²/Hz) produced at 1000 Hz. The same pressure fluctuation data represented as SPL (dB) is shown in Fig. 6.23 and the tonal peak at 1000 Hz was adjusted accordingly using a multiplication factor until it was close to 94 dB.
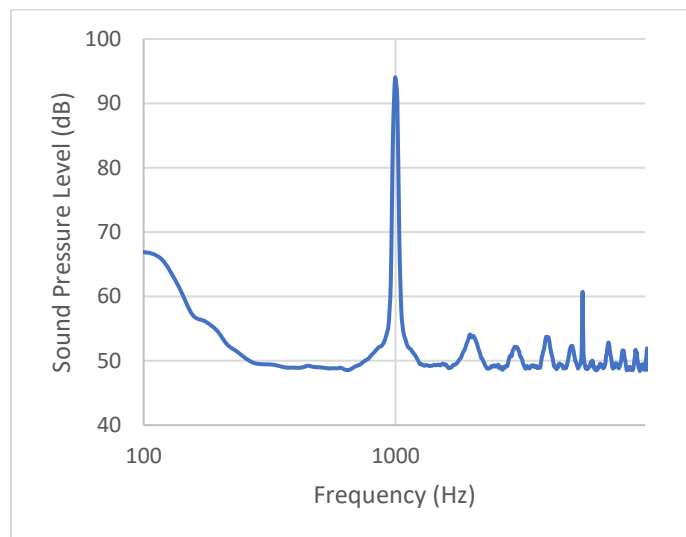
Fig. 6.25: Microphone calibration – Sound Pressure Level

6.5.2. Background Noise measurements

After calibration, the microphone was inserted into the wind tunnel test section through an opening present in the roof of the test section, which corresponds to a location that is 26" downstream of the baseline flat-plate's trailing-edge and 21" above its trailing-edge. More details regarding the choice of microphone location is provided in Section 6.8.

Initially, background noise was measured inside the wind tunnel at wind speed of 15 m/s when no acoustic liners were applied on to the test section walls. After this, acoustic liners were applied on four sides of the wind tunnel test section as seen in Fig. 6.24 and background noise measurements were recorded with acoustic liners for 4 trials. Multiple trials were performed to check for repeatability of data-sets.
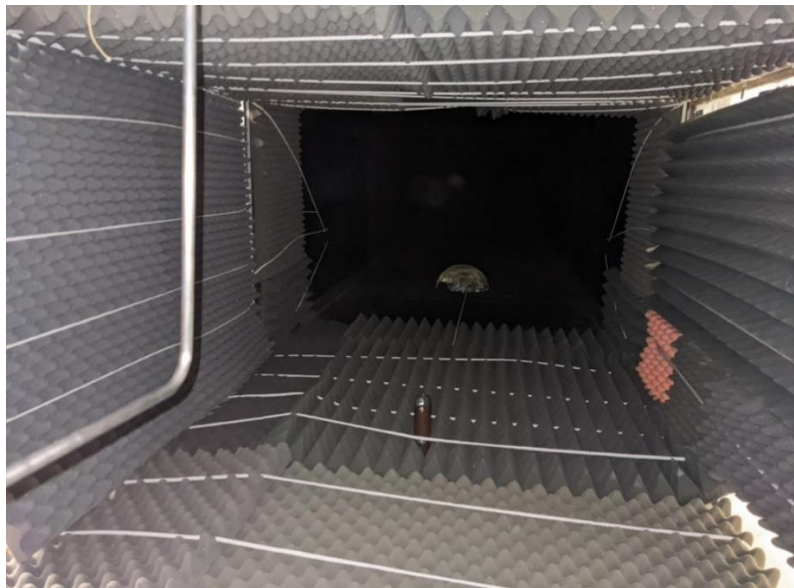
Fig. 6.26: Acoustic liners applied inside wind tunnel test section
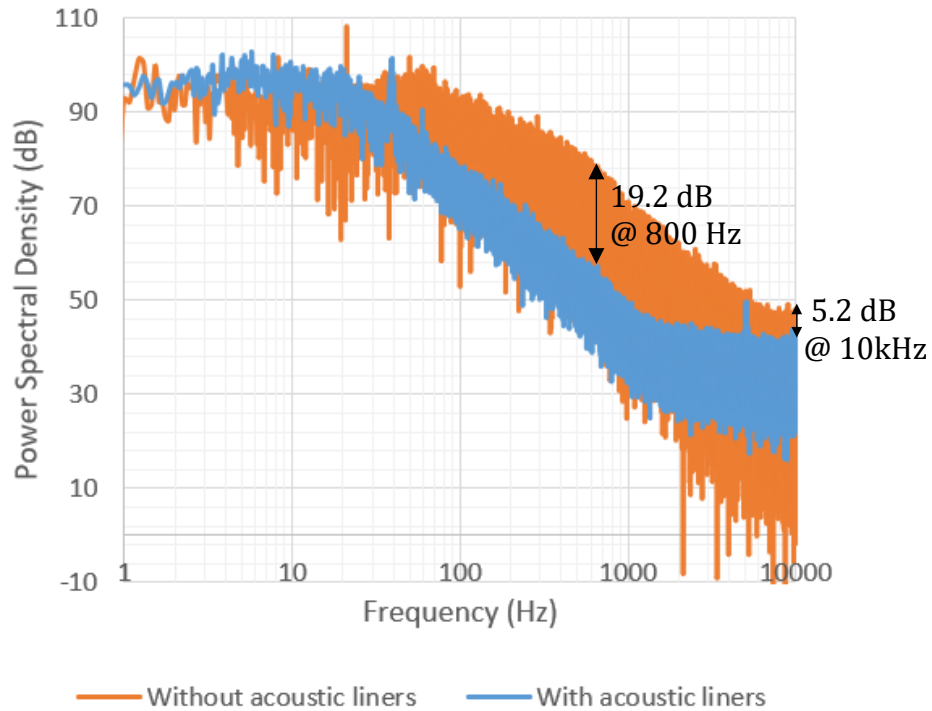
Fig. 6.27: Effects of acoustic liners at wind speed of 15 m/s

Fig. 6.27 demonstrates that application of acoustic liners on wind tunnel walls help reduce the background noise by 5.2-19.2 dB for a frequency range from 30 – 10,00 Hz, when acoustic liners were applied inside the wind tunnel test section. Considering the benefits of acoustic liners, further noise measurements shall be recorded retaining acoustic liners inside the wind tunnel test section.

6.5.3. *Trailing-edge noise dominant in microphone measurements*

Experiments were performed by Moreau et al. [48] in an anechoic wind tunnel at the University of Adelaide on a flat plate in fully turbulent flow at wind speeds from 15-38 m/s. Several microphones were used in this study, as shown in Fig. 6.28, with all microphone oriented at 90° with respect to the flow. These microphones were used to record noise emanating from different parts of the flat-plate such as its leading-edge and

trailing-edge to identify the dominant noise source. The cross-correlation of noise from the top TE microphone and top LE microphone were analyzed.
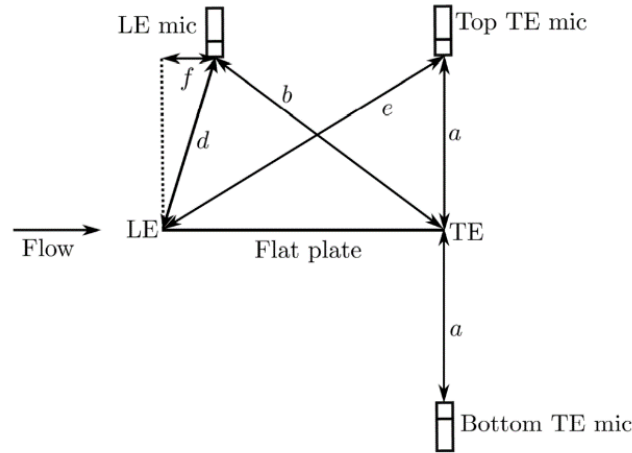
Fig. 6.28: LE and TE microphones to record farfield noise [48]

The time delay of sound radiated from the leading-edge to the LE mic and Top TE mic was estimated and compared with the time delay of sound radiated from the trailing-edge to the LE mic and Top TE mic. It was observed that the magnitude of cross-correlation function, Δt_{TE} was much greater than Δt_{LE}, which indicated that trailing-edge noise dominates the farfield noise spectra. The present study uses the same flat plate dimensions for experimentation. Based on studies conducted by Moreau et al., it can be inferred that the farfield acoustic spectra recorded by microphones in the present study would be dominated by trailing-edge noise.

6.5.4. *Effects of compliant coating on trailing-edge noise*

Similar to background noise measurements performed in the present study, the microphone was located on the roof of the wind tunnel, 26" downstream of the flat plate's trailing-edge and 21" above the trailing-edge, where an opening is present in the wind

tunnel test section. The microphone was oriented 90° with respect to the incoming flow, as shown in Fig. 6.29.
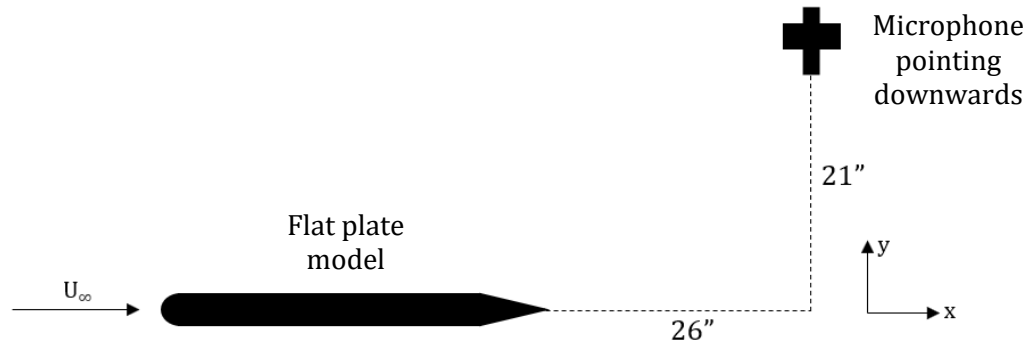
Fig. 6.29: Microphone location with respect to trailing-edge of flat plate

The choice of microphone location was based on experimental studies conducted by Moreau et al. [48], who placed their microphone 585 mm (or 23 inches) above the trailing-edge. The microphone location which is closest that used by Moreau et al. is an opening on the roof of the closed loop wind tunnel test section at KUAE. This is located 26" downstream of the trailing-edge and hence is chosen for our study.

Similarly, the choice of microphone orientation is also based on experimental studies conducted by Moreau et al. [48] and other studies where noise measurements were recorded 90° with respect to the flow. This orientation records a reliable noise data and doesn't record stray fluctuations from other noise sources.

The baseline flat plate model and the flat plate with compliant coating applied on its surface are placed inside the test section, as seen in Fig. 6.30 and Fig. 6.31. Noise measurements were recorded for four trials in each case to check for repeatability of data-sets.

168

Fig. 6.30: Baseline flat plate inside wind tunnel test section

Fig. 6.31: Flat plate with compliant coating inside wind tunnel test section
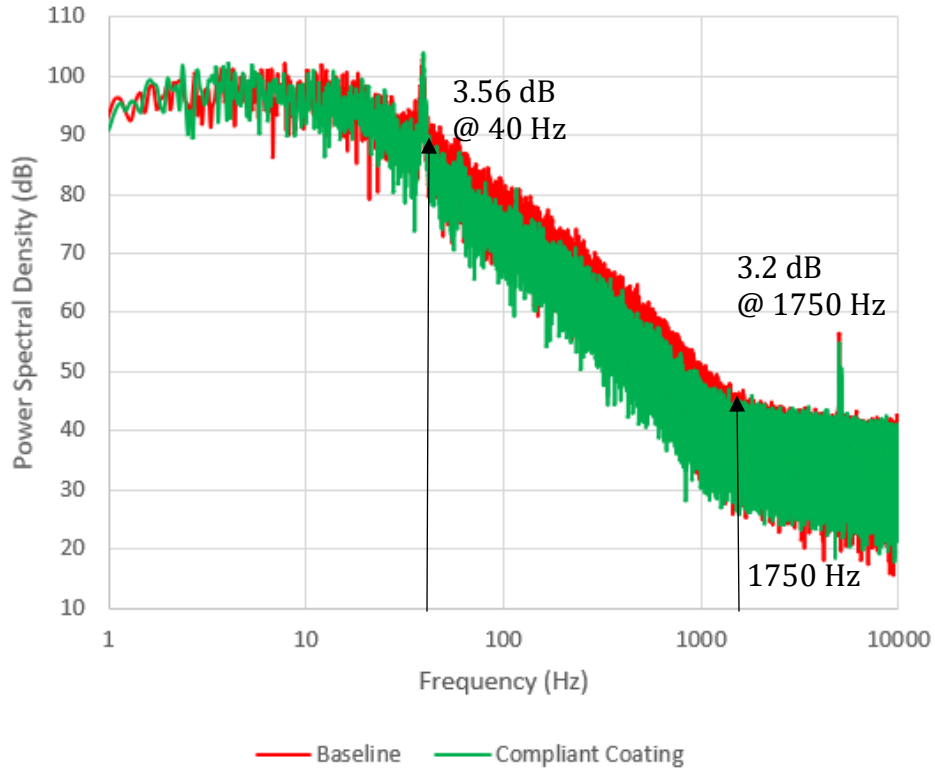
Fig. 6.32: Effects of compliant coating on trailing-edge noise

As seen in Fig. 6.32, it was observed that using the compliant coating on the flat plate model reduced farfield noise by 3 dB for a frequency range from 40 Hz – 1750 Hz. Farfield noise reduced by 3.56 dB at 40 Hz, 3.2 dB at 1750 Hz and a maximum reduction of 5.11 dB was observed at 475 Hz. Furthermore, for a frequency range from 1-40 Hz and from 1750 – 10,000 Hz, the coating had negligible effects on noise measurements compared to the baseline.

6.6. Conclusions

Experiments were conducted in the closed loop wind tunnel in the Aerospace Engineering Department at the University of Kansas at a wind speed of 15 m/s to investigate the effects of passive compliant coatings on trailing-edge noise. The use of acoustic liners on wind tunnel test section aided in significantly reducing the background

noise from 30 Hz – 10,000 Hz. Therefore, further noise measurements were recorded retaining the acoustic liners inside the wind tunnel test section.

Application of compliant coating on the flat plate model reduced farfield noise by 3 dB for a frequency range from 40 Hz – 1750 Hz. Farfield noise reduced by 3.56 dB at 40 Hz, 3.2 dB at 1750 Hz and a maximum reduction of 5.11 dB was observed at 475 Hz. However, for a frequency range from 1-40 Hz and from 1750 – 10,000 Hz, the coating had negligible effects on noise measurements compared to the baseline.

Based on these experiments, it is recommended that this research may be extended to investigate the effects of compliant coatings on propellers of Unmanned Aerial Vehicles. The effects of compliant coatings on laminar to turbulence transition and noise characteristics in this regime may also be explored. More details on recommendations for future study are included in Chapter 7.

7. RECOMMENDATIONS FOR FUTURE STUDY

Compliant coatings offer passive flow control to favorably modulate the flow boundary layer and has shown its potential in mitigating trailing-edge noise. This technique would be well suited for UAV applications. This is because most of the noise mitigation techniques [70-80] explored previously for UAV applications employ passive flow control and address the same noise sources as compliant coatings. Furthermore, the effects of compliant coatings on laminar to turbulence transition and noise characteristics in this regime may also be explored. More details on these recommendations are included in this chapter.

7.1. Effects of compliant coatings on UAV propeller noise

To investigate the effects of passive compliant coatings on propellers of unmanned aerial vehicles, the research problem can be addressed through the following steps:

7.1.1. Computational Fluid Dynamics on UAV Propellers

A research study was conducted by Kutty et al. [88] to perform 3D CFD simulations on a UAV propeller to predict its aerodynamic characteristics. Aerodynamic characteristics obtained from these simulations were validated through experimentation. Fig. 7.1 shows the distribution of pressure on the surface of a UAV propeller performed by Kutty et al. to illustrate a typical CFD analysis that can be performed on a UAV propeller.
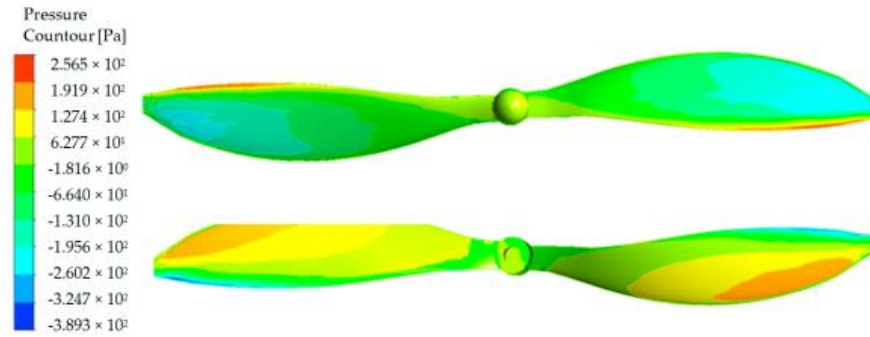
Fig. 7.1: Pressure contour distribution around a UAV propeller [88]

A similar research methodology can be adopted to initially perform steady CFD analysis on a UAV propeller to accurately predict the flowfield around its geometry. Aerodynamic characteristics such as pressure distribution at different sections of the blade along with torque and thrust generated by the propeller at different RPMs can be predicted through simulations. The flowfield information predicted in this can be validated through experiments performed on an electric motor test stand and record the thrust and torque measurements at the desired RPM.

7.1.2. *Computational Aeroacoustics Analysis*

Using accurate flowfield predicted through CFD analysis, unsteady CFD simulation and Computational Aeroacoustics Analysis can be performed using the Ffowcs Williams and Hawkings model to predict farfield noise radiated by the propeller. Experiments were conducted by the Institute of Turbomachinery at Lodz University, Poland [79] to record noise measurements radiated from a *KDE* propeller which has a diameter, d=15.5". Four microphones were radially placed at R=1m away from the propeller at 0°, 30°, 60° and 90°, as shown in Fig. 7.2 to record farfield noise measurements.

Fig. 7.2: Noise measurements from a KDE propeller in the anechoic test chamber at the Institute of Turbomachinery, Poland [79]

Similarly, four point-receivers can be placed at a distance of R/d = 2.54 and farfield noise measurements can be predicted through Computational Aeroacoustics Analysis. Furthermore, to simulate the effects of compliant coating on UAV propellers *Fluid Structure Interaction* technique can be employed. Farfield noise predicted from this analysis can be compared with the baseline noise predictions to understand the effects of compliant coatings on propeller noise characteristics.

7.1.3.   Noise measurements in the anechoic chamber

Experiments can be conducted on the same UAV propeller model used in Sections 7.1.1-7.1.3 to record farfield noise radiated from this propeller in an anechoic test chamber, as shown in Fig. 7.3. These measurements would form the baseline data to be used for comparison.
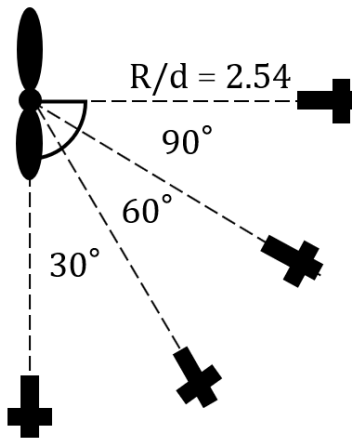
Fig. 7.3: Noise measurements from UAV propeller

To apply compliant coating on a UAV propeller, a suitable mold has to be created. A schematic diagram of an enclosed mold as shown in Fig. 7.4. A base propeller model is placed inside a cavity present inside the mold. The shape and size of the cavity would be determined by the coating thickness to be applied on the base propeller.
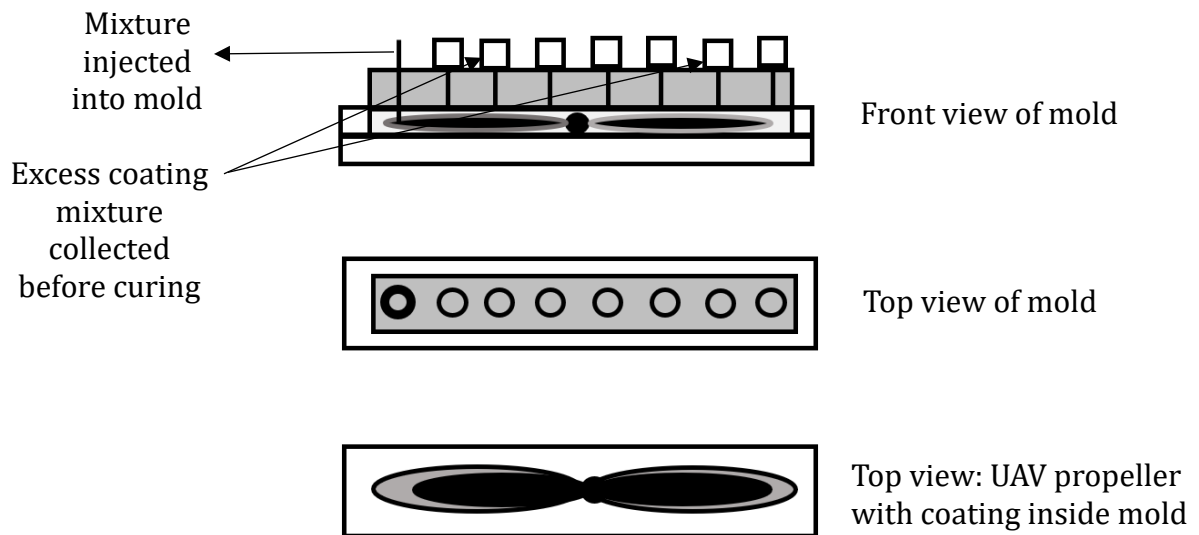
Fig. 7.4: UAV propeller with compliant coating prepared inside a mold

When the propeller is enclosed inside the mold as shown in Fig. 7.4, the coating mixture can be injected into the mold from the opening on its left, as seen in the *front view of the mold* in Fig. 7.4. Once the cavity containing the base propeller is filled with the

175

coating mixture, the excess coating mixture can be collected in containers located on top of the mold, before curing. After 48 hours of curing time at room temperature, the UAV propeller with compliant coating applied on its surface would be prepared.

Similar to baseline noise measurements, experiments can be conducted on the propeller with compliant coating applied on its surface and noise measurements can be recorded at the four microphone locations shown in Fig. 7.3. These noise measurements can be compared with the baseline case to understand the effects of compliant coatings on UAV propeller noise.

7.2. Addressing scalability of compliant coating usage to mitigate propeller noise

When extending this research to propellers used in different applications, a key aspect to consider is the scalability of this technique and to identify a range of propeller sizes and operating speeds where compliant coatings may be effective. There are two plausible factors that may influence the scalability of compliant coating usage to mitigate propeller noise for a given rotational speed:

7.2.1. Compliant coating thickness (t)

The compliant coating is only effective when it has sufficient thickness to experience a level of deformation at the frequencies of interest that allows it to absorb energy from the flow boundary layer, which enables noise mitigation. When compliant coating is applied on the surface of a propeller, the coating thickness must be scaled accordingly based on the propeller dimensions. For propellers with very small sizes, the corresponding coating thickness may be too small to experience the necessary deformation to produce significant energy absorption and hence may not be effective.

Therefore, further research may be conducted to understand the relationship between coating thickness and propeller size and identify a minimum propeller size and its corresponding coating thickness up to which compliant coatings may display their noise mitigation characteristics.

7.2.2. Wavelength of pressure fluctuations versus propeller chord-length (λ/c)

Furthermore, the effectiveness of compliant coatings might be dependent on the relationship of the wavelength of pressure fluctuations (λ) associated with noise sources present within the flow boundary and the propeller chord-length (c). With decrease in propeller size, the effectiveness of the coating may decrease. Furthermore, the coating may not show any desirable effects in noise mitigation when the wavelength of pressure fluctuations is comparable to the chord-length dimensions, i.e. $\lambda \sim c$. This factor would also limit the effectiveness of the compliant coating to a minimum propeller size (c) based on its λ/c ratio. Therefore, further research may be conducted to investigate the relationship between the wavelength of pressure fluctuations (λ) associated with noise sources present within the flow boundary layer and propeller chord length to identify a minimum propeller size up to which compliant coatings may display their noise mitigation characteristics.

7.3.   Effects of compliant coatings on laminar to turbulence transition

Compliant coatings have also shown their ability to delay transition of boundary layer from laminar to turbulent flow. The natural transition of boundary layer over a flat plate from laminar to turbulence is shown in Fig. 7.5 (from F.M. White) [89].
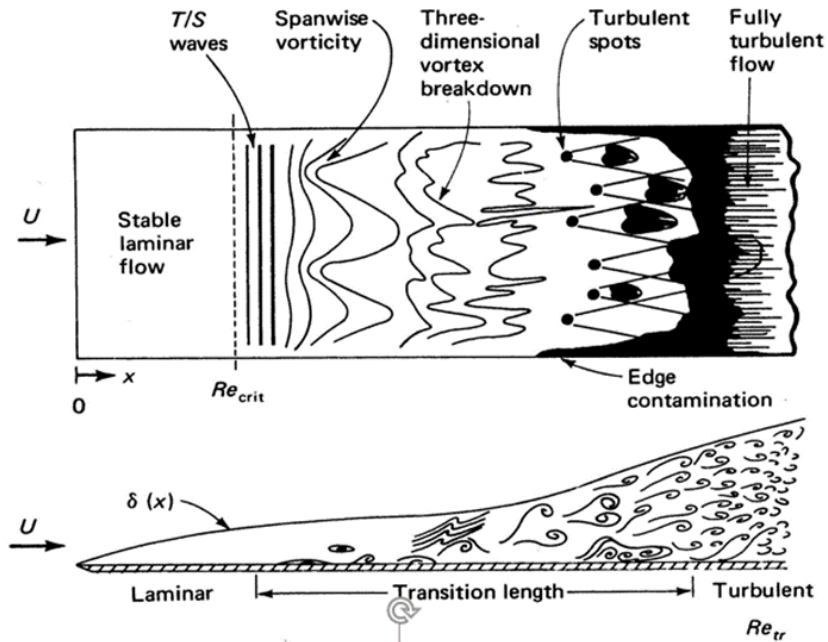
Fig. 7.5: Natural transition of boundary layer from laminar to turbulence [89]
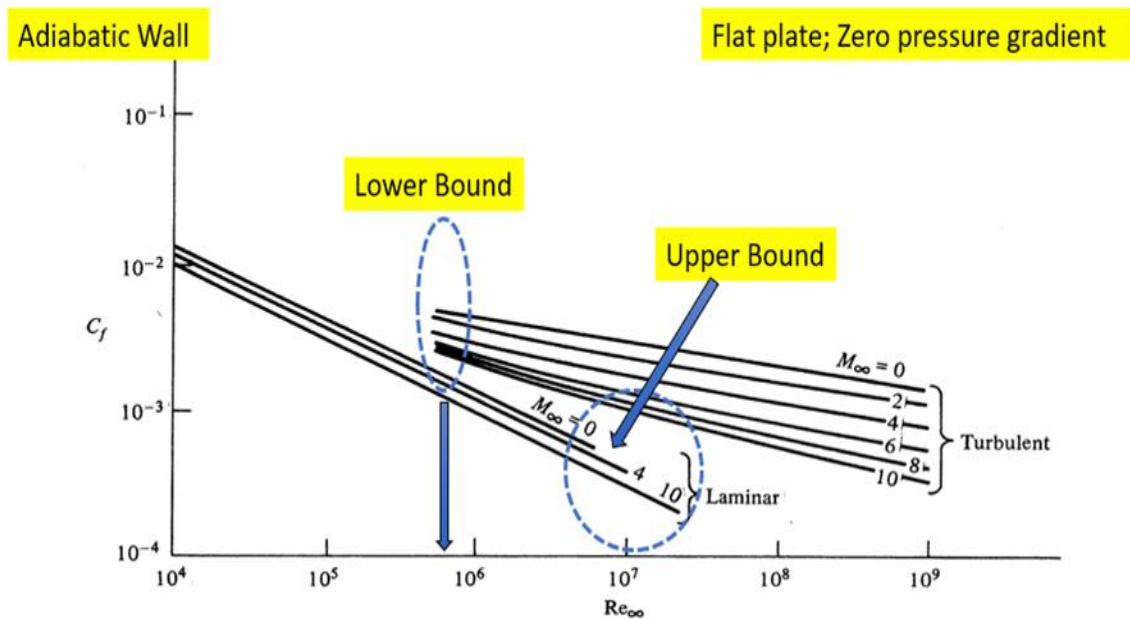
Fig. 7.6: Skin friction coefficient VS Chord based Reynolds number [90]

As shown in Fig. 7.6, there is a range of chord-based Reynolds number where the laminar to turbulence transition takes place within the flow boundary layer. Introduction of complaint coating, as shown in Fig. 7.7, has the potential to delay this transition point and extended the laminar boundary region. Compliant coatings would also help reduce

the strength of Tollmien-Schlichting (TS) instability waves within the transition region [27], which in turn delays transition to turbulence.
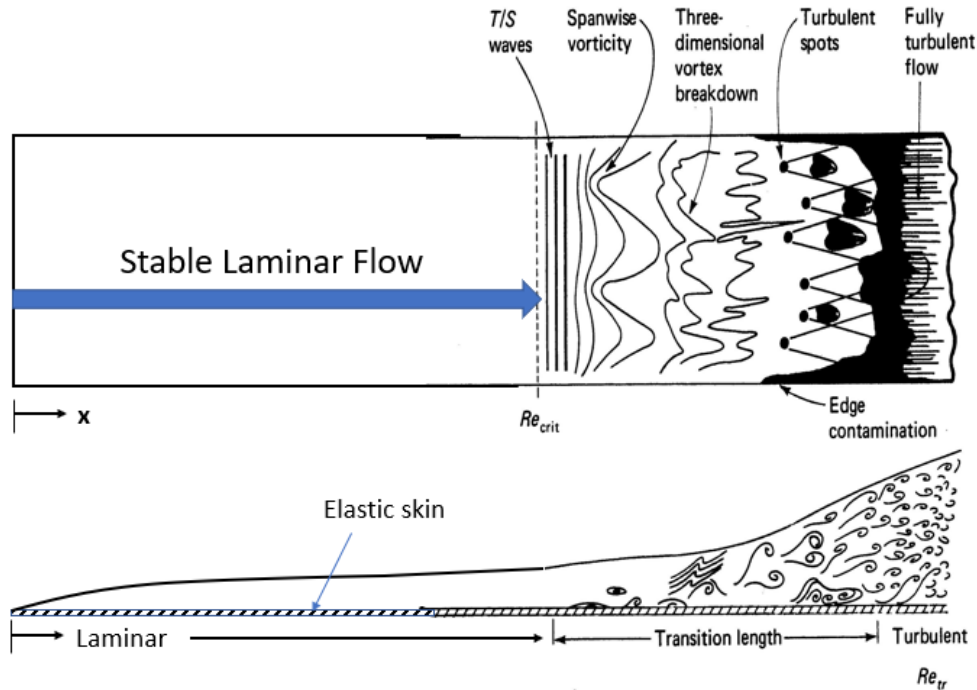
Fig. 7.7: Effect of compliant coating on laminar to turbulence transition within boundary layer (From S. Farokhi)

7.3.1. CFD Simulations

To study the effects of compliant coatings and its ability to delay laminar to turbulence transition would require accurate flow prediction in the transition region. According to the transition and linear stability theory, a relationship exists between the amplification rate 'N' and the unstable disturbances present within the Tollmien-Schlichting instabilities. The amplification rate depends on pressure gradient, freestream turbulence and transition point. This approach is called the e^N-method [90, 91].

As shown in Fig. 7.8, the local skin friction coefficient obtained using the sophisticated e^N-method shows very high accuracy in predicting the transition characteristics within the flow boundary layer.
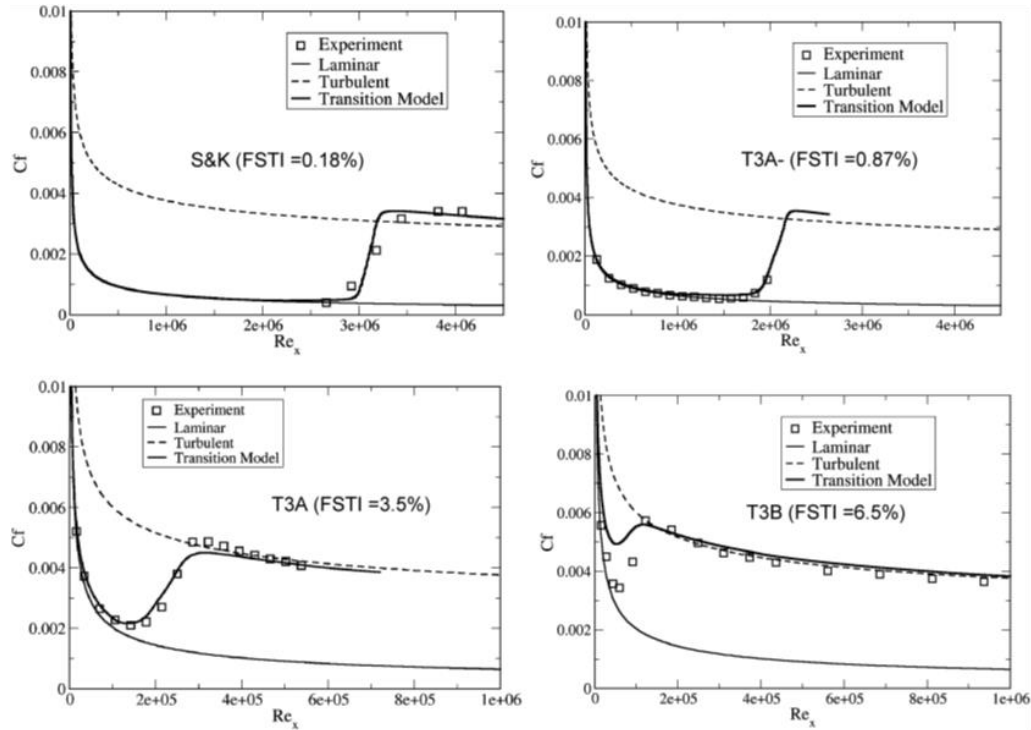
Fig. 7.8: Prediction of transition characteristics within flow boundary layer [90, 91]

This transition-turbulence model can be used in CFD analysis to simulate laminar to turbulence transition and study the favorable effects compliant coating in reducing drag and mitigating flow-induced noise.

7.3.2. Experimental studies

This transition-turbulence model can be used in CFD analysis to simulate laminar to turbulence transition and study the favorable effects compliant coating in reducing drag and mitigating flow-induced noise.

Effects of passive compliant coatings on laminar to turbulence transition may also be investigated through experimental studies and flow visualization techniques. Flow visualization techniques can be used to study and understand the extent to which the laminar to turbulence transition point gets delayed within the flow boundary layer and correlate these behaviors with farfield noise measurements. This research may also be extended from flat plate geometry to airfoil profiles used in various rotor applications. National Renewable Energy Laboratory has performed extensive research on various wind turbine airfoils and have recorded a wealth of experimental data. These measurements include aerodynamic characteristics such as pressure distribution, lift coefficient and drag coefficient and various angles of attack [92] and their corresponding farfield noise measurements [93]. The experimental data-sets, flow conditions and results obtained from this study may be used as baseline for comparison in future studies.

8. REFERENCES

[1] "Clean Power Facts and Statistics." American Clean Power Association. Accessed April 21, 2021: https://cleanpower.org/facts/

[2] Oerlemans, S., Fisher, M., Maeder, T., and Kögler. K. "Reduction of Wind Turbine Noise Using Optimized Airfoils and Trailing-Edge Serrations." *AIAA Journal*, Vol. 47, No. 6 (2009): 1470–81.

[3] Oerlemans, S. "Reduction of Wind Turbine Noise Using Blade Trailing Edge Devices." *22nd AIAA/CEAS Aeroacoustics Conference*, May 30-June 1, 2016.

[4] Seltenrich, N. "Wind Turbines: A Different Breed of Noise?" *Environmental Health Perspectives,* Vol. 122, No. 1 (2014).

[5] Shepherd, D., Welch, D., Hill, E., McBride, D., and Dirks, K. "Evaluating the Impact of Wind Turbine Noise on Health-related Quality of Life." *Noise and Health,* Vol. 13, No. 54 (2011): 333.

[6] Howe, M. S. "Noise Produced by a Sawtooth Trailing Edge." *The Journal of the Acoustical Society of America*, Vol. 90, No. 1 (1991): 482–87.

[7] Moreau, D. J., and Doolan. C.J. "Noise-Reduction Mechanism of a Flat-Plate Serrated Trailing Edge." *AIAA Journal,* Vol. 51, No. 10 (2013): 2513–22.

[8] Avallone, F., Van Der Velden, W. C. P, Ragni, D., and Casalino, D. "Noise Reduction Mechanisms of Sawtooth and Combed-Sawtooth Trailing-Edge Serrations." *Journal of Fluid Mechanics*, Vol. 848 (August 2018): 560–91.

[9] Avallone, F., Van Der Velden, W. C. P., and Ragni, D. "Benefits of Curved Serrations on Broadband Trailing-Edge Noise Reduction." *Journal of Sound and Vibration,* Vol. 400 (2017): 167–77.

[10]   Finez, A., Jacob, M., Jondeau, E., and Roger, M. "Broadband Noise Reduction with Trailing Edge Brushes." *16th AIAA/CEAS Aeroacoustics Conference*, June 7-9, 2010.

[11]   Herr, M., and Dobrzynski, W. "Experimental Investigations in Low-Noise Trailing Edge Design." *AIAA Journal*, Vol. 43, No. 6 (2005): 1167–75.

[12]   Geyer, T., Sarradj, E., and Fritzsche, C. "Measurement of the Noise Generation at the Trailing Edge of Porous Airfoils." *Experiments in Fluids,* Vol. 48, No. 2 (2009): 291–308.

[13]   Koh, S. R., Zhou, B. Y., Meinke, M., Gauger, N., and Schröder, W. "Numerical Analysis of the Impact of Variable Porosity on Trailing-Edge Noise." *Computers & Fluids,* Vol. 167 (2018): 66–81.

[14]   Zhou, B. Y., Koh, S. R., Gauger, N. R., Meinke, M., and Schöder, W. "A Discrete Adjoint Framework for Trailing-Edge Noise Minimization via Porous Material." *Computers & Fluids*, Vol. 172 (2018): 97–108.

[15]   Clark, I. A., Alexander, W. N., Devenport, W., Glegg, S., Jaworski, J. W., Daly, C., and Peake, N. "Bioinspired Trailing-Edge Noise Control." *AIAA Journal*, Vol. 55, No. 3 (2017): 740–54.

[16]   Afshari, A., Dehghan, A. A., and Azarpeyvand, M., "Novel Three-Dimensional Surface Treatments for Trailing-Edge Noise Reduction." *AIAA Journal*, Vol. 57, No. 10 (2019): 4527–35.

[17]   Szőke, M., Fiscaletti, D., and Azarpeyvand, M., "Effect of Inclined Transverse Jets on Trailing-Edge Noise Generation." *Physics of Fluids,* Vol. 30, No. 8 (2018): 085110.

[18]   Wolf, A., Lutz, T., Würz, W., Krämer, E., Stalnov, O., and Seifert, A. "Trailing Edge Noise Reduction of Wind Turbine Blades by Active Flow Control." *Wind Energy,* Vol. 18, No. 5 (2014): 909–23.

[19]   Arnold, B., Lutz, T., and Krämer, E. "Design of a Boundary-Layer Suction System for Turbulent Trailing-Edge Noise Reduction of Wind Turbines." *Renewable Energy,* Vol. 123 (2018): 249–62.

[20]   Arnold, B., Lutz, T., Krämer, E., and Rautmann, C. "Wind-Turbine Trailing-Edge Noise Reduction by Means of Boundary-Layer Suction." *AIAA Journal,* Vol. 56, No. 5 (2018): 1843–54.

[21]   Fitzgerald, J. W., Fitzgerald, E. R., Carey, W. M. and Winkle, W. A. "Blubber and compliant coatings for drag reduction in water II. Matched shear impedance for compliant layer drag reduction." *Materials Science and Engineering: C 2,* Vol. 4, (1995): 215-220.

[22]   Gad-el-Hak, M. "Compliant Coatings for Drag Reduction." *Progress in Aerospace Sciences,* Vol. 38, No. 1 (2002): 77–99.

[23]   Carpenter, P.W., Lucey, A. D. and Davies, C. "Progress on the Use of Compliant Walls for Laminar-Flow control." *Journal of Aircraft,* Vol. 38, No. 3 (2001): 504-512.

[24]   Boiko, A. V., Kulik, V. M., Chun, H. and Lee, I. "Verification of drag-reduction capabilities of stiff compliant coatings in air flow at moderate speeds." *International Journal of Naval Architecture and Ocean Engineering,* Vol. 3, No. 4 (2011): 242-253.

[25]   Moreau, D. J., Brooks, L. A., and Doolan, C. J., "Broadband Trailing Edge Noise from a Sharp-edged Strut." *The Journal of the Acoustical Society of America,* Vol. 129, No. 5 (2011): 2820-829.

[26]   Lee, T., Fisher, M. and Schwarz, W. H. "Investigation of the stable interaction of a passive compliant surface with a turbulent boundary layer." *Journal of Fluid Mechanics,* Vol. 257, No. 373. (1993).

[27]   Lee, T., Fisher, M., and Schwarz, W.H., "Investigation of the effects of a compliant surface on boundary-layer stability." *Journal of Fluid Mechanics,* Vol. 288 (1995): 37-58.

[28]   Khanafer, K., Duprey, A., Schlicht, M., and Berguer, R. "Effects of strain rate, mixing ratio, and stress-strain definition on the mechanical behavior of the polydimethylsiloxane (PDMS) material as related to its biological applications." *Biomedical Microdevices,* Vol. 11, No. 2 (2008): 503-508.

[29]   Dogru, S., Aksoy, B., Bayraktar, H., and Alaca, B. E. "Poisson's ratio of PDMS thin films." *Polymer Testing,* Vol. 69 (2018): 375-384.

[30]   Folch, A. "Introduction to BioMEMS", CRC Press. (2016).

[31]   Brungart, T. A., Olson, S. T., Kline, B. L., and Yoas, Z. W. "The reduction of Quadcopter Propeller Noise." *Noise Control Engineering Journal,* Vol. 67, No. 4 (2019): 252-269.

[32]   Kramer, M. O. "Boundary-Layer Stabilization by Distributed Damping." *Journal of the Aerospace Sciences,* Vol. 27, No. 1 (1960): 69-69.

[33]   Pureyar, F. W. "Boundary layer control: drag reduction by use of compliant coatings." *David Taylor Model Basin Washington DC*: (1962). Accession Number: AD0292933.

[34]   Carpenter, P. W. and Garrad, A. D. "The hydrodynamic stability of flow over Kramer-type compliant surfaces. Part 1. Tollmien-Schlichting instabilities." *Journal of Fluid Mechanics,* Vol. 155, No. 465 (1985).

[35]   Davies, C. and Carpenter, P. W. "Numerical simulation of the evolution of Tollmien–Schlichting waves over finite compliant panels." *Journal of Fluid Mechanics,* Vol. 335 (1997): 361-392.

[36]   Benjamin T.B. "Fluid flow with flexible boundaries." *In: Görtler H. (eds) Applied Mechanics.* Springer, Berlin, Heidelberg: (1966).

[37]   Blick, E. F. and Walters, R. R. "Turbulent boundary-layer characteristics of compliant surfaces." *Journal of Aircraft,* Vol. 5*,* No. 1 (1968): 11-16.

[38]   Blick, E. F. and Chu, H. H. "Compliant surface drag as a function of speed." *Journal of Spacecraft and Rockets,* Vol. 6,   No*.* 6. (1969): 763-764.

[39]   Bushnell, D. M., Hefner, J. N. and Ash, R. L. "Effect of compliant wall motion on turbulent boundary layers." *Physics of Fluids,* Vol. 20*,* No. 10. (1977).

[40]   Choi, K.S., Yang, X., Clayton, B., Glover, E., Atlar, M., Semenov, B. and Kulik, V. "Turbulent Drag Reduction Using Compliant Coatings." *Proceedings: Mathematical, Physical and Engineering Sciences,* Vol. 453, No. 1965. (1997): 2229-2240.

[41]   Benjamin, T.B. "The threefold classification of unstable disturbances in flexible surfaces bounding inviscid flows." *Journal of Fluid Mechanics,* Vol. 16, No. 3. (1963).

[42]   Landahl, M. T. "On the stability of a laminar incompressible boundary layer over a flexible surface." *Journal of Fluid Mechanics,* Vol. 13, No. 4: (1962): 609-632.

[43]   Marshallsay, P., Brooks, L. A., Cederholm, A., Doolan, C. J., Moreau, D. J., and Albarracin, C., "Improved Delayed Detached Eddy Simulation Modeling and Far-field Trailing-edge Noise Estimation of a Sharp-edged Symmetric Strut." *Proceedings of Meetings on Acoustics, Acoustical Society of America*, 2013.

[44]   Karimi, M., Croaker, P., Skvortsov, A., Moreau, D. J., and Kessissoglou, N., "Numerical Prediction of Turbulent Boundary Layer Noise from a Sharp-edged Flat Plate." *International Journal for Numerical Methods in Fluids* (2019).

[45]   Croaker, P., Kessissoglou, N., Karimi, M., Doolan, C., and Chen, L., "Self-noise prediction of a flat plate using a hybrid RANS-BEM technique." *43rd International Congress on Noise Control Engineering: Improving the World through Noise Control, Internoise,* 2014.

[46]   Giridhar, R., Farokhi, S., and Taghavi, R. "Aerodynamic Noise Generated by the NREL Phase VI Wind Turbine Rotor." *37th Wind Energy Symposium - AIAA SciTech Forum,* January 7-11, 2019.

[47]   Valleru, V., Taghavi, R., and Farokhi, S. "Aeroacoustic Analysis of a Wind Turbine with Sinusoidal Leading-Edge Blade." *37th Wind Energy Symposium - AIAA SciTech Forum,* January 7-11, 2019.

[48]   Moreau, D. J., Brooks, L. A., and Doolan, C. J., "Broadband Trailing Edge Noise from a Sharp-edged Strut." *The Journal of the Acoustical Society of America,* Vol. 129, No. 5 (2011): 2820-829.

[49]   Tadamasa, A., and Zangeneh, M., "Numerical Prediction of Wind Turbine Noise." *Renewable Energy,* Vol. 36, No. 7 (2011): 1902-912.

[50]   Ghasemian, M., and Nejat, A., "Aerodynamic Noise Prediction of a Horizontal Axis Wind Turbine Using Improved Delayed Detached Eddy Simulation and Acoustic Analogy." *Energy Conversion and Management,* Vol. 99 (2015): 210-20.

[51]   Ma, P., Lien,F-S., and Yee, E., "Coarse-resolution Numerical Prediction of Small Wind Turbine Noise with Validation against Field Measurements." *Renewable Energy,* Vol. 102 (2017): 502-515.

[52]   Wasala, S.H., Storey, R.C., Norris, S.E., and Cater, J.E., "Aeroacoustic Noise Prediction for Wind Turbines Using Large Eddy Simulation." *Journal of Wind Engineering and Industrial Aerodynamics,* Vol. 145 (2015): 17-29.

[53]   STAR-CCM+ v.15.02.009-R8 Documentation.

[54]   Shur, M.L., Spalart, P.R., Strelets, M. K., and Travin, A.K., "A hybrid RANS-LES approach with delayed-DES and wall-modelled LES capabilities", *International Journal Heat and Fluid Flow*, Vol. 29, No. 6 (2008): 1638-1649.

[55]   Brentner, K.S., and Farassat, F., "Modeling aerodynamically generated sound of helicopter rotors", *Progress in Aerospace Sciences*, Vol. 39, No. 2-3 (2003): 83-120.

[56]   Farassat, F., "Derivation of formulations 1 and 1A of Farassat", *Technical Memorandum* (2007): TM-2007-214853, NASA-Langley Research Center (USA).

[57]   Moreau, D.J., Brooks, L. A. and Doolan C.J. "The effect of boundary layer type on trailing edge noise from sharp-edged flat plates at low to moderate Reynolds number." *Journal of Sound and Vibration*, Vol. 33, No. 17 (2012): 3976-3988.

[58]   Tong, F., Qiao, W., Chen, W., Wang, L. and Wang, X. "Broadband noise prediction using large eddy simulation and a frequency domain method." *Applied Acoustics,* Vol. 117 (2017): 94-105.

[59]   Lee, F., and Cheong, C. "Frequency-domain prediction of broadband trailing edge noise from a blunt flat plate." *Journal of Sound and Vibration*, Vol. 332, No. 21 (2013): 5322-5344.

[60]   Lighthill, M. "On sound generated aerodynamically: general theory." *Proceedings of the Royal Society of London*, Vol. 231 (1952): 564-587.

[61]   Solis-Gallego, I., Meana-Fernandez, A., Oro, J. F., Diaz, K. A. and Velarde-Suarez, S. "LES-based numerical prediction of the trailing-edge noise in a small wind turbine airfoil at different angles of attack." *Renewable Energy,* Vol. 120 (2018): 241-254.

[62]   Zhang, C., Wang, J., Blake, W., and Katz, J. "Deformation of a compliant wall in a turbulent channel flow." *Journal of Fluid Mechanics,* Vol. 823 (2017): 345-390.

[63]   Zhang, C., Miorini, R., and Katz, J. "Integrating Mach-Zehnder interferometry with TPIV to measure the time-resolved deformation of a compliant wall along with a 3D velocity field in a turbulent channel flow." *Experiments in Fluids,* Vol. 56, No. 11 (2015).

[64]   Endo, T., and Himeno, R. "Direct numerical simulation of turbulent flow over a compliant wall surface." *Journal of Turbulence,* Vol. 3. (2002).

[65]   Fukagata, K., Kern, S., Catelain, P., Koumoutsakos, P. and Kasagi, N "Evolutionary optimization of an anisotropic compliant surface for turbulent friction drag reduction." *Journal of Turbulence,* Vol. 9 (2008).

[66]   Xia, Q.-J, Huang, W.-X., and Xu, C.-X "Direct numerical simulation of turbulent boundary layers over a compliant wall." *Journal of Fluids and Structures,* Vol. 71 (2017): 126-142.

[67]   Nakanishi, R., Mamori, H., and Fukagata, K. "Relaminarization of turbulent channel flow using traveling wave-like wall deformation." *International Journal of Heat and Fluid Flow*, Vol. 35 (2012): 152-159.

[68]   Kim, E., and Choi, H. "Space-time characteristics of a compliant wall in a turbulent channel flow." *Journal of Fluid Mechanics,* Vol. 756 (2014): 30-53.

[69]   Xia, Q.-J, Huang, W.-X, and Xu, C.-X. "Direct numerical simulation of a turbulent boundary layer over an anisotropic compliant wall." *Acta Mechanica Sinica,* Vol. 35, No. 2 (2019): 384-400.

[70]   Intravartolo, N., Sorrells, T., Ashkharian, N., and Kim, R. "Attenuation of vortex noise generated by UAV propellers at low Reynolds Numbers." *55th AIAA Aerospace Sciences Meeting*: (2017).

[71]   Van Treuren, K., and Wisniewski, C. "Testing propeller tip modifications to reduce acoustic noise generation on a quadcopter propeller." *ASME Journal of Engineering for Gas Turbines and Power*, Vol. 141 (2019): 121017-1 – 121017-12.

[72]   Brungart, T. A., Olson, S. T., Kline, B. L., and Yoas, Z. W. "The reduction of Quadcopter Propeller Noise." *Noise Control Engineering Journal*, Vol. 67, No. 4 (2019): 252–269.

[73]   Leslie, A., Wong, K. C., and Auld, D. "Broadband noise reduction on a mini-UAV propeller." *14th AIAA/CEAS Aeroacoustics Conference,* May 5-7, 2008.

[74]   Guo, J., Zhou, T., Fang, Y., and Zhang, X. "Experimental study on a compact lined circular duct for small-scale propeller noise reduction." *Applied Acoustics*, Vol. 179, No. 108062: (2021).

[75]   Ning, Z., Wlezien, R. W., and Hu, H. "An experimental study on small UAV propellers with serrated trailing edges." *47th AIAA Fluid Dynamics Conference.* 5-9 June, 2017.

[76]   Ning, Z., and Hu, H. "An experimental study on the aerodynamic and aeroacoustic performances of a bio-inspired UAV Propeller." *35th AIAA Applied Aerodynamics Conference.* 5-9 June, 2017.

[77]   Malgoezar, A. M. N., Vieira, A., Snellen, M., Simons, D. G., and Veldhuis, L. L. M. "Experimental characterization of noise radiation from a ducted propeller of an unmanned aerial vehicle." *International Journal of Aeroacoustics*, Vol. 18, No. 4-5, (2019): 372–391.

[78]   Ben-Gida, H., Faran, M., and Kogan, T. "Noise Reduction of a UAV Propeller Using Grit-Type Boundary Layer Tripping." *Proceedings of the 57th Israel Annual Conference on Aerospace Sciences, Tel-Aviv & Haifa, Israel.* 15-16 March, 2017.

[79] Podsedkowski, M., Konopinski, R., and Lipian, M. "Sound noise properties of variable pitch propeller for small UAV." *2022 International Conference on Unmanned Aircraft Systems (ICUAS)*. 21-24 June, 2022.

[80] Pang, E., Cambray, A., Rezgui, D., Azarpeyvand, M., and Showkat Ali, S. A.. "Investigation towards a better understanding of noise generation from UAV Propellers." *2018 AIAA/CEAS Aeroacoustics Conference*. 25-29 June, 2018.

[81] Yu, Y. H., Gmelin, B., Splettstoesser, W., Philippe, J. J., Prieur, J., and Brooks, T. F. "Reduction of helicopter blade-vortex interaction noise by Active Rotor Control Technology." *Progress in Aerospace Sciences*, Vol. 33, No. 9-10 (1997): 647–687.

[82] Szulc, O., and Doerffer, P. (2018). "Numerical study of potential application of active suction and blowing through blade tip perforation to reduction of helicopter rotor thickness noise." *Journal of Physics: Conference Series*, Vol. 1101, No. 012042: (2018).

[83] Sun, Y., Xu, G., and Shi, Y. "Numerical investigation on noise reduction of rotor blade-vortex interaction using blade surface jet blowing." *Aerospace Science and Technology*, Vol. 116, No. 106868, (2021): 1 –16.

[84] Chen, P. C., Baeder, J. D., Evans, R. A., and Niemczuk, J. "Blade-vortex interaction noise reduction with active Twist Smart Rotor Technology." *Smart Materials and Structures*, Vol. 10, No. 1, (2001): 77–85.

[85] Edwards, B., and Cox, C. "Revolutionary concepts for helicopter noise reduction – S.I.L.E.N.T program" *NASA Library, Langley Research Center, Hampton, VA*. NASA/CR-2002-211650.

[86] Pegg, R. J., Hosier, R. N., Balcerak, J. C., and Johnson, K. "Design and preliminary tests of a blade tip air mass injection system for vortex modification and possible noise

reduction on a full-scale helicopter rotor." *Technical Memorandum – NASA Langley Research Center, Hampton, VA.* Report No. NASA TM X-3314.

[87]   Technical Data Sheet, Sylgard 184 Silicone Elastomer, *Dow Corning Corporation*

[88]   Kutty, H., and Rajendran, P. "3D CFD simulation and experimental validation of small APC Slow Flyer Propeller blade." *MDPI Aerospace*, Vol. 4-1, No. 10: (2017).

[89]   White, F., M., *Viscous Fluid Flow*, Mc Graw-Hill, 2005.

[90]   Farokhi, S., *Future Propulsion Systems and Energy Sources in Sustainable Aviation*, John Wiley, Ltd., Chichester (UK), 2020.

[91]   Cebeci, T., *Engineering Approach to the Calculation of Aerodynamic Flows,* Springer Verlag, Berlin, 1999.

[92]   Selig, M.S., and Mcgranahan, B. D., "Wind Tunnel Aerodynamic Tests of Six Airfoils for Use on Small Wind Turbines." *Journal of Solar Energy Engineering,* Vol. 126, No. 4 (2004): 986-1001.

[93]   Migliore, P., and Oerlemans, S. "Wind Tunnel Aeroacoustic Tests of Six Airfoils For Use on Small Wind Turbines". *Journal of Solar Energy Engineering,* Vol. 126, No. 4 (2004): 974-985.

9. APPENDIX

9.1. Compliant coating preparation

The compliant coating is prepared using silicone oil and Dow Corning Sylgard 184 by mixing the two in the ratio of 9:1 by mass. Its molecular formula is polydimethylsiloxane and a structural formula $[-O-Si(CH_3)_2-]_n$. The mixture takes 48 hours to cure through room temperature vulcanization and is ready for use after 7 days. The steps employed in preparing the coating sheets are outlined below:


Fig. 9.1: Using syringe to transfer base material

1. Firstly, 180 grams silicone oil, normally stored at room temperature conditions, is drawn using a syringe and transferred into a cup, as shown in Fig. 9.1-9.2.

2. A mass balance, as shown in Fig. 9.2 is used to measure the amount of silicone oil being transferred to the cup.

3. To this cup, 20 grams of Dow-Corning Sylgard is added using a dropper, as shown in Fig. 9.3.

4. This mixture is stirred slowly for 20 minutes to ensure that the binding agent and base material blend uniformly.

Fig. 9.2: 180 grams of base materials transferred to a cup
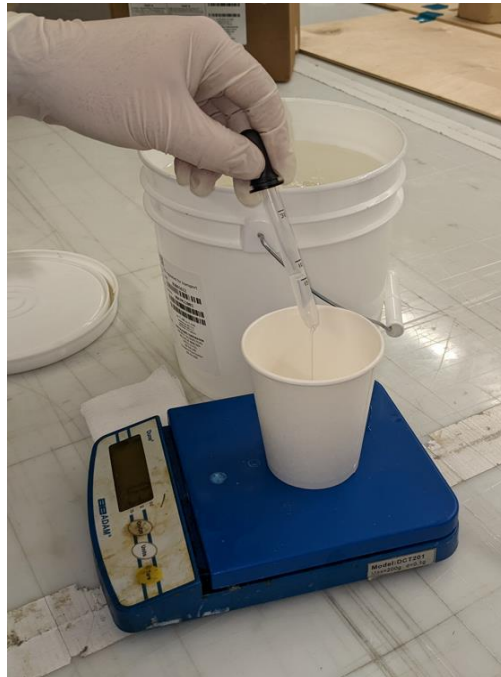
Fig. 9.3: 20 grams of binding agent added using a dropper

Fig. 9.4: Stir mixture for 20 minutes

5. Once the mixture is stirred thoroughly, it is left to rest for about 30 minutes. During this time, the bubbles formed inside the mixture rises to the surface and disappears over time.

Fig. 9.5: Bubbles disappearing from mixture at different stages of time

6. Fig. 9.5 shows bubbles disappearing from the mixture at different stages of time. It is crucial to wait for the bubbles to disappear from the mixture. Otherwise, these would

form air-pockets inside the compliant coating after it has cured, thus weakening its material stiffness.

Fig. 9.6: Teflon release tape used to create base of mold

7. A teflon release tape, shown in Fig. 9.6, is applied onto a flat surface. Length of the tape is equal to half of the flat plate span (24.1") and width of the tape is equal to 18.4" which is sufficient to wrap the suction and pressure surfaces of the flat plate.
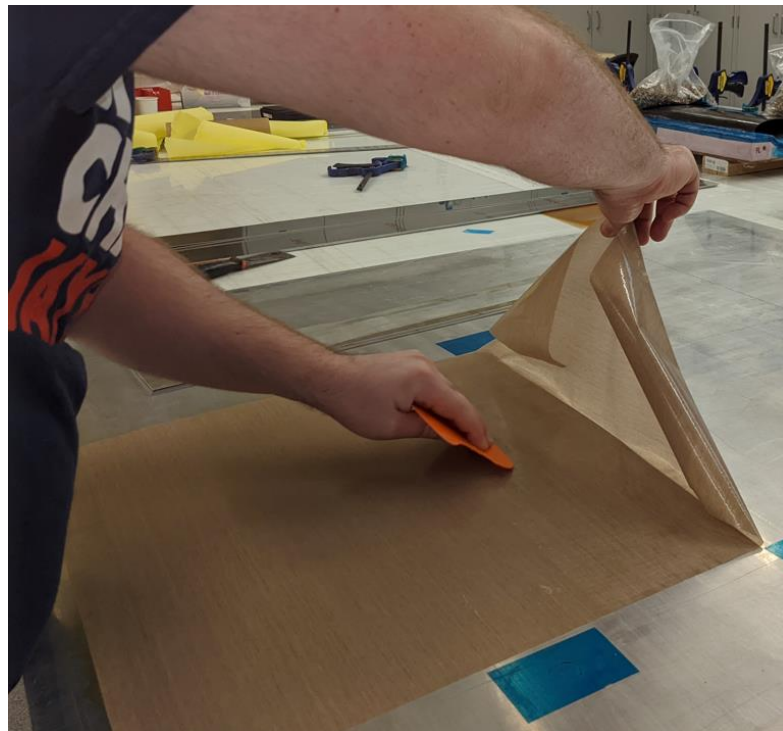

Fig. 9.7: Teflon release tape cut to dimensions of 24.1"x18.4"

Fig. 9.8: Peel back layer of the teflon release tape

8. Once the teflon release tape is cut to the appropriate dimensions, the back layer of the teflon is peeled and applied onto a steel board.
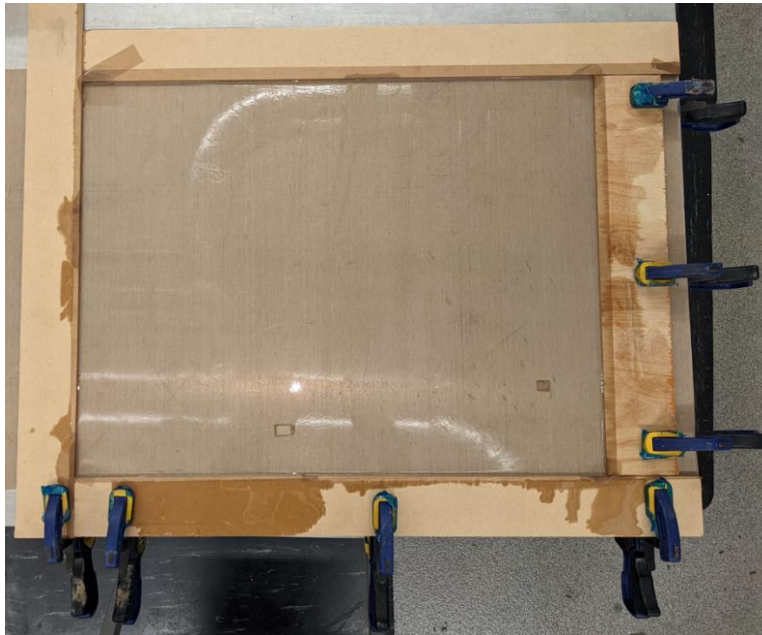

Fig. 9.9: Paste teflon release tape on a steel board

Fig. 9.10: Remove any air-pockets formed while laying the tape

9. Care must be taken to remove any air-pockets formed while applying the tape on the steel board.


Fig. 9.11: Mold with thickness of 5 mm

10. Based on the desired coating thickness, a wooden frame of 5 mm thickness is provided along the circumference of the teflon tape and is held in position using clamps and sandbags, as seen in Fig. 9.11 and Fig. 9.12.

198

Fig. 9.12: Sand bags and clamps to keep mold intact

11. The mixture from Step 5 is now poured into the frame and allowed to rest for 48 hours. The coating solidifies through room temperature vulcanization process and finally yields a sheet of coating, as seen in Fig. 9.13 that is wrapped around the flat plate. We prepared 2 such coatings for our experiments.
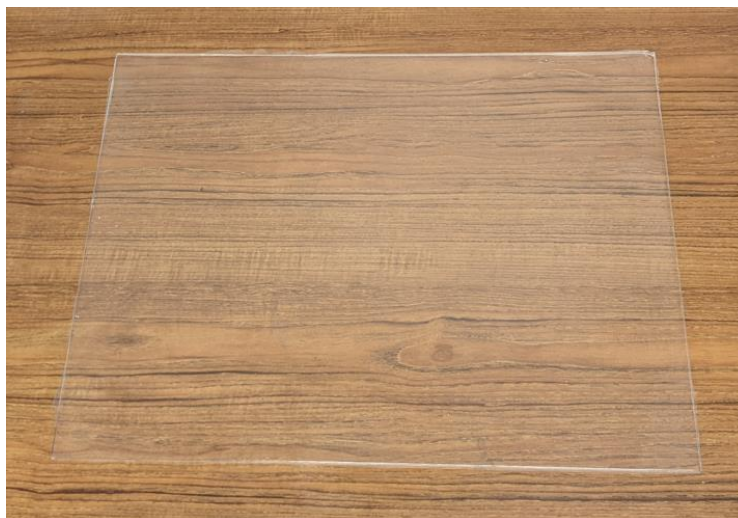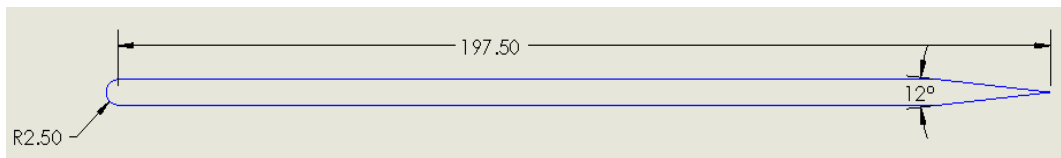

**Fig. 9.13: Compliant coating sheet**

9.2.   Flat plate preparation

1. To prepare the flat plate with compliant coating applied to it, we first created the base flat plate model whose shape has the same dimensions as the flat plate model used in the experimental studies conducted by Moreau et al. [48] in their anechoic wind tunnel at the University of Adelaide.


Fig. 9.14: Flat plate geometry used for experiments by Moreau et al. [48]

2. As seen in Fig. 9.14, the flat plate model consisted of three components; a semi-circular leading-edge with a diameter of 5 mm, a sharp trailing-edge with an apex angle of 12° and a flat portion of the plate with an approximate length of 173.72 mm. Based on the width of the closed loop wind tunnel's test section, the span of the flat plate was chosen to be 48 inches to prevent tip-vortices and ensure two-dimensional flow behavior across its span.
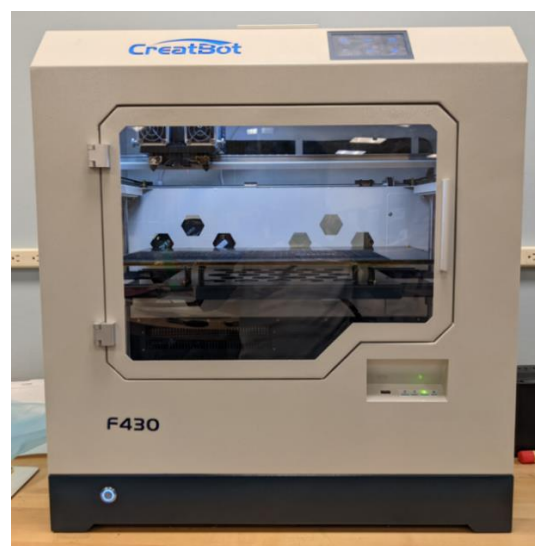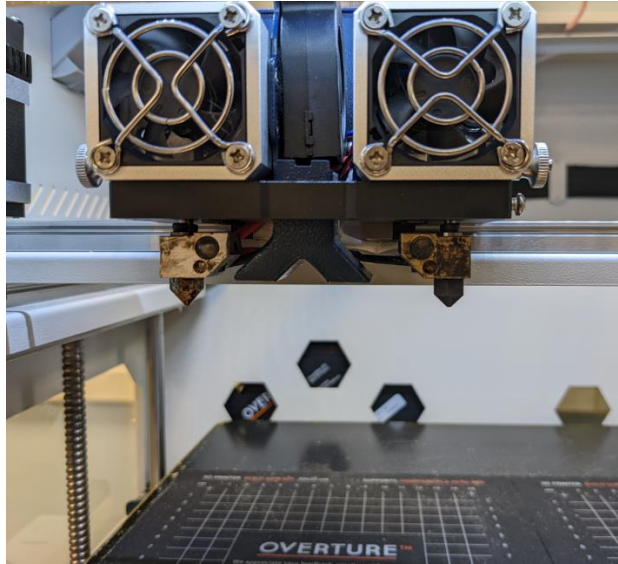

Fig. 9.15: 3D Printer to create leading-edge and trailing-edge of flat plate

3. A wooden plank of the appropriate dimensions was used to prepare the flat portion of the plate. The leading-edge and trailing-edge was prepared using a 3D printer at the Garrison Flight Center at the University of Kansas, as seen in Fig. 9.15.
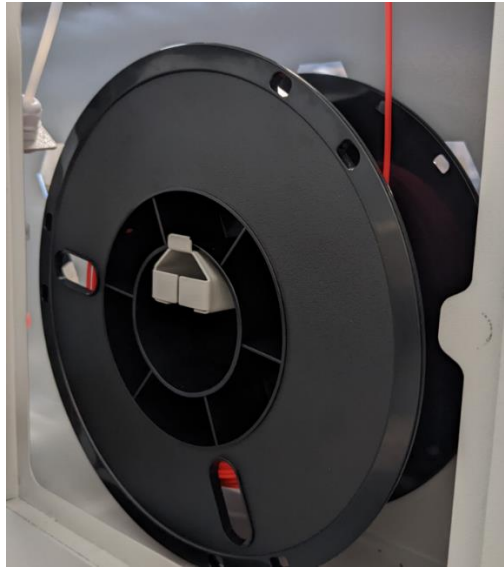
Fig. 9.16: Polylactic acid (PLA) used for 3D printing

4. A spool of polylactic acid (PLA), as seen in Fig. 9.16, was used to prepare the leading-edge and trailing-edge pieces. This PLA was heated, melted and passed through injection nozzles, as seen in Fig. 9.17. This nozzle injects PLA onto the test-bed to obtain the desired shape.

5. Due to the 3D printer's limited test bed size, 5 leading-edge pieces were prepared with a span of 200 mm and 2 leading-edge pieces were prepared with a span of 112.5 mm. The total span of these 7 pieces would equal the flat plate span. Similarly, 5 trailing-edge pieces of 200 mm and 2 trailing-edge pieces of 112.5 mm were prepared using the 3D printer.

Fig. 9.17: Nozzle injects PLA to create leading-edge and trailing-edge of flat plate

6. Trailing-edge pieces obtained from the 3D printer are shown in Fig. 9.18. The flat surface of the trailing-edge pieces that would be attached to the wooden plank required smoothening of its surface. An 80 grit sand paper was used for this purpose and the finished trailing-edge pieces are shown in Fig. 9.19.
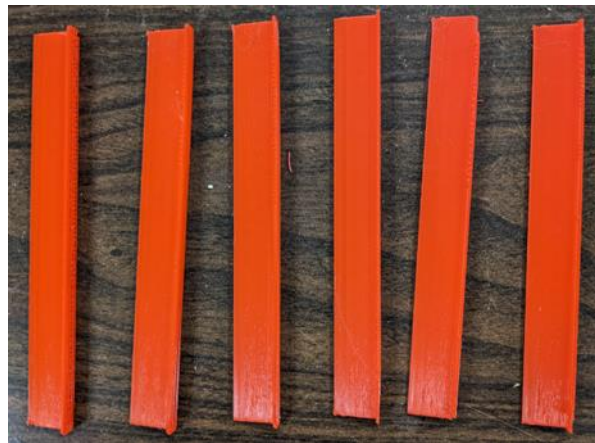
Fig. 9.18: Trailing-edge pieces before sanding
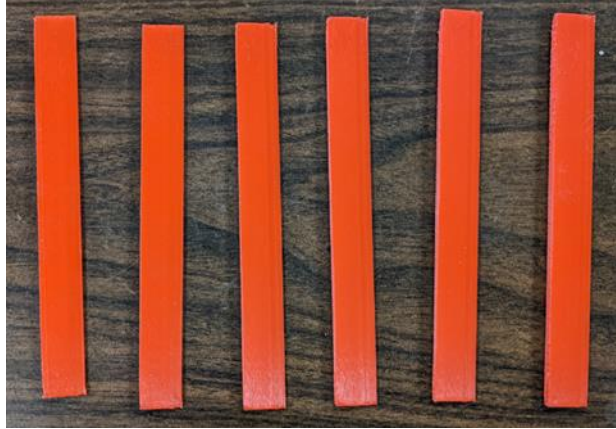
Fig. 9.19: Finished trailing-edge pieces

7. Similarly, the leading-edge pieces from the 3D printer are shown in Fig. 9.20 and the

    80 grit sand paper was used to smoothen the flat surface of the leading-edge before

    it is attached to the wooden plank.

Fig. 9.20: Leading-edge pieces before sanding

8. The finished leading-edge pieces are shown in Fig. 9.21, which would be attached to

    the wooden plank using 5-minute epoxy resin and hardener.
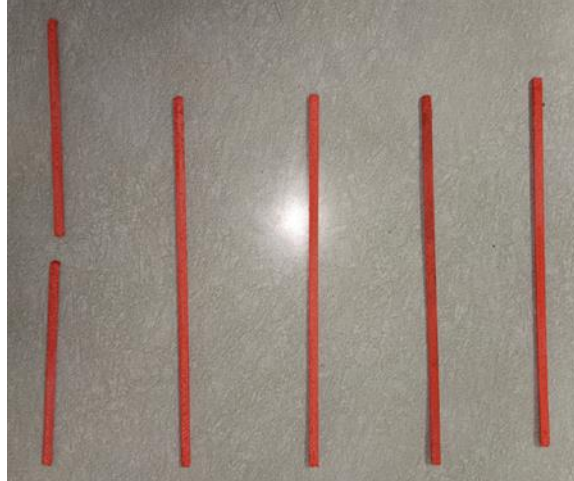
Fig. 9.21: Finished leading-edge pieces

9. The five-minute epoxy resin, as seen in Fig. 9.22, is mixed with hardener in 1:1 ratio by mass. A mass balance, as seen in Fig. 9.23 is used to measure mass of the mixture to ensure accuracy of mixture ratio.

Fig. 9.22: Five-minute epoxy resin and hardener

Fig. 9.23: Mass balance

10. The resin and hardener are mixed thoroughly and applied on the flat surface of a trailing-edge piece. Next, the trailing-edge piece is held against the wooden plank as seen in Fig. 9.24 and pressure is applied on this piece for 10 minutes until the epoxy resin cures and the trailing-edge piece attach to the wooden plank.

11. This process is repeated for each trailing-edge piece and leading edge-piece until the entire flat plat is assembled, as seen in Fig. 9.25.


Fig. 9.24: Trailing-edge attached to flat plate using epoxy resin

Fig. 9.25: Leading-edge and trailing-edge attached to flat plate geometry

12. To apply the compliant coating on the flat plate model shown in Fig. 9.26, 30-minute epoxy resin and hardener is used. It is important to use 30-minute expoxy resin at this step and not any other adhesive with a lower curing time as we require this duration to apply the epoxy resin on the flat plate surface and apply the compliant coating around, as seen in the follwing steps. Failure to do this will result in air-pockets between the coating and the flat plate model.
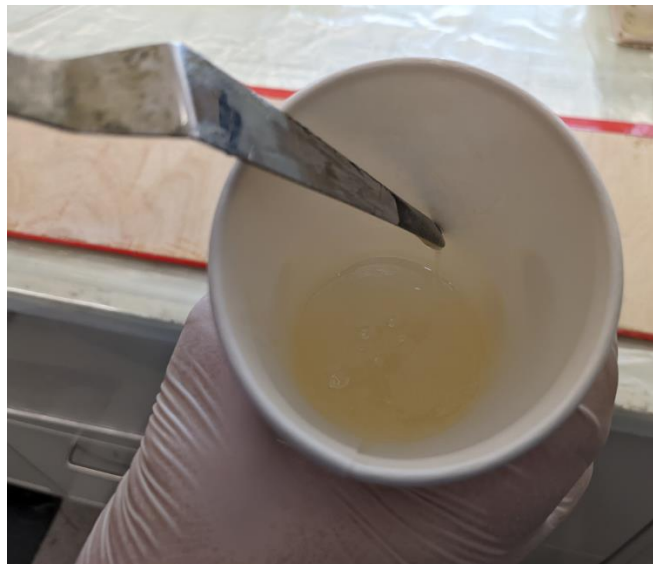
Fig. 9.26: Thirty-minute epoxy resin and hardener

13. The 30-minute epoxy resin and hardener is mixed in the ratio of 1:1 by mass, as seen in Fig. 9.26. This mixture is first applied to the bottom side of the flat plate along half the span of this plate on its left side, as seen in Fig. 9.27.

206

Fig. 9.27: Binding mixture applied on left side of flat-plate surface

14. The compliant coating is placed below this flat plate where 30-minute epoxy is applied and made sure that the coating and plate are aligned appropriately. After this, sand bags are placed on of the flat-plate, as seen in Fig. 9.28 to apply pressure. It takes a minimum of 30 minutes for the coating to bind itself to the flat-plate. An additional 30 minutes time is provided for the epoxy to cure, after which the process is repeated on its top surface and the flat plate is wrapped by the compliant coating on its left side.

Fig. 9.28: Sand bags used to apply pressure on compliant coating
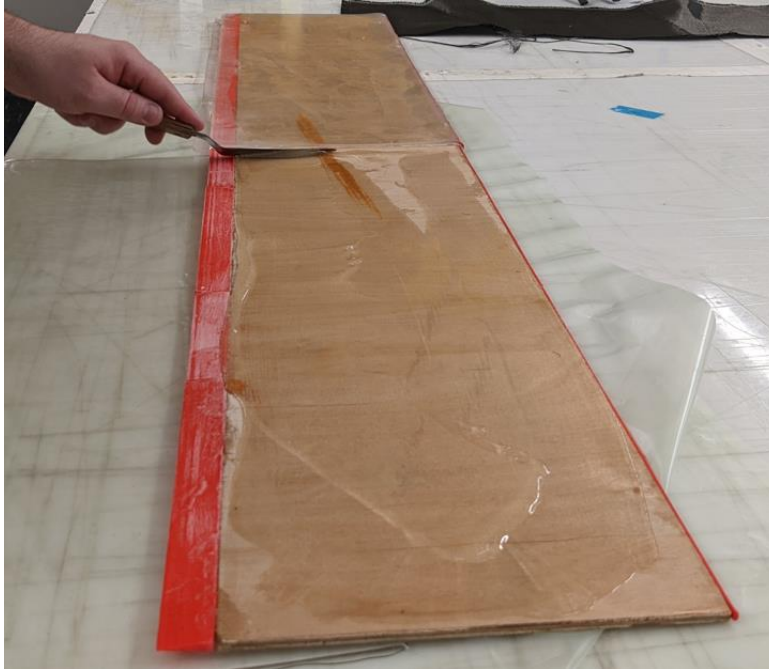
Fig. 9.29: Binding mixture applied on right side of flat-plate surface

15. The same procedure is employed to apply the compliant coating on the right side of the flat plate. Epoxy resin is first applied on its bottom surface, as seen in Fig. 9.29 Once compliant coating is placed below this plate, sand bags are used to apply pressure on the plate, as seen in Fig. 9.30. The process is repeated on its top surface and finally the flat plate is wrapped by the compliant coating.

Fig. 9.30: Sand bags used to apply pressure on compliant coating

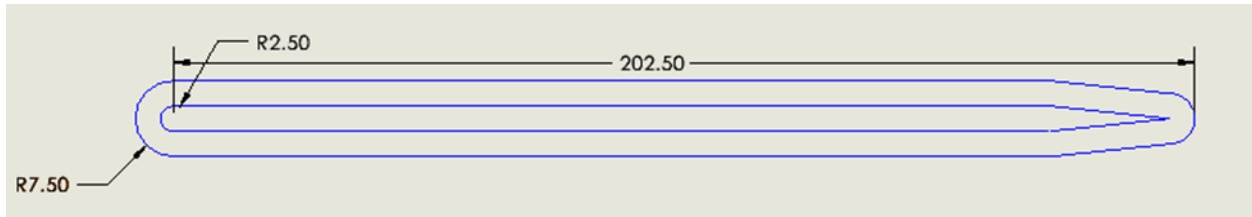**Fig. 9.31: Schematic diagram of compliant coating applied on flat plate**

16. A schematic diagram of the compliant coating applied on the flat plate is shown in Fig. 9.31 and the finished model of the compliant coating applied on the flat plate is shown in Fig. 9.32. This model will be mounted inside the wind tunnel test section for experimentation.

Fig. 9.32: Finished model – compliant coating applied to flat plate

17. The same procedure as outlined earlier is used to prepared the baseline flat plate model. The only difference is that the thickness of the baseline flat plate model is greater and is equal to 7.5 mm, as shown in Fig. 9.33.
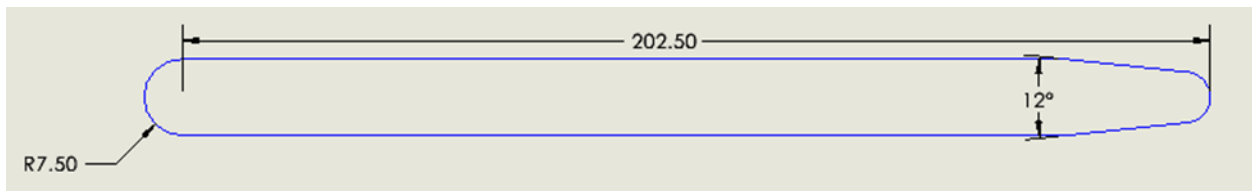
Fig. 9.33: Schematic diagram of baseline flat plate model

Fig. 9.34: Finished baseline model

18. Finally, the finished baseline model is shown in Fig. 9.34 which would be mounted inside the wind tunnel test section for experimentation and farfield noise measurements.

9.3.   Microphone calibration and noise data collection

1. Connect the Ethernet cable to the Lab Room Next door, as shown in Fig. 9.35.
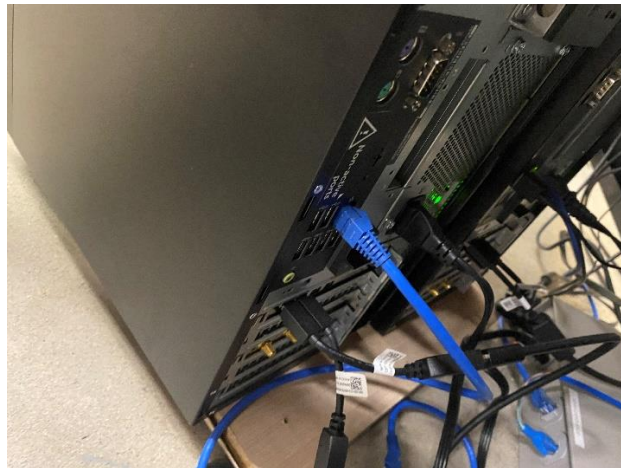
Fig. 9.35: Make sure Ethernet is connected to CPU

2. Switch on the Computer

3. Login into the computer:

   A. Username: .\transverse

   B. Password: Windtunnel2021!

4. Double click on Lab View and MATLAB

5. Test the batteries in the microphone's amplifier

    A. Push the **RED Button** to the right so that the needle points to <mark>"Batt ok!"</mark>

    B. Else Replace Batteries!!

Fig. 9.36: Microphone Amplifier

6. Push the **RED Button** to the middle position to switch on the Microphone Amplifier, as shown in Fig. 9.36.

7. Open Lab View: Once Lab View is open, Hit Ctrl+E

8. Double click on "Write to Measurement file" and change filename to

    "MM_DD_YYYY_Trial_NN.lvm"

9. Ctrl+E to minimize the back end of Lab View

10. Place the calibrator such that the microphone is seated inside the calibrator.

Fig. 9.37: Microphone positioned inside the calibrator

11. Hit the RUN button *(An arrow mark present on the top left corner of Lab View)*

12. Hit the Disable Button and change it to **Enable** to record data

13. Give a thumbs up! to the person using the calibrator

14. Press the ON Button on the Microphone calibrator

15. The calibrator produces a tone of 94 dB at a frequency of 1000 Hz for a few seconds.

16. The using the Calibrator gives a thumbs up, after the tonal noise stops.

17. Press the Enable button and change it to **Disable** to stop collecting data

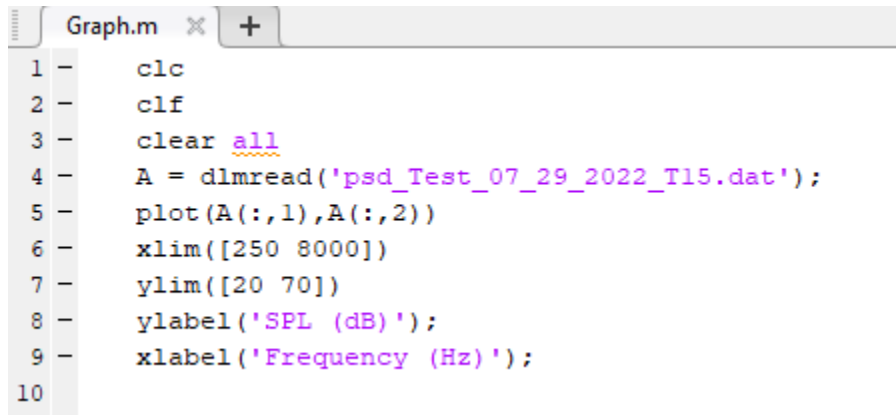18. Hit the **STOP** Button

9.3.1. Post Processing Data

1. Using the command prompt in a Windows system, run the fftpsd in-house code

   created at KUAE to extract noise measurements. Command is as follows:

   fftpsd2.exe -i Test_DD_MM_YYYY_Trial_NN.lvm -l 22 -w rectangular -s 0. -spl

   spl_Test_DD_MM.dat -spec

In the Graph.m MATLAB script, change the filename to

'SPL_Test_MM_DD_YYYY_Trial_NN.dat'

2. Run Graph.m MATLAB script and obtain graph of SPL VS Frequency

```
1   clc
2   clf
3   clear all
4   A = dlmread('psd_Test_07_29_2022_T15.dat');
5   plot(A(:,1),A(:,2))
6   xlim([250 8000])
7   ylim([20 70])
8   ylabel('SPL (dB)');
9   xlabel('Frequency (Hz)');
10
```

Fig. 9.38: Sample code used to extract noise measurements from dat file

3. *Please note:*

A. To find power spectral density, change the term 'spl' to 'psd' in the above commands.

B. If one requires Hann window function, the following command is to be used:

fftpsd2.exe -i Test_DD_MM_YYYY_Trial_NN.lvm -l 0.04 -w hann -spl spl_Test_DD_MM.dat -spec

9.3.2. Adjusting Peak Frequency

1. In Lab View, Hit Ctrl + E to view back end of program

2. Change the multiplication factor located after DAQ Assistant ICON.

3. Run the program using the above two set of steps and keep repeating the process until a peak SPL of 94 dB is obtained at a frequency of 1000 Hz.

213

9.4. Closed loop wind tunnel operating procedure

PLEASE CHECK FOR ANY DEBRIS OR UNSECURED EQUIPMENT IN WIND TUNNEL TEST SECTION

1. Insert master-key into the main-power input, as shown in the **RED** box in Fig. 9.39, and turn the key in counterclockwise direction to supply power to the wind tunnel control system.
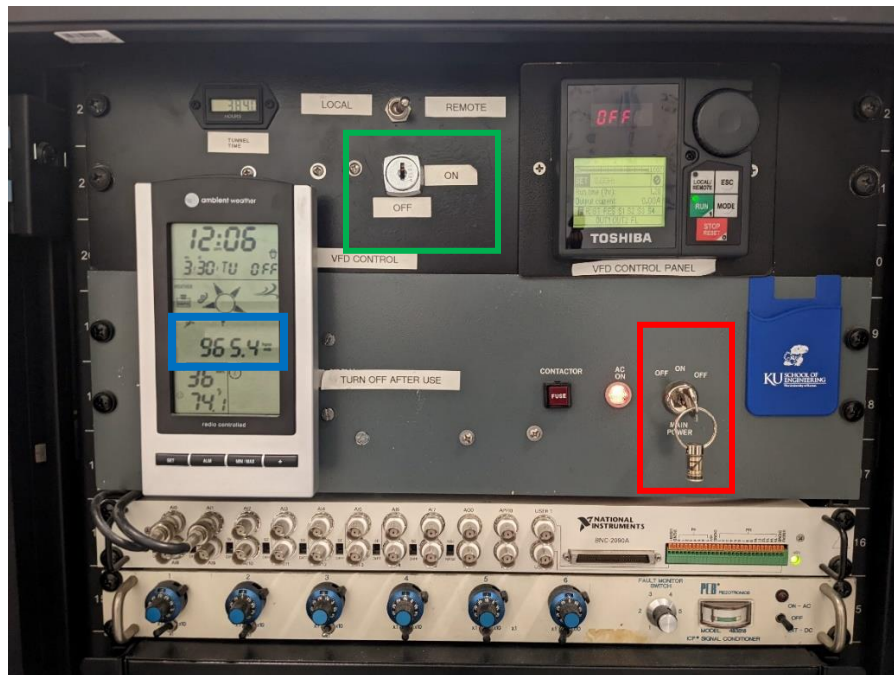
Fig. 9.39: Wind tunnel Control System

2. When the computer boots, hit Ctrl+Alt Delete.

   Please note:

   If the computer displays a warning on startup, hit F1 to continue to next step.

3. To login the computer, enter:

   Username- *.\kulwt*

   Password- *Foulwind2021*

4. Make sure to connect to university's WiFi Internet.

5. Double click on Wind Tunnel VI, a LabVIEW icon present on Desktop.

6. The Wind Tunnel virtual interface, as seen in Fig. 9.40, now opens.

Fig. 9.40: LabVIEW Interface

7. On the top toolbar of the LabVIEW Interface, select Windows > Block Diagram

8. This opens a block diagram used to collect measurement data from the wind tunnel test section.

9. Double click on the icon called "Write to measurement".

10. Choose an appropriate path file and change *Filename* suitably to reflect the test conditions for which the data is being collected.

11. Make sure the file extension is set to *.lvm*.

12. Click on the log button and change its color to **RED** which enables data collection.

13. Note down the ambient pressure in hecta-pascals from the wind tunnel control system, as shown in the **BLUE** box in Fig. 9.39 and enter this value in the **BLUE** box shown in Fig. 9.40.

14. Insert the secondary key in the wind tunnel control system, as shown in the **GREEN** box in Fig. 9.39, to switch on the wind tunnel.

15. Hit the **RUN** Button, a white arrow mark ⇨ located on the top toolbar in LabVIEW.

16. Press the **Zero** button in LabVIEW Interface, as shown in the **YELLOW** box in Fig. 9.40. This ensures that there are no zeroing errors in the pressure and velocity measurements.

    Please note:

    After **Zero** button is pressed, it takes 5-10 seconds for LabVIEW to address zeroing errors.

17. To run the wind tunnel at the desired speed, increase the percentage power supplied to the motor using the **UP**-arrow mark shown in the **GREEN** box in Fig. 9.40. Make increments in steps of 1% and monitor the **Pitot-Static velocity (mph)** until the desired wind speed is attained.

18. Allow 1-2 minutes for flow to stabilize before starting experiment. This is indicated by a constant pitot-static velocity reading.

19. Once experiment is completed, decrease percentage motor power by 1% gradually until 0%.

Please note:

If at the end, motor power is in fraction (for example: 0.5%), manually change this number to 0% instead of pressing the **DOWN**-arrow mark. Using the **DOWN**-arrow mark will crash LabView.

20. Wait for some time until the pitot static velocity reduces to 0 ft/s.

21. Switch **OFF** the wind tunnel using the secondary key as shown in the **GREEN** box in Fig. 9.39.

22. Remove the secondary key for safety purposes.

23. Hit the **STOP** button present in the top toolbar of LabVIEW interface.

24. Close LabVIEW Interface by hitting the (X) mark on the top right corner of GUI

25. Transfer *.lvm* output file from CPU to your storage device.

26. Start > Shutdown!

27. Switch OFF the wind tunnel control system using the master-key shown in the **RED** box of Fig. 9.39.

28. Remove master-key from the wind tunnel control system

29. Return master-key and secondary key to the Lab Coordinator.

9.4.1. Data collection:

A. Test section temperature is recorded in *Column 1* of the output file and has units of T (°R)/500

B. Test section temperature is recorded in *Column 2* of the output file and has units of T (°F)

C. Test section air density is recorded in *Column 3* of the output file and has units of slugs/ft^3

D. Pitot static wind velocity is recorded in *Column 4* of the output file and has units of ft/s

E. Manually note down test section static pressure reading (psf) from LabVIEW interface during each trial.